Thermolabile molecules deposited by electrospray probed by STM

PATRICK LAWES

Defence date: **16 July 2025**

To obtain the following grades:

Doktors der Natruwissenscahften (Dr. rer. nat.) von der KIT-Fakultät für Chemie und Biowissenschaften des Karlsruher Instituts für Technologie (KIT)

Docteur de l'Université de Strasbourg en Nanophysique, ÉCOLE DOCTORALE de Physique et Chimie Physique (ED182), (UMR 7504 CNRS – Unistra)

THESIS supervisors:

RUBEN MARIO	Professor, Karlsruhe Institute of Technology
BUCHER JEAN-PIERRE	Professor, Université de Strasbourg

Reporters:

PAPAGEORGIOU ANTHOULA	Professor, National and Kapodistrian University of Athens
BARTH JOHANNES	Professor, TU München

Examiners:

ALOUANI MEBAREK	Professor, Université de Strasbourg
WULFHEKEL WULF	Professor, Karlsruhe Institute of Technology

Thermolabile molecules deposited by electrospray probed by STM

Zur Erlangung des akademischen Grades eines

DOKTORS DER NATURWISSENSCHAFTEN

von der KIT-Fakultät für Physik des

Karlsruher Instituts für Technologie (KIT)

Docteur de l'Université de Strasbourg en Nanophysique, ÉCOLE DOCTORALE de Physique et Chimie Physique (ED182), (UMR 7504 CNRS – Unistra)

angenommene DISSERTATION

von

Patrick Lawes MSc

aus Hitchin

Tag der mündlichen Prüfung:	16.07.2025
Betreuer:	RUBEN Mario BUCHER Jean-Pierre
Referent/Referentin:	PAPAGEORGIOU Anthoula BARTH Johannes
Prüfer:	ALOUANI Mebarek WULFHEKEL Wulf

Declaration

According to §13 paragraph 2 number 3 of the doctoral degree regulations of the Karlsruhe Institute of Technology for the KIT Faculty of Chemistry and Biosciences:

1. The submitted dissertation titled “Thermolabile molecules deposited by electrospray probed by STM” is my own independent work.
2. I have only used the sources and aids indicated and have not made use of any unauthorized help from third parties. In particular, I have marked content taken literally or analogously from other works as such.
3. I have not previously submitted the thesis or parts thereof to a university in Germany or abroad as part of an examination or qualification.
4. I confirm the accuracy of the above declaration.
5. I am aware of the significance of the affidavit and the consequences under criminal law of an incorrect or incomplete affidavit.

I declare on oath that I have stated the absolute truth to the best of my knowledge and have not concealed anything.

. . . . . .

Eidesstattliche Erklärung

Eidesstattliche Versicherung gemäß§13 Absatz 2 Ziffer 3 der Promotionsordnung des Karlsruher Instituts für Technologie für die KIT-Fakultät für Chemie und Biowissenschaften:

1. Bei der eingereichten Dissertation zu dem Thema “Thermolabile molecules deposited by electrospray probed by STM“ handelt es sich um meine eigenständig erbrachte Leistung.
2. Ich habe nur die angegebenen Quellen und Hilfsmittel benutzt und mich keiner unzulässigen Hilfe Dritter bedient. Insbesondere habe ich wörtlich oder singemäß aus anderen Werken übernommene Inhalte als solche kenntlich gemacht.
3. Die Arbeit oder Teile davon habe ich bislang nicht an einer Hochschule des In- oder Auslands als Bestandteil einer Prüfungs- oder Qualifikationsleistung vorgelegt.
4. Die Richtigkeit der vorstehenden Erklärung bestätige ich.
5. Die Bedeutung der eidesstattlichen Versicherung und die strafrechtlichen Folgen einer unrichtigen oder unvollständigen eidesstattlichen Versicherung sind mir bekannt.

Ich versichere an Eides statt, dass ich nach bestem Wissen die reine Wahrheit erklärt und nichts verschwiegen habe.

.....

Abstract

Creation and study of new materials exploiting sophisticated quantum physics, requires studying equally sophisticated chemistry integrated into structures via novel means. The self-organization of magnetic atoms dressed by ligands, so called single molecule magnets (SMMs), is widely studied and reported. Utilizing electrospray deposition (ESD) permits the study of intricate thermolabile, modifications on the bis(phthalocyaninato) terbium complexes $[TbPc_2]^0$ on surfaces, overcoming limitations of traditional sublimation methods. Functionalization allows for specific tuning of pyhsiochemical properties on the surface. The interdisciplinary methodology—spanning ligand synthesis, precision deposition, and quantum-level probing—underscores the imperative of cross-disciplinary innovation to address emergent scientific challenges within quantum technologies. The study of functionalised unsublimable molecules deposited by ESD probed by STM within this work pertains to multiple goals. A better understanding of the scientific methodology required to carry out these studies, would permit similar experiments outside of the scope of this thesis. By integrating synthetic chemistry, surface science, and quantum technologies, the work studies new quantum materials, with a particular focus towards quantum information processing (QIP) applications.

The first project within this framework is the validation of ESD as a viable technique, demonstrating intact deposition of $[TbPc_2]^0$, with the restored radical property confirmed by a Kondo resonance, matching sublimation results. This is of particular relevance as the molecule is necessarily charged for ESD. Based on the successful measurement of Kondo effect of $[TbPc_2]^0$ deposited on surface via ESD, a study into tuning the Kondo properties towards the goal of studying quantum critical Kondo lattices will be progressed. Towards this goal, a tuned lattice of alkyl functionalised $[TbPc_2]^0$ has been created and measured on surface. Where differing alkyl chain lengths of 2 and 6 carbons allow for a size tuned lattice, and thus, tuning of the intermolecular interactions, in particular indirect magnetic coupling. Additionally, The successful deposition on the surface of a novel stable diradical molecule was explored. The $[NO\text{-}Pc(TbPc)]^0$ studied is promising for applications towards QIP, acting as a potential 2 qubit system. By observing NO-group-mediated interactions and conformational switching this suggests a retained diradical character.

The findings underscore ESI-CIBD's potential to study non-sublimable molecules, enabling bottom-up synthesis of quantum materials. The interdisciplinary approach spanning ligand design, advanced deposition techniques, and quantum-level measurement highlights the necessity of cross-field collaboration to tackle modern scientific frontiers towards new quantum technologies.

Zusammenfassung

Die Entwicklung und Untersuchung neuer Materialien zur Ausnutzung hochentwickelter Quantenphysik erfordert die Nutzung ebenso hochentwickelter Chemie, und neuartige Verfahren zur Integration in funktionelle Strukturen. Die Selbstorganisation magnetischer Atome, die von Liganden umgeben sind, Einzelmolekülmagnete, wurde umfassend untersucht und dokumentiert. Die Verwendung der Elektrospraydeposition (ESD) ermöglicht die Untersuchung komplexer thermolabiler, Modifikationen an Bis(phthalocyaninato)-Terbium-Komplexen $[TbPc_2]^0$ auf Oberflächen und überwindet damit die Grenzen herkömmlicher Sublimationsverfahren. Diese Funktionalisierungen ermöglichen eine spezifische Abstimmung der physiochemischen Eigenschaften auf der Oberfläche. Die interdisziplinäre Methodik – die Ligandensynthese, Präzisionsabscheidung und Untersuchung auf Quantenebene umfasst – unterstreicht die Notwendigkeit interdisziplinärer Innovationen, um neue wissenschaftliche Herausforderungen im Bereich von Quantentechnologien anzugehen. Die Erforschung funktionalisierter, nicht sublimierbarer Moleküle, die durch ESD abgeschieden und mit STM untersucht wurden, dient mehreren Zielen. Ein besseres Verständnis der wissenschaftlichen Methodik, die zur Durchführung dieser Studien erforderlich ist, würde ähnliche Experimente außerhalb des Rahmens dieser Arbeit ermöglichen. Durch die Integration von synthetischer Chemie, Oberflächenwissenschaft und Quantentechnologien ergründet diese Arbeit neue Quantenmaterialien mit besonderem Schwerpunkt auf Quanteninformationsverarbeitung (QIP).

Das erste Projekt in diesem Rahmen ist die Validierung von ESD als praktikable Technik, wobei die intakte Ablagerung von $[TbPc_2]^0$ nachgewiesen wird und die wiederhergestellte Radikaleigenschaft durch eine Kondo-Resonanz bestätigt wird, die mit den Sublimationsergebnissen übereinstimmt. Dies ist von besonderer Bedeutung, da das Molekül für ESD notwendigerweise geladen werden muss.

Basierend auf der erfolgreichen Messung des Kondo-Effekts von $[TbPc_2]^0$, das mittels ESD auf der Oberfläche abgeschieden wurde, wird eine Studie zur Abstimmung der Kondo-Eigenschaften mit dem Ziel der Untersuchung quantenkritischer Kondo-Gitter durchgeführt. Zu diesem Zweck wurde eine regelmäßige Struktur aus alkylfunktionalisiertem $[TbPc_2]^0$ auf der Oberfläche erzeugt und gemessen. Unterschiedliche Alkylkettenlängen von zwei und sechs Kohlenstoffatomen ermöglichen ein größenangepasstes Gitter und damit die Abstimmung der intermolekularen Wechselwirkungen, insbesondere der indirekten magnetischen Kopplung. Darüber hinaus wurde die erfolgreiche Abscheidung eines neuartigen stabilen Diradikals auf der Oberfläche untersucht. Das untersuchte $[NO\text{-}Pc(TbPc)]^0$ ist vielversprechend für Anwendungen im Bereich der QIP und fungiert als potenzielles 2-Qubit-System. Die Beobachtung der von den NO-Gruppen vermittelten Wechselwirkungen und Konformationswechseln deutet auf den Erhalt dessen diradikalen Charakters hin.

Die Ergebnisse unterstreichen das Potenzial von ESI-CIBD für die Untersuchung nicht sublimierbarer Moleküle, wodurch eine Bottom-up-Synthese von Quantenmaterialien ermöglicht wird. Der interdisziplinäre Ansatz, der Ligandendesign, fortschrittliche Abscheidungstechniken und Messungen auf Quantenebene umfasst, unterstreicht die Notwendigkeit einer bereichsübergreifenden Zusammenarbeit, um

moderne wissenschaftliche Grenzen im Hinblick auf neue Quantentechnologien zu überwinden.

Résumé

La création et l'étude de nouveaux matériaux exploitant la physique quantique sophistiquée nécessitent l'étude d'une chimie tout aussi sophistiquée intégrée dans des structures par des moyens novateurs. L'auto-organisation d'atomes magnétiques revêtus de ligands, appelés single molecule magnets (SMM), est largement étudiée et documentée.

L'utilisation du electrospray deposition (ESD) permet d'étudier des thermolabiles et fonctionnalisées complexes bis(phtalocyaninato) terbium $[TbPc_2]^0$ sur les surfaces, surmontant ainsi les limites des méthodes de sublimation traditionnelles. La fonctionnalisation permet un réglage spécifique des propriétés physico-chimiques à la surface. La méthodologie interdisciplinaire, qui englobe la synthèse des ligands, le dépôt de précision et l'analyse au niveau quantique, souligne la nécessité d'une innovation interdisciplinaire pour relever les défis scientifiques émergents dans le domaine des technologies quantiques. L'étude des molécules fonctionnalisées non sublimables déposées par ESD et analysées par STM dans le cadre de ce travail poursuit plusieurs objectifs. Une meilleure compréhension de la méthodologie scientifique nécessaire pour mener à bien ces études permettrait de réaliser des expériences similaires en dehors du cadre de cette thèse. En intégrant la chimie synthétique, la science des surfaces et les technologies quantiques, ce travail étudie de nouveaux matériaux quantiques, avec un accent particulier sur les applications du quantum information processing (QIP).

Le premier projet dans ce cadre est la validation de l'ESD en tant que technique viable, démontrant le dépôt intact de $[TbPc_2]^0$, avec la propriété radicalaire restaurée confirmée par une résonance Kondo, correspondant aux résultats de sublimation. Cela est particulièrement pertinent car la molécule est nécessairement chargée pour l'ESD. Sur la base de la mesure réussie de l'effet Kondo du $[TbPc_2]^0$ déposé sur la surface via ESD, une étude sur le réglage des propriétés Kondo sera menée dans le but d'étudier les réseaux Kondo quantiques critiques. À cette fin, un réseau réglé de $[TbPc_2]^0$ fonctionnalisé par des groupes alkyle a été fabriqué et mesuré sur la surface. La différence de longueur des chaînes alkyle (2 et 6 atomes de carbone) permet d'ajuster la taille du réseau et donc d'ajuster les interactions intermoléculaires, en particulier le couplage magnétique indirect. De plus, le dépôt réussi sur la surface d'une nouvelle molécule diradicale stable a été exploré. Le $[NO\text{-}Pc(TbPc)]^0$ étudié est prometteur pour des applications vers le QIP, agissant comme un système potentiel à 2 qubits. L'observation des interactions médiées par le groupe NO et du changement de conformation suggère un caractère diradical conservé.

Ces résultats soulignent le potentiel de l'ESI-CIBD pour l'étude de molécules non sublimables, permettant la synthèse ascendante de matériaux quantiques. L'approche interdisciplinaire, qui englobe la conception de ligands, les techniques de dépôt avancées et les mesures au niveau quantique, met en évidence la nécessité d'une collaboration entre différents domaines pour aborder les frontières scientifiques modernes vers de nouvelles technologies quantiques.

Acknowledgments

I would like to thank my two supervisors, Prof. Jean-Pierre Bucher and Prof. Mario Ruben, for the wealth of academic and scientific support offered to me, as well as the opportunity to undertake this ambitious research project split between two universities.

I also greatly recognise the contribution from Dr. Svetlana Klyatskaya, both in terms of very detailed scientific assistance with any problem I encountered, as well as being a kind and supportive presence within the group, and helping me to navigate the complication related to doing a PhD between multiple cities.

The molecules studies within this thesis were synthesised by Dr. Svetlana Klyatsakya, Dr. Asato Mizuno and Dr. Joe Komeda. Without their expertise in the field of chemistry this PhD would not have been possible. In particular working closely with Joe, allowed for the development of these projects, as well as support in academic endeavors, with many suggestions of relevant literature to read.

From my stay at the TUM, I would like to give thanks to Andreas Walz for the support in using his prototype ESI-CIBD system that forms the basis of this work, as well as the detailed technical discussions. Further I would like to thank Joachim for regular disucssion and answers to daily questions across a broad range of topics and constant support thorughout my stay at the TUM.

Moving so many times throughout the Phd presented a significant social challenge, but the support of the many friends I made throughout the 3 cities I studied in, as well as everyone back home in England made it easy. I would not have been able to complete this thesis without everyone being so welcoming each time I had to move to an unfamiliar new place. I am deeply grateful for all of their support and companionship through good times and bad. Most of all I would like to thank my family for all of their support up to and including the completion of this PhD.

Contents

Résumé étendu

L'auto-organisation des centres de spin des atomes magnétiques habillés par des ligands, appelés aimants à molécule unique (SMM), est largement étudiée et rapportée. Dans cette thèse, l'étude se limite aux modifications des complexes bis(phthalocyaninato) de terbium $[TbPc_2]^0$. Afin d'étudier ces molécules plus en détail, des ligands complexes peuvent être fonctionnalisés sur la molécule afin d'ajuster les propriétés sur la surface, ce qui permet un développement plus large des technologies quantiques, telles que le traitement de l'information quantique. L'étude sous ultra-vide (UHV) de certaines classes de molécules à la surface par microscopie à effet tunnel (STM) est souvent limitée par leur thermolabilité. Les molécules de plus grand volume et donc de plus grande complexité sont généralement très thermolabiles et ne peuvent donc pas être déposées par la méthode standard de dépôt de sublimation sous UHV. C'est pourquoi la technologie émergente du dépôt par électrospray a été utilisée, en particulier le système de dépôt par faisceau d'ions contrôlé par ionisation électrospray (ESI-CIBD).

Un STM est un instrument puissant qui met en œuvre le phénomène quantique de l'effet tunnel. Le courant d'effet tunnel dépend de la tension entre la pointe et l'échantillon, de la distance entre la pointe et l'échantillon et de la densité locale d'états (LDOS) de l'échantillon. En balayant la pointe sur la surface, le changement de la distance pointe-échantillon, et donc, le courant pointe-échantillon peuvent être utilisés pour imager la topographie de l'échantillon, jusqu'à l'échelle atomique. En maintenant une position constante de la pointe, on peut effectuer une spectroscopie avec un biais variable afin d'estimer la LDOS de l'échantillon avec une haute résolution énergétique.

Pour le développement de nouveaux matériaux et technologies quantiques, il est nécessaire d'étudier des molécules plus complexes. Les études de molécules sur des surfaces via l'utilisation du STM sont limitées par la stabilité de ces molécules pendant la sublimation. De nombreuses molécules d'intérêt significatif ne peuvent pas être étudiées sur des surfaces métalliques, car la sublimation est la technique de dépôt standard mise en œuvre dans la plupart des systèmes UHV. De nombreuses molécules d'intérêt nécessitent d'être chauffer pour être sublimées. En conséquence, pour certaines classes de molécules, les liaisons chimiques et les structures sont détruites, ce qui rend les molécules fragiles inopérantes et donc non viables pour l'étude sur surfaces.

Dans le cadre de ce travail, le dépôt par électrospray (ESD) a été appliqué, pour déposer des molécules intactes sur la surface d'une manière propre dans des environnements UHV. Dans cette thèse, le système de dépôt par faisceau d'ions contrôlé par ionisation électrospray sera mis en œuvre (ESI-CIBD). Les molécules en solution sont pulvérisées dans l'ESI-CIBD par l'application d'une haute tension entre la solution moléculaire et l'entrée du système UHV. La haute tension pulvérise les molécules, et puis les ionise. Dans l'UHV du système ESI-CIBD les molécules sont guidées à travers un analyseur de masse et un filtre, ce qui permet de prendre des spectres de masse pour mesurer le contenu du faisceau et de ne sélectionner que les masses correspondant à la molécule cible. Enfin, un champ électrique retardateur

peut être appliqué à la cible, ralentissant les ions et permettant à un "atterrissage en douceur". Le système ESI-CIBD permet une plus grande stabilité moléculaire pendant le dépôt et un meilleur contrôle de l'uniformité de l'échantillon résultant, évitant ainsi le niveau élevé de contamination que l'on peut attendre de la sublimation des molécules thermolabiles.

Des progrès récents ont permis à l'ionisation par électrospray de devenir une méthode de dépôt largement utilisée dans les recherches scientifiques de pointe. L'ionisation par électrospray est particulièrement utile en raison de l'ionisation relativement "douce" via le champ électrique, ce qui permet d'amener des molécules complexes en phase gazeuse avec une fragmentation minimale. Appliquée à l'UHV, elle a permis de développer de nombreux domaines et d'étudier avec des techniques UHV autres que le STM, comme la spectroscopie photoélectronique (XPS) et le microscope à force atomique (AFM).

Dans l'autre cote, le traitement de l'information quantique (QIP), ou informatique quantique (QC), diffère fondamentalement de l'informatique classique en ce qu'il repose sur des bits quantiques, ou "qubits", plutôt que sur des bits binaires conventionnels. En informatique classique, un bit est représenté par un paramètre occupant soit l'état 0, soit l'état 1, alors qu'un qubit peut exister dans une superposition quantique des deux états simultanément. En exploitant les principes uniques de la mécanique quantique, tels que la superposition, l'intrication et l'interférence quantique, il est possible de traiter l'information d'une manière fondamentalement nouvelle, ce qui permet de réaliser des algorithmes exponentiellement plus rapides. Cela représente un changement de paradigme dans notre capacité à résoudre des problèmes complexes, qui dépassent les capacités des ordinateurs classiques. Parmi ces problèmes, la cryptographie quantique, le calcul du repliement complexe des protéines, et l'apprentissage automatique quantique, où les simulations quantiques peuvent fournir des informations inaccessibles par les méthodes classiques. Compte tenu de son potentiel à surmonter les limites dans une série de disciplines, le QIP représente l'une des frontières les plus prometteuses de la science et de la technologie contemporaines.

Le $[TbPc_2]^0$ possède un centre nucléaire de terbium porteur de spin, ce qui permet des études de couplage hyperfine, et donc l'utilisation de 4 états non dégénérés. Cela permet d'utiliser la molécule $[TbPc_2]^0$ comme, ce qu'on appelle, un qudit. Ici le d de qudit se réfère au nombre d'états quantiques possibles dans le système, qui dans ce cas est de 4. En utilisant des qudits, on a accès à ces états supplémentaires, à la fois pour l'application d'algorithmes autres que ce disponibles dans un système binaire, mais aussi, ces états supplémentaires peuvent être utilisés pour d'autres applications au sein du QIP, tels que la correction d'erreur. Ces systèmes moléculaires ont la capacité de former des structures chimiques spécifiques et, en outre, des structures spécifiques sur surface, ce qui permet un degré élevé de contrôle sur leurs propriétés quantiques. En outre, une étude plus large de ces molécules, par exemple sur la surface, peut faire progresser la compréhension de ces molécules et sonder de nouvelles propriétés qui peuvent être exploitées pour le développement de la QIP.

Dans le cadre de cette thèse, une autre étude sur les systèmes de réseaux paramétrable a été réalisé. Elle permettrait, en approfondissant cet axe de recherché, d'explorer les réseaux de Kondo quantiques critiques sur les surfaces. Contrairement à l'effet Kondo d'une impureté unique ou d'un réseau d'impuretés uniques, un réseau Kondo est l'endroit où les interactions collectives entre de nombreux moments magnétiques provoquent un effet d'écrantage collectif cohérent. Comme ces spins sont écrantés, on peut s'attendre à ce qu'il n'y ait pas d'ordre à longue portée. Comme certaines interactions, telles que l'interaction Ruderman-Kittel-Kasuya-Yosida (RKKY),

sont médiées par les électrons de conduction, elles entrent en concurrence avec l'effet Kondo. En réglant les interactions magnétiques entre les molécules, on peut régler les propriétés du réseau de Kondo et passer d'une phase où il existe un écrantage Kondo cohérent à une autre phase où l'on observe un ordre à longue distance, une fois que le couplage d'échange J surpasse l'échange Kondo J_k. Comme le couplage d'échange varie en fonction de la distance entre les centres de spin r, tout réglage du paramètre du réseau permettra effectivement de régler l'interaction d'échange, ce qui permet en principe d'affiner les propriétés de l'échantillon et d'effectuer une transition contrôlée entre les deux phases. En créant un réseau paramétrable, on peut potentiellement étudier les phases décrites, ainsi que la transition entre ces phases. Ce réglage des interactions d'échange présente un autre avantage pour le développement du QIP. Les interactions d'échange qui couplent les moments magnétiques utilisés comme qubits augmentent la décohérence car les spins commencent à s'aligner. Par conséquent, en accordant cette interaction d'échange, via l'ajustement des paramètres du réseau, on peut améliorer le temps de cohérence des qubits disposés en réseau. L'étude des réseaux ajustable de molécules sur des surfaces peut s'appliquer à des travaux de recherche qui sortent du cadre de ce projet. La motivation de ce projet ne se limite donc pas à ce type spécifique de molécules.

La méthode pour régler l'espacement entre les molécules consiste à ajouter des groupes latéraux plus volumineux au ligand afin d'ajuster la taille physique de la molécule et donc de régler l'espacement entre les centres de la molécule. En utilisant des chaînes d'alkyle attachées aux anneaux de benzène de la molécule $[TbPc_2]^0$, on crée une molécule symétrique dont la taille est ajustée, où l'ion terbium reste au centre de la molécule. Des études similaires de molécules de phtalocyanine alkylées sur des surfaces sont disponibles dans la littérature. En outre, il est possible d'ajouter d'autres groupes latéraux instables complexes à la base $[TbPc_2]^0$ pour lui donner une fonctionnalité supplémentaire de QIP. Les divers groupes supplémentaires fonctionnalisés sur la base $[TbPc_2]^0$ dans ces systèmes nécessitent l'utilisation du système ESI-CIBD .

Le plan de la thèse, après une brève introduction faisant office de premier chapitre, est présenté ici .

Le chapitre 2 motive la thèse. Il commence par une discussion sur la molécule de $[TbPc_2]^0$ étudiée et sa pertinence pour le traitement de l'information quantique. Une discussion sur les recherches récentes dans le domaine de la déposition par électrorayonnement est également présentée.

Le chapitre 3 aborde les spécificités des différentes méthodes employées tout au long de ce travail. Il commence par décrire les techniques STM, comprenant à la fois un aperçu théorique des techniques mises en œuvre et un aperçu technique avec schémas détaillant l'installation de chaque équipement et présentant les composants importants . Cette présentation est suivie d'une discussion sur la théorie du système d'électrospray. La théorie de l'électrospray sera expliquée, ainsi que les systèmes de guidage d'ions et le spectromètre de masse quadripolaire, puis un aperçu de la configuration spécifique est donné. L'utilisation d'une valise à vide pour le transfert entre les systèmes UHV est également abordée.

Le chapitre 4 traite des molécules étudiées ainsi que de la théorie qui sous-tend leurs propriétés. Un aperçu de l'état actuel des connaissances est donné, y compris une discussion sur les applications techniques de ces molécules. Une attention particulière est accordée à l'état de l'art des molécules étudiées sur la surface pour bien comprendre comment les modifications appliquées à la molécule dans des expériences ultérieures peuvent affecter les propriétés mesurées des systèmes de surface construits ici.

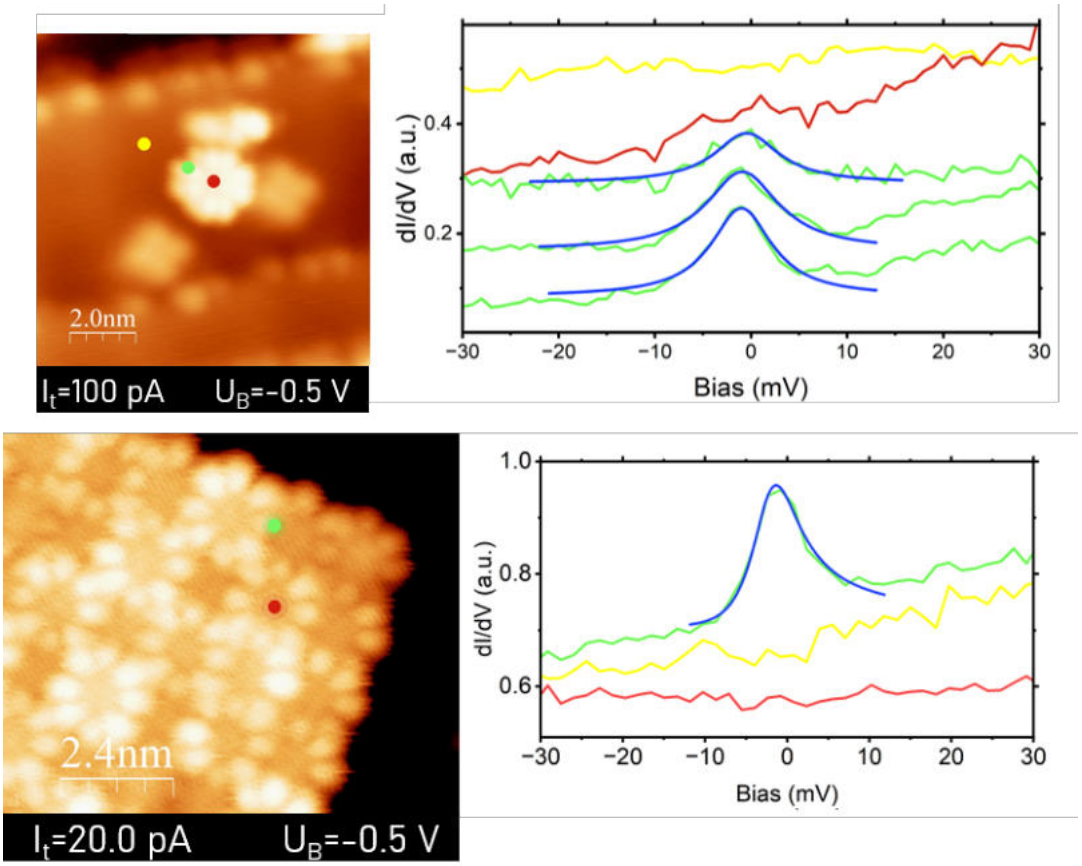

FIGURE 1: Spectroscopie à effet tunnel d'un monomère $[TbPc_2]^0$ proche du niveau de Fermi montrant des pics à polarisation nulle a)Image STM d'un $[TbPc_2]^0$ isolé, avec des points colorés indiquant les positions de spectroscopie. U_B=-0.5 V I_t=100 pA b) dI/dV spectres dI/dV des positions indiquées. Les courbes bleues représentent les fonctions de Fano ajustées. Spectroscopies réalisées à l'aide d'un amplificateur à verrouillage avec une tension de modulation de 1 mV. Spectroscopie à effet tunnel d'un îlot $[TbPc_2]^0$ proche du niveau de Fermi montrant des pics de polarisation nulle c) Image STM d'une couche $[TbPc_2]^0$avec des points colorés pour représenter les emplacements de spectroscopie. U_B=-0.5 V I_t=20.0 pA d) Spectres pris aux emplacements indiqués, où le jaune représente les spectres pris sur de l'Au(111) nu. La courbe bleue représente la fonction de Fano ajustée. Spectres pris à l'aide d'un amplificateur à verrouillage avec une tension de modulation de 2 mV.

Le chapitre 5 explore l'altération des radicaux dans les systèmes moléculaires $[TbPc_2]^0$ décrits ici. Afin de vérifier comment la modification des ligands de ces molécules affecte leurs propriétés de surface, il est nécessaire de s'assurer que la procédure d'ionisation par électrospray n'affecte pas le résultat observé. La molécule $[TbPc_2]^0$ possède un radical délocalisé sur les deux phtalocyanines, qui peut être mesuré en surface sous la forme d'un pic Kondo. Au cours du processus de pulvérisation, des charges sont ajoutées à la molécule et, par conséquent, le radical est supprimé. Lorsqu'il est mesuré sur la surface Au(111), un effet Kondo dû à l'électron de valence non apparié délocalisé sur les anneaux Pc a été observé, confirmant que cette molécule est à nouveau un radical. Ceci est illustré dans la figure 1.1. Bien que l'utilisation du système ESI-CIBD pose quelques difficultés pour l'observation de molécules totalement intactes, il est clair que l'utilisation du système ESI n'affecte

pas la structure électronique des molécules observées une fois qu'elles arrivent intactes sur la surface. Il n'y a également pas de différence expérimentale pertinente par rapport aux échantillons préparés via l'utilisation de la sublimation. Cela confirme que le système ESI-CIBD est une technique viable pour étudier les radicaux, bien que le radical soit supprimé pendant la pulvérisation. Cette expérience élargit le champ d'application de ces expériences à des molécules similaires revêtues de ligands qui rendent les molécules trop thermolabiles pour être viables pour le dépôt par sublimation.

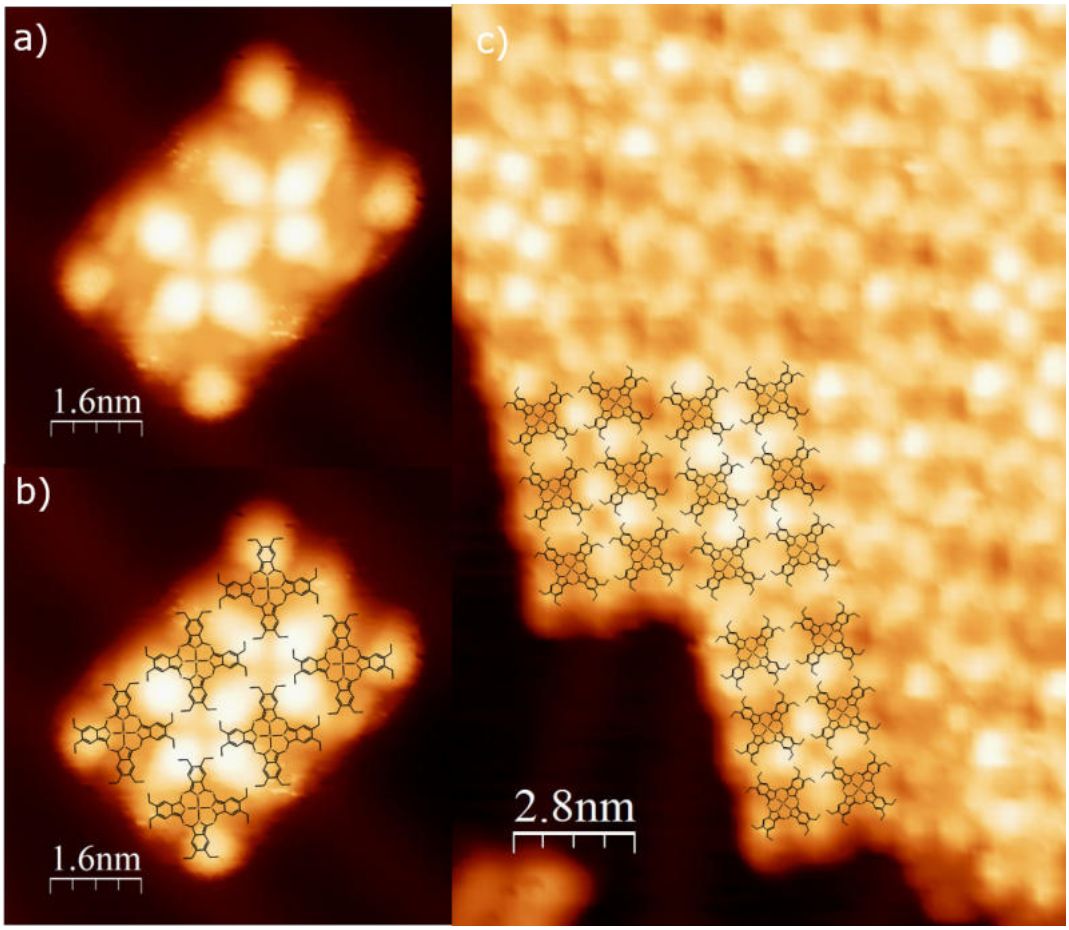

FIGURE 2: Comparaison des modèles moléculaires potentielles pour $[Tb(Et\text{-}Pc)_2]^0$ sur Au(111) a) Image topographique STM montrant l'hexamère $[Tb(Et\text{-}Pc)_2]^0$ sur Au(111). U_B=-1 V I_t=50 pA. b), Montre une copie de a) avec un modèle superposé. Seule la couche supérieure de Pcs est modélisée. e) un modèle similaire à celui de a) superposé sur une couche de $[Tb(Et\text{-}Pc)_2]^0$sur Au(111)

Le chapitre 6 traite du dépôt de molécules de $[TbPc_2]^0$ aklylées, utilisées pour augmenter l'espacement du réseau de la structure auto-organisée bien définie du $[TbPc_2]^0$. En ajustant la taille physique de la molécule, avec l'ajout de chaînes alkyles volumineuses, la taille physique du réseau peut être ajustée. En sélectionnant la longueur de la chaîne alkyle, on peut créer un réseau dont le paramètre d'espacement est ajusté. Cette observation sert de preuve de concept pour des travaux de recherche ultérieurs sortant du cadre de ce projet. Par la suite, il est également prévu dans le cadre de cette thèse, d'observer comment la structure électronique de la couche organisée change, étant donné que la modification de l'espacement du réseau modifie la distance intermoléculaire et donc l'intéraction intermoléculaire. Les dépôts sur

Au(111) et Cu(111) sont étudiés et les expériences résultantes sur ces structures sont discutées. Une exploration est faite dans la structure électronique modifiée, mais seules des données limitées ont été produites. La figure 1.2 montre un hexamère composé de la molécule de $[TbPc_2]^0$ éthylée déposée par ESI-CIBD sur Au(111). Des îlots plus grands sont également observés et discutés. Dans le but de le projet, un réseau accordé sur la surface a été construit, en ajustant le paramètre de réseau du $[TbPc_2]^0$ de 1,43nm à 1,76nm pour le réseau de TbPc2 éthylé.

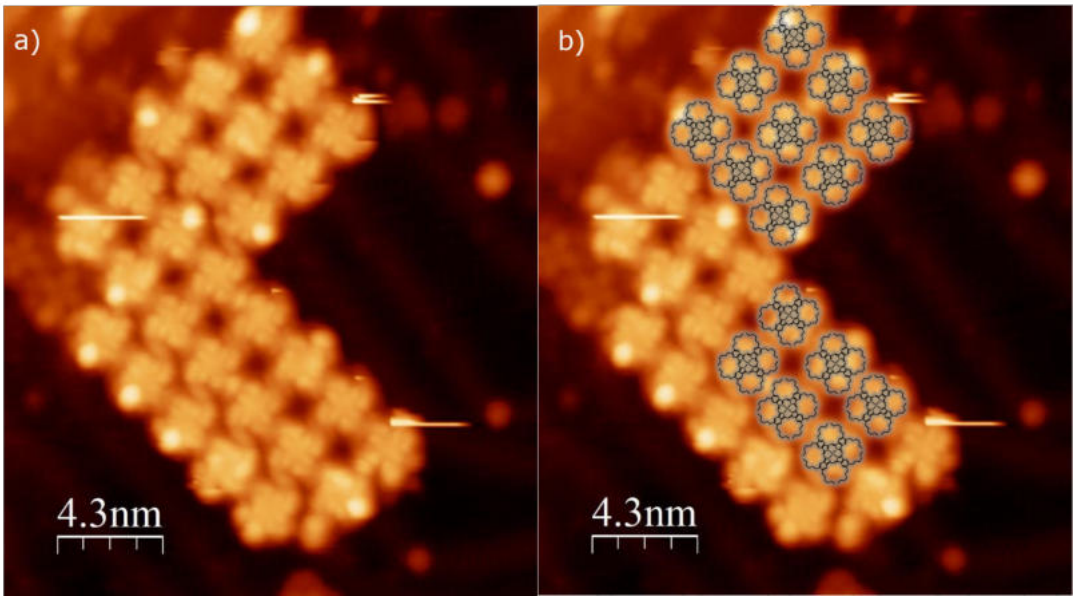

FIGURE 3: Analyse de la structure $[Tb(Hex\text{-}Pc)_2]^0$ a) Image STM montrant la couche $[Tb(Hex\text{-}Pc)_2]^0$. U_B=-2 V I_t=3.6 pA. b) Modèle provisoire superposé à 3a)

En outre, une molécule de $[TbPc_2]^0$ à chaîne hexyle a été déposée pour explorer une augmentation supplémentaire de l'espacement du réseau. Le dépôt résultant sur Au(111) est discuté ainsi que diverses caractéristiques intéressantes de l'arrangement de la surface. Une étude est faite de l'effet de la structure physique changeante sur les propriétés électroniques du système, mais elle est limitée en raison des propriétés spécifiques de l'organisation de la surface qui ne sont pas entièrement comprises. Cette étude est suivie d'une brève discussion sur d'autres molécules alkylées pulvérisées à l'aide du système ESI. La figure 1.3 montre un îlot moléculaire composé de la molécule $[TbPc_2]^0$ à chaîne hexyle déposée par ESI-CIBD sur Au(111). Le paramètre de réseau des îlots de la chaîne hexyle $[TbPc_2]^0$ augmente jusqu'à 2,52 nm. En outre, il y a une brève discussion sur d'autres molécules à base de chaînes d'alkyle qui ont été mesuré dans le système ESI-CIBD mais qui n'ont pas encore été étudiées sur la surface, ce qui sert pour de futures expérimentations.

Sur la base des interprétations les plus simples des objectifs du projet, un système de réseau paramétrable de molécules thermolabiles déposées par ESI-CIBD a été créé sur la surface. La molécule$[Tb(Et\text{-}Pc)_2]^0$ et $[Tb(Hex\text{-}Pc)_2]^0$ ont toutes deux été déposées avec succès sur une surface Au(111). Dans les deux cas, des îlots semi-réguliers de molécules intactes ont été observés, les paramètres de réseau de chaque îlot étant perpendiculaires. Les paramètres de réseau de ces îlots augmentent avec la longueur de la chaîne alkyle. En raison de la nature thermolabile de ces molécules, le dépôt réussi de ces molécules intactes sur des surfaces métalliques est un résultat nouveau. Dans la littérature, les molécules de ce type avec de grandes chaînes

alkyles sont limitées à l'interface solide-liquide en raison de leur insublimabilité. Les méthodes alternatives telles que la coulée de gouttes ou les dépôts assistés par matrice sont possibles, mais la technique ESI-CIBD permet un meilleur contrôle de l'espace des paramètres impliqués dans les dépôts, ce qui, en principe, peut conduire à des dépôts plus reproductibles une fois que l'espace des paramètres est correctement compris et contrôlé.

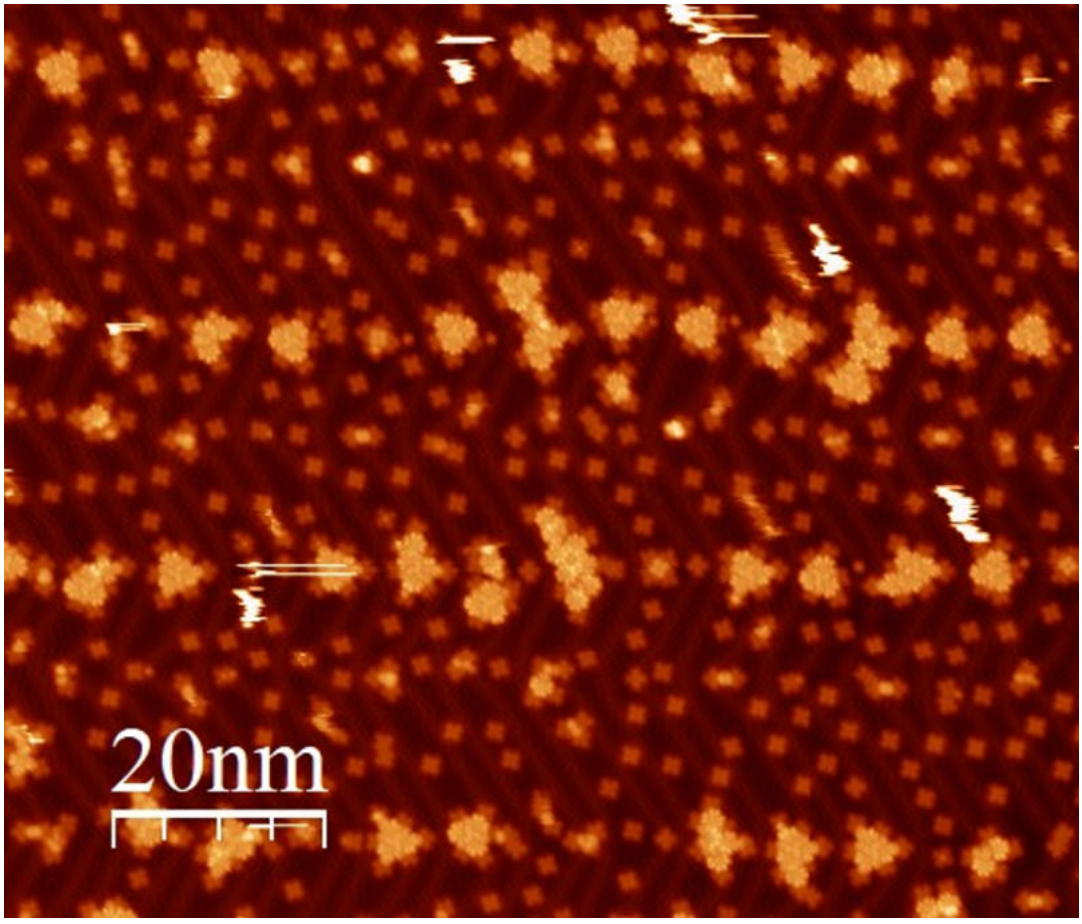

FIGURE 4: Vue d'ensemble d'un dépôt de [NO-Pc(TbPc)]$^-$ sur Au(111) a) Image STM d'une grande terrasse Au(111)avec plusieurs espèces, U_B=-0.7 V I_t=11.6 pA

Le chapitre 7 présente une molécule de $[TbPc_2]^0$ fonctionnalisée avec un groupe contenant un radical NO attaché. Cette molécule radicalaire a été déposée via le système ESI-CIBD. Si l'on tentait de sublimer cette molécule, il est très probable que le groupe radical réactif réagirait immédiatement au chauffage et la décomposerait ainsi. C'est pourquoi le système ESI-CIBD est nécessaire. Les radicaux sur la surface représentent une section intéressante de la science des surfaces, et en améliorant l'utilisation des molécules contenant des radicaux sur la surface via un dépôt stable à l'aide de l'ESI-CIBD, il existe un champ d'application intéressant pour les expériences futures en dehors du cadre de cette thèse. Ce chapitre discute des divers succès du dépôt de cette molécule contenant des radicaux et de son observation sur la surface. La figure 1.4 montre les différentes espèces observées sur la surface à partir du dépôt de la molécule contenant le radical NO, déposée sur Au(111) via ESI-CIBD.

Sur certaines molécules isolées, des protubérances probablement dues aux groupes NO ont été observées. Ces protubérances étaient rares et n'ont été observées que lors

de dépôts à très faible couverture. Ces molécules intactes étaient capables de passer d'une orientation du groupe NO à l'autre, ce qui donne des preuves que la molécule est toujours un diradical à la surface, en raison d'un électron non apparié restant sur le groupe NO. À des taux de couverture plus élevés, les molécules interagissent fortement et forment des grappes. On a supposé que cette forte interaction était due aux groupes NO, ce qui confirme que la molécule peut être un diradical au contact de la surface. De grands îlots de $[NO\text{-}Pc(TbPc)]^0$ intacts où les groupes NO interagissent clairement ont été trouvés.

Des études spectroscopiques ont tenté de comprendre la structure électronique de ces molécules mais elles n'ont pas été concluantes. Des progrès intéressants ont été réalisés en ce qui concerne le dépôt de radicaux intacts sur la surface. Les molécules arrivent certainement à la surface en tant que radicaux, mais il n'est pas exclu qu'elles soient supprimées dès que elles commencent à interagir sur la surface. Pour son application potentielle au traitement de l'information quantique, l'étude de ces molécules sur la surface doit encore faire l'objet d'une expérimentation et d'un développement important. La présence du diradical n'a été ni prouvée ni réfutée; elle reste donc une possibilité.

D'un point de vue plus général, le principe du dépôt de molécules hautement instables sur la surface a été couronné de succès. L'ESI est une méthode prometteuse pour déposer des groupes très réactifs sans éteindre la propriété radicale, ce qui ouvre de nombreuses possibilités d'expériences en dehors du champ d'application de l'étude discutée ici

Une discussion des projets est donnée, suivie d'une discussion sur d'autres expériences futures qui pourraient être entreprises.

List of Figures

Part I

Introduction: Preamble and Methodology

Chapter 1

Introduction

As science advances ever forward into the future, the nature of research becomes increasingly complex. Towards the goal of new materials, technologies, and a more complex understanding of our world, it becomes necessary to explore ever further and deeper into fields unexplored, necessitating collaboration between diverse fields. This thesis on the application of the emerging technology of controlled electrospray deposition (ESD) to deposit and study thermolabile functionalised $[TbPc_2]^0$ derivatives on the surface that cannot be deposited intact by other methods. The goal of the project is to study these molecules via STM, which is a precision probing technique, to better understand interactions of surface structures, towards the goal of quantum information processing, which represents a paradigm shift in scientific and technological potential.

The phrase 'standing on the shoulders of giants' is attributed to Isaac Newton as a metaphor for building on the progress of great thinkers who have come before. It is only by standing on these shoulders that one may advance science and understanding ever onward into the future, and for any contribution provided by this thesis to be further built on in the research and development of new ideas and technologies, that may be further used to extend human knowledge. Over the course of history, major advances in physics, chemistry, and engineering have precipitated developments in new technologies and expanded scientific understanding. However, the end of the 20th and into the 21st century has brought forth a paradigm shift, driven by the growing recognition that humanity's most pressing challenges, from the curing of diseases, to climate science, to artificial intelligence, are not confined to the boundaries of a single field.

Via significant advances in synthetic organic chemistry, the fine control of functionalised ligands has allowed for deeper study across a range of topics, from tuned properties of spin crossover complexes [1–4], catalysis [5–8], and the manipulation of interesting physical properties [9].

These advances in ligand functionalisation have allowed for the synthesis and study of single molecule magnets [10, 11] with tunable properties. Studying these molecules on surfaces allows for a detailed exploration towards understanding these molecules on a more fundamental level [12–15].

Within surface science, these significant advances in synthesis and ligand functionalisation have allowed for the bottom-up synthesis of promising novel materials. This allows for a fine control of surface properties towards various applications, including biology [16–19], green technologies [20], and many others [21–25]. Specifically, one may tune and probe the surface properties of interesting surface structures. In this case, the aim is to tune the organisation of molecules in order to verify and modify the surface properties [26–31].

Unfortunately, many of the most interesting molecules produced by advanced research in chemistry can be challenging to study due to the difficulty in bringing

the functionalised species to the surface. Many molecules of interest are highly thermolabile, meaning they are unstable against high temperatures, and thus cannot be heated for deposition by sublimation, a technique that is often used for surface science studies. In order to unite these diverse fields, this thesis employs the novel technology of electrospray ionisation for deposition [32–34]. Specifically, an Electrospray ionisation controlled ion beam deposition system will be implemented (ESI-CIBD).

Some fascinating research has already been conducted, many towards biological molecules [35–37], as well as creating more complex and interesting surface structures [38, 39]. Through developments in technology and engineering, previously impossible experiments have become possible using complex and interesting molecules, further pushing and breaking boundaries in science.

By using the ESI-CIBD system, one may create specially tuned surface structures to explore how certain molecules interact with each other on surface. The findings of these experiments play some role towards developments in the field of quantum information processing (QIP). QIP depends on the realisation of quantum bits or 'qubits', which are used in place of a classical bit. Computing is performed on qubits that can be in a state $|0\rangle$ or $|1\rangle$ or a superposition of both. This allows for scaling of computing speed, up to an exponential rate for some algorithms.

One potential platform for constructing a qubit is to use molecules. There have been significant developments towards molecular qubits [40, 41], particularly focusing on ligand tuning and radical molecule properties [42, 43], as well as studying these as surface frameworks [44, 45]. In order to study these molecules and to integrate them into any potential quantum information device, one must understand how these molecules interact with each other and how to tune these interactions. In this thesis, this is done via functionalisation with ligands.

The development of QIP represents one of the most significant frontiers in contemporary scientific research. Feynman famously discussed that the simulation of a quantum world needs a quantum simulator[46, 47]. The development of QIP allows for an exponential calculation rate increase. This may unlock new strategies for resolving highly complex scientific challenges [48–53].

To summarise, by bridging molecular-level insights with device-oriented applications, this work aims to advance the fundamental understanding of ligand functionalised molecules while paving the way for their integration into next-generation quantum technologies. The findings presented herein not only deepen our grasp of ligand driven surface properties but also contribute to the broader goal of harnessing quantum effects for transformative technological innovation.

Following the introductory first chapter, this thesis is divided into the following chapters:

The second chapter discusses the motivation behind the project, detailing the relevance and interest of the $[TbPc_2]^0$ molecules studied, and their applications towards QIP. Followed by a discussion of the development of ESD for the development of new materials.

The third chapter gives an overview of the theory underpinning the technologies applied to this thesis, as well as a presentation of each instrument used throughout this thesis.

The fourth chapter reviews the state of the art and examines prior research that forms the foundation of this thesis. It also presents the theoretical background necessary to understand the developments and results discussed in subsequent chapters.

The fifth chapter discusses the deposition of the $[TbPc_2]^-$ via ESI-CIBD and verifies that the system does not affect the surface properties when deposited via ESD, as opposed to simple sublimation.

The sixth chapter discusses the addition of alkyl chains to the $[TbPc_2]^0$ molecule in order to increase the physical dimensions of the molecule in order to tune the size of the lattice of these molecules on the surface. Firstly, a two carbon chain alkyl substituted molecule is measured and deposited onto the surface. Data is presented to prove that the molecule is found on the surface. The project is then continued to compare to a six carbon hexyl chain substituted molecule, in order to further tune the size of the lattice and attempt to observe an expanded lattice.

The seventh chapter explores functionalisation of the molecule to add a radical group, making the molecule a diradical. The nature of the diradical molecule on the surface is discussed, with some reference to evidence of a diradical property on the surface. A series of different depositions of varying coverages are compared in order to study how these potential diradical molecules interact with each other.

Finally, an eighth chapter briefly concludes the results of this thesis.

Chapter 2

Motivation

2.1 Introduction

This thesis discusses the application of the emerging technology of electrospray deposition and how it can be used to deposit exotic and interesting molecules onto surfaces towards the development of exciting new physics and new technologies. A discussion will be made surrounding the motivation of the projects, and what future research and potential technologies they may progress.

2.2 Overview of the $[TbPc_2]^0$ Single Molecule Magnet

Phthalocyanines (Pcs) are a class of synthetic macrocyclic compounds characterised by their highly conjugated, planar aromatic structure. The free base phthalocyanine (H_2Pc) is an aromatic macrocyclic organic compound, composed of four isoindole units and a ring of nitrogen atoms. One of the main points of interest of these molecules is the 18 π electron system, where the π electrons are delocalised over the ring shaped backbone. There are also two hydrogens at the centre of the ring of nitrogen that saturate the molecule. But this centre can also host a broad variety of metals. Phthalocyanines have garnered immense scientific and industrial interest due to their exceptional chemical stability, tunable electronic properties, and versatility in applications[54–59]. In modern contexts, their applications have evolved to address global challenges: they serve as active components in organic photovoltaics (OPVs) [60, 61] and light-emitting diodes (OLEDs), important catalysts for energy conversion reactions towards green technologies [60, 62] and sensitisers in photodynamic therapy for cancer treatment [63, 64].

One significant advantage of the phthalocyanines is that one may make a variety of chemical modifications to tune their properties. The molecule can be coordinated with a central metal atom, and the Pc ligand can also be functionalised with peripheral groups to give further interesting properties for specific applications. One of the main aims of this thesis is to investigate these properties on Pcs where specific groups have been attached. If these scientifically promising groups do not share this stability against elevated temperature, and are thus thermolabile, then it becomes more complex to study them, especially in the necessarily pristine ultra high vacuum environments employed throughout this thesis. As a result, the ESI-CIBD system that will be discussed in detail in chapter 3 will be implemented to deposit and study these thermolabile molecules.

In particular, this thesis will be concerned with the study of bis(phthalocyaninato)

terbium(III) complexes, or $[TbPc_2]^0$, as well as similar molecules composed of further functional groups attached to the benzene rings of the $[TbPc_2]^0$ to provide functionalised properties. The $[TbPc_2]^0$ molecule, as displayed in Figure 2.1 a), is composed of a central Terbium (III) ion sandwiched between two phthalocyanine (Pc) ligands via coordination bonds.

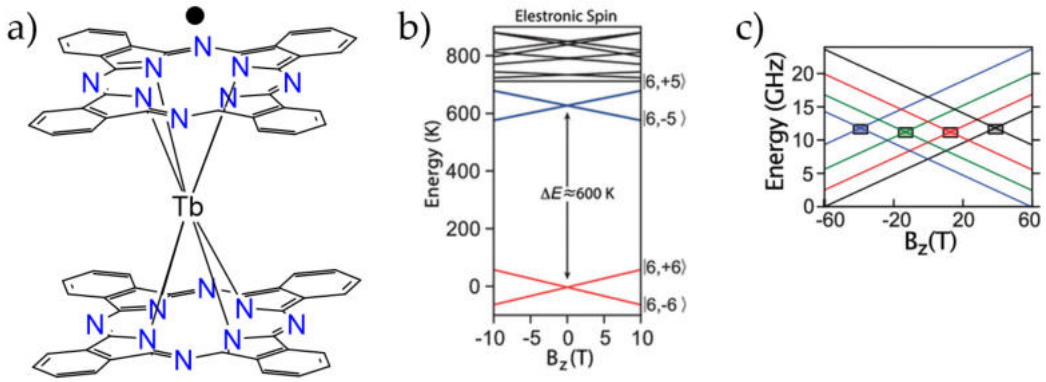

FIGURE 2.1: Molecular and electronic structure of $[TbPc_2]^0$ a) Molecular model of $[TbPc_2]^0$, b) Zeeman diagram of the $[TbPc_2]^-$, showing the electronic and spin level structure. c) Hyperfine structure of the ground state doublet, mJ = ±6, as a function of the applied longitudinal field. Reproduced from [65]

The most stable state of Terbium is the 3+ oxidation state, where the electron configuration is $[Xe]4f^8$. When coordinated with the two phthalocyanine ligands, the oxidation state of the ligand leaves one unpaired electron on the ligand, and thus, an S=1/2 radical. By the simplest definition, a radical is a molecule with an unpaired valence electron [66]. This electron is delocalised over both Phthalocyanine ligands, and partially enables the intriguing properties of this molecular system.

Interestingly, the ionic radii of the lanthanides decrease with increasing atomic number. As the 4f orbital of the Terbium ion is located close to the nucleus, it is challenging to access in electron transport experiments. This improves the screening of the 4f electron from the external environment, which becomes relevant to the further applications of these molecules. In summary, the $[TbPc_2]^0$ has two spin systems, one originating from the unpaired ligand electron and the second from the unpaired 4f electron of the Terbium.

2.2.1 Single Molecule Magnets

Single-molecule magnets (SMMs) are a class of molecular materials that exhibit slow relaxation of magnetisation at low temperatures[67]. Unlike conventional bulk magnets, where long-range magnetic order arises from collective interactions between numerous magnetic moments, SMMs function as isolated magnetic units. The fundamental origin of an SMMs magnetic behaviour lies in the interplay between spin–orbit coupling, ligand field effects, and exchange interactions within the molecule. These SMMs are capable of maintaining a strong magnetic moment below a characteristic blocking temperature dictated by the uniaxial magnetic anisotropy. There is a certain energy barrier separating the states that define the magnetic moment, enabling SMMs to retain magnetisation in the absence of an external field, and thus an open hysteresis can be observed. When the temperature is raised sufficiently high

(above the blocking temperature) such that this energy barrier can be overcome, the molecule will become paramagnetic.

The first SMM synthesised and measured was the $[Mn_{12}O_{12}(OAc)_{16}(H_2O)_4]$, studied by Sessoli et al. [10], which is composed of an $Mn(IV)_4O_4$ cage surrounded by 8 Mn(III) units in a ring. The central Mn(IV) ions have a spin of S = 3/2, and the ring of Mn(III) ions have a spin of S = 2. The antiferromagnetic coupling of the two ferromagnetically coupled groups of Mn ions leads to a ground state of S = 10, giving a large energy barrier.

The measurement of the SMM property of the $[TbPc_2]^0$ was first reported by Ishikawa et al. [68, 69]. The $[TbPc_2]^0$ molecule has a large magnetic anisotropy, due to the inherent anisotropy of the Tb (III) ion, with a J=6 spin ground state. Further, the ligand field due to the phthalocyanine macrocycles, tailors the 4f electron density. This lifts the degeneracy of the Terbium ion's ground state, splitting into 2J+1 eigenstates. This results in a well separated ground state and a first doublet excitation with $m_J \pm 6$ and $m_J \pm 5$, respectively. Ishikawa et al. measured the energy separation between the states as 600K for $[TbPc_2]^-$ [68], as shown in Figure 2.1 b) [65, 70, 71].

Future research efforts aim to enhance their operational temperature range, suppress quantum tunnelling effects that lead to magnetisation relaxation, and integrate SMMs into functional nanostructures for technological applications. Furthermore, the molecule's planar structure and extended -conjugated ligand system facilitate its integration into supramolecular architectures and hybrid devices. The tunability of these magnetic properties can be altered via ligand modifications to achieve these goals. In this thesis, ligand alterations do not aim to tune the magnetic properties of the complex, but aim to investigate the implications on the molecule's surface self assembly structure and interactions.

2.2.2 Quantum information processing

Quantum information processing (QIP), or quantum computing (QC), differs fundamentally from classical computing in that it relies on quantum bits, or 'qubits', rather than conventional binary bits. In classical computing, a bit is represented by a parameter occupying either the 0 or 1 state, whereas a qubit can exist in a quantum superposition of both states simultaneously.

Leveraging the unique principles of quantum mechanics, such as superposition, entanglement, and quantum interference, one may process information in fundamentally new ways, enabling exponentially faster algorithms, such as Shor's algorithm for factorisation and Grover's algorithm for search problems. This represents a paradigm shift in our ability to address complex problems that lie beyond the capabilities of classical computers, primarily due to the exponential scaling of the algorithms involved. Some of these problems include quantum cryptography [48–50], calculating complex protein folding [51, 52], and quantum machine learning[53], where quantum simulations can provide insights unattainable by classical methods.

Given its potential to overcome longstanding limitations across a range of disciplines, QIP stands as one of the most promising frontiers in contemporary science and technology. Progress in QIP, however, is deeply intertwined with advancements in enabling technologies, such as electrospray deposition. Where developments towards technologies which can facilitate the precise preparation and integration of complex molecular qubits and nanostructures may further other advancements towards scalable quantum architectures.

The important considerations for a qubit are outlined and summarised by the Di Vincenzo criteria [72]. One requires a defined number of qubits with states that can be addressed, manipulated, and read out. It must be possible to apply a universal set of quantum gates. It is important to be able to couple multiple qubits together so that the number of bits can be scaled to a relevant number for various algorithms. Finally, the coherence time of the state must be of a relevant length. If one prepares a qubit in a particular state in order to apply some algorithm, there is some possibility to lose this quantum state over time. The coherence time is a measurement of how long a particular state stays in a predictable phase, and thus how long one can apply coherent manipulations to the state.

There are many possible qubit platforms, each with its own advantages and disadvantages [73]. These include Nitrogen vacancies in a diamond lattices [74–76], spin quantum dots [77, 78], topological qubits based on 'anyons' [79, 80], superconducting qubits controlled by electromagnetic fields [81–84], optical quantum computers, [85, 86] and trapped ion qubits [87–89].

As discussed, this thesis focuses on $[TbPc_2]^0$ SMMs. These have potential applications in molecular quantum information processing, where molecules are used to store and manipulate quantum states [70, 90, 91]. The biggest advantages of Molecular QIP are the chemical tunability of the molecules and very long coherence times. The difficulties include some challenges of addressability of the qubits, as well as their scalability.

The $[TbPc_2]^0$ has a nuclear spin-bearing Terbium centre, which enables hyperfine coupling studies, allowing for the use of 4 non-degenerate states, as shown in Figure 2.1 c). This allows the advantage of using the $[TbPc_2]^0$ molecule as a so called qu*d*it. Where the *d* refers to the number of possible quantum states in the system, which in this case is 4. By using qu*d*its, one has access to these additional states, both for the application of algorithms different to those available in a binary system, but further, these additional states can be used towards other applications within QIP, such as hardware-based error correction states [92, 93].

The $[TbPc_2]^0$ molecule has found some success towards the aim of quantum computing, being used to implement Grovers algorithm, which has a quadratic rate improvement over similar conventional search algorithms applied to a classical computer [94, 95].

These molecular systems benefit from the ability to engineer specific chemical structures and, further, specific structures on the surface, providing a high degree of control over their quantum properties. Furthermore, a wider study of these molecules, such as on the surface, may further advance the understanding of these molecules and probe new properties that can be exploited towards the development of QIP.

2.3 Novel research using electrospray deposition

Towards the development of new quantum materials and technologies, the need to research more complex molecules arises. Investigations of molecules on surfaces via the use of STM are limited by the stability of these molecules during sublimation. Many molecules of significant interest cannot be studied on metal surfaces, as sublimation is the standard deposition technique implemented in most UHV systems. It is often implemented as a simple but effective technique. Even at the low pressure of 10^{-10} mbar in standard UHV chambers, many molecules of interest will require significant heating to sublimate. As a result, chemical bonds and structures are destroyed, rendering the fragile molecules no longer functional and thus non-viable

for study on surfaces. This is especially challenging for molecules of greater volume. It is likely that the required sublimation temperature is sufficiently high for the molecule to begin reacting or for bonds to break. In this case, one is likely to find disorder on the surface with multiple species of broken molecules, as well as possibly contaminating the chamber. As a result, there are many classes of molecules that are not viable for use in UHV via sublimation. Particular to this thesis the ligand of the $[TbPc_2]^0$ will be modified to derive special properties. In one project, a reactive group will be added to the ligand of the molecule to verify if it remains intact on the surface. The second project focuses on attaching alkyl groups to the ligand, which will greatly increase the volume of the molecule, making it inappropriate for study via sublimation.

Electrospray ionisation (ESI) is an often applied and highly useful tool, particularly in the field of chemistry for use in mass spectrometry systems. Electrospray allows for the 'soft' ionisation, where other techniques, such as Matrix assisted laser deposition (MALDI) or Electron impact ionisation (EI), often lead to higher levels of fragmentation. Soft ionisation allows for many molecules, ranging from small reactive molecules, to large complex bio-molecules to be ionised into gas phase for further experimentation, allowing for a wide range of potential classes of molecules to study [96–98]. As a result, ESI has been applied more recently as a technique to deposit molecules intact on the surface in a clean manner in UHV environments. Rather than spraying molecules towards an opposite pole electrode for deposition, one may create a bore hole on the electrode, leading to a UHV chamber, such that ions are fired into UHV. By guiding molecules into UHV, they can then be manipulated in a clean environment. This technique allows for innovative experiments when applied to classes of molecules that cannot be introduced simply into the gas phase intact by other means, with many of the major developments only being realised more recently [32, 33, 35, 99–101]. As such, many classes of molecules previously considered too challenging to deposit become available for study, enabling new avenues of investigation into newer more complex 2D materials.

Furthermore, in many systems, a mass spectrometer is integrated to measure the content of the ion beam and ensure that the molecules have not fragmented. In this system, a Quadrupole mass spectrometer (QMS) is implemented, which can also act as a mass filter to select only the desired ions in case of fragmentation. In the experimental equipment employed in this thesis, it is also possible to set the potential of crystal substrate in order to apply a retarding potential opposing to the potential of the ion beam in order to select the kinetic energy of the ions as they impact the surface producing a so called 'Controlled' Ion beam. The use of electrospray as a deposition technique does have additional complications that must be considered, but for this project, it is regarded as the most viable option.

Recent advancements have positioned electrospray ionisation as a critical deposition method in cutting-edge scientific investigations. Electrospray ionisation deposition has been used in many instances for much advanced research [102, 103]. However, when applied to UHV, it has allowed for developments towards many fields, and studying with UHV techniques other than STM, such as XPS and AFM. Research constantly pushes onward to study more complex molecules with more specifically functionalised properties, as the molecule can be deposited in a well-controlled manner from solution without any requirement for heating. Commonly, there have been many explorations to study biomolecules on surfaces [33, 35–37, 104]. Furthermore, given the possibility of fragmentation, there have been studies to synthesise new materials in an ion beam [105]. Some studies focus on interesting non sublimable molecules in the single nanoparticle regime [106].

This thesis specifically focuses on creating specially tuned nanosystems on surfaces [39, 107–109], towards the aim of creating new materials, often via on surface synthesis [38, 110, 111]. Furthermore, one may implement surface collisions, driven by adjusting the landing energy onto the surface, to create new materials[34, 112]. However, as this is a relatively novel technique when applied to UHV systems, the research already produced towards this field is somewhat limited, allowing a wide scope of possible research to be carried out using this technique, and thus requiring significant study.

Chapter 3

Experimental methods

3.1 Introduction

In order to both create and probe the molecular systems discussed in this thesis with sufficiently high precision, state of the art scientific equipment must be implemented. A combination of surface science techniques, spectroscopic tools, and advanced microscopy methods was used to characterise samples at the atomic and molecular scale. Additionally, the electrospray system implemented, was a custom-built prototype instrument, and as such, requires some attention to understand the deposition procedure. Each method is described in detail in the following sections, with supporting diagrams, as well as the scientific theory behind its operation. Furthermore, the experiments performed in this thesis require an ultra high vacuum (UHV) environment to maintain a clean, well-defined environment for preparation of samples. A brief overview of these UHV systems will be provided.

3.2 Principles of scanning tunneling microscopy

In 1981, with the invention of the Scanning Tunneling Microscope by Binnig and Rohrer [113–115], the ability to probe surfaces in finer detail was greatly improved. So much so that Binnig and Rohrer won the Nobel prize for their efforts [116]. The basic principle of STM works by bringing a sharp tip so close to a surface that a tunneling current can be measured. Where the tunneling current is a current of electrons that quantum tunnel across the gap between tip and surface, when a voltage is applied between the tip and the sample. The tip sample gap acts as a potential barrier. This current depends exponentially on the distance between tip and sample. As the tip is scanned across the surface, the current will change depending on changes in surface topography, but also the electronic structure of the surface. The current data, and the lateral position of each data point during scanning, allows one to generate an image of the surface in 3 dimensions. The extremely high sensitivity of the tunneling current to the tip sample distance, allows a sample to be measured down to the level of atomic resolution.

This invention led to many further advancements in scanning probe technology, allowing one to measure many surface properties, such as atomic forces, bond resolution, spin sensing, as well as those in continuous development [117–123].

It also allowed the use of the STM tip to manipulate molecules, both physically, and to alter the properties such as chemical bonds, or magnetic properties [12, 124–131].

3.2.1 Tunneling current

The tunneling current in STM arises from the square of the wavefunction of an electron being non-zero on both sides of a potential barrier, where the square of the wavefunction at a certain position is the probability of finding that electron at that position. Thus a net flow of electrons between the metallic tip and conductive sample can be measured, where a voltage bias is applied between the tip and sample. Classically, a particle entering a potential barrier of greater energy than that of the particle, will not be able to enter this region and thus cannot cross it. In quantum mechanics, the wavefucntion of a particle decays as it travels within a classically forbidden region, and has some finite probability to cross the classically forbidden region. This can be modelled by solving the one-dimensional Schrödinger equation.

$$\psi = \psi(0)e^{(\pm kz)}, k^2 = 2m(V_B - E)/\hbar^2. \tag{3.1}$$

Equation 3.1 describes the wavefunction ψ of a particle of energy E as it travels through a potential barrier V_B. k is the decay constant based on the parameters of the potential barrier, including the reduced Planck constant $\hbar$. In the case of the STM, the vacuum gap between tip and sample acts as the potential barrier. This potential barrier is partially defined by the work function of both the tip and sample, as well as the bias applied between them. The tunneling probability is proportional to the squared amplitude of the wavefunction, which itself is proportional to the current, as shown in equation 3.2 [113, 132]

$$I \propto e^{-2kz}, k = \sqrt{\frac{2m\phi}{\hbar^2}} \tag{3.2}$$

Where ϕ is the effective barrier height, assuming that the work function is greater than the applied bias voltage. For the materials generally studied by STM, the work function is of the order of 5 eV. Therefore, the decay constant k is of the order 1 $Å^{-1}$. A change in tip sample distance of 1 Å results in a change of tunnel current by a factor of 10. As the current has an exponential relationship to the tip-sample distance, if the tip is very close to the sample, then contributions to the current are strongly confined to sites directly beneath the tip. The width of a gold atom is $\sim$2 Å, therefore if one imagines the tip is $\sim$2 Å from the atom, then the adjacent atom is $\sim \sqrt{8}$ Å away from the tip. Therefore the percentage contribution from the adjacent atom compared to the atom under the tip can be approximated as follows, $\approx e^{-2\kappa\Delta z} = e^{-2\times1\times(\sqrt{8}-2)} \approx e^{-1.65} \approx 19\%$ This gives the STM it's sub-angstrom resolution, allowing for resolution of individual atoms.

3.2.2 Scanning modes

When operating the STM, the tip can be scanned across the surface at a constant height close to the surface, and the current varies as the tip sample distance changes due to changes in surface topography. Whilst this does allow for highly detailed images to be taken, as the tunneling distance for a typical current of a few 100 pA, is only a few angstrom, it is not possible to move over a surface that varies in height more than these few angstrom.

As such, an alternative scanning mode is implemented, where a feedback loop adjusts the height of the tip continuously, by attaching the tip to a piezo ceramic and varying the voltage applied to the piezo crystal to adjust the tip position, and thus tip-sample distance. A feedback loop is applied to vary the piezo voltage, in order to maintain a constant current. This allows the tip to move over a surface with larger

topographic changes without colliding with the surface. As the height of the tip is being adjusted above the sample, the output of the image is a reading of apparent height. However, due to the convolution of tip sample distance and the electronic structure of the sample(see eqn 3.3), when scanning in this mode, the real height of the topographical changes is not measured. The measured apparent height by STM at a given voltage with a well defined tip is reproducible, and as such, some comparison of apparent height can be made, but must not be confused with the real height of the sample.

Figure 3.1 displays how a tip moves across the surface in each instance.

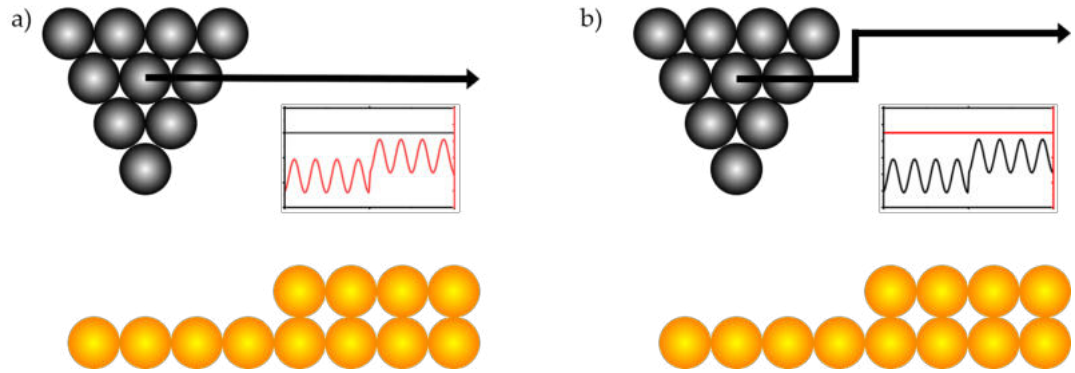

FIGURE 3.1: Scanning modes in STM a) diagram showing constant height mode, b) shows constant current mode. Arrows show tip trajectory. Graph to the right of each diagram shows STM output. Black line in graph displays height, red line shows current

3.3 Scanning tunelling spectroscopy

Scanning tunneling spectroscopy (STS) is a powerful and important technique that is used to probe the local density of states (LDOS) of a sample with atomic resolution [133, 134].

One of the primary theoretical tools for modeling the current is provided by Bardeen's perturbation theory [132], where the wavefunctions of the sample and tip are considered. Tunneling is treated as a first-order process in the transfer Hamiltonian formalism. In this approach, the tip and sample are considered independent systems. The current is modeled by the following:

$$I = \frac{4\pi e}{\hbar} \int_0^{eV} \rho_t(E_F - eV + E)\rho_s(E_F + E)|M|^2 dE \tag{3.3}$$

Where ρ_t and ρ_s are the density of states of the tip and sample respectively. M is the tunneling matrix, which is a surface integral of the tip and sample wavefunctions, taking into account their overlap.

The Tersoff-Hamannn approximation to theory was tailored to the configuration of the STM. This approximation assumes a spherically symmetric s-wave like tip and at the limit of small tunneling voltage (below the work function of either material). This reduces the tunneling matrix element to a function of the sample's LDOS at the tip position. By differentiating the current with respect to voltage, one obtains the following.

$$\frac{dI}{dV}(V) \propto \rho_s(V) \tag{3.4}$$

Therefore, with a well defined tip, where one can approximate the density of states of the tip as constant, the measured dI/dV at is proportional to the density of states of the sample at that voltage.

With a fixed tip position, one may perform spectra by varying the bias voltage and measuring the resultant current. The derivative is proportional to the LDOS. One may further improve measurements by modulating the bias voltage. By applying a small modulation to the bias ΔV around bias V, one may measure ΔI and calculate the dI/dV at V. Clearly, the modulation must be smaller than the size of the measured features so that they can be accurately resolved.

Importantly, this gives further context for equation 3.2. Imaging of the sample is a convolution of the topography and changes in the local density of states of the sample directly below the tip, as the tip scans across the surface. Thus, STM does not measure real topography, but only the 'apparent height' of the sample.

3.3.1 Measurement and interpretation of spectra

In order to take high quality reproducible measurements, one must be certain that the tip is well defined, meaning that the measured dI/dV does not show features of the LDOS of the tip, and that the approximations made in the prior section are applicable. The Shockley surface state [135–137] is a well defined reference for noble metals. One should measure a sharp step in the dI/dV at a certain position, depending on the metal and crystal structure, with no additional features. In order to exclude any contribution from the LDOS of the tip, it is best practice to condition the tip, usually by stabbing the tip into the surface until the Shockley surface state is seen as a clear step function.

It is common practice to normalise dI/dV spectra, for the purpose of comparison. From literature [138], one may divide the dI/dV at each point by the I/V measured at that point, to eliminate the non-linear voltage dependence of the I/V. This does cause the resultant value to approach infinity as V approaches 0, so it is common to either delete some data points close to 0 V, or to broaden the V by some value, this value can be somewhat arbitrarily chosen to mediate between equalising peaks and distorting the data. Critically, this procedure also slightly shifts the peak position, so must be carefully applied. This normalisation procedure is implemented in this thesis at times, but will be mentioned where relevant, with untreated data shown in SI.

Importantly, thermal broadening will affect the shape of peaks, as well as limiting the minimum energy resolution. Furthermore, there are many features which only become visible below a certain temperature, including the Kondo effect, which will be studied in this thesis. As a result, STS is often performed at low temperatures. In the case of this thesis, all STS are performed at 4.5 K

3.4 UHV sample preparation

The noble metal crystal substrates Au(111) and Cu(111) were cleaned by multiple cycles of argon ion bombardment and thermal annealing to 400°C. The molecular samples were deposited onto the crystal substrates held at room temperature. The pressure in the deposition chamber was $2\text{x}10^{-9}$ mbar during deposition and transferred between vacuum systems via the vacuum suitcase. The samples were initially degassed to 50°C to remove any small amount of dirt adsorbed during transfer.

3.5 Electrospray deposition

As discussed in chapter 2, electrospray deposition will be implemented in this thesis, to deposit thermolabile molecules onto metal substrates for study with STM. In order to fully understand the function of the prototype ESI-CIBD system, the physical properties and mathematics underpinning the physics of this system will be discussed.

3.5.1 Electrospray mechanism

The electrospray mechanism works by driving a solution containing the target molecule through a narrow capillary with a high voltage applied to the solution, usually via a conductive capillary. The capillary is pointed towards the counter electrode. This induces the accumulation of charge carriers to form at the edge of the droplet protruding from the capillary. This protruding droplet shape is dependent on many factors [139–141] and is highly complex. The important factors one strictly controls are spray voltage, flow rate and the combination of solvent used. These factors can greatly affect the results of any experiment. By optimising these parameters, one may create a so-called Taylor cone. [142]. A fine mist of charged droplets is ejected from this cone towards the counter electrode.

Once these droplets are sprayed into a mist, they begin to shrink in size, initially due to evaporation of the neutral solvent. Eventually, the forces from coulomb repulsion of these charges approache the surface tension as the droplet decreases towards the 'Rayleigh limit'[143, 144]. The Rayleigh limit is $q_R = 8\pi\sqrt{\epsilon_0 \gamma r^3}$, where q_R is the Rayleigh limit charge, ϵ is the permittivity of free space, γ is the surface tension, and r is the droplet radius. As the droplet is unstable, the radius of the droplet will drop below the Rayleigh limit and coulomb fission occurs, where smaller higher charge droplets are ejected from the mother droplets, which must further split to increase their radius above the Rayleigh limit. This continues in a cascade.

Throughout this thesis, the molecules are ionised in solution prior to spray, and as a result, the droplet simply continually decreases in size and all solvent is evaporated, until only the ion remains.

Via the spray process, kinetic energy is imparted to the solution molecule combination, and thus to the ions. As there is some level of randomness during the spray procedure, some collisions occur while the ions travel in the ambient conditions, this kinetic energy is quite random, and has a certain distribution, which is dependent on many spray parameters. Once inside the chamber, collisions are reduced, and once the ions reach a chamber of 10^{-2} mbar, one may assume the mean free path of the ions is greater than the dimensions of the chamber, and thus one may assume no collisions. It is possible to control the ions with electric fields, but any adjustment of the kinetic energy is assumed elastic in vacuum. Therefore, the non elastically controlled component of the kinetic energy of the ions is dependent only on the spray parameters. Some parameters of the spray procedure are challenging to control to a high degree, such as the humidity of the room where the experiment takes place. While the ambient conditions of the experimental room are not expected to significantly influence the spray procedure, the vastness of the parameter space makes it difficult to assert this with certainty.

3.5.2 Quadrupole mass spectrometer

A quadrupole mass spectrometer is implemented in the electrospray deposition system used throughout this thesis. The quadrupole is a form of multipole ion guide that uses electronic fields to stabilise ions that travel through it. The quadrupole, as the name implies, is simply 4 long conductive poles, which are used to create an electric field, which confines the ions. For the most effective confinement, the poles must be arranged symmetrically around a central axis, often with micrometer precision. An oscillating radio frequency (RF) field is applied with a DC component. All rods are placed under the same oscillating RF field at the same DC potential. Adjacent rods are applied with fields shifted in phase by 180°.

In the 1950s, the quadrupole was first used by Paul and Steinwedel to filter ions by m/z, the idea of which was used to build a QMS, which was awarded the Nobel prize in physics in 1989 [145–147].

The quadrupole is implemented, as the mathematics underpinning the fields generated by this system are more dependent on the mass to charge ratio (m/z), and thus allows it to serve more effectively as a filter. This allows one to tune the quadrupole parameters such that only the ions of a specific m/z are successfully guided through the system. Ions that do not correlate to this m/z begin to oscillate unstably, eventually landing on one of the electrodes and will not successfully pass fully through the analyser.

By measuring the ion current at the exit of the analyser, one may sweep through all DC voltages for a given RF that correlate to a specific m/z range and observe the ion current where peaks correspond to successful transmission of an ion at the RF and voltage that corresponds to a particular m/z, thus producing a mass spectrum. Furthermore, the mass analyser can be set to a specific m/z, such that it acts as a mass filter. This allows one ot first measure the m/z of ions in the ion beam, and then select only the desired ions. Importantly, only the m/z is defined; this does not allow for multiple charge states. Therefore, one cannot deposit multiple charge states of the same molecule simultaneously, and furthermore, it can be. challenging to analyse the composition of fragments if the charge state of these fragments is unknown.

The specifics of the mathematics behind how a QMS confines ions are complex, so only a limited discussion will be presented here. A more thorough discussion is given in the following references [32, 148–151].

The quadrupole mass filter operates by the Mathieu stability equations, which describe the motion of ions in the combined RF and DC fields. The stability of a given ion's trajectory depends on two dimensionless parameters, a and q, which are functions of the ion's mass, charge, RF frequency, and applied voltages.

This model assumes an infinite length of rod to remove any z-component.

$$a_u = \pm\frac{8qV_{DC}}{mr_0^2\Omega^2}, q_u = \pm\frac{4qV_{RF}}{mr_0^2\Omega^2} \tag{3.5}$$

a and q are dimensionless stability parameters for the trajectory of the ions in the QMS. u reflects a combination of x and y displacement, where a_u is the positive component of a_x and the negative component of a_y. q is the charge of the ion, and m is its mass. Ω is the angular frequency of the applied voltage. V_{DC} and V_{RF} are the DC voltages and RF voltages respectively. r_0 is the inscribed radius of the quadrupole system, which is the length of the straight line extending from the centre of the quadrupole, to where it first touches one of the quadrupole rods. Once an ion

exceeds this radius, it has either exited the quadrupole and is lost or impinges onto the electrode.

Ion motion is confined in regions where solutions to the Mathieu equations remain bounded, as can be seen in Figure 3.2 a) and b). Generally speaking, most QMS systems operate in the first stability region, shown in a) although operation in other regions has been performed [152, 153].

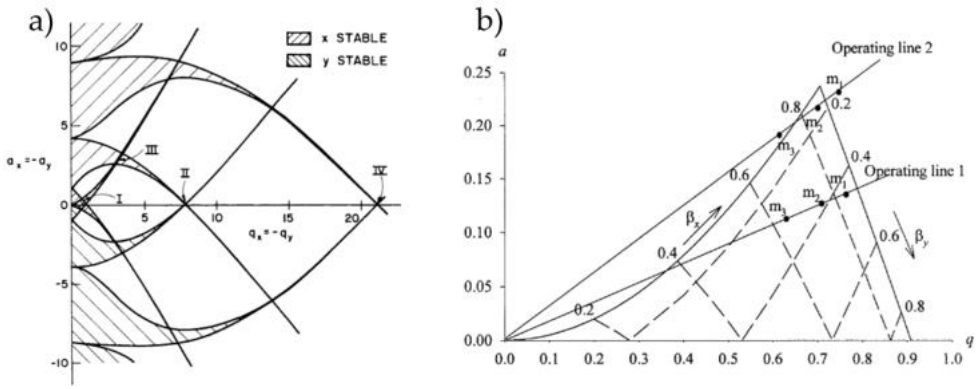

FIGURE 3.2: Ion stability diagrams for ions in quadrupole a) Ion stability regions for stable ion transmission, roman numerals depict each stability region taken from [149], b) Ion stability dependent on selecting slope of ratio of a and q, adapted from [148].

Figure 3.2 b) shows how, for a givens mass, one may select the slope of the a and q parameters for a given scanning of parameters, such that the slope intersects the allowed regions in such a way that a tuned range of ions can pass through the quadrupole in a stable manner. If one lowers the slope, then more m/z ions will pass through for some range of a and q parameters. If one raises the slope, the range of allowed m/z will decrease, improving the reoslution, but does limit the ion transmission somewhat. Observing operating line 1, m_1, m_2, and m_3 are all within the stability region, so will all transmit, whereas if one steepens the slope to operate on line 2, only m_2 will transmit stably.

3.5.3 Overview of ion optics

As the depositions will be performed in ultra high vacuum, the ions sprayed from solution need to be brought into increasingly higher levels of vacuum through a series of differentially pumped chambers. It is critical to ensure that the ions successfully transmit through the various chambers, and this is done via the use of an ion guide. These work on a similar principle to the QMS, but due to the higher order of the multipole [154, 155], a broader m/z transmission is enabled, and thus does not have the same mass selectivity and can be used to transfer all ions through to the UHV environment. The ion guides carry the ions through differential vacuum chambers with minimal losses, less than 10% of ions between each chamber.

3.5.4 Calibrating the mass spectrometer

As discussed, at a certain RF frequency, a certain DC voltage corresponds to a certain m/z. In order to use the mass spectrometer, one must first establish the correlation between these values through calibration. This can also be done post spectrum, as the mass spectra should be close to linear at similar frequencies, especially for

small adjustments. As the mass analyser was repaired multiple times throughout the PhD work, a calibration was performed using a few well defined molecules. Whilst this calibration was applied to all data within the thesis, it may be the case that different spectra were taken during different stages of repair, and thus the calibration is not perfectly valid. This may introduce some error into the quoted measured ion masses, but as will be discussed later, this error is not high enough to invalidate the assertions made about the mass of ions.

3.5.5 Kinetic energy measurements

During the spray procedure, kinetic energy is necessarily imparted to the ions. As well as any possible collisions within the system, the kinetic energy of the ions can significantly affect the resultant experiment. Once inside the vacuum system, at pressures below 10^{-2} mbar, one may assume that as the mean free path of the ions is far above the dimensions involved, there are no collisions. The only relevant energy transfer involved once within the vacuum system is from the various applied electric fields, and can thus be assumed elastic.

For many experiments, one may want to measure and control the ion kinetic energy. If one applies a retarding field of a certain voltage, ions of an energy lower than the energy of the field form this retarding voltage, will not arrive to the surface and a contribution to the ion current from these ions will not be detected. This system is known as a retarding field analyser (RFA). By scanning over a voltage range, one may define the counts of ions within this range. By scanning the voltage between the maximum and minimum ion kinetic energy, i.e between where 0% and 100% of ions are detected, one may plot a kinetic energy distribution and thus define an average ion kinetic energy. An example kinetic energy test from within the thesis is displayed in Figure 3.3.

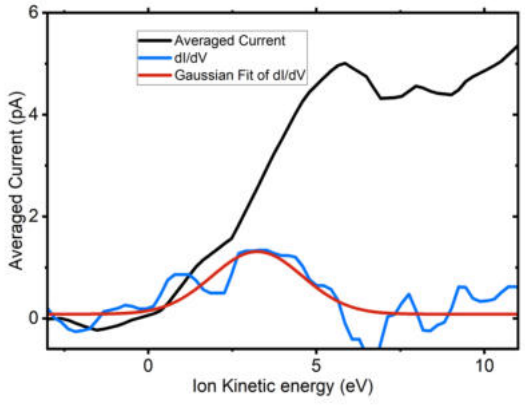

FIGURE 3.3: Example Ion Kinetic energy scan of [$TbPc_2$], with Gaussian fit of dI/dV.

Where the 0 energy is defined as the position where turning the ion beam on or off does not change the resultant current, i.e. 100% of ions do not reach the target. In principle, this should be 0 current, but due to some leakage current from the applied DC potential, there is some background. The calculated dI/dV (blue trace) displays the distribution of ions across this kinetic energy. One may then set the potential anywhere in this distribution to capture only ions of this energy and higher. In real

terms, the retarding potential is defined by the potential of the sample, relative to the prior electrode, which in this case is the final ion optic. One will shift the distribution by adjusting the sample offset. By the definition implemented here, any ions with an apparent negative kinetic energy on impact are ions that do not reach the surface. If one sets the kinetic energy very low, or even to an apparent negative, only a small fraction will reach the surface, and this small fraction has a very low distribution, allowing for better definition of the kinetic energy. Therefore, generally speaking, a thinner distribution gives a greater control of the ion kinetic energy.

While a Gaussian has been fitted here, the distribution is not necessarily a Gaussian, and depends on both the spray parameters, and the parameters of the various fields used while carrying th ions thorough the ESI system. As study of kinetic energy doe snot play a significant role in the experiments in this thesis, a deep discussion of how the distribution can be modified will not be explored and discussed.

3.6 Presentation of experimental setup

To provide a clear understanding of the experimental procedures and instrumentation used throughout this thesis, this section presents detailed diagrams of the experimental setup. These schematics illustrate the key components and configurations of the equipment, including vacuum chambers, sample preparation stages, and measurement systems, in order to provide a better grasp of how the work was conducted. Each setup is accompanied by a brief explanation highlighting its purpose and relevance to the experiments conducted.

3.6.1 LT-STM UHV setup

Figure 3.4 shows all relevant sections of the STM chamber used for all measurements within this thesis. Each chamber and component serves a specialised function towards the aims of the project, which will be discussed sequentially.

Firstly highlighted in purple is the differential pumping system, used to bring the pressure down to the $\sim 10^{-10}$ mbar regime. Roughing pumps initially evacuate the chamber to the 10^{-2}-10^{-3} mbar regime, followed by a pre-vaccum system consisting of a small turbomolecular pump, bringing the pressure down to the 10^{-7} mbar regime. This pre-vaccuum system is connected to the exhaust of a large turbomolecular pump, which pumps the chamber to the 10^{-9} mbar regime. An ion pump is equipped in both the STM and preparation chambers to reduce the pressure to the 10^{-10} mbar regime. These pumps do not contain moving parts and so can run without coupling in noise ot this system. The turbomolecular and roughing pumps can couple significant noise into this system, therefore, they may be turned off, and the pressure maintained by the ion pumps for a finite amount of time. Finally, a titanium sublimation pump is used to coat the walls in a thin layer of titanium, which can further reduce contamination by trapping impurities in the walls. This is often used following a dirtier sample preparation. Importantly, in order to reach these low pressures more rapidly, the system is baked to roughly 150°C, to desorb as much water and other contaminants to be pumped away. After the bake is complete and the system is cooled back to room temperature, a pressure of $\sim 1 \times 10^{-10}$ mbar is achieved.

Highlighted in green is the manipulator, with a linear motion feedthrough to transfer the sample between chambers. It is further equipped with a heating stage where thermal annealing and sputtering can be performed to clean the crystalline metal substrates used throughout this thesis.

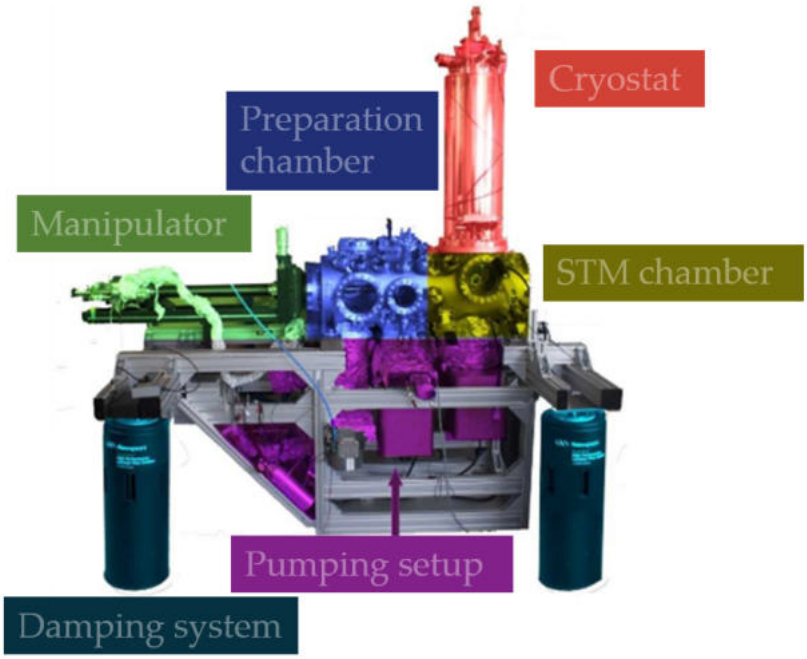

FIGURE 3.4: Colour-coded image of JT-STM setup, adapted from [156]. Port for attaching vacuum suitcase not shown.

The blue highlights the preparation chamber of the system. In general, preparations are performed in the other chamber, but simple sample heating and sample cleaning post experiment were performed here using the attached sputtergun and heating stage.

The cryostat, which is highlighted in red, is used to maintain the low temperature necessary for these experiments. An outer cryostat, which holds 25 L, is filled with liquid nitrogen (77 K) to cool the inner cryostat and conserve liquid helium. The inner cryostat, which holds 5 L, is filled with liquid helium (4 K), which cools the STM head to as low as 4.5 K. Additionally the cooled nitrogen and helium shields which isolate the STM from external noise, also act as a cryopump, bringing the chamber pressure to the 10^{-11} mbar regime. A helium recovery system is integrated to reprocess the gas helium into liquid.

Turquoise highlights the damping system, which is a commercially available system that uses compressed air to raise the entire STM off the ground, decoupling it from mechanical noise. Further, the air system passively reacts to any perturbation of the STM and corrects any vibrations.

Finally, in yellow, the STM chamber is highlighted. This contains a parking lot for up to 5 samples, as well as a wobble stick for transfers. Additionally, there are the nitrogen, helium and Jt shields. Within the shields is the STM head, the specifics of which are detailed below.

3.6.2 STM head technical details

A technical drawing of the Omicron Joule Thomson Scanning Tunneling Microscopy (JT-STM) Scan Head is displayed in Figure 3.5, alongside an image of the scan head as well as a tip on the sample.

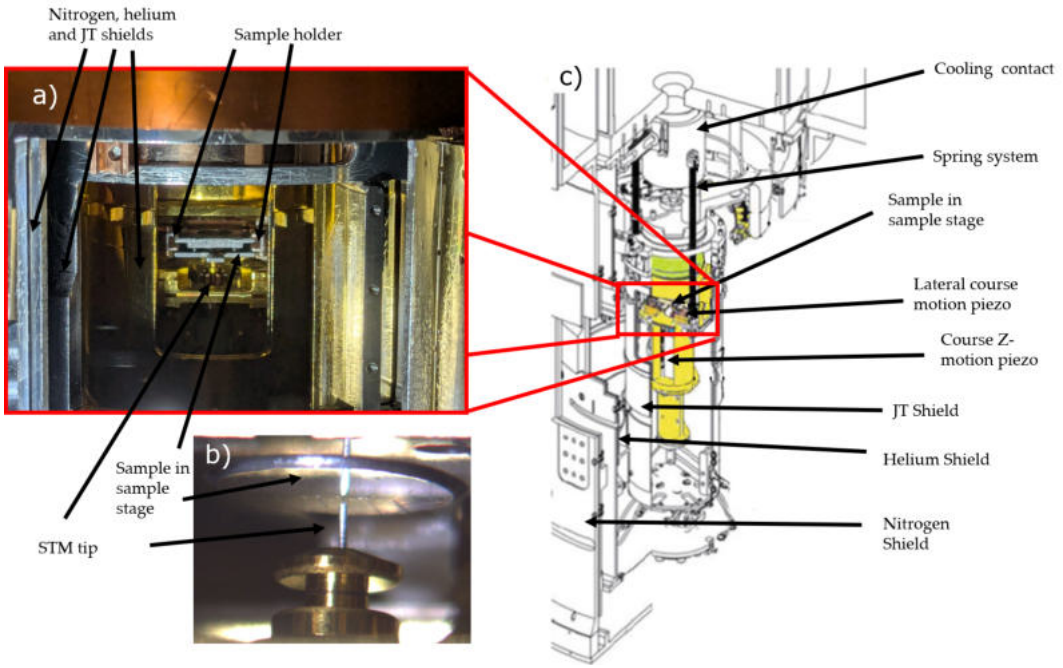

FIGURE 3.5: JT-STM head overview, a) Shows an image of the interior of STM, with some components labelled, b) shows close to contact with Ag(111) substrate c) Schematic of JT-STM taken from Omicron manual.

c) shows a schematic taken from the manual of the Omicron company [157]. The spring system indicated at the top of the image is used to damp passively against oscillations. When on the spring system, the STM is no longer in thermal or electronic contact with the rest of the system, reducing both electrical and mechanical noise.

The shields are used to shield each inner section from temperature, improving stability and keeping the sample at base temperature for a longer time. All images and STS spectra presented in this thesis were taken with the STM cooled to 4.5 K.

The tip and scan piezo rest upon a Z coarse motion piezo system, which allows the tip to move away from the surface for safe transfer into and out of the STM head. This coarse motion allows the tip to move $\sim$3mm away from the surface, via the slip and stick motion of the piezo stack.

a) shows a user view into the scan head, the omicron type sample plate is placed into its sample holder, which is capable of moving laterally to allow for some coarse motion across the sample. This allows one to scan different local areas around the surface. The sample can be moved laterally by a few mm, which is greater than the $\sim$6 mm diameter of the surface.

The tip is upon the scan piezo, which can move the tip towards/away from the surface by 400 nm, and laterally by 2 µm when the STM is cooled to 4.5 K. The tip is approached to the surface by repeatedly moving the tip towards the surface via the coarse motion by roughly 150 nm, and then the scan piezo fully extends. If the feedback loop does not detect a tunneling current before extending fully, it will retract fully, and another coarse motion of 150nm is made. This is repeated until the tip enters into tunneling contact.

3.6.3 ESI-CIBD UHV setup

Figure 3.6 displays the UHV system of the ESI deposition chamber. This figure is taken from [158]. An initial treatment of the setup of the UHV chamber will be provided, followed by an in depth discussion of the setup of the various ion guides within the chamber.

Highlighted in green is the ion source, which is in ambient conditions. It is contained inside a box to protect the user from the high voltage that will be applied to the emitter needle. This section contains a syringe with a controlled plunger mechanism which pushes the solution through plastic tubing into the 'emitter box'. The emitter box is a metal box from which the emitter protrudes, and through which the high voltage is applied. It can be heated if desired, and gas can be introduced into the emitter box in order to control the spray environment more precisely, although this feature was not used. Furthermore, it allows the rapid exchange of emitters, in order to change between emitter dimensions or materials. At the boundary between these regions is the counter electrode (to which a small voltage can also be applied if necessary). The electrode narrows into a capillary which protrudes into the UHV system and the subsequent chamber. The capillary can be heated to ~200°C, in order to accelerate the evaporation of the neutral solvent. A small rubber seal can be pushed into place to cover the capillary when the system is inactive and maintain pressure inside the UHV chambers.

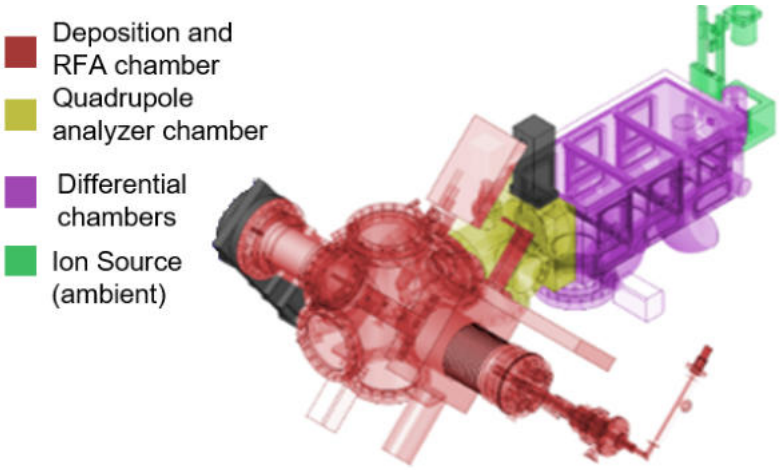

FIGURE 3.6: Colour coded schematic of ESI-CIBD UHV setup, additional pumping system not shown, adapted from [158]

Highlighted in purple are the series of differential chambers. A small membrane pump keeps these chambers at vacuum when the system is not in use. Scroll pumps are used to pump the large volume of gas within this chamber, and a turbo pump in the last of the 3 chambers to pump this chamber to UHV condition. As the final chamber will be opened to the entire UHV system, this can only be opened once the final differential chamber is at least in the 10^{-5} mbar regime. Finally, there are large roots pumps which are used to pump the very large volume of air that enters once the seal is removed at the capillary, and the differential chambers are open to the ambient environment. With all pumps running and the capillary open, the 1st, 2nd, and 3rd differential chambers are at the 1 mbar, 10^{-2} mbar and 10^{-6} mbar regime respectively. These chambers contain the ion funnel and the first two ion guide optics. The final feature of this chamber, is that it can be moved to that the

final guide can be inserted into or retracted from the UHV chamber, so that the space between ion guides is minimised, and the exit of ion guide 2 is as close as possible to ion guide 3, in order to reduce losses.

The chamber highlighted in yellow contains the final ion guide and the quadrupole mass analyser. This chamber is also pumped by a small turbomolecular pump, connected to a pre-vaccuum system. This chamber is maintained in the high 10^{-9} mbar regime.

The final chamber, highlighted in red, is the preparation chamber for depositions. It is equipped with a sputtergun and a sample stage with an integrated oven for annealing. The sample stage can be moved in XYZ directions and rotated to orient the sample. The stage can also be cooled using cryoliquids. The potential of the sample on the stage can be set, in order to perform the retarding field analysis, and set the kinetic energy of the ions. The final blade ion guide is housed here, which focuses and collimates the ion beam exiting from the QMS to target directly onto the sample. This chamber is pumped by a large turbomolecular pump and has also been baked. The base pressure in this chamber is in the high 10^{-10} mbar regime, but rises to the 10^{-9} mbar regime during deposition.

3.6.4 ESI-CIBD technical drawing

Below is a schematic of the ESI-CIBD system. The diagram is not to scale.

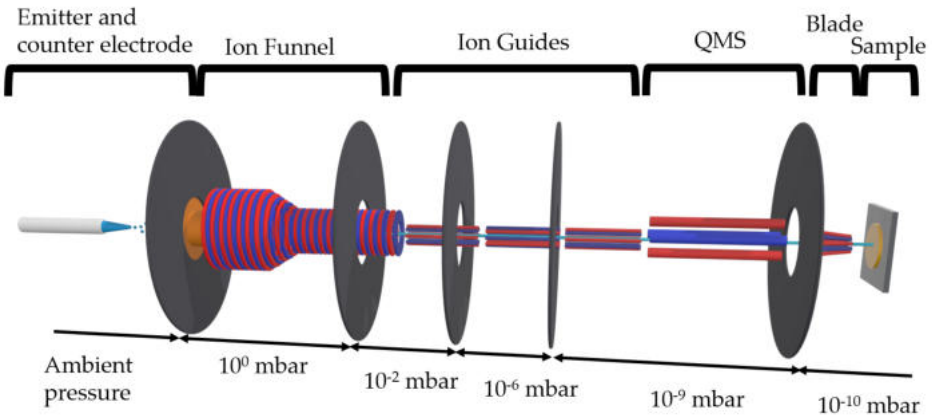

FIGURE 3.7: Schematic diagram of ESI-CIBD

The specific construction of the ion funnel can be seen here, with stacked RF electrodes of decreasing diameter. This collimates the beam and allows it to be focused through the multiple 16 pole ion guides, significantly reducing losses.

As the current can be measured on the sample, it is also possible to measure how much charge builds up on the surface, and assuming the charge state has been well defined, one may count the total charge buildup on surface during the deposition, and thus a specific number of individual molecules deposited onto surface. This allows one to calibrate coverages between separate depositions.

Each individual component can have its voltage potential set in the range ±100 V. Therefore, the kinetic energy of the ions can be controlled at any point inside the UHV system. Furthermore, the current on each component can be measured in order to verify the losses of ions throughout the system in order to troubleshoot and perform diagnostics.

3.6.5 Setup and use of the vacuum suitcase

As the STM connected to the UHV chamber of the ESI-CIBD system can only measure at a minimum of ∼80K, and the intention of this project is to take scanning tunneling spectroscopy of features that are only visible at temperatures below 30K, it was necessary to transfer between UHV systems to the low temperature STM, depicted in Figure, 3.4 This was achieved via the use of a vacuum suitcase, as depicted in Figure 3.8

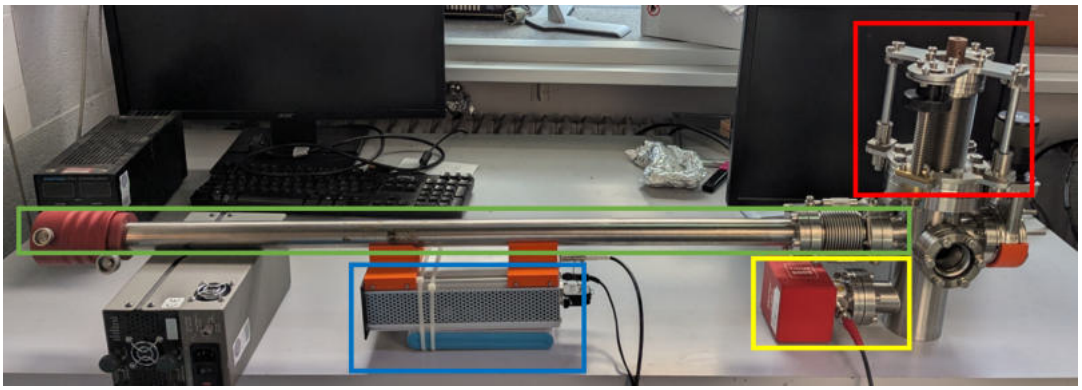

FIGURE 3.8: Image of Vacuum suitcase with important components highlighted by colour.

This portable UHV-compatible transfer chamber allows for the transport of samples under vacuum conditions, preserving their surface integrity between preparation, deposition, and measurement stages. The suitcase is equipped with a rubber gasket for rapid attachment to the port system. This rubber gasket can maintain pressure down to as low as 10^{-9} mbar regime and can be baked to up to 200°C. The port is attached to a chamber by a standard CF-40 flange interface and thus can be simply attached to most chambers. The suitcase itself contains a multistage adjustable parking, transfer arm, compact ion pump, ion getter material and a simple commercial battery pack to remotely power the system. This ensures consistent UHV conditions throughout the transfer process, and allows the suitcase to be carried for as long as the system remains powered. Its use was essential for these experiments, where deposition and analysis took place in separate chambers.

Chapter 4

State of the art

4.1 Introduction

In order to fully discuss the relevance of the results taken in this thesis, it is important to first discuss some of the prior work already completed on and around these topics. This section will discuss the $[TbPc_2]^0$ molecule studied in this thesis and how it has been studied on surface, as well as explaining the Kondo effect and its relevance.

4.2 Kondo effect

The Kondo effect is a spin-flip scattering process of conduction electrons with magnetic sites in a material. The Kondo effect is only measurable below a certain characteristic 'Kondo temperature'. The Kondo temperature of the materials studied in this thesis is ∼40 K, thus necessitating the low temperature STM described in chapter 3.

Above the Kondo temperature T_k thermal energy disrupts the formation of a screening cloud, therefore, the spin of the magnetic site remains unscreened. Below T_k, a cloud of antiferromagnetically coupled spins orbit the magnetic site creating a screening 'Kondo cloud', as depicted in figure 4.1. The magnetic site is screened as the conduction electrons are entangled with the spin of the magnetic site, creating a singlet state. Itinerant electrons are scattered off of the screened impurity in a spin flip scattering process.

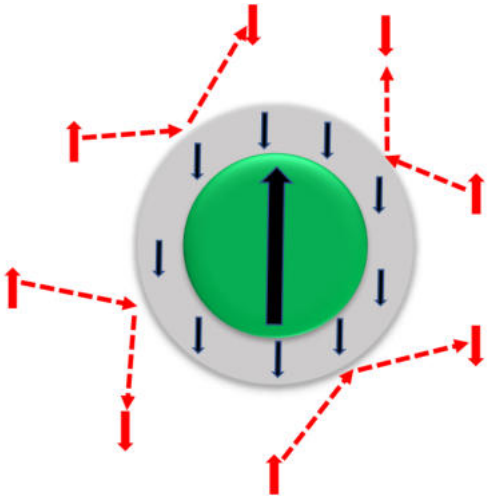

FIGURE 4.1: Diagram of an example Kondo cloud, where the green circle shows the magnetic site, the grey the Kondo cloud, arrows depict spin orientation, and red arrows show itinerant electrons.

Generally, in this thesis, the identification of the Kondo effect is used only to probe radicals on the surface and to observe unpaired spins in radical molecules. As these unpaired spins have some interest towards QIP, it is useful to study how these radicals change by measuring this Kondo effect.

4.2.1 Origin and history

The Kondo effect was first observed in the 1930s when researchers noticed an unexpected increase in electrical resistance at low temperatures in metals such as gold, copper and platinum [159, 160]. This behavior was puzzling because, according to standard theories of metallic conduction, resistance should decrease as temperature is lowered due to reduced phonon scattering. After some experimentation, this unexpected behaviour was eventually attributed to dilute magnetic impurities, such as iron, within these metals. The mystery remained unresolved until 1964, when Jun Kondo developed a theoretical model to explain the phenomenon. Using perturbation theory, Kondo demonstrated that conduction electrons in a metal interact with localised magnetic impurities via spin exchange, leading to a localisation of the conduction band electrons at low temperatures [161].

This effect was found to arise from the formation of a many-body quantum state in which conduction electrons screen the impurity's magnetic moment, a process later understood in terms of a Kondo singlet.

4.2.2 Theoretical discussion

The theoretical foundation of the Kondo effect is based on the interaction between a localised magnetic impurity and the conduction electrons in a metallic host. The Kondo effect is a spin flip scattering process, where a magnetic moment in a material screens electrons [161–167]. This scattering raises the resistivity of a material as temperature decreases. Normally, this effect is not visible. The resitivity of a material was modelled by Jun Kondo as the following.

$$\rho = aT^5 + b\rho_0 - c\ln T \tag{4.1}$$

Where the T^5 term is due to phonon scattering, and dominates until one reaches lower temperatures. a, b and c are constants and ρ is the resistivity. The $\ln(T)$ term is due to scattering from these magnetic sites. The Kondo temperature is the temperature at which the $\ln(T)$ term begins to dominate and the resistivity reaches a minimum value.

This modelling shows an obvious problem, that as T approaches 0, $\ln(T)$ diverges. This was known as the Kondo problem. This issue was only resolved many years later by K. Wilson [168, 169], who found an alternative model at low temperatures. The exact solutions were found by Andrei [170] and Wiegmann [171] in 1980.

In order to understand a single impurity in a magnetic host, such as is the case for a magnetic molecule on a surface, the 'Anderson single impurity model' was proposed [172, 173]. This was proposed for a delocalised d-orbital, however, in this case it will be discussed in the context of a Ce impurity on the surface of a host metal. In the example shown in Figure 4.2, the $4f^1$ state of a Cerium atom is filled, and the $4f^2$ state unfilled. They are separated due to coulomb repulsion, with an energy gap of U. ϵ_f is the energy gap between Fermi level and the singly occupied orbital $4f^1$. Δ is the broadening of the state due to hybridisation with the continuum from the host metal. $\Delta = \rho_0|V|^2$, where ρ_0 is the DOS at Fermi level, and V is the hybridisation matrix. An exchange process can take place where either the electron in the $4f$ state

empties into the host metal and then the opposite spin electron relaxes back into the $4f$, or both an electron in the host metal, and the $4f$ state are together in the $4f^2$ state, and again the opposite spins relax to their initial positions. In both cases, a spin flip occurs.

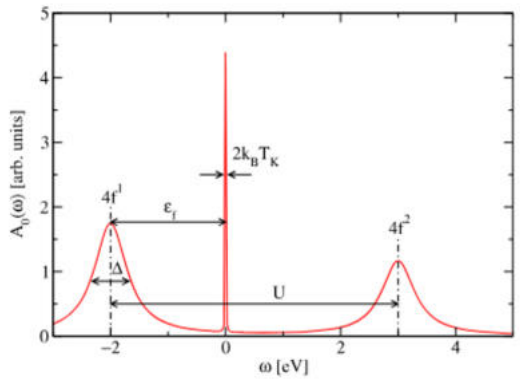

FIGURE 4.2: Exemplary spectrum of DOS in the framework of the Anderson model, simulated for a cerium atom, where ϵ_f= -2 eV, U= 5 eV, Δ = 0.34 eV, figure taken from Ternes et al.[173]

One may question where the energy comes from for the electron in the $4f^1$ state to enter the other states. Due to Heisenberg's uncertainty principle, the energy difference is small enough that this excitation can occur as a virtual process for a timescale of 10^{-15} seconds, which is sufficient time for this spin flip scattering process to occur.

Many spin flip scattering events, such as those described above, cause a screening effect of the local magnetic moment.

As the conduction electrons in the host metal are screened by the impurity, this causes a singlet ground state, due to a many body interaction. This screening of the impurity by the conduction electrons condenses the density of states around the Fermi level.

4.2.3 Observation of Kondo effect on surfaces via STM and STS

As discussed, the Kondo effect screens the conduction electrons, causing a a peak in the conductance at the Fermi level. Therefore, when one measures dI/dV of some magnetic molecules, one may measure a feature at zero bias due to the Kondo effect. This feature at Fermi level, called a Kondo resonance, was first observed on the surface via STS by Madhavan et al. for Co on Au(111) system [174].

One important parameter that is characteristic of the material is the Kondo temperature. The width of the Kondo feature is dependent on Kondo temperature, and thus can be used to probe the properties of the material being measured. Within the Anderson model at $T = 0K$, the Half Width Half Maximum (HWHM) of the Kondo peak Γ is dependent on the following [172].

$$\Gamma = k_B T_k \approx \sqrt{2\Delta \frac{U}{\pi}} e \left[-\frac{\pi}{2\Delta} \left(\left| \frac{1}{\epsilon_f} \right| + \left| \frac{1}{\epsilon_f + U} \right| \right)^{-1} \right] \tag{4.2}$$

For a non-zero temperature, there is some broadening of the observed Kondo resonance. The Kondo peak width grows linearly with temperature above T_k within the

framework of the Fermi-Liquid model [167, 173] due to the smearing of the Fermi-Dirac distribution of initial and final states of the spin flip process described in the prior section. This leads to a peak width at finite temperature being calculated as follows.

$$2\Gamma = \sqrt{(\alpha k_B T)^2 + (2k_B T_K)^2} \tag{4.3}$$

Where α is the slope of the linear relationship between temperature and peak width.

The shape of the zero bias feature is dependent on how the electrons transport from the surface to the tip. There are two possible channels for the electrons to tunnel into the tip, one of virtual tunneling as described above, and one of direct tunneling. This adjusts the feature such that either a dip or a peak is observed, depending respectively, if the virtual or direct tunneling dominates, as well as an asymmetric peak due to quantum interference between both channels. This can be modelled by a Fano lineshape of the following form [175].

$$\rho = \rho_0 + \frac{(q+\epsilon)^2}{(1+\epsilon^2)} \qquad \epsilon = \frac{E - E_0}{\Gamma} \tag{4.4}$$

Where q is the q-factor that determines the shape of the resonance as seen in Figure 4.3. When the q factor is 0, all tunneling occurs directly into the metal sample, and at infinity all tunneling occurs via the Kondo resonance state.

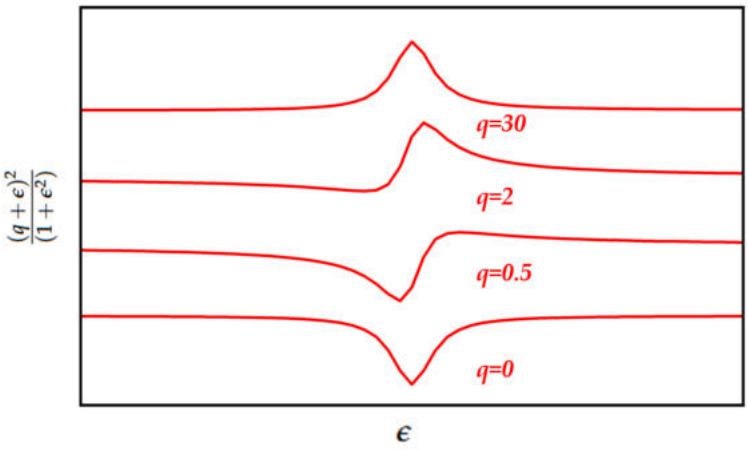

FIGURE 4.3: Calculated Fano functions depicting variation in q-factor

The q-factor is also somewhat dependent on the experimental parameters, such as tip sample distance and substrate material. If one controls these parameters, one may study the interplay of the Kondo effect with other physical phenomena, such as magnetic anisotropy, quantum confinement, and surface interactions, making it a crucial tool for exploring correlated electron physics at the nanoscale.

It must be stated that the appearance of a zero bias anomaly is not necessarily due to a Kondo effect. For example, the measurement of hydrogen from the surface upon magnetic atoms. [176]. Therefore, it is important to verify the origin of these zero bias features. A key parameter defining the Kondo effect that has already been discussed is the relationship between peak width and temperature. If one measures the

same Kondo feature with the same Kondo temperature at different sample temperatures, one expects a linear change in peak width. The linear change in peak width is a strong signature of the Kondo effect. If it is non linear, it may be the Kondo effect convoluted with some other phenomenon. By measuring the peak width at multiple temperatures, and extracting from the linear relationship, the Kondo temperature may be measured with high accuracy.

One very clear signature that an observed feature is a Kondo feature is the splitting of a Kondo resonance in the presence of a magnetic field [119, 177–182]. By applying a magnetic field to a sample where a Kondo resonance can be observed, one will observe two peaks symmetric around the Fermi energy, where the peak to peak distance is dependent on the applied magnetic field strength. This Zeeman splitting is described as follows [183–185].

$$\Delta_V = 2g\mu_B B \tag{4.5}$$

Where Δ_V is the width of splitting in volts, is the inherent g-factor, is the magnetic field, and μ_B is the Bohr magneton. The value of the Bohr magneton is 57.9 μeV. Therefore the splitting is of the order of $0.1\mathrm{mV/T}$ and as such, a large magnetic field is required for visible splitting of peaks in many materials.

The most accurate measurement of Kondo temperature is achieved from the linear relationship of peak width to varying sample temperature. If this is not possible, one may approximate the Kondo temperature of a material with a q-factor approaching infinity using the derivation from Nagaoka et al.[186], which is derived from eqn 4.2. This assumes a Lorentz type function.

$$\Gamma = \sqrt{(\pi k_B T_K)^2 + 2(k_B T_K)^2}. \tag{4.6}$$

This is an imperfect method to derive Kondo temperature, but it does allow a simple comparative study of different systems studied within this thesis.

4.3 Molecular conformation and imaging of [TbPc$_2$]0

[TbPc$_2$]^0 has been extensively studied on various surfaces using STM to investigate its electronic, magnetic, and structural properties at the atomic scale. High-resolution STM imaging reveals the characteristic lobed structure of the phthalocyanine ligands, where the split 8-lobe structure, as seen in Figure 4.4 a) taken from Lawes et al. [187] and through the literature [12–15, 188–193], is due to the 4 lobe structure caused by the phthalocyanine being split by interaction with the phthalocyanine in the lower level. Furthermore, the orbitals due to the central Terbium ion are visible. As discussed in chapter 3, STM does not measure directly topography, but a convolution of topography and electronic structure, therefore, despite the fact that the physical ion is below the plane of the upper Phthalocyanine, the orbitals of the ion are still measurable and identifiable in imaging.

As the ligand of these molecules has been heavily modified during the experiments in this thesis, it is important to understand the structure of the molecule without any substituent for the purpose of further discussion. Importantly, the 4 lobe structure, which in this case is split into 8 lobes, is due to the upper phthalocyanine. This 4 lobe structure, due to the 4 benzene rings of the upper phthalocyanine in a cross structure, will be referred to as the 'aromatic backbone' of the molecule.

Many molecules, when deposited onto surfaces, organise into regular islands, as depicted in Figure 4.4 b). This is due to a combination of molecule-substrate

and intermolecular interactions. The highly planar phthalocyanine ligands of the $[TbPc_2]^0$ molecules, with their extended -conjugated systems, often adsorb flat on metallic substrates such as the Au (111) and Cu (111) crystals studied within this thesis.

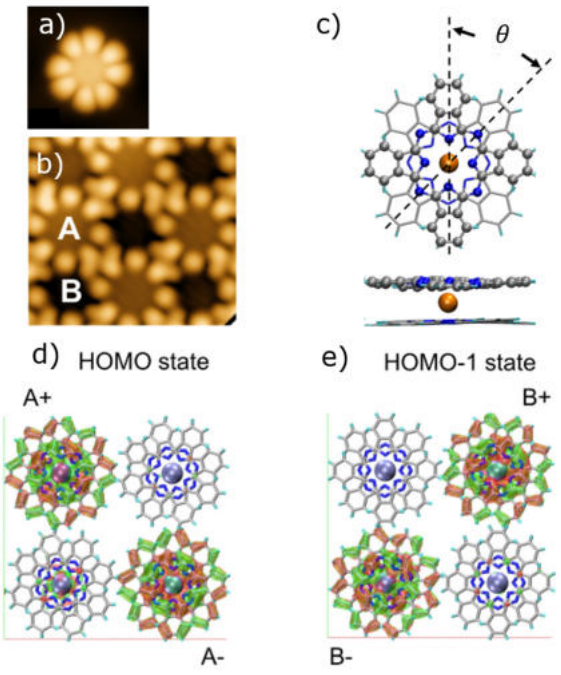

FIGURE 4.4: Overview of differential contrast in islands of $[TbPc_2]^0$ a) STM image of isolated $[TbPc_2]^0$ molecule deposited onto Au(111), U_B=300 mV I_t=60 pA, b) Image of $[TbPc_2]^0$ island on Au(111), with A and B type molecules indicated U_B=300 mV I_t=70 pA, c) Schematic of molecule, where θ depicts the dhedral angle, d) and e) Top view of HOMO and HOMO-1 wavefunctions for d) and e) respectively, where + and - refer to spin up and down respectively, taken from Lawes et al. [187].

These islands have long-range order, forming full self-assembled monolayers adopting a square lattice on both Au (111) and Cu (111) as depicted. One of the aims of this project is to adjust the ligand of the molecule such that the parameters of this lattice is tuned. The islands are reported to form in both a compact and non-compact phase. Thus, two sets of lattice parameters are recorded. 1.43 nm and 1.50 nm [193, 194].

Furthermore, it is also noted that each upper phthalocyanine is rotated by 15° relative to its neighbors in a checkerboard pattern, which is widely reported in literature [13, 14].

Because the STM tip probes only the surface directly beneath it, resolving the underlying structure beneath the upper phthalocyanine layer is challenging. The azimuthal angle is defined through this thesis as the angle of the entire molecule relative to some axis parallel to the substrate. The dihedral angle, depicted in figure 4.4 is defined as the rotational angle between the upper and lower phthalocyanines. For a free phthalocyanine, this angle is 45°.

It is not clear from imaging alone, if the relative 15° rotation between adjacent phthalocyanines in the upper layer is due to alternately differing dihedral angles, or alternately differing azimuthal angles.

The centre of the molecules of $[TbPc_2]^0$ organised into islands on Au (111) show an alternating light and dark contrast in a checkerboard pattern, as seen in Figure 4.4 b). These two contrasts are labelled as A and B. This contrast has been observed by Komeda et al. and Amokrane et al. [12, 14] It was initially proposed that this pattern results from a checkerboard like variation in the dihedral angle between the molecular layers. Meaning that the lower phthalocyanines all have the same orientation, and the upper layer has an alternate conformation, as can be seen from the image. This is surprising, given that one would expect steric repulsions from the groups in the lower phthalocyanines, and this is considered not possible.

From Lawes et al. [187], it is argued that this contrast is in fact due to the electronic properties of the molecules. By performing a molecular dynamics simulation, and ab initio DFT calculations, one finds that the model relaxes into a conformation where the dihedral angles of adjacent phthalocyanines are the same, and the azimuthal angle is rotated by 15°, i.e the entire molecule is rotated in a checkerboard pattern, not just the upper phthalocynaine.

Furthermore, by an energy level analysis performed on states close to Fermi level, one may observe the localisation of states at different energies, as depicted in Figures 4.4d) and e). It was found that the wave function of the HOMO state is localised to the A type molecules, and the B type shows localisation of the HOMO-1. Therefore, the checkerboard symmetry is highly likely to be electronic in origin, and that ultimately the situation is not fully clarified.

4.4 Spectroscopy of $[TbPc_2]^0$

The $[TbPc_2]^0$ molecule has been measured on many different substrates in many different conformations, and when organised into various structures. It has been found that, particularly when deposited onto Au(111), the measured dI/dV spectra can vary greatly depending on various parameters of what has been measured. As the intention of this project is to modify how these molecules organise and interact on the surface, mostly focusing on Au(111), it is important to understand how these parameters may affect the resultant measured spectroscopy.

Firstly, when deposited onto Cu(111), the situation appears quite clear [193]. A band gap of 2.3-2.4 V is measured, depending on measurements being taken on the centre of the molecule or a lobe. The LUMO (Lowest Unoccupied Molecular Orbital) is measured at 1.8 V, and the HOMO (Highest Occupied Molecular Orbital) at -600 mV when measured on the lobe, and -500 mV when measured on the centre. Similar observations are found for other substrates [189, 190].

The situation becomes markedly more complex when deposited onto Au(111). There is a distinct difference between spectroscopy when an isolated molecule is measured, compared to when measuring islands of molecules [13, 14]. Furthermore, there are significant differences when measuring different locations within islands, as well as depending on the variations within the island.

From Amokrane et al. [14], there is a strong dependence of the measured spectroscopy upon both measuring on lobes compared to the centre of molecules. Additionally, when in the compact phase, there is a difference in spectroscopy when measuring lobes that overlap with lobes of adjacent molecules. The overlap of multiple orbitals causing differing spectroscopy is not surprising, but certainly requires consideration. Finally, a difference is observed when measuring the centre of the two types of molecular contrast seen in imaging, called A and B type molecules, but this is summarised in one of the following subsections.

From Komeda et al. [13] a difference in spectroscopy was found on differing lobes, due to a tilt in the upper Phthalocyanine ring of the molecules. This differential tilting caused each lobe to have a differing distance to the sample, and thus, a differing transport. This tilt was not found in pristine layers by Amorkane et al. and thus these two observations of variation in spectroscopy do not conflict with each other.

This will be discussed in detail later, when it becomes relevant to compare to spectra taken in this thesis, but the most important point to discuss is that the many possible complex molecular interactions, the resulting spectra can be difficult to interpret and require strong experimental validation. It should be noted that other possible additional complications could cause differences in spectroscopy, such as something simple like differing adsorption sites, or something further and more complex relating to the adjustment of the ligand intended within this thesis.

4.4.1 Kondo effect measured on $[TbPc_2]^0$ on the surface

The appearance of the Kondo effect on the $[TbPc_2]^0$ on the surface has been widely studied [12–15]. As discussed prior, the $[TbPc_2]^0$ molecule hosts an unpaired 4f electron in the Terbium centre, as well as an unpaired electron delocalised over the Pc ligand. When measured on Au(111) Kondo effect is only observed on the ligand, due to the delocalised unpaired electron.

Barhoumi et al. [15] found that when deposited onto Cu(111), a Kondo resonance was found both when measuring over the Pc ligand, as well as on the centre. In order to verify that this resonance on the centre was due to the terbium 4f electron,$[YPc_2]^0$ was deposited onto Cu(111), and no resonance was found on the centre. Given that Yttrium has no 4f electron and as such should show no Kondo effect. This proves that the measurement on the $[TbPc_2]^0$ centre was due to the 4f electron, which was the first measurement of Kondo due to the Terbium metal centre. A similar Kondo measurement on the metal centre of $[DyPc_2]^0$ deposited onto Cu(100) has also been reported [195]. Similar measurements were attempted on Ag(111), but no Kondo effect was measured, neither on the centre, nor on the ligand. The lack of a Kondo resonance measured on the ligand was considered due to the charge transfer from the surface into the ligand, quenching the spin moment, and thus no Kondo effect is measured.

The lack of a Kondo resonance when deposited onto Ag(111) and Au(111) from the Terbium centre is attributed to a weak molecule-substrate interaction not allowing sufficient electrons to tunnel through the Terbium ion and scatter allowing the Kondo effect to be observed.

The organic Kondo due to the ligand on Au(111) has been widely studied. From Amokrane et al. [14], an isolated molecule was compared to clusters and islands of $[TbPc_2]^0$. Kondo was found on all lobes of the isolated molecule, on 3 lobe overlaps of trimer and tetramers, but only on non-overlapping lobes of semi infinite islands of $[TbPc_2]$.

One of the aims of this thesis was to further functionalise the $[TbPc_2]^0$ molecule in order to adjust interactions on surface, including intermolecular interactions, to verify how the measured Kondo resonance may change. As such, it is essential to clarify the prior observations of the Kondo effect on Au(111).

Part II

Results: Discussion and Conclusion

Chapter 5

Study of the Surface Oxidation of $[TbPc_2]^-$ using ESI-CIBD

5.1 Introduction

To comprehensively study molecular structures on surfaces deposited by ESI-CIBD, it is necessary to fully understand the change the molecule undergoes during the spray process and verify thoroughly that the use of the ESI-CIBD system has no effect on the structure on the surface when compared to other deposition methods. As a control experiment, one must first observe the resultant system when one deposits unsubstituted $[TbPc_2]^0$ via the use of the ESI-CIBD system and compare it to the system observed when $[TbPc_2]^0$ is deposited via sublimation. $[TbPc_2]^0$ has been well characterised when deposited by sublimation, and thus, a direct comparison can be made. This allows a comprehensive study of $[TbPc_2]^0$ with more complex substituents. Since deposition by sublimation will not be possible for the further systems investigated within this thesis, the viability of the ESI-CIBD system must be verified in advance of these further experiments. Of particular relevance to this thesis, the molecules must be ionised in order to guide them through the ESI-CIBD system. Thus, the electronic structure of the molecule is modified. As discussed in chapter 4, interesting properties of these molecules, as well as future potential applications, depend on the unpaired electron delocalised over both Pcs. Furthermore, it is the intention to attach additional groups to these molecules in order to study them on the surface. The addition (or removal) of electrons into (from) this system will likely quench the radical property. As discussed in chapter 3, a kilo-volt range potential difference is applied between the spray nozzle of the ESI-CIBD system and the entrance to the UHV. Due to the high potential, charged droplets are sprayed towards and into the UHV system, and due to the fields, ions are ripped from the droplets by a series of different processes.

Thus, the charge state of the molecule is not strictly defined, and one would expect many charge states. By charging the molecules in solution prior to spraying, one may better define the charge state and charging process, allowing an understanding of how electrons are added or removed from the sprayed molecules. Furthermore, charging in solution reduces the necessary voltage to spray at a high ion beam intensity, lowering the likelihood of less defined and higher charge states. Whether charging the molecules in solution or by the spray process, the radical property will likely be suppressed due to additional electrons pairing with the unpaired electron.

It is the expectation that due to adsorption on a metallic surface, the ionised molecule returns to its neutral radical form[188], and the molecular system on the surface will be identical to that of molecules deposited via sublimation. Confirming this is essential for the study of $[TbPc_2]^0$ molecules studied in this thesis, as well as for further projects outside of the scope of this thesis.

5.2 Alternative deposition methods

Whilst the ESI-CIBD system used in this thesis is considered the most viable method for depositing thermolabile molecules onto metal surfaces, some alternatives will be briefly discussed here.

Drop casting is the process of simply dropping a controlled quantity and concentration of a molecule in solution onto a surface. Once the solution evaporates, only the intact molecule is left on the surface. Drop casting is often implemented to deposit onto non-metals when used in conjunction with STM [196–199], often in non-UHV conditions, but has also been reported for use on metal surfaces [200, 201]. This method has many advantages and disadvantages. It can be highly cost-effective, depending on the complexity of the system. No heating of the molecule is required, so it is unlikely that the molecule decomposes during deposition, allowing the use of molecules sensitive to temperature. This procedure does not allow for the removal of contaminants from the chemical sample. Additionally, because one is releasing a droplet of solvent from ambient conditions directly to UHV, this may cause sample contamination. More complex drop-casting setups can be constructed to limit this contamination. As a result, reports of drop casting for use in STM on metal surfaces are limited.

Secondly, the emerging technique of matrix-assisted deposition (MAD) is reported for the deposition of molecules onto metal surfaces for use in STM [202, 203]. MAD uses a fibreglass applicator dipped into a powder formed from a melted mixture of the target molecule and an inert 'matrix' material. This applicator is placed into UHV and then pressed onto the substrate. The substrate is heated to remove the 'matrix' material, leaving only the target molecule. This technique has the advantage that the metal substrate will not be exposed to ambient conditions and can remain clean. The requirement for heating the sample is incompatible with the thermolabile nature of the molecules studied in this thesis.

5.3 Charging molecules in solution

In order to better control the charge state of the molecule in these experiments and increase ionisation efficiency, the molecule is charged in solution via a redox reaction. Charging the molecule in solution before spraying gives numerous advantages. Increasing the number of ions in the system improves current, and thus, intensity in mass spectra, which allows a better resolution of individual peaks and an improved understanding of the specific content of the ion beam. Furthermore, a higher current intensity decreases the required deposition time.

In this case, a redox reaction is performed using Hydrazine, which can donate up to four electrons per molecule, specifically to the Pc ring, as displayed in Figure 5.1. In principle, only 1/4 of the molecular concentration of Hydrazine relative to the target molecule is necessary, as the hydrazine can donate 4 electrons. In the presence of oxygen, the [$TbPc_2$]$^-$ oxidises back to its neutral form. As the syringe used in spraying needs to be refilled periodically, to avoid either preparing a sample multiple times each deposition or risking oxidation of the moelcular sample in the bottle prior to spraying, additional Hydrazine was added to counteract this oxidation during the long deposition time.

The reduction of phthalocyanines by this process is widely reported [204–210]. This modification of the charge state can be verified by UV-Vis spectroscopy. Further,

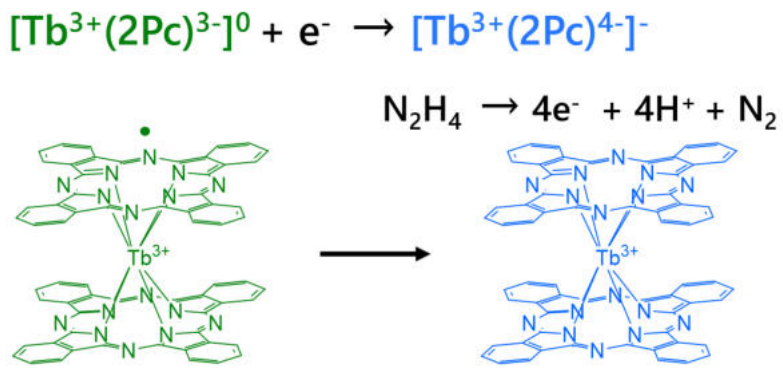

FIGURE 5.1: The reaction scheme of Hydrazine charging, displayed with molecular models. The green dot depicts the unpaired electron delocalised over both Pcs

it can be qualitatively observed by the change of the molecule's solution colour from its green (neutral) state to its blue (anionic) state[204, 208].

The redox potential of phthalocyanine complex molecules is minimally altered by the functionalisation of its ligands [205, 207]. For more complex molecules studied later in this thesis, only the change in colour of the molecule was used to verify the electronic structure of the Pc ring of the molecule in solution. Once sprayed, the charge state of the molecules can be verified to ensure that the expected single charging from Hydrazine has been achieved.

One aim of this thesis concerns adjusting the electronic properties of these molecules on surfaces, with a specific focus on tuning ligand parameters to study the electronic structure, specifically the unpaired electrons in the system. From the Hydrazine reaction depicted in Figure 5.1, the electron donated to the molecule pairs with unpaired electron de-localised over the Pc ligands, and thus suppresses the radical property of the molecule[204].

As a result, it is necessary to verify if this charging procedure affects the electronic structure of the sample during the resultant experiment. This can be tested by observing if the delocalised Pc ligand unpaired valence electron is restored once the molecule reaches the surface. Due to the low reduction potential of the negatively charged molecule with respect to the Au(111) metal surface studied here, it is not certain whether the electron is donated upon contact with the Au(111) surface. Therefore, the resultant deposition from ESD must be compared to a similar deposition via sublimation, in order to verify if it affects the resultant molecular charge on surface, and confirm ESD as a viable alternative to sublimation.

The Kondo effect observed on the $[TbPc_2]^0$ molecule when deposited onto Au(111) is attributed only to the unpaired electron delocalised over the Pc ligand [12–15], but no Kondo peak is observed associated to the Terbium centre spin, as discussed in chapter 4. Therefore, the appearance of a Kondo feature on the $[TbPc_2]^0$ molecule deposited onto Au(111) via ESI-CIBD would verify that the molecule is a radical, and thus verify the viability of the ESI-CIBD system for use in the subsequent experiments.

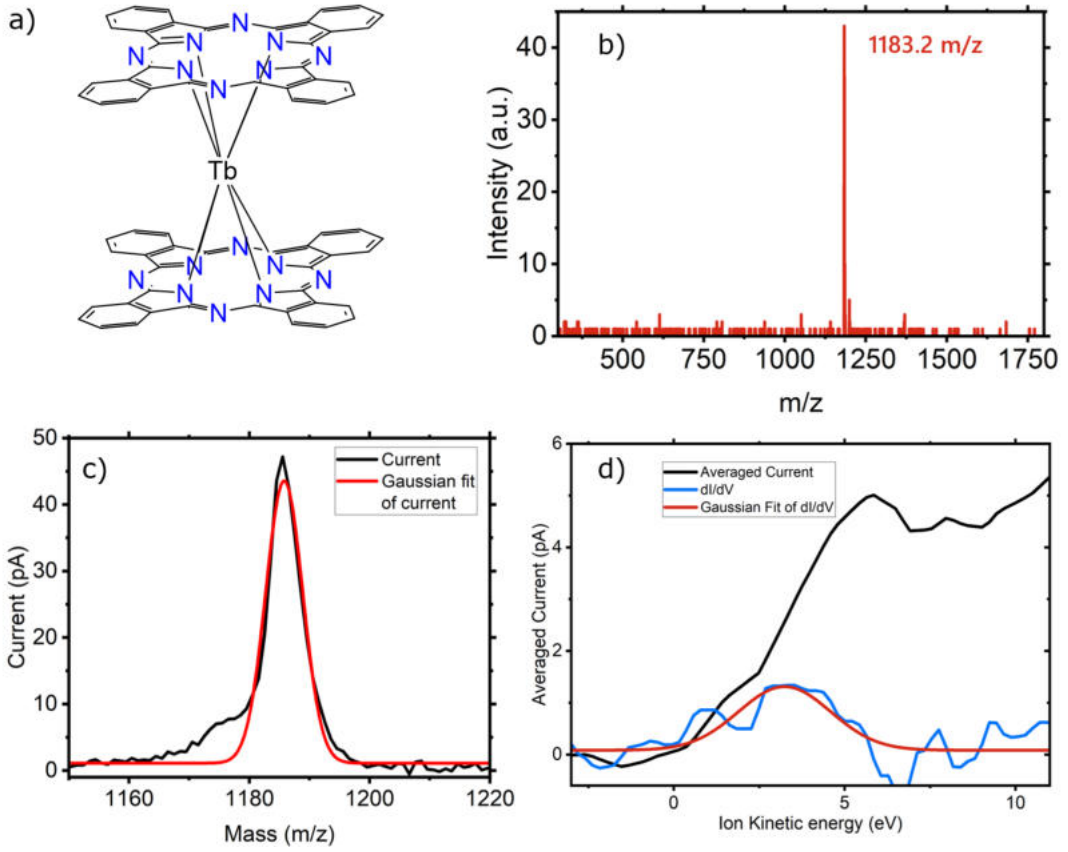

FIGURE 5.2: a) Molecular model of $[TbPc_2]^0$, b) ESI-TOF measurement of $[TbPc_2]^+$ with $[TbPc_2]^0$ peak indicated. c) ESI-CIBD mass spectrum of $[TbPc_2]^-$, with fitted 'Gaussian. d) Kinetic energy scan of $[TbPc_2]^-$, with Gaussian fit of dI/dV.

5.4 Electrospraying $[TbPc_2]^-$

For the depositions, mass spectra, and kinetic energy test presented here, the following solvent combination was used:

2.5 mM Hydrazine and 200 µM $[TbPc_2]^0$ solved in 200 µl of tetrahydrofuran, acetonitrile, and trichloromethane in a ratio 2:1:1 with 0.5 µl of water. The water was used only to handle the Hydrazine. In principle, a ratio of 1:4 Hydrazine to $[TbPc_2]^0$ is sufficient, but in order to improve the reaction rate, a concentration well over the stoichiometric level of Hydrazine was used.

Figure 5.2 b) shows that the mass of the $[TbPc_2]^-$ was measured as 1183.2 m/z. From Figure 5.2 c), the fitted Gaussian peak was measured as 1185.8 m/z after applying calibration, with a peak-width of 7.2 m/z. This discrepancy represents only a 0.2% error and is likely due to an imperfect calibration.

The origin of the small shoulder seen at roughly 1177 m/z in Figure 5.2 c) is unknown. The roughly 9 m/z discrepancy of the shoulder from the expected peak would correlate close to a loss of 8 hydrogens or a missing nitrogen. Few high resolution measurements were taken, and this additional shoulder was only observed once. Thus, it was assumed that only the correct molecule was deposited, which was also verified on the surface.

In Figure 5.2 d), the average ion kinetic energy was measured as 3.2±0.15 eV, distributed over 3.2±0.4 eV, where the errors are calculated from the fitting procedure.

The measurement of the kinetic energy of the ions in the ion beam allows comparison for further depositions. Many parameters can affect this energy profile. For the sake of simplicity, the landing energy of subsequent depositions will be defined by the average ion kinetic energy measured here, despite the fact that different depositions may have slightly different energies due to a differing spray environment during various depositions.

5.5 ESI-CIBD deposited $[TbPc_2]^-$ on Au(111)

Comparing the physical structure and surface character of the ESI-CIBD deposited $[TbPc_2]^-$ to $[TbPc_2]^0$ deposited via sublimation, allows for an initial confirmation of the viability of ESD. In STM imaging, one may analyse the physical structure of the molecule, their appearance in STM, and their self-organisation in order to verify that the molecules exhibit the expected characteristics. Furthermore, an overview of the surface structures allows one to verify that there is no anomalous behaviour caused by the use of ESD.

For the following deposition, the $[TbPc_2]^-$ was deposited onto an Au(111) crystal, with the average landing energy set to 6.8 eV ±3.2 eV.

From the images in Figure 5.3 a) and b), two molecular species are observed. A closer zoom of the two species observed is shown in Figure 5.3 b). The many molecules of low contrast are ascribed to a single Pc that has dissociated from the intact molecule upon impact with the surface. The island to the right side of the image in 5.3 b) is composed of intact $[TbPc_2]^0$ molecules, and the bright spot to the left of the image is an isolated $[TbPc_2]^0$ molecule. By comparing to imaged c), d) and e) the same island structure is observed, as well as the dissociation of $[TbPc_2]^0$ into component Pcs. The dissociation of $[TbPc_2]^0$ into single Pc components is widely observed and reported [191–193].

Given that the mass filter was applied to a beam with a well defined mass spectrum, one can be certain that the molecule was intact upon exiting the mass spectrum analyser. Given that the mass analyser is in a UHV environment of 10^{-9} mbar, the mean free path of these molecules is far higher than the $\sim$0.5 m distance between the mass analyser and the sample, one can be certain that there is no intermolecular collision, and thus the dissociation must occur upon surface impact.

It is unclear from imaging alone if there is still a Terbium atom at the centre of the molecule. In principle, it is likely that the ratio of TbPc to empty Pc is 1:1. From literature, dependent on the coordination metal, there is a difference in imaging between a free base Pc and MetalloPc in imaging from literature [211, 212]. In the case of Terbium [191, 192, 213, 214] this difference in imaging is minute and spectroscopy is a better confirmation. No spectroscopy of these single molecules was conducted to clarify the ratio of metalated Pcs to free base Pcs. Given that an empty Pc must be stabilised, the 'empty' Pcs are likely to be H_2Pc, where the hydrogen presumably comes from residual contamination in the chamber and during transfer. As a result of this uncertainty, all dissociated phthalocyanine species will be referred to hereafter simply as a Pc molecule.

From Figure 5.3 a), there is a high level of dissociation; however, many islands of intact $[TbPc_2]^0$ are also observed. The rate of breakage when depositing via sublimation is not reported, from the image in e), the dissociation is of a similar order of magnitude. In the image from Figure 5.3 b), the expected checkerboard pattern discussed in chapter 4 was observed.

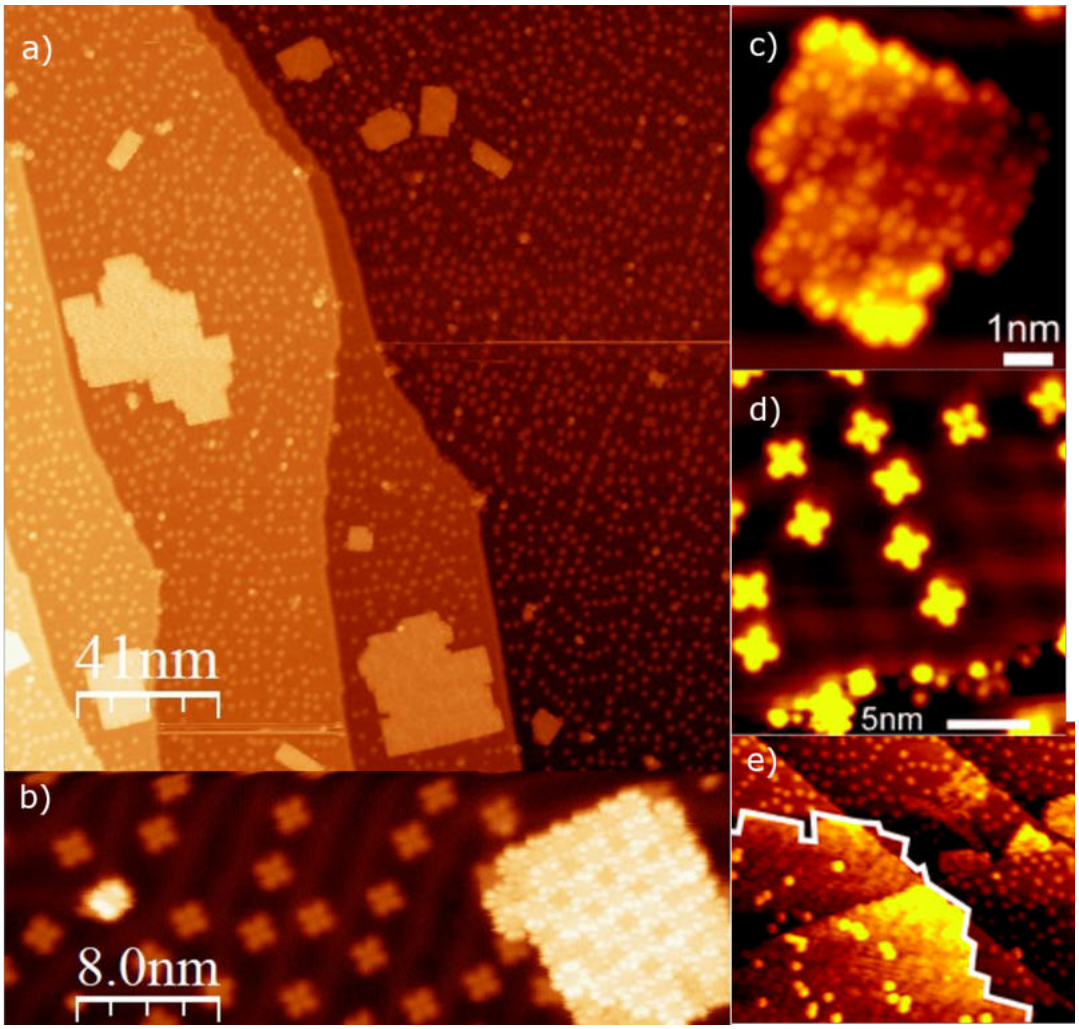

FIGURE 5.3: Overview of deposition of $[TbPc_2]^-$ onto Au(111) a) STM image of large terraces showing multiple species and many islands of $[TbPc_2]^0$. Imaged at U_B=-1V I_t=75.7pA. b) Zoomed image highlighting an island of $[TbPc_2]^0$ and monomers of the two species observed. Imaged at U_B=-0.5 V I_t=19.9 pA. c), d) and e) are adapted from Katoh et al. [191] and depict a deposition by sublimation of $[TbPc_2]^0$ onto Au(111), the images respectively depict, an island of $[TbPc_2]^0$, a terrace containing isolated TbPc molecules, and a large scale image overview of the deposition with a white line drawn to delineate the edge of the layer of $[TbPc_2]^0$.

The dissociated single Pcs are strongly localised between the bridge sites of the herringbone reconstruction. The intact $[TbPc_2]^0$, however, predominantly organises into islands.

To confirm the nature of the two species described above, apparent height profiles were measured on the molecules, as shown in Figure 5.4. Between 5.4 d) and e), the apparent height of the Pc is less than half that of the intact $[TbPc_2]^0$. The 1.4 Å measured in e) and the 4 Å in f), when compared to Katoh et al., [191] confirm that this is the same molecule. The apparent height of the isolated molecule was measured as 3.4 Å and was found to be regularly smaller than molecules ordered into islands, unlike what was observed by Katoh et al.[191]. The reason for this slight discrepancy to literature is unclear. Given that geometric height cannot be measured by STM and the fact that the scanning bias is not given in the literature, a

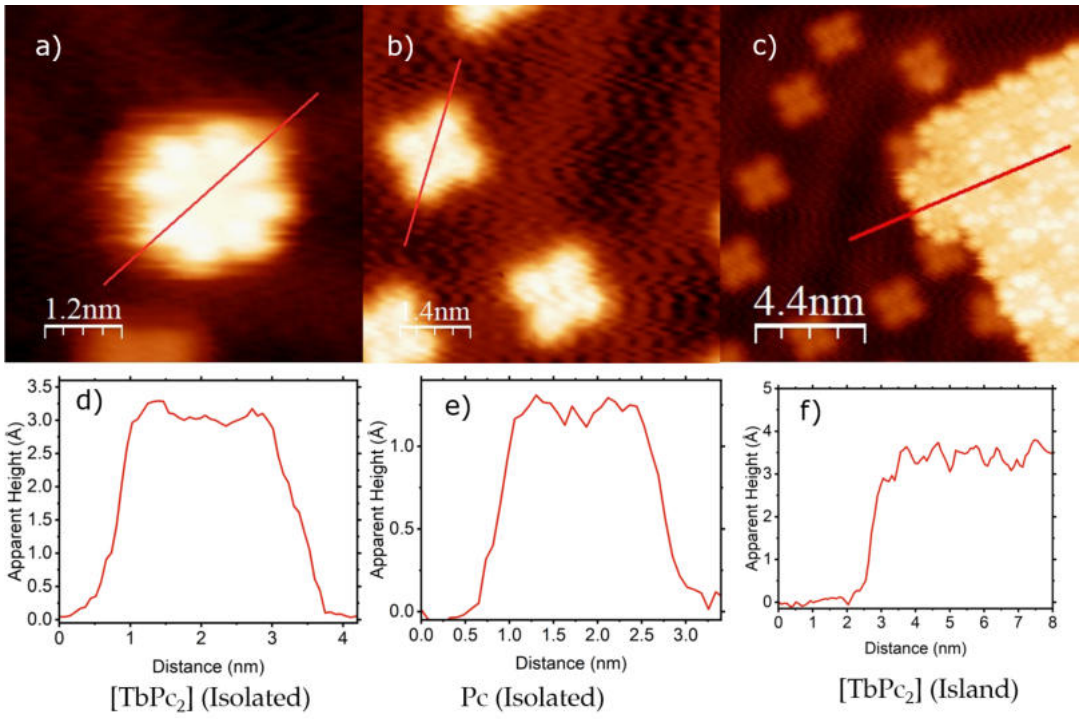

FIGURE 5.4: Comparative apparent height profiles of different species and islands for $[TbPc_2]^0$ deposited onto Au(111) a-c) Zoomed sections of the image shown in Figure 5.3, corresponding to the $[TbPc_2]^0$ monomer, the Pc monomer, and the $[TbPc_2]^0$ island respectively, with red arrows to indicate direction of profiles. d)-f) apparent height profiles corresponding to a)-c) respectively.

direct comparison is challenging and is unlikely to be relevant.

In summary, $[TbPc_2]^0$ deposited by has no visual physical difference from $[TbPc_2]^0$ deposited via subliamtion. A direct comparison to statistical significance of the dissociation of $[TbPc_2]^0$ into component Pcs was not made, but is clearly of the same order of mangitude. From imaging alone, there is no clear relevant consideration that must be made when using ESD as a technique, when compared to sublimation.

5.5.1 Kondo effect on the isolated molecule

As discussed prior, the electronic structure of the molecule has been modified during the spray procedure. In order to verify fully that the oxidation of the $[TbPc_2]^-$ into the neutral $[TbPc_2]^0$, the Kondo effect must be measured on the ligand of the $[TbPc_2]^0$, to verify the presence of the unpaired valence electron on the ligand, and thus, that the quenched radical property has been restored on the surface. This must be verified, both for the isolated $[TbPc_2]^0$, as well as when organised into islands.

From 5.5 b), the expected zero-bias peak only observed on the lobe positions of the molecule is shown. Some variation in intensity was observed; however, the peak width was consistent, measured as 8.4±0.6 mV where the standard deviation in measurements is given as error. From equation 1.0 discussed in chapter 4, the Kondo temperature is calculated as 33 K, which correlates well to literature [12, 14, 15]. Clearly an upwards peak is measured, meaning a q-factor of > 1, meaning that almost all tunneling is via the Kondo resonance state. This is as expected for the

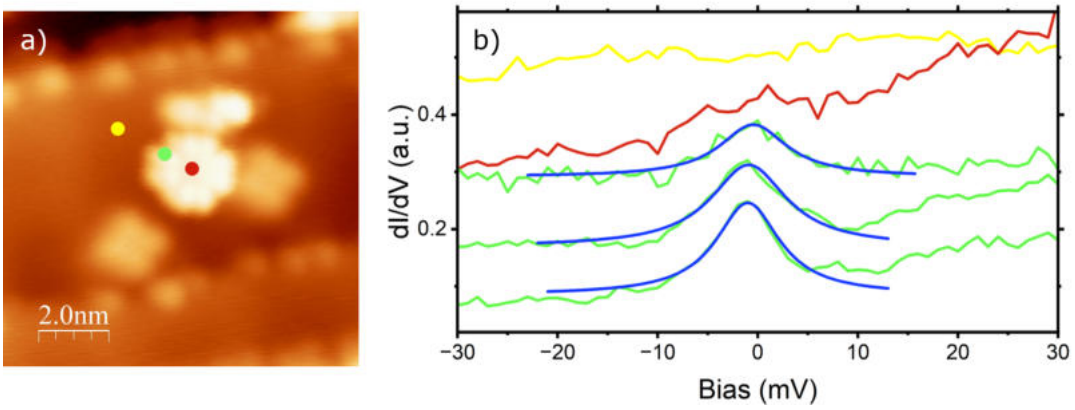

FIGURE 5.5: Scanning tunneling spectroscopy of a $[TbPc_2]^0$ monomer close to Fermi level showing zero bias peaks a) STM image of an isolated $[TbPc_2]^0$, with coloured dots to show spectroscopy positions. U_B=-0.5 V I_t=100 pA b) dI/dV spectra of indicated positions. Blue curves depict fitted Fano functions. Spectroscopies taken using a lock-in amplifier with a modulation voltage of 1 mV.

$[TbPc_2]^0$. For the Fano fitting, due to the noisy data, no correction was made for modulation voltage and so the real width measurement is only approximate.

5.5.2 Kondo effect on molecular islands

Furthermore, when measuring Kondo peaks on islands, a similar peak width is observed, as seen in Figure 5.6. An average peak width of 9.0±2 mV where error is the standard deviation. The gold background spectrum is not perfectly flat, due to a poorly defined tip state. As result, there is also a slight increase in the dI/dV on the island as bias increases. This made accurate peak fitting challenging and contributed to the high variation in the measured peak width. A peak width of 9 mV corresponds to a Kondo temperature of 38.5 K, which once again correlates well to literature [12, 15]. Once again the q-factor of the Fano function was > 1 therefore tunneling dominates through the Kondo resonance. These measurements were not corrected for effect of modulation voltage. Due to an issue regarding the specific tip location during spectroscopy, it was not possible to distinguish spectra taken on the overlapping lobes against non-overlapping lobes. As a result, it was assumed that any Kondo peaks observed must have been recorded over non-overlapping lobes to correlate to the result already observed by Amokrane et al. [14].

The presence of a Kondo effect on the ligand of the $[TbPc_2]^0$, both when it is isolated, and when organised into islands, confirms the presence of the unpaired electron delocalised over the ligand. This confirms that despite charging of the molecule in solution, the neutral oxidation state of the molecule is restored upon surface, and thus for the deposition of $[TbPc_2]^-$ derived thermolabile molecules, the ESI-CIBD system is viable.

5.6 Conclusion

To verify the viability of the ESI-CIBD system as a technique to study the further $[TbPc_2]^0$ derivatives in this thesis, the resultant stucutres from $[TbPc_2]^-$ deposition using the ESI-CIBD system were compared to subliamtion.

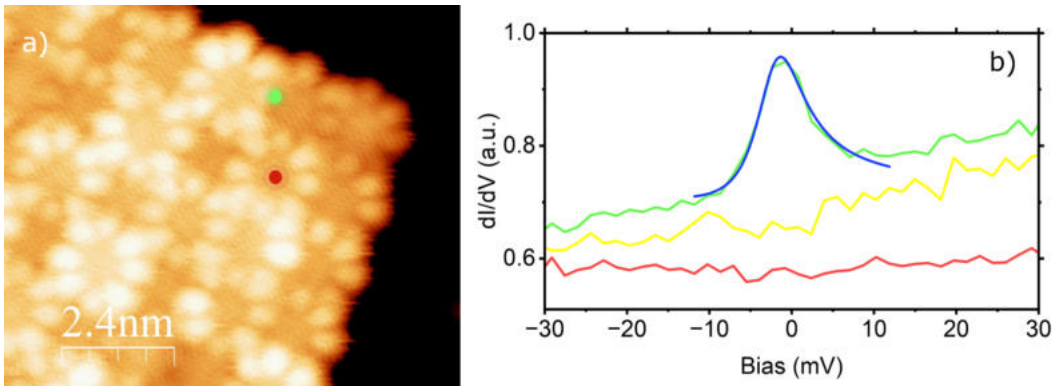

FIGURE 5.6: Scanning tunneling spectroscopy of a $[TbPc_2]^0$ island close to Fermi-level showing zero bias peaks a) STM image of a $[TbPc_2]^0$ layer, with coloured points to depict spectroscopy locations. U_B=-0.5 V I_t=20.0 pA b) Spectra taken on indicated locations, where yellow depicts spectra taken on bare Au(111). The blue curve depicts the fitted Fano function. Spectra taken using a lock-in amplifier with a modulation voltage of 2 mV.

A deposition of $[TbPc_2]^-$ onto Au(111) showed an identical surface structure of intact $[TbPc_2]^0$, showing the expected 8 lobe isolated molecule, as well as large island of self-assembled molecules. Some fragmentation into component Pcs was observed, however this is also observed for $[TbPc_2]^0$ deposited via sublimation.

During electrospray ionisation, the molecule is necessarily charged, and in the process the radical is quenched. As the ligand Kondo effect observed in literature when the molecule is deposited onto Au(111) is due to the unpaired electron delocalised over the phthalocyanine ligand. In this oxidation state, the observation of a Kondo effect over the ligand is not possible.

When measured on the Au(111) surface. a Kondo effect due to the unpaired valence electron delocalised over the Pc rings has been observed, confirming that this molecule is once again a radical. As is recorded in literature, the Kondo effect was found both on the isolated $[TbPc_2]^0$ and in islands of $[TbPc_2]^0$. Whilst the use of the ESI-CIBD system does cause some difficulty with observing fully intact molecules, it is clear that the use of the ESI system does not affect the electronic structure of the observed molecules once they arrive intact on the surface and does not have an experimentally relevant difference to samples prepared via the use of sublimation. This confirms the ESI-CIBD system as a viable technique for studying radicals, despite the radical being suppressed during spraying. This widens the scope of these experiments to similar molecules dressed with ligands that make the molecules too thermolabile to be viable for deposition via sublimation.

Chapter 6

Tunable Lattices of Alkylated Molecules on Surfaces

6.1 Introduction

From chapter 4, a variation in both spectroscopy and the appearance of the Kondo effect based upon the organisation of the $[TbPc_2]^0$ molecules has been observed and discussed. In order to further explore and understand these phenomena, this project intends to adjust the ordering on surfaces to control the spacing between molecules and thus adjust various intermolecular interactions. Given that the dependence of spectroscopic features and Kondo features is highly dependent on the organisation and intermolecular interactions[13, 14, 215], this project intends to study these effects in a controllable manner.

Unlike a Kondo effect from a single impurity or lattice of single impurities, a Kondo lattice is where collective interactions between many magnetic moments cause a coherent collective screening effect [216–222].

As these spins are screened, one may expect that there can be no long range order. As certain interactions, such as the RKKY interaction are mediated via the conduction electrons, this competes with the Kondo effect. At T=0 K, where no thermal fluctuations are observed, one may tune a certain non-thermal control parameter, such as magnetic field or pressure[219, 220, 223–225], such that quantum fluctuations due to Heisenberg's uncertainty principle become sufficiently strong for the material to undergo a quantum phase transition, from a phase where the Kondo cloud screens the spins, to a phase where spins interact with each other via these interactions.

The vast majority of Kondo lattice studies have been performed on 3D bulk materials [226, 227] but by studying 2D materials such as one observes on a surface, one may expect larger fluctuation due to greater confinement. As such reports of a Kondo lattice in 2D are limited [216, 222].

By tuning the magnetic interactions between molecules, one may tune the properties of the Kondo lattice, and transition between phases where either, there is coherent Kondo screening, or where long range ordering is observed, [228] once the exchange coupling J overcomes the Kondo exchange J_k. As the strenght of the exchange coupling varies by distance between spin centres r, any tuning of the lattice parameter will effectively tune the exchange interaction, in principle allowing one to tune the properties of the sample, and transition controllably between the two phases.

Furthermore, as this transition between phases is a second order quantum phase transition, this transition is continuous. This means that the region between each phase is distinct from either phase, where highly collective low energy excitations define this quantum state of matter [223]. At T=0 K, this point between either phase is know as the quantum critical point (QCP) [221, 229, 230]. The study of quantum

critical materials has lead to studies of heavy Fermion materials, non-Fermi liquid phenomena and unconventional superconductivity.

The QCP is only observed at 0K, but at non zero temperatures a 'quantum critical' regime may be studied. This means that if one tunes the control parameter sufficiently precisely, one may transition between the two phases already mentioned, as well as the quantum critical regime, allowing for study of novel physics. By creating a tunable lattice one may potentially study the phases described, as well as study the transition between these phases.

This tuning of the exchange interactions has a further benefit towards the development of QIP. Exchange interactions that couple magnetic moments used as qubits increases decoherence as the spins used as states will begin to align. Therefore by tuning this exchange interaction, via lattice parameter tuning, one may improve the coherence time of qubits arranged in a lattice. This has been observed in literature by Yu et al. [231], where an adjustment of the lattice parameters adjusted the interqubit distance from 14 Å to 18 Å improved the coherence time by roughly one order of magnitude at 10 K. This distance tuning is of a similar order of magnitude to what is expected in these experiments, thus would likely produce a comparable result.

In order to control all intermolecular interactions, the project intends to create a tunable lattice on surfaces. The study of tunable lattices of molecules on surfaces may further apply to research outside of the scope of this project. Thus, the motivation behind this project is not limited to this specific type of molecule. The method to tune the spacing between molecules is to add bulkier side groups to the ligand in order to adjust the physical size of the molecule and thus, adjust the spacing between molecule centres. By using alkyl chains attached to the benzene rings of the $[TbPc_2]^0$ molecule, a symmetric size tuned molecule is created, where the Terbium ion position remains at the centre of the molecule. Similar studies of alkylated phthalocyanine molecules on surfaces are found in literature [26, 232, 233]. Examples of carbon chain-based molecules studied on surfaces are reported [30, 234, 235]. All of the research in the cited papers is performed at the solid-liquid interface, meaning that the molecules are deposited with greater stability in solution but, more importantly, are deposited only onto a HOPG surface. Cirera et al. [28] report an example of ethyl chain based porphyrins deposited onto a metal surface, but this is limited to only ethyl chains.

As the structure of the molecules is similar for all molecules in this project, longer alkyl chain molecules have greater volume, therefore, a higher sublimation temperature, thus, a higher likelihood of random fragmentation and decomposition during sublimation. As molecules of greater volume contain significantly more bonds, there is an elevated risk of decomposition due to the elevated temperatures. Sublimation is a common method for molecular deposition in UHV. In this project, the intention is to deposit larger alkyl chain molecules in a stable manner onto metal surfaces using the ESI-CIBD system without risking decomposition due to the higher temperatures. As these molecules all share a similar structure, only with greater lengths of alkyl chains, an elevated mass measured in mass spectra correlates to a greater volume, thus, greater difficulty in sublimating the molecule stably.

As discussed in chapter 5, some alternative deposition methods are available, such as drop-casting and Matrix-assisted deposition [200–202], but the viability of these methods is unlikely. Furthermore, the ESI-CIBD significantly improves the controllability of the deposition, leading to more reproducible samples.

6.2 Electrospraying $[Tb(Et\text{-}Pc)_2]^0$

6.2.1 Molecular overview and mass spectra

In order to study a broader range of spacings, the first molecule studied was the ethyl substituted species. A molecular model of ethylated bis(phthalocyaninato) Terbium ($[Tb(Et\text{-}Pc)_2]^0$), as displayed in Figure 6.1 a) depicts where two ethyl chains are attached to each benzene ring of the previously studied $[TbPc_2]^0$. From Figure 6.1 b), a mass per unit charge of 1632.7 m/z was measured.

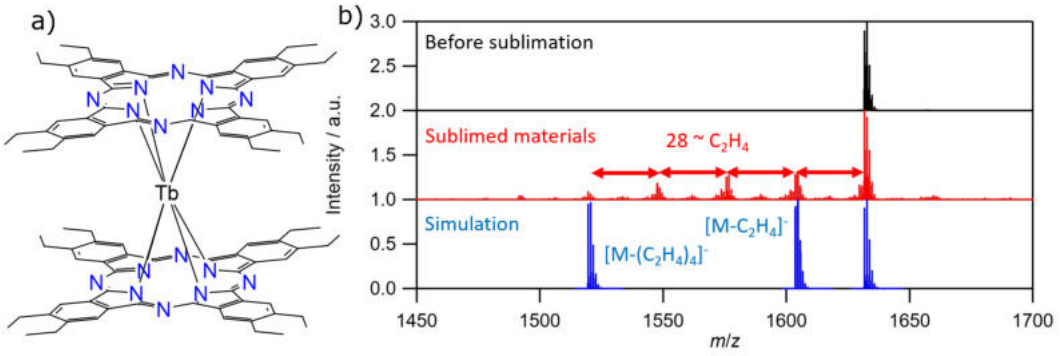

FIGURE 6.1: TOF-ESI Mass spectrum and sublimation test of $[Tb(Et\text{-}Pc)_2]^0$ a) Molecular model of $[Tb(Et\text{-}Pc)_2]^0$ b) Mass spectra of $[Tb(Et\text{-}Pc)_2]^+$ taken before (black) and after(red) the sublimation test as well as a simulation (blue) of sublimed materials. Red arrows display an m/z interval of 28m/z, which corresponds to a single ethyl chain.

In order to confirm that the $[Tb(Et\text{-}Pc)_2]^0$ is not possible to study via sublimation, the mass spectrum of the molecule was measured before and after sublimation. The molecule was sublimated at 10^{-5}mbar, and the sublimated material was collected; a mass spectrum was then taken. From Figure 6.1 b), the result of the mass spectrum of the sublimed materials shows peaks that correlate to the expected mass of the molecule minus integer numbers of alkyl chains of 28m/z missing. Evidently, the molecule decomposes into molecules with a varied number of missing chains. This would likely lead to disorder on the surface, as well as causing contamination to the chamber. A study of ethylated double decker molecules deposited by sublimation onto metal surfaces is reported [28]. However, some disorder is seen on the surface. Whilst it is possible to deposit this molecule via sublimation, it is clear that this is close to the limit of viability, and longer alkyl chains will require alternative techniques to deposition via sublimation. As a result, the use of the ESI-CIBD system becomes necessary.

6.2.2 ESI-CIBD mass spectra

As discussed in chapter 5, in order to improve the ionisation efficiency and control the oxidation state of the molecule, charging was performed in solution using hydrazine hydrate. This greater ionisation efficiency produces a higher current contribution from ions of the desired charge state. It thus gives both a higher signal-to-noise ratio for the mass spectra, and increases the deposition rate. The solution for all reported depositions of the $[Tb(Et\text{-}Pc)_2]^-$ molecule was composed as follows :

2.3mM hydrazine and 150 µM $[Tb(Et\text{-}Pc)_2]^0$ solved in 220 µl of dichloromethane and acetonitrile in a ratio of 8:3, with 0.5 µl of water. Water was used only to handle

the hydrazine. In principle, a ratio of 1:4 hydrazine to $[Tb(Et\text{-}Pc)_2]^0$ is sufficient, but it was found that the reaction occurred more slowly than when compared to the $[TbPc_2]^0$ so a high concentration was used.

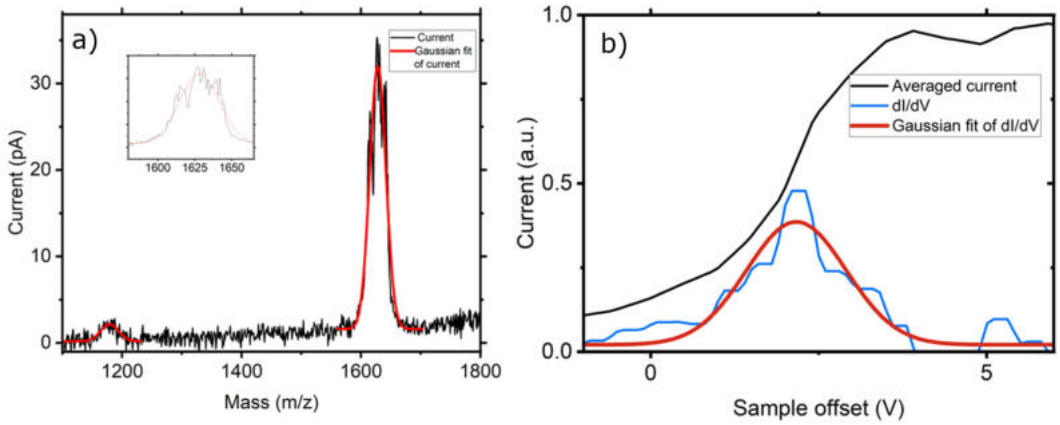

FIGURE 6.2: ESI-CIBD spectra of $[Tb(Et\text{-}Pc)_2]^-$ a) Mass spectrum taken using the ESI-CIBD system. Insert shows zoom on the molecular weight. Fitted Gaussian peaks are highlighted in red. b) Kinetic energy scan of $[Tb(Et\text{-}Pc)_2]^-$, using the same ESI-CIBD parameters as 6.2 a). The blue curve represents dI/dV, and red represents the Gaussian fit of dI/dV

The resulting mass spectrum from this solvent combination is displayed in Figure 6.2 a). By applying a Gaussian fit to the prominent peak, which is highlighted in the insert of Figure 6.2 a), a peak centre of 1628±0.3 m/z is found, and a peak width of 31.7 m/z. This peak width is attributed to the inherent resolution limit of the ESI-CIBD system. No peaks assigned to a single missing alkyl chain were observed. The molecular composition of the beam after filtering is considered highly uniform. A peak at 1179±1 m/z was observed, which correlates well to the 1183m/z expected for the $[TbPc_2]^0$. This peak is low in intensity compared to the peak for the $[Tb(Et\text{-}Pc)_2]^-$ therefore, fragmentation due to spraying is minimal. It is not clear if this peak is due to intact molecules that have lost all alkyl chains due to spraying, or if this is simply a slightly impure or decomposed sample prior to spraying, but due to the mass-filtering feature of the ESI-CIBD system, this peak is not expected to cause issues or result in disorder on the surface.

From Figure 6.2 b), the average molecule kinetic energy was measured as 2.17±0.03 eV. The width of this distribution was measured as 1.75±0.08 eV. This relatively wide distribution does not allow for fine control of the landing energy as ions of ±1.75 eV away from the target landing energy will be observed.

The profile shown in 6.2 b) is an average of multiple spectra taken using the same ESI parameters and solvent combination. Despite controlling many parameters, the parameter space is still vast, and so there is still substantial variation in the profiles, leading to significant errors and a large distribution width. This variation may be due to non-measured parameters, such as the temperature or humidity of the room during experimentation, variations in the chemical sample over time, or further parameters not directly controlled.

6.3 $[Tb(Et\text{-}Pc)_2]^-$ deposited onto Cu(111)

In order to study the variation in spectroscopy and self assembly, the $[Tb(Et\text{-}Pc)_2]^-$ was studied on differing surfaces. Following deposition, the intention is to image the

molecule, to characterise its physical structure, and dimensions, to verify that this is intact [Tb(Et-Pc)$_2$]^0. Furthermore imaging allows a study of the ability for these molecules to self-assemble. On Cu(111) one may expect that due to higher reactivity, the molecules are less likely to self assemble than in the case of Au(111). Whilst studying Cu(111) is less promising from this perspective, the fact that a Kondo effect was measured on the Terbium centre when deposited on Cu(111), means that the Terbium centre interacts sufficiently with the surface to observe a Kondo effect, and thus would be applicable for study towards quantum criticality.

6.3.1 Deposition and Observation

The [Tb(Et-Pc)$_2$]$^-$ was deposited onto a Cu(111) crystal held at room temperature. The average ion kinetic energy was set as 11.23±1.75 eV. The sample was initially degassed to 80°C to remove any contaminants due to the transfer.

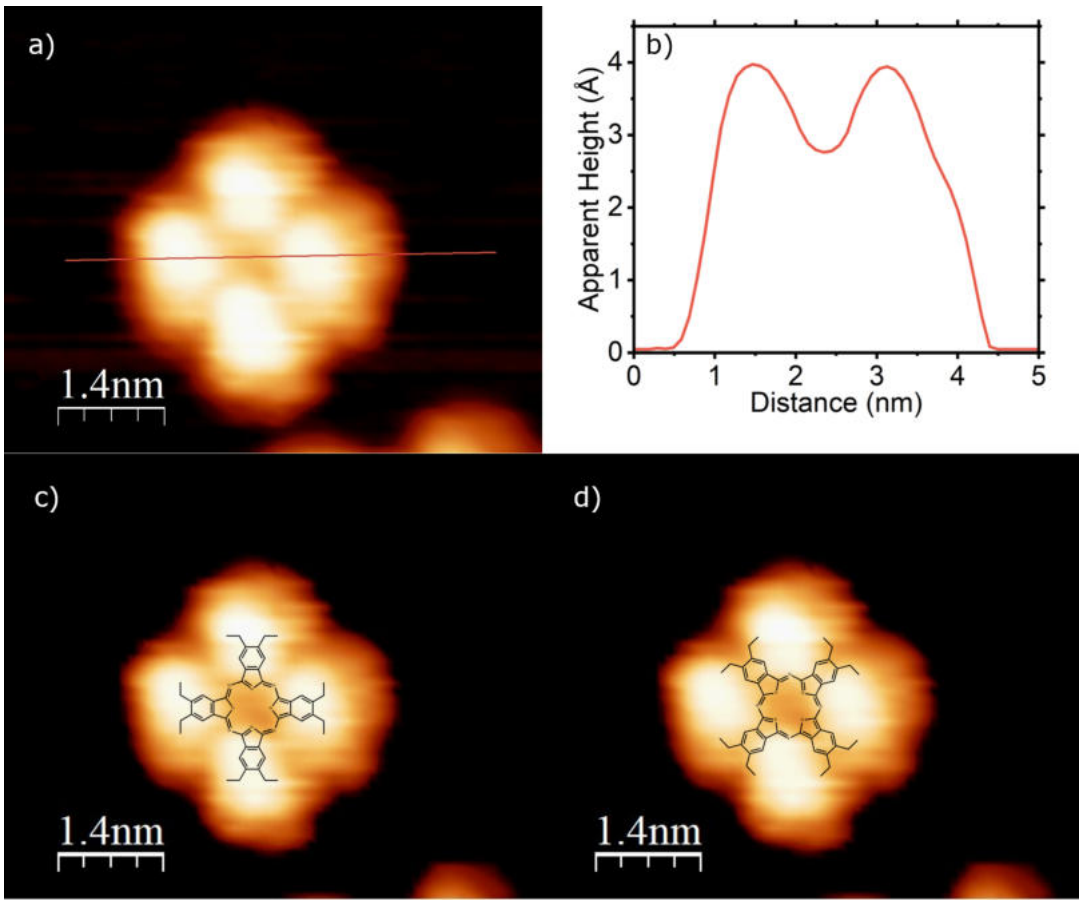

FIGURE 6.3: Overview of deposition of [Tb(Et-Pc)$_2$]$^-$ onto Cu(111) a) Topographic STM image of an isolated [Tb(Et-Pc)$_2$]^0 monomer. U_B=-1V I_t=100pA. b) Line profile of monomer in fig 2.2 a), c) and d) shows a simple molecular model of the upper Pc only overlaid onto imaged in a)

Figure 6.3 a) shows a regularly observed four lobe structure. The expected eight lobe structure of the [TbPc$_2$]^0 was not observed. The structure of these molecules, based only on this image, leaves a wide range for interpretation, due to the unclear nature of how the ethyl chains are ordered. In particular, a clear interpretation of the position of the ethyl chains attached to the upper phthalocyanine is not evident,

given that these chains are unconfined by the surface.

Figure 6.3 a)shows an example line profile of the molecule. Averaged over multiple measurements of molecules imaged using the same scan parameters, the dimensions were recorded as 3.84±0.25 Å x 38±0.27 Å height by width of the molecule. This is greater than the 2.5Å x20Å of $[TbPc_2]^0$ on Cu(111) from literature [194] and 3.5Å x22.5Å seen for the $[TbPc_2]^0$ deposited on Au(111) as seen in chapter 5 measured with the same STM at the same parameters. This correlates well to the expectation that the additional alkyl chains will increase the dimensions of the molecules seen on the surface.

Figures 6.3 c) and d) show the 2 possible orientations of the upper Pc of the molecule. From this imaging alone, it is not clear which orientation is correct.

6.3.2 Organisation and clusters

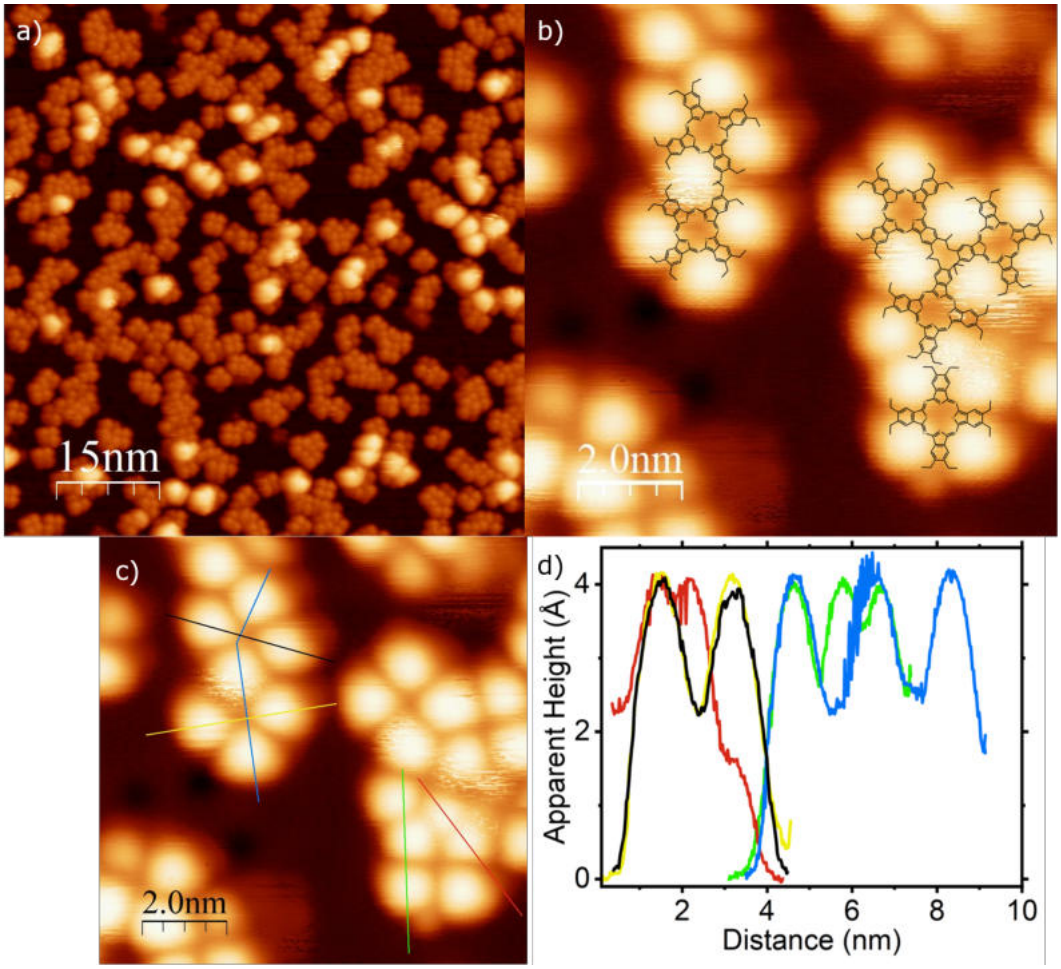

FIGURE 6.4: Overview of different polymers of $[Tb(Et\text{-}Pc)_2]^0$ on Cu(111) a) STM image of $[Tb(Et\text{-}Pc)_2]^0$ on a large Cu(111) terrace. U_B=-1 V I_t=100 pA. b) STM image of dimers, trimers and clusters of $[Tb(Et\text{-}Pc)_2]^0$ molecules. U_B=-1 V I_t=100 pA, with molecular model overlaid. c) Copy of image in b) with drawn line profiles d) Line profiles of coloured lines shown in fig 6.2.1 c), blue and green profiles are shifted right for clarity.

From Figure 6.4 a), no large-scale self-organisation was observed. Commonly, the molecule was found organised into dimers, and trimers of both chain and compact form, similar to what has been observed prior for the unsubstituted molecule [14]. Irregular higher order clusters were found. Some overlap between dimers and trimers was observed, such as on the right of the image in 6.4 b). It is unclear if the contrast in images attributed to irregular higher order clusters was simply overlap of some of these regular dimers and trimers. This orientation of upper Pcs is not necessarily correct, but does allow for an understanding of the scale of the clusters. There appears to be overlap of ethyl chains between molecules. Given that the chains in the upper layer are unconfined in 3-D space this sturcutre is still possible. It is likely that unconfined chains in the upper layer obscure the structure of the molecule.

The line profiles in Figures 6.4 c) and d), show that the apparent overlap of ethyl chains do not change the apparent height.

In order to encourage organisation, the sample was annealed to 210 °C. As a result of the high temperature treatment, the molecules have broken into single phthalocyanine components, and some reaction appears to have occurred between the single Pc units. This is somewhat similar to what has been observed prior [29, 236]. It may be possible to tune this annealing more precisely in order to achieve regular islands, such as observed for the $[TbPc_2]^0$, but this is left as a future project.

The dimensions of the $[Tb(Et\text{-}Pc)_2]^0$ were measured to characterise the molecule. The molecules imaged are larger than the $[TbPc_2]^0$ which corresponds well to the assumption that the dimensions will increase slightly by adding ethyl chains.

No successful organisation of molecules into larger layers was found, but there is still some scope to control both surface coverage and post annealing temperature to improve the self-assembly into large uniform layers.

6.3.3 Kondo effect and spectroscopy

Measuring STS on the $[Tb(Et\text{-}Pc)_2]^0$ charaterises the moelcule and one may compare to STS taken of $[TbPc_2]^0$ on Cu(111) in order to further confirm that the molecule is landing intact on surface. Despite not succeeding in creating a tunable lattice on surface, one may still measure the lower order clusters and compare to the isolated molecule, in order to verify if any interaction may affect the shape of the Kondo effect and understand how some limited tunability of intermolecular magnetic dipole interactions may tune what is observed.

The Kondo effect was not seen reproducibly on the first layer of molecules. One molecule of the $\sim$30 measured did display a clear Kondo effect-like zero bias feature, but this result was not reproduced. The relationship between the spin centre and the substrate is less well-defined as for the $[TbPc_2]^0$ due to the ethyl chains, which may partially explain the absence of the measured Kondo effect. As discussed in chapter 4, for the $[TbPc_2]^0$, the clear distinction in imaging between the Terbium centre and the phthalocyanine ligand allows for spectroscopic measurement of the Terbium centre separately from the ligand. For the $[Tb(Et\text{-}Pc)_2]^0$, this is not possible. A zero-bias peak is seen on the brighter spots due to molecules adsorbed into a 2nd layer, which is attributed to the Kondo effect. This assumed Kondo effect was not observed on every second layer molecule and not on every position, and so was likely dependent on the relative positions of one molecule above the other. No successful imaging was performed on this second layer, so this result was not successfully analysed and understood. Molecular manipulation was attempted on the 2nd layer of molecules in order to better understand the structure of the second layer; however, reproducible, interpretable manipulation was not successful. Lateral manipulation

of the molecules directly adsorbed on the surface was also attempted but unsuccessful. This result is expected, given that lateral manipulation of the $[TbPc_2]^0$ on Cu(111) has not been reported and was unsuccessful in prior experiments.

From literature, when the unsubstituted molecule is deposited onto Cu(111) and spectroscopy taken on the lobe, a LUMO peak is assigned at 1.8 V, the HOMO peak at -600 mV, a HOMO -1 peak at -1.2 V and HOMO-2 at -1.8 V [193]. There is a -100 meV shift of the HOMO when measuring on the centre, but otherwise, the lobe and centre correlate well. Similar assigned peaks are found for depositions onto other substrates [189, 190].

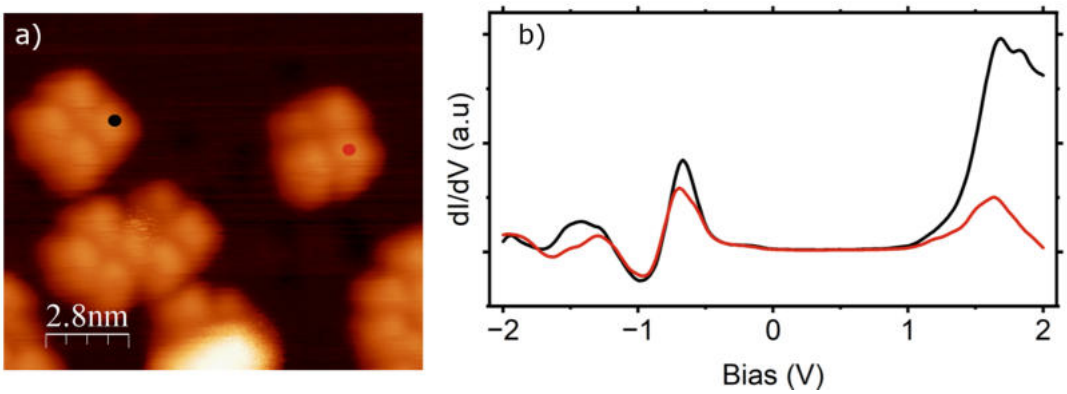

FIGURE 6.5: Spectroscopy of $[Tb(Et\text{-}Pc)_2]^0$ on Cu(111) a) STM image showing $[Tb(Et\text{-}Pc)_2]^0$ monomers and one dimer. U_B=-1 V I_t=100 pA. b) dI/dV spectra taken at the positions indicated in 6.5 a) by coloured dots, spectra taken using an external lock-in amplifier with an oscillation amplitude of 20 mV, taken at a setpoint of 100 pA current.

From 6.5a), peaks are observed at -1.9 V, -0.7 V, and 1.65 V on both molecules, and a small discrepancy is measured between the two spectra, with peaks at -1.3 V and -1.4 V for red and black positions, respectively. These correlate well with what has already been reported. Due to the unclear appearance of the molecule, the positioning of the tip over the lobe or the centre is not certain and may cause some additional discrepancies between the results. The good correlation to expected results of the mass spectrum of these molecules, their measured size on the surface, and their electronic structure is clear evidence that the correct species of molecule can be deposited successfully by the ion-beam deposition process. This result allows for greater certainty in future results of molecules deposited onto surfaces.

From the spectroscopy this molecule has been clearly characterised and strong evidence has been provided, demonstrating this is the intact $[Tb(Et\text{-}Pc)_2]^0$.

An attempt was made to study how Kondo effect may vary for differing cluster sizes, but it was not possible to take reproducible measurement of a Kondo effect on these molecules. This may be due to the chains in the upper layer interacting with the tip during measurements and could be compared to a similar heteroleptic molecule.

6.4 $[Tb(Et\text{-}Pc)_2]^-$ deposited onto Au(111)

The same deposition parameters were used for all data shown in this section. The $[Tb(Et\text{-}Pc)_2]^-$ was deposited onto the Au(111) crystal held at room temperature. The average landing energy was set to 11.23 eV ±1.75 eV, where the error is the width of

the distribution. The sample was initially degassed to 80°C to counteract minimal contamination during vacuum suitcase transfer.

6.4.1 Overview of the observed species

Given the generally higher mobility of molecules on the Au(111) surface when compared to Cu(111), it is the expectation that the molecules will more readily self assemble, thus more successfully meet the aims of the project. The surface structures imaged are mesasured and characterised in order to understand specifically how the molecules are arranged on surface, as well as to correctly assign all imaged species.

From Figure 6.6, two molecular species are observed. The molecular assembly shown in Figure 6.6 b) is ascribed to a single Ethyl phthalocyanine that has dissociated from the intact molecule. As discussed in chapter 5 and observed in literature [237, 238], this dissociation occurs on surface impact, and it is not clear if there is still a terbium atom attached to the Et-Pc. For simplicity, it will be referred to as Et-Pc. The fragmentation of $[TbPc_2]^0$ into single components is widely observed and reported [191–193], where both $[TbPc]^0$ and metal-free Pcs are observed. Given that the presence of terbium in an unsubstituted Pc is not clear from imaging alone, without a detailed study of spectroscopic measurements, the presence of the terbium cannot be confirmed.

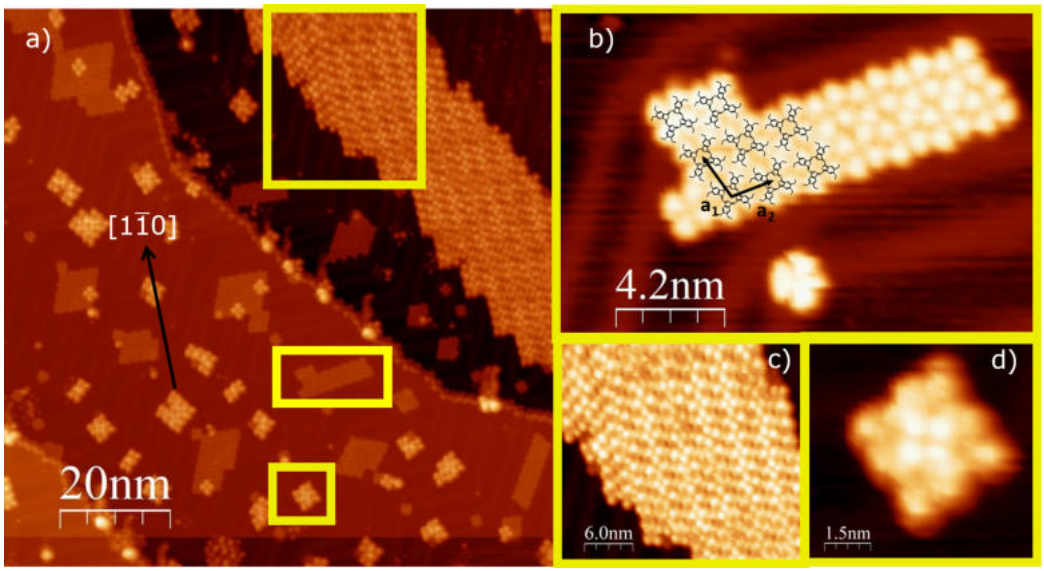

FIGURE 6.6: Overview of different species observed from $[Tb(Et\text{-}Pc)_2]^-$ deposition onto Au(111) a) Large scale topographic STM image showing $[Tb(Et\text{-}Pc)_2]^0$ deposition on Au(111), depicting organisation of 2 distinct species, examples of which are highlighted with a yellow box. U_B=-1 V I_t=40 pA The [1$\bar{1}$0] crystal direction is indicated by an arrow. b), c), d) zoomed sections of yellow highlights from Figure 6.6 a). Tentative model overlaid onto Figure 6.6 b), and unit cell vectors drawn.

A finer tuning of the landing energy towards 0 eV may result in some controllability of molecular dissociation during deposition. Importantly, the same parameters were used for both depositions on Au(111) and Cu(111), and changing substrate remains the only method of adjusting the dissociation on-surface with reproducible results. The higher level of dissociation when the molecule is deposited onto Au(111) is surprising given that Cu(111) is more reactive, and one would expect the stronger

interaction with the molecule to cause more dissociation. However, this is not the case.

A preliminary study of the dissociation effect caused by landing energy was attempted but found no correlation between landing energy and dissociation when varying the landing energy to as low as 1.23 eV, nor as high as 37.23 eV. These subsequent experiments were carried out 6 months after those shown here and found the dissociation ratio even higher despite applying a reduced landing energy in these subsequent experiments. Further preliminary experiments show some correlation between landing energy and dissociation. Given the significant difference in dissociation between experiments 6 months apart, despite using the same landing energy, some other parameter strongly controls the dissociation ratio on the surface that is yet to be fully understood.

For the model proposed in Figure 6.7, the models are scaled to the scale of the image. The unit cell vectors of the assigned single Pc layer were measured as 1.75 nm x1.8 nm and an angle of 107.5 ° between vectors. One of the vectors was always aligned perpendicular to the high symmetry direction of the Au(111) substrate.

From Figure 6.7, there is a clear distinction in apparent height between the two species. The molecules with lower apparent height are assigned as the Et-Pc layer, and the organisations with higher apparent height are assigned as the intact [Tb(Et-Pc)$_2$]^0. The dimensions of the Et-Pc layers are very close to those of the unsubstituted Pc. From literature [191] and the discussion in chapter 5, the height of the [TbPc]^0 is measured as 1.4 Å. From 6.7 a), the height of the single Et-Pc was measured as 1.5±0.1 Å. From 6.6 b), the lattice parameters of the layer show a smaller dimension than that of the isolated [TbPc]^0[191], but given that measuring lateral distances of isolated molecules is not a real measurement of the size,this is unsurprising. The strong tendency of these molecules to organise into islands compared to the unsubstituted Pc, as observed in chapter 5, implies that the chains are still intact and drive this strong self-organisation.

From the comparative line profiles in 6.7 d) and f), the heights of the assigned intact [Tb(Et-Pc)$_2$]^0 tetramer and layer are measured. The height at the centre of the molecule is 3.5 Å, and 6 Å at the positions assigned to the ethyl chain. The measured height of the benzene rings of the Et-Pc layer is 1.5 Å. The ethyl chains in the first layer are expected to lie flat due to the strong interaction of the chains with the surface[26, 30, 232, 234]. The alkyl chains in some molecular species do tend to point upwards when the monolayer is heavily constrained, and only when the organisation is sufficiently compact [235, 239–242]. This is not likely directly comparable but should be considered as a possibility. Therefore, the unconfined chains in the second layer will likely cause an increase in height combined with the additional height contribution from the Terbium centre. Therefore, from height comparison alone, the assignment of these two species as [Tb(Et-Pc)$_2$]^0 and Et-Pc is robust. AFM measurements on these structures would give a more accurate height measurement.

6.4.2 Proposed molecular structure and measured lattice parameters

Due to the many degrees of freedom in this system, a calculation of the organisation of these molecules is very complex and highly intensive. Only a few very simple models are presented in Figure 6.8 to attempt to explain the organisation of these molecules. A more robust treatment would need the support of DFT calculations. Due to the confinement of the ethyl chains in the lower layer in two dimensions and the strong π-substrate interaction, one may assume that the lower layer of Et-Pc has

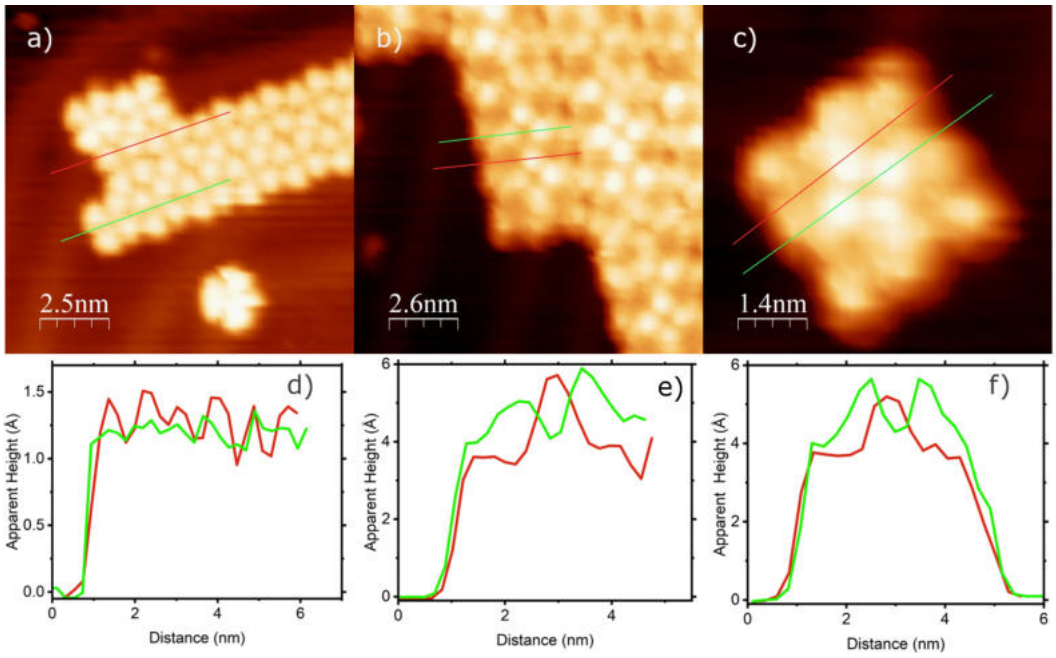

FIGURE 6.7: Profiles of different species from $[Tb(Et\text{-}Pc)_2]^0$ on Au(111) a), b), c) copy of images from Figure 6.6 b), c), d) respectively. Profiles d), e), f), taken from lines depicted in a), b), c) respectively. All profiles taken from left to right.

regular order. The orientation of the lower Pc of the $[TbPc_2]^0$ is not fully understood [12, 187], as such, these models have been proposed studying only the top Et-Pc layer. It is suggested that the overlapping chains push each other upwards. This interaction between chains is responsible for the bright spots in topography, forming the cross like shape seen in this image.

Additionally, the corners of the hexamer show a slight protrusion due to non overlapping ethyl chains, supporting the statement that the chains are the origin of the protrusions. The model for the $[Tb(Et\text{-}Pc)_2]^0$ island proposed in Figure 6.8 b) is assigned as correct. This fits well with the length scale of the molecule and explains the observed cross-structure well. Figure 6.8 c) depicts a possible alternative conformation where the top layer is rotated by 45°. This conformation does not explain the bright spots in the corners, but the tetramer observed in Figure 6.8 d) correlates more to this 45° rotated structure. Less than 1% of observed structures had the conformation shown in Figure 6.8 d).

Figure 6.8 e) shows the proposed molecular structure overlaid onto one of the large molecular layers. Every layer observed was composed of an irregular organisation of two molecule wide strips. These strips would only remain regular for 6-10 molecular units. This quasi-one-dimensional structure is intriguing but does not perfectly allow for a regular 2-dimensional lattice and so does not create a perfectly tunable lattice system. These two molecule wide strips were only found to align in one of the three high symmetry directions. As stated, the single Pc layers were not square, assembled with a lattice parameter of 1.75nm x1.8 nm and an angle of 107.5° and only aligned perpendicular to the $[1\bar{1}0]$ direction. Given that neither the lattice parameters nor the orientation of the single Et-Pc layer corresponds to the full $[Tb(Et\text{-}Pc)_2]^0$, it is not possible to directly compare the organisation of the full $[Tb(Et\text{-}Pc)_2]^0$ layers with that of the single Et-Pc layer. In particular, the Et-Pc layer does not provide a clear structure for the bottom Et-Pc constrained in the full $[Tb(Et\text{-}Pc)_2]^0$

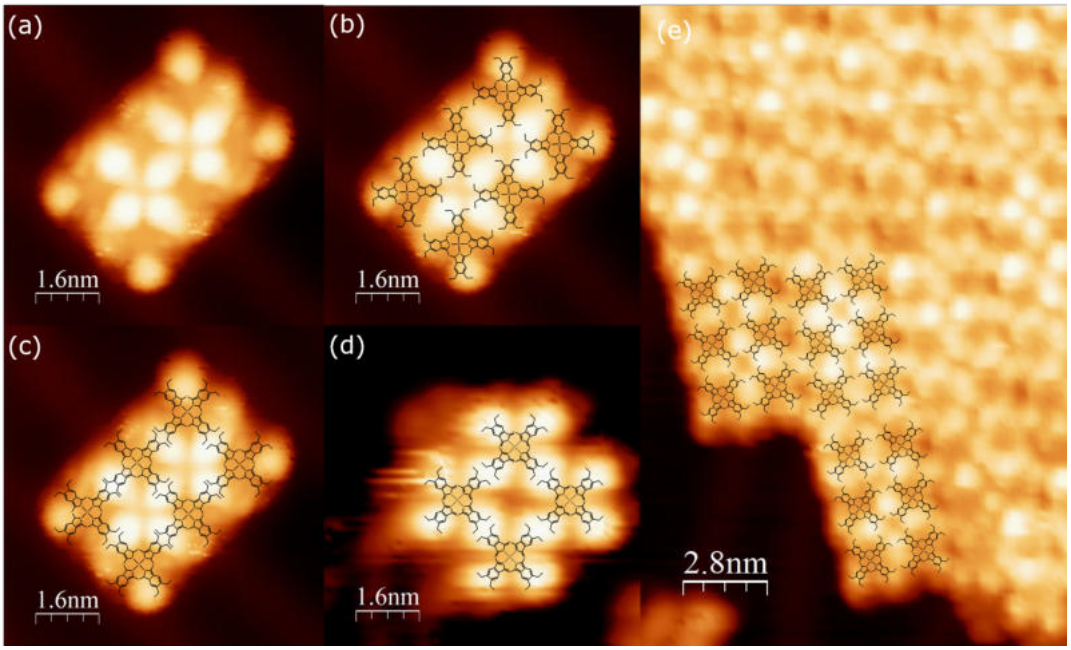

FIGURE 6.8: Comparison of tentative molecular models for $[Tb(Et\text{-}Pc)_2]^0$ on Au(111) a) Topographic STM image showing $[Tb(Et\text{-}Pc)_2]^0$ hexamer on Au(111). U_B=-1 V I_t=50 pA. b),c) Show a copy of a) with an overlaid model. Only the top layer of Pcs is modelled. d) Topographic STM image of alternate conformation tetramer, with a similar model to Figure 6.8 c) overlaid. U_B=-1 V I_t=50 pA. e) zoom of image from Figure 6.6 a), with similar model to Figure 6.8 b) overlaid.

layer. Based on the model proposed in 6.8 b), the top layer of Pcs maintains the same orientation. This was not observed for the $[TbPc_2]^0$ [12, 187], where adjacent Pcs in the top layer of islands have an angle of 15° relative to each other.

The parameters of the lattice shown in 6.8 b) and e) were 1.76 x 1.76±0.1 nm in a square lattice configuration. This measurement was an average over multiple hexamers, tetramers and full layers. The value was the same for all structures. Thus, long range interactions in large layers do not significantly affect the lattice spacing. The intermolecular spacing for the $[TbPc_2]^0$ has been reported as 1.43 x 1.43 nm or 1.5 x 1.5 nm [193] depending on whether it is in the compact or non-compact phase. Given that this is the intact $[Tb(Et\text{-}Pc)_2]^0$, which will be further established in later sections, the aim of the project was achieved. Despite some irregularity in the lattice, the lattice spacing was adjusted via the use of thermolabile alkyl substituents.

In Figure 6.9 a), an assumed single Et-Pc is organised with 3 $[Tb(Et\text{-}Pc)_2]^0$ molecules to create a mixed-species tetramer, allowing for some understanding of the conformation and orientation of the lower layer.

The 3.5 Å height of the planar section corresponds well to other tetramers and layers of $[Tb(Et\text{-}Pc)_2]^0$. The 1.5 Å height of the assigned Et-Pc corresponds well to that of the Et-Pc layer described in Figure 6.7 a). Some substructure can be seen on the $[Tb(Et\text{-}Pc)_2]^0$ molecules adjacent to the Et-Pc molecule. From the model in Figure 6.7 b) one can see that the $[Tb(Et\text{-}Pc)_2]^0$ at the bottom of the image has a clearer structure, assigned as a benzene ring with ethyl chains attached, which does not overlap with adjacent ethyl chains. Evidently, overlapping chains obscure the intramolecular contrast of the molecules. A partial cross structure is observed in Figure 6.9 a). By comparing to the cross structure in the centre of the normal tetramer

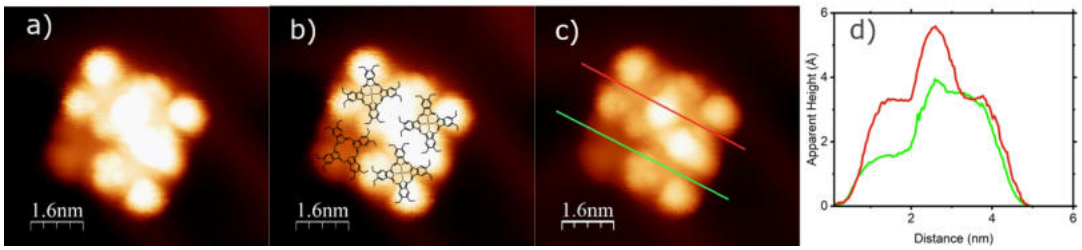

FIGURE 6.9: Analysis of a mixed layer tetramer a) Topographic STM image showing tetramer composed of 3 $[Tb(Et\text{-}Pc)_2]^0$ molecular units and 1 Et-Pc. U_B=-1 V I_t=60 pA Image contrast has been adjusted to highlight the orientation of the Et-Pc molecule b) copy of a) with molecular tentative model overlaid. c) copy of a) with line profiles. Contrast has been adjusted to highlight the top layer of the structure d) corresponding line profiles from c), indicated with colours. Profiles taken left to right.

seen in 6.7 c), one can deduce that the chains create the cross structure due to some contribution from the 4 Et-Pcs on the upper ring. This further confirms the model proposed in Figure 6.8 b). It is clear that the overlapping ethyl chains cause these bright spots and are responsible for the difficulty in imaging, obscuring the substructure of the molecule.

As discussed in chapter 4, there is no perfect agreement about the orientation of the upper Pc relative to the lower in the $[TbPc_2]^0$ molecule as well as with other double-decker complexes. The orientation of the lower Et-Pc is measured as 19°, with respect to the upper Pcs. This structure orientation does not necessarily correlate to that of the $[TbPc_2]^0$; however, it introduces an interesting application of the dissociation of molecules on-surface in order to study intermediate structures. For future studies, deeper analysis and some statistics on the observed mixed species tetramers may improve understanding of the full $[Tb(Et\text{-}Pc)_2]^0$ layers. Additionally, from the discussion in 4 and literature [13, 14], the relative rotation of the Pcs in each layer strongly affects spectroscopy and so must be further understood in order to better understand spectroscopy for layers of $[Tb(Et\text{-}Pc)_2]^0$.

Annealing to 573K was attempted to improve the regularity of the organisation, but the resultant sample was composed of only single Et-Pcs which appeared to have again reacted in a similar fashion to what was described in section 6.3.2. By attempting smaller annealing steps, it may be possible to create more regular structures without dissociating the $EtbPc_2$.

No isolated $[Tb(Et\text{-}Pc)_2]^0$ was found on surface to characterise the isoalted molecule, but assemblies of molecules allowed for a direct comparison of lattice parameters to the $[TbPc_2]^0$. Both lower order clusters and large islands were found. Significant dissociation of the molecule into component Pcs was observed. This may limit the ability of the molecule to organise into semi-infinite layers, especially towards the construction of molecular films.

6.4.3 Molecular manipulation

By manipulating molecules on surface, one may further understand both intermolecular interactions that maintain the structures observed here, as well as qualitatively observe the molecule-surface interaction. Further by breaking the tetramers observed in the prior section, one may understand more about the molecular units compromising the structures seen on surface, and thus, better characterise the surface organisations.

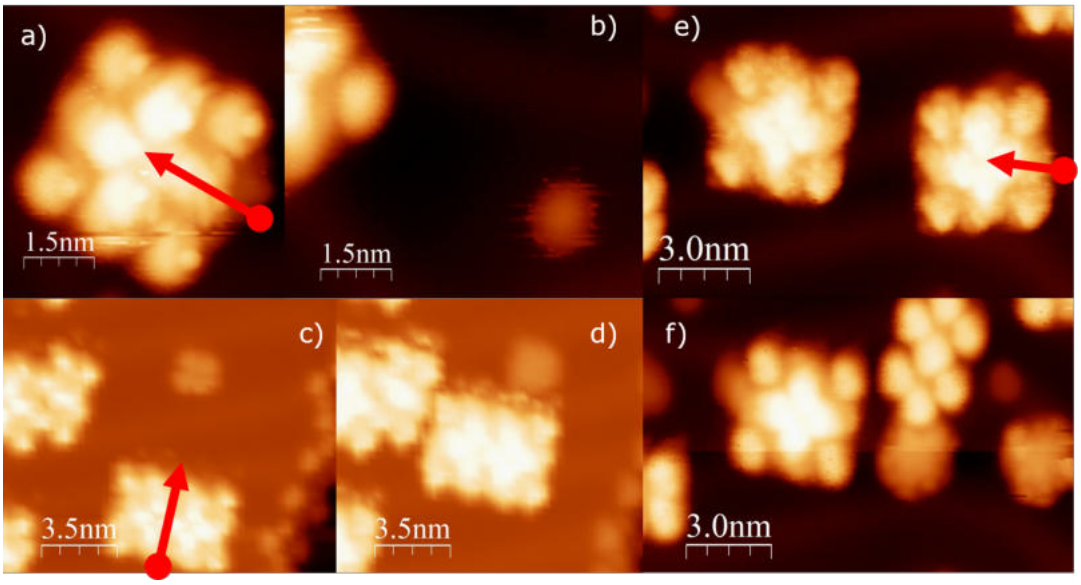

FIGURE 6.10: Molecular manipulation of $[Tb(Et\text{-}Pc)_2]^0$ on an Au(111) surface a)-f) A series of STM images taken before and after manipulation. Red arrows depicting tip trajectory are placed on images recorded before manipulation. U_B=-1 V I_t=50 pA. Manipulation was performed by switching off the feedback loop whilst over the molecule, moving to bare gold, then descending the tip by 3 Å to correlate with the rough height of the molecule, and then returning to the original position over the molecule.

By pushing the tetramer in Figure 6.10 a) with the STM tip, one can see that relative to the surface impurity observed in Figure 6.10 a) and b), the tetramer has moved as a complete unit. This behaviour can also be observed by the manipulation of a hexamer in Figure 6.10 c) and d). The fact that these polymers move as complete units implies that the intermolecular interactions are stronger than the interaction with the substrate. Given that the two layers stay intact during manipulation, one can deduce that the bonding between Pc layers is also strong compared to the substrate interaction. Therefore, it is likely that the Terbium ions are still forming coordination bonds and that this is the intact molecule. The intermolecular interactions are strong, but the exact nature of the interaction is not clear. Bond-resolved AFM could confirm whether there are bonds linking these molecules into tetramers,

By pushing the tetramer in Figure 6.10 e) towards another tetramer, the tetramer separates apart into four component units, depicted in Figure 6.10 f), assumed as the four molecules composing the tetramer. Two of the molecules from the broken tetramer are seen in the form of a dimer similar to what was observed when the molecule is deposited onto Cu(111). This further confirms that the tetramers are composed of intact $[Tb(Et\text{-}Pc)_2]^0$. By comparing to the proposed structure in Figure 6.8 b) and e), the lobes overlap, so this dimer appears to be in a configuration rotated by 45°. The orientation of the lower Pc is not clear. Given that this rotation conflicts with the model in Figure 6.8 b) and e), it is assumed that the dimer re-formed in a new configuration after manipulation. Whilst the structure proposed in the prior section may need further experiment or calculation to confirm, from the components of the broken tetramer, it is clear that the tetramer is a specific configuration of 4 molecular units. Furthermore, from this manipulation, it appears that the interaction holding the layers together is stronger than the intermolecular interactions, which again is stronger than the substrate interaction; this further supports that the

Terbium ion is still in position maintaining these two layers together, allowing one to strongly assert that this is the intact $[Tb(Et\text{-}Pc)_2]^0$.

By molecular manipulation, one can qualitatively assert that the intermolecular interactions are stronger than the molecule-surface interactions, even when discussing higher order clusters, such as the hexamer. By breaking the tetramer into component pieces, it was observed that the individual molecules appear similar to what was observed when the $[Tb(Et\text{-}Pc)_2]^-$ was deposited onto Cu(111). This supports that the specific structure observed in layers and clusters, is due to the intermolecular interactions, and how the molecules are arranged collectively.

6.4.4 Spectroscopy on $[Tb(Et\text{-}Pc)_2]^0$ on Au(111)

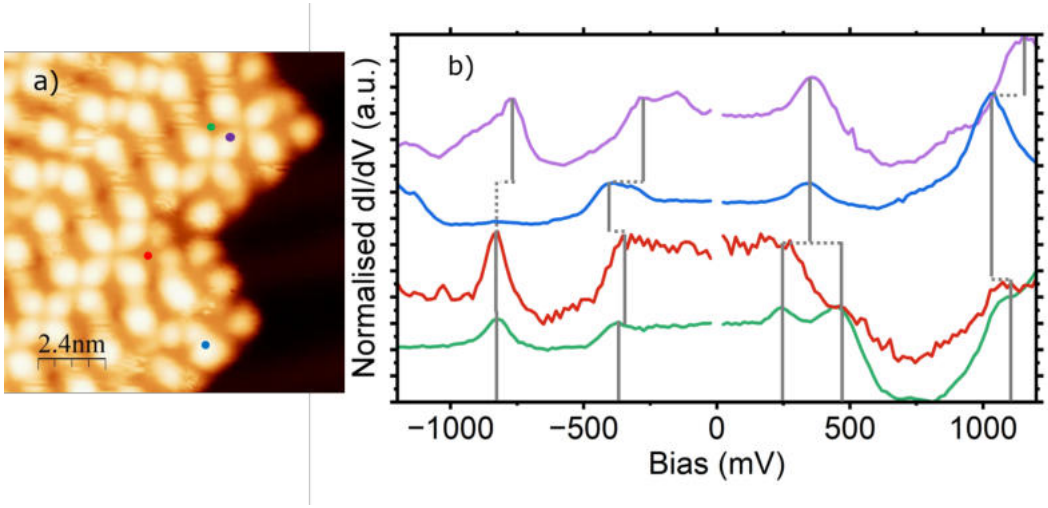

FIGURE 6.11: Spectroscopy of $[Tb(Et\text{-}Pc)_2]^0$ organised layer a) STM image showing $[Tb(Et\text{-}Pc)_2]^0$ layer on Au(111) with spectroscopy locations indicated with coloured dots. U_B=-1 V I_t=40 pA. b) Set of normalised dI/dV spectra taken at the positions indicated in a). Spectra acquired using a lock-in amplifier with 20 mV modulation. Normalisation is performed as described in chapter 3, with I/V arbitrarily broadened. Normalisation performed to equally emphasise peaks. Central points were deleted due to anomalies from normalisation. Grey lines show peaks where discontinuities are depicted with dotted lines.

Due to an experimental issue, it was not possible to precisely control the position where a spectrum was taken. As a result, these spectra were not very reproducible. In order to confirm these spectra, more reproducible measurements must be performed. Additionally, due to the very bright contrast from the overlapping alkyl chains, it is not trivial to distinguish between spectra taken on the lobe and the centre of the molecule. As will be discussed, from Amokrane et al. [14], there is not a big difference between molecule and lobe for the case of the organised layer, so this difficulty in localisation of spectra may not be relevant. The molecules are further spaced apart due to the alkyl chains, so one would expect not to observe any overlapping lobes. Therefore, the comparison to the non-overlapping case is more relevant.

Despite the lack of reproducibility when attempting to measure on the same position, some regular peaks are observed, implying that similar, but not identical, positions may show similar results. Background measurements of a clear Au(111) surface state were observed to be reproducible between measurements.

From Figure 6.11 b), some similarities to the spectra from Amokrane et al. are oberved, as seen in Figure 6.13 below. From the purple, red and green spectra, peaks are observed at ∼-850 mV, and a shoulder is observed at ∼1050 mV. These do not correlate perfectly to the assigned HOMO-LUMO of the $[TbPc_2]^0$ from literature [13, 14], which are shown in Figure 6.13. Additional peaks close to the Fermi level are observed in all spectra at -350 mV and at positive bias, between 250 mV and 500 mV, but it is unclear if this assignment of peaks is correct. Depending on which lobe is measured, the peak at negative bias close to Fermi can shift dramatically for the $[TbPc_2]^0$ [13, 14]. From Figure 6.11 b), the position of the negative peak closest to the Fermi level also shifts. The positive peak close to the Fermi level at 450mV is distinct from what has been reported prior, as all positive peaks close to the Fermi level were observed in literature in the range 50mV to 250mV.

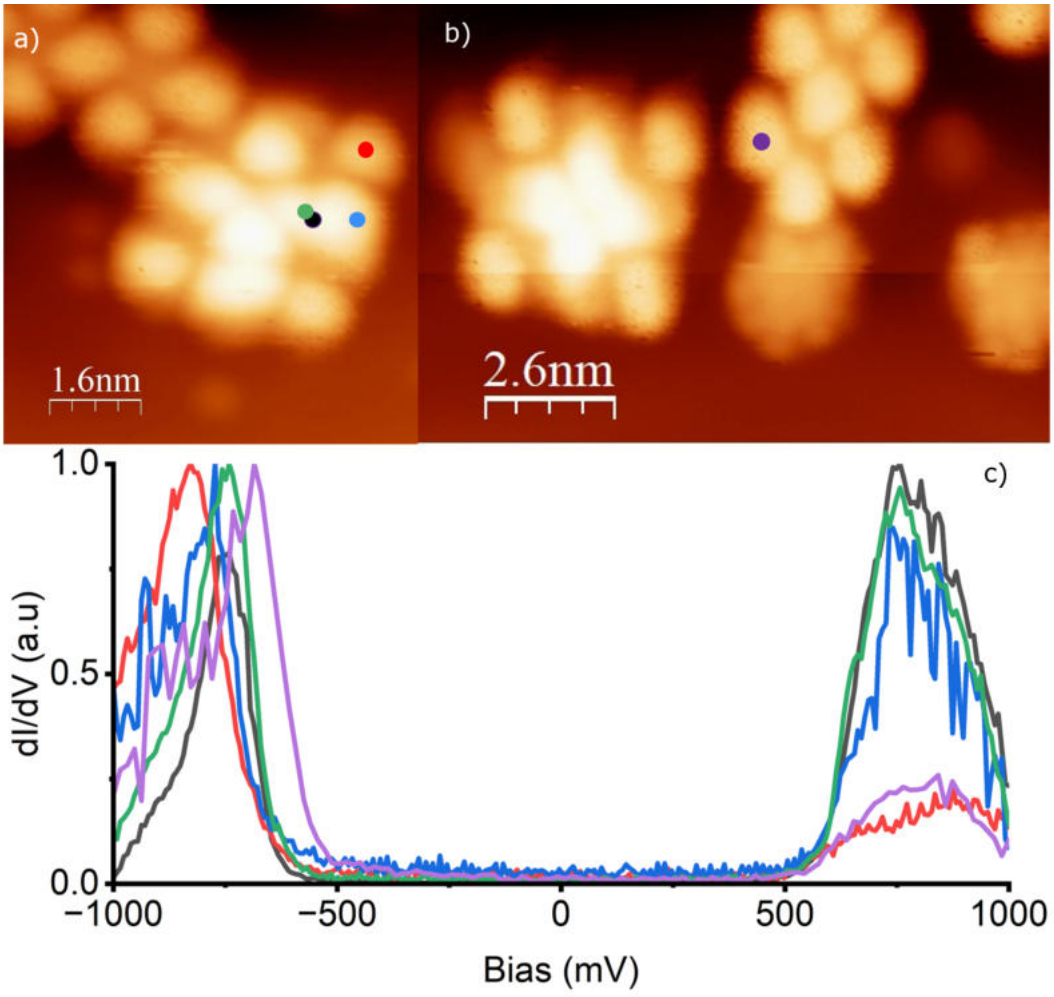

FIGURE 6.12: Spectroscopy of an $[Tb(Et\text{-}Pc)_2]^0$ tetramer on Au(111) a) STM image of a tetramer overlapping with a dimer. U_B=-1 V I_t=50 pA. Coloured dots indicate the location of measured scanning tunnelling spectra. b) STM image of a broken tetramer by molecular manipulation as described in Figure 6.10 f), with a coloured dot to display tip location c) Spectra taken over positions in Figure 6.12 a),b) where colours indicate positions. Spectra have been normalised for clarity. Spectra were taken using a lock-in amplifier with an oscillation of 10 mV

Figure 6.12 a) displays spectra taken on many different positions on a tetramer.

A well defined gold surface state was found prior to measurement, to use as a well defined background. There is little variation in the spectra besides a slight shift of the peak at negative bias. The green and black spectra were taken on the same position, and no variation in peak position was observed, implying that these spectra were more reproducible than those shown in Figure 6.11. The peak at negative bias in 6.12 c) varies from -700mV to -850mV. This shift is similar to the previously observed [13, 14] shifting peak at negative bias; however by its position, it correlates closer to the HOMO at -850 mV for the $[TbPc_2]^0$. The peak at 750 mV correlates well to some peaks from literature, as displayed in Figure 6.13 below, but given that no other comparable peaks are observed, the electronic structure is difficult to interpret from these limited data. As these were the most reproducible measurements, and given that many factors may cause the $[TbPc_2]^0$ spectra to change, this differing spectra due to the addition of ethyl chains is expected. By assigning a HOMO at $\sim$-750 mV, and a LUMO at 750 mV, the bandgap is measured as $\sim$1.5 V, depending on some shift of the HOMO.

Displayed in Figure 6.12 b) a spectrum was taken on one of the molecules in the dimer created by tip manipulation of a tetramer. Despite the apparent rotation of 45° of the upper Pc of the molecules in this dimer, as discussed in section 6.4.3, no variation in spectroscopy was observed. STS of the molecule in this structure closely resembles spectra taken on the tetramer in Figure 6.12 a). Given that the spectra shown here are significantly different from that of the layer, as shown in Figures 6.13 and 6.11, a more comprehensive study must be performed. There appears to be a correlation between dimer and tetramer spectra, but with significant differences when studying a layer. Possibly larger organisations exhibit differing spectroscopic features, but this needs further reproducible measurement for a clear interpretation.

No isolated molecules were found other than those resting on a layer of Et-Pc, so a comparison to isolated $[TbPc_2]^0$ was not possible.

The spectroscopic features of $[TbPc_2]^0$ observed strongly depend on both the position of measurements on the molecules as well as their specific organisation when deposited onto Au(111) [13, 14]. STS provides some characterisation of the molecules, but given the possible parameters that may affect spectroscopy, a direct comparison may be challenging, but the results from literature are shown below to explain how the measured spectra may vary.

Figure 6.13 is adapted from Amokrane et al. [14]. A distinct difference is seen between spectroscopy on A and B type molecules. A and B type molecules are defined by the two contrasts seen in a checkerboard arrangement, as shown in Figure 6.13 a) and b). The explanation for this contrast was discussed in chapter 4 but is related to the intermolecular interactions and may partially be due to the relative orientations of the upper Pcs with respect to the lower. There is a clear difference in spectroscopy when measurements are taken on overlapping lobes in a layer against non-overlapping lobes, as shown in Figure 6.13 b) and d). Komeda et al. [13] measured a variation in the SOMO peak due to a tilt in the upper Pc. this was not observed in pristine semi-infinite layers by Amokrane et al. but possibly some similar tilt was observed here that was not seen in imaging due to some effect of the ethyl chains.

To summarise the findings from literature, the appearance and position of peaks strongly depend on many parameters. The organisation of the molecule, from monomer, to large semi-infinite islands, affects the spectral features. The position on the molecule where the spectrum is taken, between measuring the Terbium centre or differing lobes of the Pc ring, produces varying results. Different lobe spectra depend on lobe overlap with neighbouring lobes and may have some contribution from tilt effects

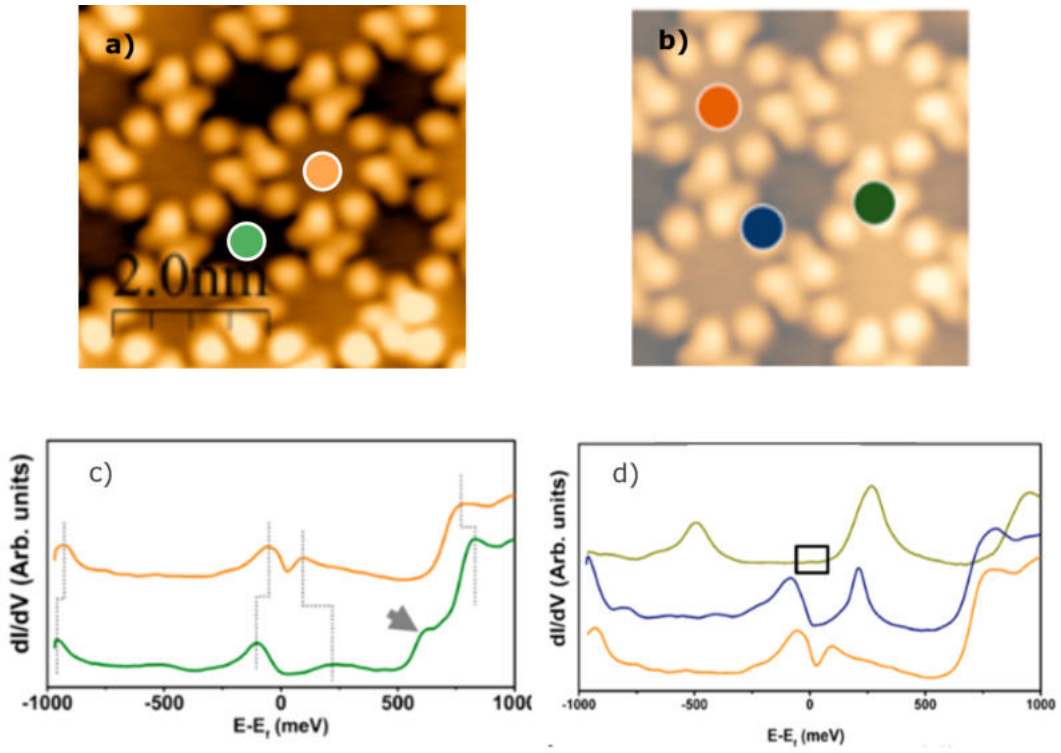

FIGURE 6.13: $[TbPc_2]^0$ spectroscopy on Au(111) taken with permission from Amokrane et al.[14] a) Topographic STM image showing a $[TbPc_2]^0$ molecule on Au(111) with coloured dots to depict spectroscopy locations. b) Topographic STM image of $[TbPc_2]^0$ layer, showing the distinction between bright and dark spots, with coloured dots to depict spectroscopy locations. c) and d) Spectroscopies taken on positions correlating to the coloured dots from a) and b) respectively.

of the upper Pc ring in non-pristine layers. The orientation of the top Pc with respect to the lower and the orientation of the lower Pcs with respect to each other influence the observed spectrum.

One final complication, is that, as shown in chapter 5, the reduction of the molecule with the use of hydrazine does not affect the Kondo property of the molecule, as the quenched radical property is restored on the surface when the charged $[TbPc_2]^-$ molecule contacts the substrate, however, this has not been confirmed for the $[Tb(Et\text{-}Pc)_2]^-$ molecule.

Overall, the spectra measured here are quite distinct from what has been published [13, 14]. In larger layers, a similar structure of two peaks close to the Fermi level is observed, with the peak at negative bias shifting, depending on the position of measurement. One would expect the addition of alkyl chains to affect the spectroscopy, but given that two distinct spectral shapes were measured, it may be the case that some other parameter is affecting spectroscopy. This may be due to the ethyl chains moving during spectroscopy and a measurement of heteroleptic molecules may clarify this issue.

6.4.5 Structure dependent Kondo effect

As clusters of various size and large layers have been imaged, one may measure variable sized structures, in order to study how differing organisations, and thus differing magnetic exchange interaction may affect the Kondo effect and it's appearance.

From Amokrane et al. [14], the Kondo effect is observed on the ligand when the molecule is isolated but is suppressed when the molecules are organised into dimers. The effect is once again observed on 3-fold overlapping lobes of the ligand when the molecule is organised into compact trimers or tetramers. For full layers of pristine $[TbPc_2]^0$, the effect is observed only on non-overlapping lobes. Given that the appearance of the effect is organisation dependent, by tuning the organisation with the addition of alkyl chains, some deeper understanding of the mechanisms for these phenomena can be found.

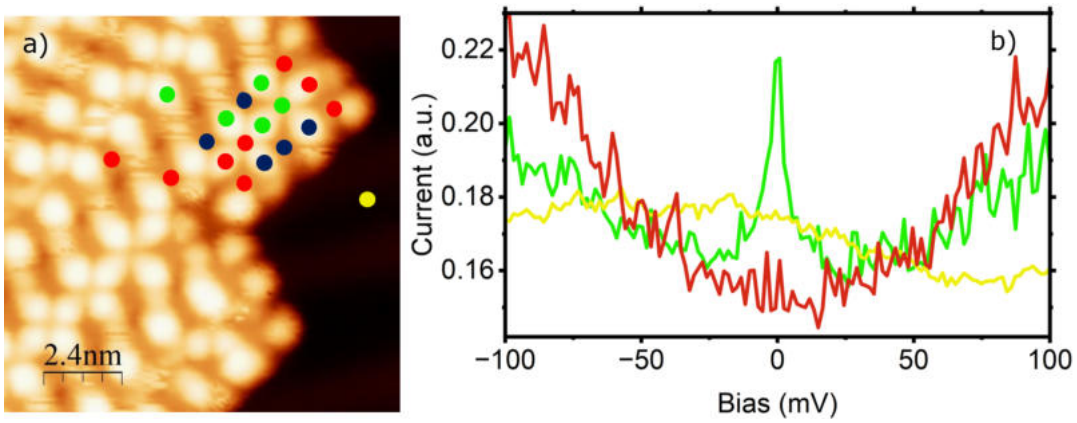

FIGURE 6.14: Kondo effect on $[Tb(Et\text{-}Pc)_2]^0$ deposited onto Au(111) a) STM image with of an island with spectroscopy locations indicated. Green dots depict where a zero bias peak was reproducibly seen, and red dots where no zero bias peak was seen in reproduced measurements. Blue depicts points of uncertainty. Yellow indicates a background on the bare Au(111). U_B=-1 V I_t=40 pA. b) A comparison of dI/dV spectra, showing an example from a green dot, red dot and a gold background. Spectra taken using a lock-in amplifier with a modulation voltage of 1 mV. The average FWHM peak width was measured as 8.2±1.2 mV.

No zero bias peak was measured on the molecules when organised into tetramers or hexamers. No single isolated intact $[Tb(Et\text{-}Pc)_2]^0$ molecule was found, and thus, no measurement for isolated molecules was performed.

Zero bias peaks were found on different positions within the larger islands of $[Tb(Et\text{-}Pc)_2]^0$, as shown in Figure 6.14. These peaks are assumed to be Kondo features given the wide observance of Kondo features on the $[TbPc_2]^0$ molecule, as reported in [12, 14, 15, 191] and explored in chapter 4. The q-factor of measured peaks was > 1, as was observed for the unsubstituted molecule, meaning that transport is similarly dominant through the molecule.

Reproducible measurements of specific Kondo features observed in equivalent locations within a given island were unsuccessful. This is partially due to the same issue described in section 6.4.4 where the precise location of the tip during spectroscopy is uncertain. From Figure 6.14 a), some positions did show reproducible Kondo peaks. An example of a zero bias peak, as well as background and negative

result, are shown in 6.14 b). No reproducible zero bias peaks were found at the edges of the layer.

Given that in the case of the $[Tb(Et\text{-}Pc)_2]^0$ system presented here, there are assumed to be no overlapping lobes; one would only expect to see Kondo on the isolated molecule or on large layers. The observation in the centre of large layers may be due to some specific intermolecular interaction, and at the edge of the layers, this interaction is not present, and thus, no zero-bias peak is observed. This may imply some result towards tuning of the control parameter towards quantum criticality and a possible phase transition, but this is not certain from the lack of a clear reproducible position in the layer where a Kondo effect is measured.

There is a defect in the centre of the image in Figure 6.14; therefore, locally, the structure is not regular. This may cause this lack of a distinct position where the Kondo effect is reproducibly observed. Perhaps a reproducible position could be found on a more regular island. Other islands did show some zero bias peaks. From prior discussion, and observed from the Kondo study on the tetramer, hexamer, the appearance of the Kondo effect is highly structure dependent. Therefore, more studies are required on a more regular lattice to clarify any results.

It appears that some transition from smaller clusters and edges of islands, to the centre of large islands, is observed, possibly due to a lesser effect of interactions from nearest neighbours and, furthermore, next nearest neighbours. This transition may partially explain the significant difference in spectroscopy for lower order clusters, such as those shown in Figure 6.12, when compared to the spectroscopy of layers, as observed in Figure 6.11, due to this varying interaction from neighbours and next-nearest neighbours. It may be the case that some other confounding factor causes this change, for example some interaction with the tip via the ethyl chains. One could further argue that larger islands have more confined chains, reducing this effect; thus causing this apparent variation during spectroscopy due to island size.

The critical observation is that Kondo peaks are not found in smaller organisations but are found in larger layers. Although it must be noted that whilst no Kondo effect was observed in some positions there may be other confounding factors meaning that a Kondo effect is present, but not successfully observed.

The average peak width was defined as the FWHM of the Fano fit. This value differs significantly from spectrum to spectrum. They all showed a similarly high value of q-factor, therefore likely originate from similar transport channels through the molecule. Assuming that these peaks all have the precise same origin, a Kondo temperature of 31 K can be calculated. This is close to the range for the $[TbPc_2]^0$ from literature [12, 15], so is likely to be of similar origin, i.e. an organic π radical.

The Kondo effect was measured on the $[Tb(Et\text{-}Pc)_2]^0$ on Au(111) when organised into layers. There did appear to be some dependence on position within the organisation. No Kondo effect was found on molecules organised into lower order clusters. This implies some dependence on intermolecular interactions, but this may be something more simple that has not been considered, due to some interaction with the ethyl chains, and as such, requires further experimentation.

6.5 Electrospraying $[Tb(Hex\text{-}Pc)_2]^0$

6.5.1 Molecular overview and mass spectra

To further increase the lattice spacing, the following molecule studied was the Hexyl chain molecule, shown in 6.15 a) where two six-carbon Hexyl chains are attached to

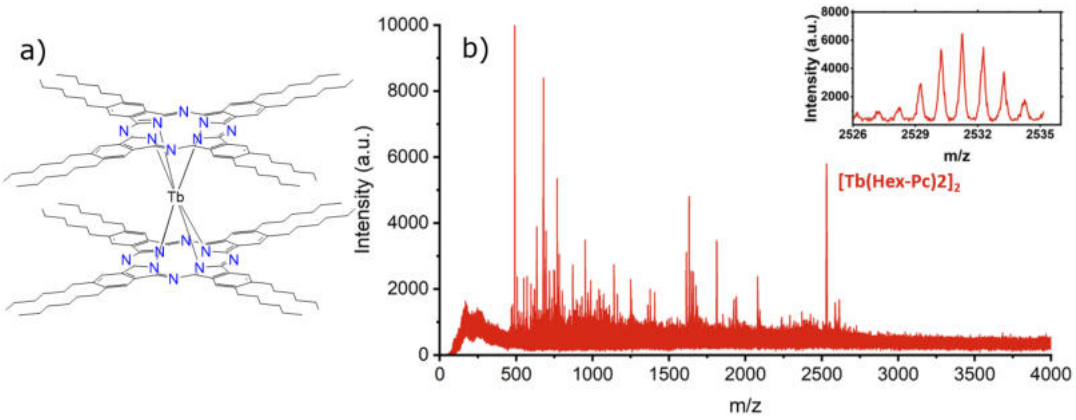

FIGURE 6.15: Structure of $[Tb(Hex\text{-}Pc)_2]^0$ with MALDI spectrum a) Molecular model of $[Tb(Hex\text{-}Pc)_2]^0$. b) TOF-MALDI spectrum, with peak indicated, inset shows a zoom of the spectrum, with assigned peak at 2529.7 m/z

each benzene ring. The addition of Hexyl chains drastically increases the $[Tb(Hex\text{-}Pc)_2]^0$ mass, which from the MALDI spectrum in 6.15 b) is measured as 2529.7 m/z. Due to the limited resolution of the ESI-MS spectra, due to lesser ionisation efficiency, MALDI was used to acquire a better defined mass. An attempt to test the sublimability of the molecule, identical to that in section 6.2.1, was performed. The correct peak was found above the noise level in ESI-MS before sublimation. During sublimation, the material in the crucible solidified from its initial oily liquid crystal form. ESI-MS on the collected material from the sublimation test showed no distinctive peak. A simple Thin layer chromatography test of the sublimed and unsublimed materials showed no distinct spots. The molecule seems to have decomposed completely, and as a result, it is not possible to study via sublimation in UHV.

6.5.2 ESI-CIBD mass spectra

For electrospraying the $[Tb(Hex\text{-}Pc)_2]^0$ molecule, the solvent combination used for depositions was as follows:

2.5mM hydrazine and 100 µM $[Tb(Hex\text{-}Pc)_2]^0$ solved in 600 µl of acetonitrile, tetrahydrofuran and trichloromethane in a ratio 1:1:1 with 1.5 µl of water. Water was used only to handle the Hydrazine.

From Figure 6.16 a), the centre of the fitted Gaussian was found at 2526.9±0.2 m/z, with a width of 22.4±0.43 m/z. This does not correspond perfectly to the 2529.7 m/z measured by MALDI. This is not correct within the calculated error, but as discussed in chapter 3, the precise error of the calibration performed is difficult to quantify. The offset applied was assumed to be linear, but this is not necessarily true. These errors may change over time due to changes in the system or during repair. Additionally, the masses used in calibration were lower than that of $[Tb(Hex\text{-}Pc)_2]^0$, so it is unclear if non-linear offsets would begin to dominate. This discrepancy between the MALDI value and ESI-CIBD value represents a 0.1% error and so can be considered correct. The 22.4 m/z peak width is far below the 97 m/z mass of a single Hexyl chain, so one may assume that the molecules are intact during deposition.

From Figure 6.16 b), the average molecular kinetic energy was measured as 2.14±0.14 eV with a distribution of ±2.25 eV. This means that there was a large spread of energies during deposition.

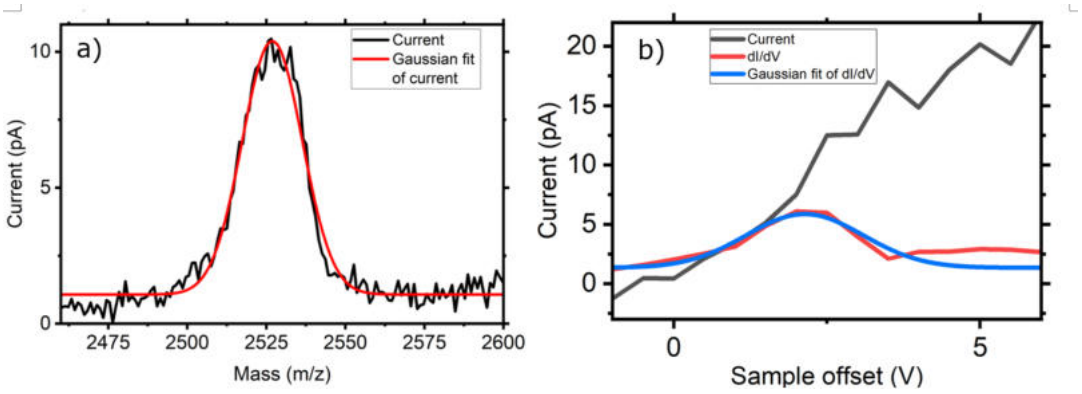

FIGURE 6.16: Mass spectrum and kinetic energy test of $[Tb(Hex\text{-}Pc)_2]^-$ sprayed with ESI a) ESI-Mass spectrum of $[Tb(Hex\text{-}Pc)_2]^-$ curve fitted with a Gaussian. b) Kinetic energy profile taken using the same parameters as used for 6.16a).

6.6 $[Tb(Hex\text{-}Pc)_2]^-$ deposited onto Au(111)

The $[Tb(Hex\text{-}Pc)_2]^-$ was deposited onto an Au(111) crystal held at room temperature. The average ion energy was set as -2.14±2.25 eV. The sample was initially degassed to 50°C to counteract minimal contamination during vacuum suitcase transfer.

6.6.1 Overview of observed species

Measurement of $[Tb(Hex\text{-}Pc)_2]^0$ allows for characterisation of the molecule and an understanding of how it organises on the Au(111) surface. By comparing $[Tb(Hex\text{-}Pc)_2]^0$ on Au(111) to that of $[Tb(Et\text{-}Pc)_2]^0$, the relationship between alkyl chain length and intermolecular distance can be established, thus opening the project further to studying other chain lengths, and thus further improving the tunability of islands of SMMs.

As observed in prior depositions, two distinct species were measured on the surface, assigned to the intact $[Tb(Hex\text{-}Pc)_2]^0$ and the single Hex-Pc which has broken off from the intact molecule. Importantly to note, the average ion energy is set to a negative number. As discussed in 3, this simply means that the majority of ions do not reach the surface, due to the strong retarding field. Only ions at the very edge of the distribution reach the surface, making the distribution of real ions that impact narrow and close to 0, limiting the impact energy. Thus, for the average of all ions, the apparent kinetic energy is negative. The choice was made to display the data in this way in an attempt to simplify, despite the issue of discussing an apparent 'negative kinetic energy'. The -2.14 eV average ion energy was significantly lower than any of the depositions of $[Tb(Et\text{-}Pc)_2]^-$, and by comparison to later $[Tb(Et\text{-}Pc)_2]^-$ experiments not shown here, the $[Tb(Hex\text{-}Pc)_2]^0$ shows significantly less dissociation. It is not trivial to directly compare different molecules, but this may imply that there is a critical landing energy above which molecular dissociation occurs. By finding this critical landing energy, one may tune the amount of dissociation on the surface.

In Figure 6.17, a) and b) islands of the $[Tb(Hex\text{-}Pc)_2]^0$ and Hex-Pc ring are shown, respectively. By analysing height profiles, the assigned single Hex-Pc is again less than half the height of the assigned $[Tb(Hex\text{-}Pc)_2]^0$ layer.

The height of the aromatic backbone of the $[Tb(Hex\text{-}Pc)_2]^0$ layer is measured as 4 Å. From section 6.4.1 and as observed in Figure 6.7, the height of the aromatic backbone of the $[Tb(Et\text{-}Pc)_2]^0$ layer was measured as 4 Å. Assuming that the observed

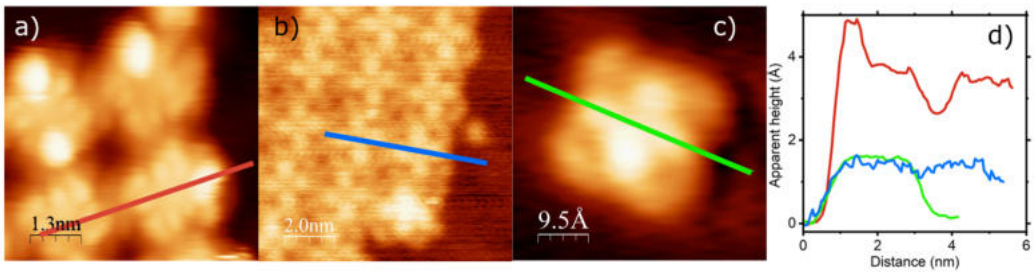

FIGURE 6.17: Overview of species from [Tb(Hex-Pc)$_2$]$^-$ deposition onto Au(111) a) STM image of a [Tb(Hex-Pc)$_2$]^0 island, U_B=-1.05 V I_t=4.3 pA b) STM image of a Hex-Pc island, U_B=-1 V I_t=106 pA c) STM image of an isolated Hex-Pc, U_B=-1 V I_t=16 pA. d) line profiles taken from Figures 6.17 a)-c) over positions indicated with coloured lines

aromatic backbone is due to the benzene rings, the height of the molecule itself is unchanged by the additional length of the alkyl chains and, in principle, should have the same molecule-substrate distance, and critically the same distance between the surface and the central terbium ion.

From the profiles taken from 6.17 c), the central cross, which is assigned to the cross shape made by the four benzene rings, is measured as being 1.5 Å in height; this is very close to that of the 1.5 Å recorded for the similar cross structure of the Et-Pc from Figure 6.7, which was discussed in section 6.4.1. There does not appear to be a significant increase in the height of the Hex-Pc layer due to the additional alkyl chains, likely because they lie flat on the surface. This explains the square-like shape observed in Figures 6.17 b) and c).

Commonly, bright spots are observed at the edges of the [Tb(Hex-Pc)$_2$]^0 layer, one of which is measured in the profile in 6.17 d). The bright spots observed in profiles from both Figure 6.7 of the [Tb(Et-Pc)$_2$]^0 and Figure 6.17 of the [Tb(Hex-Pc)$_2$]^0 do not correlate well to the expected result of increasing dimension from longer alkyl chains. From Figure 6.7 of [Tb(Et-Pc)$_2$]^0, more than 5Å was measured for the cross like protrusion. However, in the profile taken from Figure 6.17 a), the protrusion measured has a height of 4.7Å. Given that the length of a C-C bond is 1.54 Å, one would expect the protrusions due to chains on the [Tb(Hex-Pc)$_2$]^0 to be significantly larger than that of the [Tb(Et-Pc)$_2$]^0. Therefore, it is unlikely that the chains attached to the upper Pc of the [Tb(Hex-Pc)$_2$]^0 are pointing directly upwards, as was hypothesised for the [Tb(Et-Pc)$_2$]^0. The positioning of these bright spots appears random. It is also similar to what has been observed in literature [243]. Likely the STM tip pulls these chains out of position into some random orientation. The specific orientation of the chains will be further discussed in a later section.

6.6.2 Discussion of Hex-Pc self-organised structure

The chains on the Pc rings on the surface are assumed to lay flat as observed prior [26, 30, 232, 234, 235], reducing the degrees of freedom of the chains. Assuming that the chains are confined in 2 dimensions and given that each C-C bond has two possible allowed angles in 2-D, for each chain, there are $2^6 = 64$ possible orientations. Therefore, the possible orientations of the chains on each molecule are $64^{16} = 7.9\text{x}10^{28}$. This presents a significant challenge for calculation. The images show a 4-fold symmetric structure, so one may assume that each set of 2 chains on each benzene ring has the same conformation, giving 4096 possible conformations of the hexyl chains on the lower Pc, but this remains heavily intensive. Due to

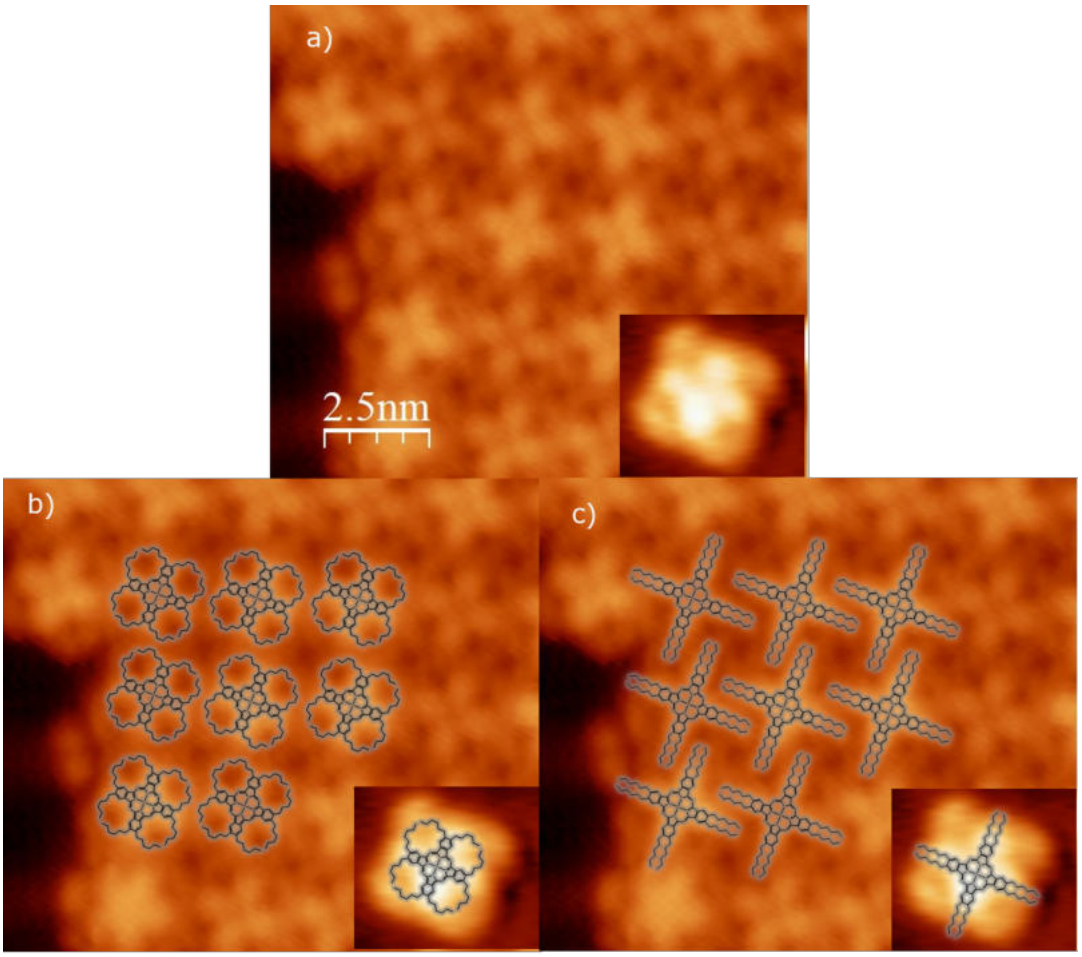

FIGURE 6.18: Comparison of tentative models for Hex-Pc structure a) STM image of Hex-Pc island, U_B=-0.7 V I_t=45.9 pA, with an insert showing an isolated Hex-Pc, U_B=1 V I_t=16 pA. Scale accurate for all images. 2 suggested models are overlaid onto b) and c), which are directly copied from a)

the many degrees of freedom, a precise structure is not presented, only a tentative model. In order to perform a calculation for this system, it would likely need to be a less sophisticated model, for example, some spring-like system, where the intermolecular interactions are assumed as some form of potential well, and no quantum mechanical effects are considered. In place of calculation, two possible structures are proposed in Figure 6.18. One where the square structure is caused by strong intramolecular interactions between chains, creating a square-like loop, as depicted in Figure 6.18 b). The model proposed in Figure 6.18 c) assumes that intermolecular interactions dominate, where the chains are straight, and the interaction between chains creates the observed square structure. One would expect that the alkyl chains would interact heavily, but the specifics are not immediately apparent. The isolated Hex-Pcs, as depicted in the insert of Figure 6.18 a), were very uncommon, representing less than 0.1% of Hex-Pcs observed. The isolated Hex-Pc, given its square shape, is much more likely to conform to the structure proposed in 6.18 b), whereas the straight chains proposed in 6.18 c) do not conform to this square-like structure. One would expect that it is not possible for the methyl groups at the ends of the hexyl chain to interact so closely, as in the stucture proposed in b). Given that there is not a clear alternative model for the isolated Hex-Pc, this unexpected interaction

is possible at least for the isolated molecule.

Given that these molecules have a very strong tendency to organise into islands, one would expect strong interaction between chains of adjacent molecules, supporting the structure in 6.18 c) as more likely. The structure proposed in Figure 6.18 c) is the more promising structure for the aims of the project. If the chains organise in this configuration for longer lengths of alkyl chain, then the lower layer of Pcs may become precisely tunable as one adjusts the alkyl chain length. The square-like structure proposed in 6.18 b) would not linearly increase the spacing between molecules with increasing alkyl chain length. The conformation suggested in 6.18 c) has been previously reported [26, 232]. However, this is when deposited on HOPG at the solid-liquid interface.

Conversely, the images from literature do not look similar to the image in Figure 6.18 a) and possibly do not correlate. The situation on HOPG is somewhat different, in that the chains interact strongly with the surface via Van der Waals interactions, and the chains lie commensurate with the honeycomb structure of the HOPG. The square structure is maintained at the edges of the structure in a), and thus, the contrast at these positions would not be due to overlapping chains from adjacent molecules. Given that the Pcs at the edges have a lower coordination with other molecules, the may adopt this square structure at the edges only, but the molecules at the centre of the island have interacting straight chains. The structure in 6.18 b) is correct for the isolated Hex-Pc, but the conformation of a single molecule does not give a clear understanding of the same molecule in an organisation.

The edges of the island and the insert in Figure 6.18 a) correlate strongly to the model proposed in b). No boundary between regions is observed, which could explain some mixture of the models in b) and c), where the edges correlate to b) and the centre correlates to c). In summary, it is challenging to assign either model with certainty, and would need calculation to be verified.

Despite the uncertainty in the modelling and positioning of the chains, the position of the Pc ring is clear from these images. As a result, lattice parameters can easily be measured. The measured lattice was square, aligning always along one of the high symmetry directions. The lattice parameter was measured as 2.37 nm x 2.37 nm±0.08 nm. Interestingly, in every instance, the orientation of the Pc ring was offset by an angle of 20 °, with respect to the lattice vectors, and thus offset from the high symmetry direction.

6.6.3 Discussion of [Tb(Hex-Pc)$_2$]^0 self-organised structure

By measuring the length parameters of the islands of intact [Tb(Hex-Pc)$_2$]^0 molecules, again a square unit cell is seen, with length parameters of 2.52 nm x2.52 nm ±0.05 nm, where one of the vectors aligns with one of the high symmetry directions. These lattice parameters do not correspond to the Hex-Pc unit cell within the measured error but are very close. The error was calculated by taking the standard deviation from multiple islands, so it may not fully account for systematic experimental error, and so the lattice parameters of the Hex-Pc and [Tb(Hex-Pc)$_2$]^0 may be equal. If they are not equal, the difference is minimal, and one would not expect a significant adjustment to the position and conformation of the Hex-Pcs in the lower layer of the [Tb(Hex-Pc)$_2$]^0 islands when compared to the island depicted in 6.18. The lower Hex-Pc layer would likely correspond to one of the models depicted in Figure 6.18. By observing the cross like structure originating from the four benzene rings of the upper Hex-Pc, one can see that the upper Hex-Pc is rotated by 20° relative to the high symmetry direction. As a result, the upper Hex-Pc appears to be either aligned

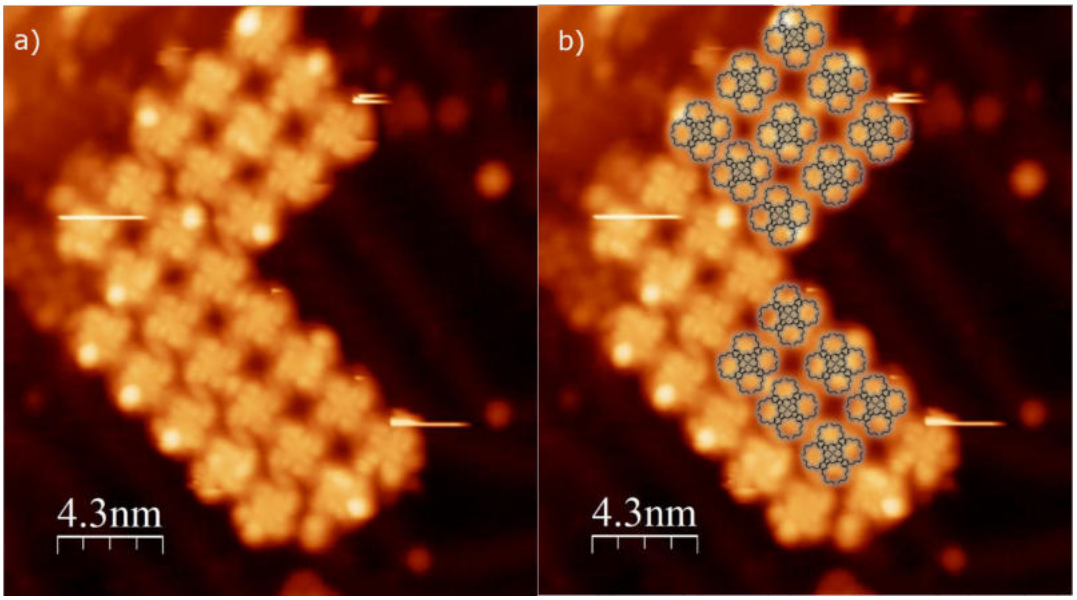

FIGURE 6.19: Analysis of[Tb(Hex-Pc)$_2$]^0 structure a) STM image showing [Tb(Hex-Pc)$_2$]^0 layer. U_B=-2 V I_t=3.6 pA. b) Tentative model overlaid onto 6.19a)

or rotated by 45° relative to the lower Hex-Pc, as suggested for the [TbPc$_2$]^0 [12, 191]. At the extreme left of the organisation in Figure 6.19 a), one can see Hex-Pcs seemingly organised with the layer, and these Hex-Pcs are rotationally aligned with the Pcs of the upper layer of the [Tb(Hex-Pc)$_2$]^0 structure. This implies that they are aligned in all cases, but further mixed species layers would need to be observed in order to confirm.

From Figure 6.19, there is no obvious interpretation of the molecular structure of the upper layer of hexyl chains without calculation. Given that the long chains are unconfined from the surface, it is not possible to simplify the model by assuming the structure is only 2-dimensional. The 2-dimensional molecular model shown is not proposed as the correct configuration, only to give a sense of scale.

Given that in section 6.4.2, when ethyl chains came close to colliding, a significant protrusion was seen in the topography. One would assume that similarly, the chains on adjacent molecules would strongly interact with each other. Given that there is no clear regular protrusion, the chains do not overlap in the same way as was observed for the [Tb(Et-Pc)$_2$]^0 islands. It may be that the protrusions observed at the edges of the molecule and measured in 6.6.1 are caused by the chains not being perfectly organised into a regular lattice and pointing upwards. Given that the hexyl chain extended to its maximum possible length is over 7 Å, this protrusion measured in 6.17 a) is either only a section of the chain pointing upwards or simply some contaminant. Some contamination was observed on the surface, but these protrusions were more common at the edges of [Tb(Hex-Pc)$_2$]^0 islands than the contaminants on the bare Au(111), and in principle, the chains would be least confined at the edges of the structure. Given that the apparent height is measured as too small to be due to the chains, and there is no tip interaction one could attribute to upwards pointing chains, this is most likely a contaminant. The conformation of molecules in the island is unclear, but at a very minimum, one may assume that the chains do not point upwards in the same way as observed for the [Tb(Et-Pc)$_2$]^0.

In summary, a regular lattice of greater intermolecular spacing has been observed on the surface via the use of thermolabile alkylated molecules deposited by ESI-CIBD. A series of tunable lattices have been successfully created by varying the length of chemical substituents and depositing these variable size molecules stably onto metals. The 2.52 nm x 2.52 nm lattice of $[Tb(Hex\text{-}Pc)_2]^0$ is bigger than that of the 1.76 nm x 1.76 nm lattice of the $[Tb(Et\text{-}Pc)_2]^0$, which is bigger than the 1.43 nm x 1.43 nm lattice spacing observed for the $[TbPc_2]^0$. These interesting results can be used to further similar goals and allow explorations of further properties of these structures that can be tuned via the method presented here.

6.6.4 Differing intramolecular contrast imaged at variable bias

By measuring at different biases, one can adjust not only the changing image contrast due to differing electron localisation over differing orbitals, but also any differing image contrast due to changes cause by differing tip-molecule interaction.

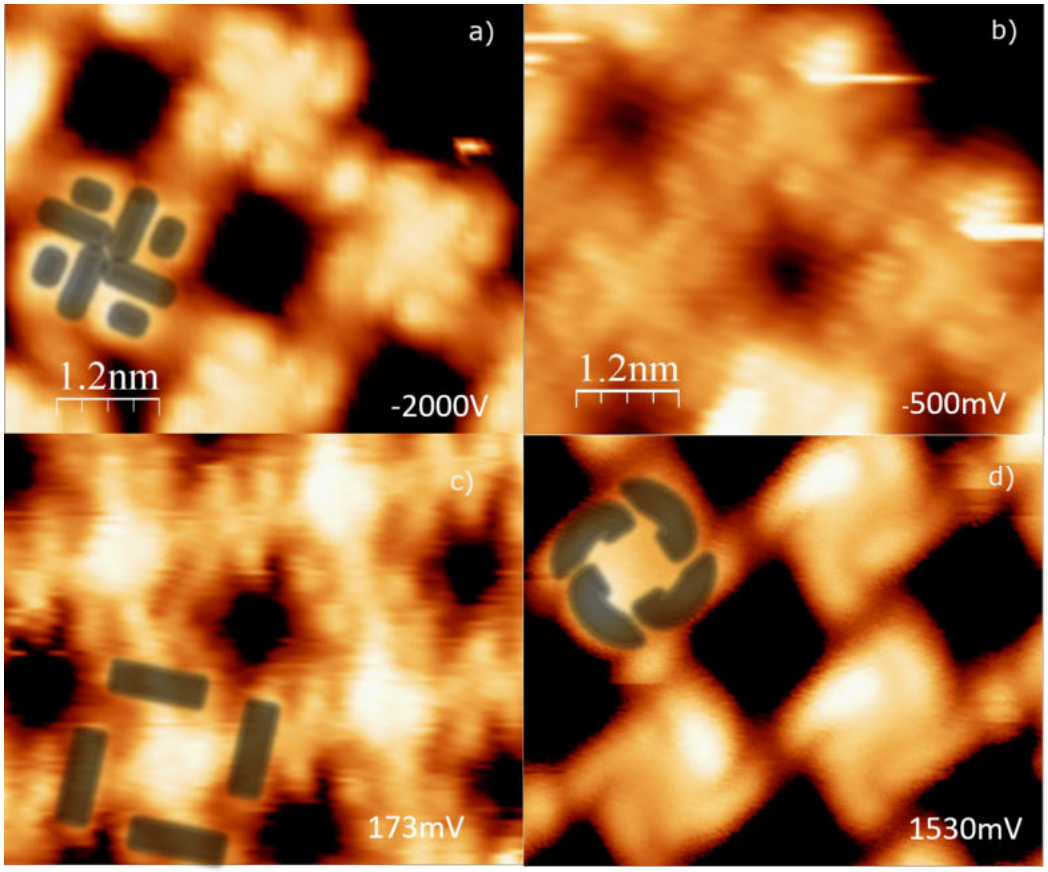

FIGURE 6.20: STM images of $[Tb(Hex\text{-}Pc)_2]^0$ at differing biases a-d) STM images showing similar $[Tb(Hex\text{-}Pc)_2]^0$ islands. Imaging parameters for a)-d) respectively were I_t=3.6 pA, I_t=9.4 pA, I_t=4.3 pA, I_t=4.3 pA.Grey lines are drawn to highlight chirality

From Figure 6.20, several different specific appearances of the molecule were observed at particular biases. The measurement of differing biases, thus measuring differing electronic states causing differing appearances in images, is regularly observed and may be considered trivial. As discussed in chapter 3, the differing electronic states of the molecule have differing electron densities, and thus, when

measuring at a particular bias, a different image of the molecule is produced, corresponding to the electron density of the molecule at that bias. However, such an extreme difference is not common, and one would expect the case here to be more than purely an imaging of different electronic states and not this trivial case.

Four main intramolecular contrast types were observed. It was found more challenging to image these molecules with a high level of detail at positive bias. Firstly, a 'cross-like' molecule was observed at high negative bias, as depicted in Figure 6.20 a). This was observed from -2 V up to -0.7 V. Close to the Fermi level, a 'fern-like' molecule was observed, as depicted in Figure 6.20 c). This molecule was observed between -0.4 V and 0.5 V. An intermediate appearance was observed between these biases, as is depicted in Figure 6.20 b), only observed at -0.5 V. This 'intermediate' molecule has features of both the 'cross-like' and 'fern-like' molecules. Finally, a 'spiral-type' molecule was observed, as depicted in Figure 6.20 d), which was observed between 0.7 V and 2 V. In 6.20 a)-c) a central cross is observed, due to the four benzene rings, as observed in prior measurements, and seen clearly in Amokrane et al. for the double decker molecule [14]. Therefore, the additional intramolecular contrast not forming the cross, is assumed to originate from the hexyl chains.

Figures 6.20 a) and c) show the same island, only imaged at different biases. The crosses have rotated by 20 ° in Figure 6.20 c) and the cross structure now aligns with the $[1\bar{1}0]$ direction. Assuming that the lower Hex-Pc has maintained its orientation, the dihedral angle of the $[Tb(Hex\text{-}Pc)_2]^0$ has changed by 20 °. This result will be further discussed in a later section.

Such a significant difference in imaging dependent on bias has not been observed for the $[TbPc_2]^0$ in literature [14, 15, 28, 189, 191, 193, 194, 244, 245], nor was it observed for the $[Tb(Et\text{-}Pc)_2]^0$ as discussed in section 6.4.2. This implies that these different molecular appearances are caused mainly by the hexyl chains. Notably, the height of the tip during these measurements was not kept constant. Given that adjusting the bias also changes the height of scanning, and as discussed in section 6.6.3, it is expected that the tip interacts with the chains. To rule out that the changes in intramolecular contrast are not caused by varying tip interaction, the tip height should be more strictly controlled in subsequent experiments. Alternatively, AFM measurements could be performed on these molecules to better understand the conformation of these molecular islands without any contribution from the changing bias and electronic structures.

Particularly at high bias, there appears to be some bridge connecting adjacent molecules, as can be strongly seen in Figure 6.20 a) and d). The level of contrast in these images has been selected to emphasise the differing appearances seen for different biases. As a result, these 'bridges' between molecules are exaggerated. The nature of this feature in topography is unknown.

6.6.5 Chirality of $[Tb(Hex\text{-}Pc)_2]^0$ in islands

At all biases, the molecules exhibit some chirality, as shown in Figure 6.20. The chirality is most obvious in the 'spiral-type' molecule seen in Figure 6.20 d) and is also obvious in Figure 6.20 a) for the 'cross-like' molecule. The chirality was only ever in the direction shown. Given that the cross structures in Figure 6.20 a)-c) are caused by the aromatic backbone, there does not appear to be any molecular chirality in the aromatic backbone in Figures 6.20 b) and c). The hexyl chains likely cause any chirality observed. There are many examples of molecular chirality on surfaces [244, 246–249], in particular some observation of molecular chirality in the $[TbPc_2]^0$ [189, 246] from Fu et al., the chirality observed for the $[TbPc_2]^0$ is due to a bias pulse

controlled rotation of 4°. This is presumed as a rotation of only the upper Pc relative to the lower Pc away from its usual angle of 45°. This rotation is performed by applying a bias pulse of ±2 V. From other sources [12], the upper Pc of a [TbPc$_2$]^0 can be rotated by the application of a ±2 V bias pulse.

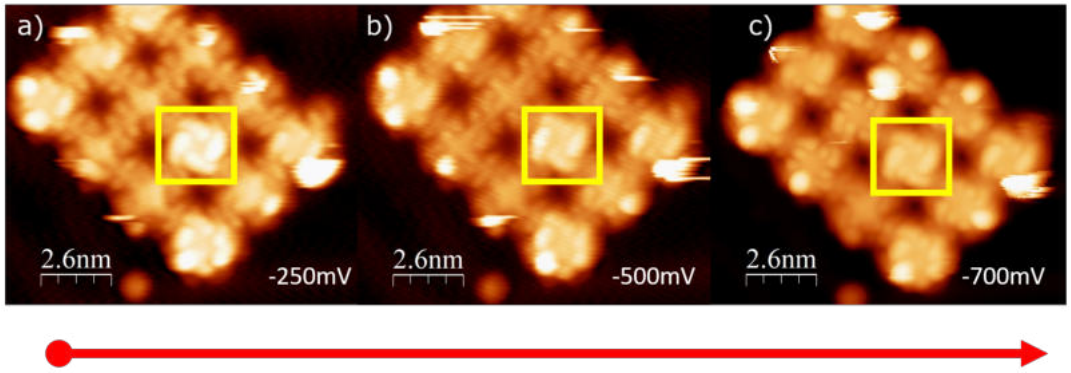

FIGURE 6.21: Chiral type [Tb(Hex-Pc)$_2$]^0 molecules a-c) STM images showing one [Tb(Hex-Pc)$_2$]^0 island scanned at differing biases. I_t=9.4 pA for all images. The arrow shows the sequence of images in time. Yellow boxes highlight the molecule displaying permanent chirality.

Whilst the bias-dependent appearance measured in Figure 6.20 was reproducible, some specific molecules that did not follow this switching between intramolecular contrasts were observed. From Figures 6.21 a)-c) a 'spiral-type' molecule, as discussed in the prior section, is imaged in two instances on an island and remains in this 'spiral-type' configuration at all biases. This would imply that this difference is not purely electronic. The molecule highlighted in yellow exhibits the same chirality as the molecule in Figure 6.20 d).

The apparent height of the 'spiral-type' molecule observed in Figure 6.21 is the same as that of other 'spiral-type' molecules and so has a bigger apparent height than the other molecules observed in this island. Despite having a bigger apparent height than other molecules in the island, it has the correct apparent height for the 'spiral-type' molecule. Thus, it is expected that the molecule is not simply resting upon a contaminant or surface defect. Further, there is no obvious difference in appearance from the previously observed 'spiral' type molecules; thus, it is likely an intact molecule, simply with some other conformation. As discussed prior, there is an apparent rotation of 20 ° of the cross structure assigned to the aromatic backbone observed in the transition between Figures 6.20 a) and b), as well as between Figures 6.21 b) and c). Given that the molecules have a scanning bias-dependent rotation, this rotation may be driven by some other influence or process, causing a permanent 'chiral-type' molecule independent of scanning bias.

Compared to literature, [12, 189] no change in orientation of the Pc ring is observed by simply scanning. The clear movement of the cross structure assigned as the aromatic backbone shows that these cases are different.

In Figure 6.22, more 'chiral-type' molecules independent of bias are observed. Interestingly, the change to a bias-independent molecule happens during or between scans. Between images 6.22 b) and c), two of the expected non-chiral molecules (highlighted in yellow) at bias close to Fermi-level change into a chiral form despite the bias remaining close to Fermi. Other molecules in the organisation maintain the

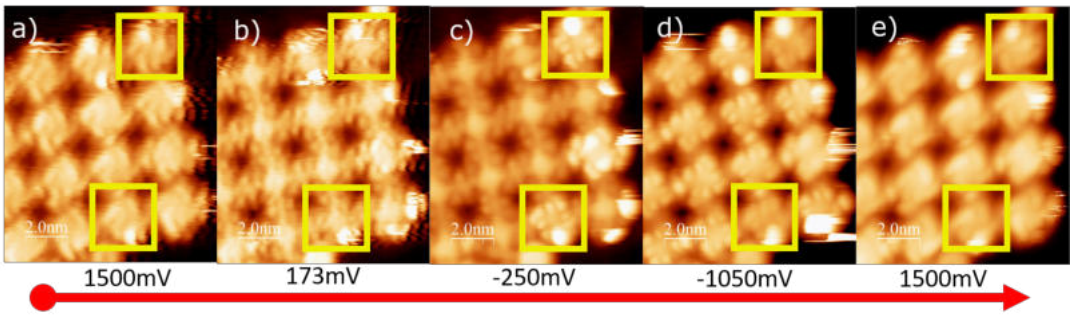

FIGURE 6.22: Secondary chiral type $[Tb(Hex\text{-}Pc)_2]^0$ molecules a-e) STM images showing one $[Tb(Hex\text{-}Pc)_2]^0$ island scanned at differing biases, as indicated below each image. I_t=4.3 pA for all images. The arrow indicates the sequence of images in time. Yellow boxes highlight molecules of interest.

same expected structure observed close to Fermi level. From 6.22 d) and e), the highlighted molecules still switch between the expected appearances at positive and negative bias; this implies that there is still some involvement of the electronic structure in the appearance of the molecules imaged. The identical appearance of the highlighted molecule to the other molecules in 6.22 a) and b) further supports the claim that the molecular structure is identical for these permanently chiral structures. The most obvious interpretation is that some rotation occurs. This is still surprising and would need further exploration for confirmation and a better understanding of the system. The exact influence of conformational changes of the alkyl chains is still yet to be understood.

Differing bias measurements have been shown to adjust image contrast. Whilst this is partially dependent on the localisation of molecular orbitals, evidence has been shown that this may be also due to both changes in dihderal angle of the $[Tb(Hex\text{-}Pc)_2]^0$, but also upon how the chains move during measurements.

6.6.6 Variable spectroscopy

In order to characterise and compare to what was studied spectroscopically for the $[Tb(Et\text{-}Pc)_2]^0$, a spectroscopic study of $[Tb(Hex\text{-}Pc)_2]^0$ was also carried out. This may also allow some study into the effect of alkyl chain length on spectroscopy, given that the spectroscopy on $[Tb(Et\text{-}Pc)_2]^0$ was not comprehensively understood.

In Figure 6.23, some spectroscopic features are observed similar to those observed both for the $[TbPc_2]^0$ [13, 14], as depicted in Figure 6.13 and from the $[Tb(Et\text{-}Pc)_2]^0$ molecule spectra over large islands, as shown in Figure 6.11. In Figure 6.11 b) asymmetric peaks close to the Fermi level are again observed, separated by 425 mV. Peaks are also observed at -1.1 V and 0.9 V.

The repeated measurements on the same position were taken with different tip states, with good corresponding background gold spectra, according to the procedure described in chapter 3, but do not show reproducible features. In contrast to the $[Tb(Et\text{-}Pc)_2]^0$, there is much clearer intramolecular contrast of the molecule in topography, thus likely showing more distinction between spectra taken on the molecule centre compared to the molecule lobe. The middle spectrum shows only a shoulder at -150mV and no large peak at positive bias close to the Fermi level. This is very similar to the spectrum taken on a dark B-type molecule for the $[TbPc_2]^0$ described in Amokrane et al. [14], as depicted in Figure 6.13 c).

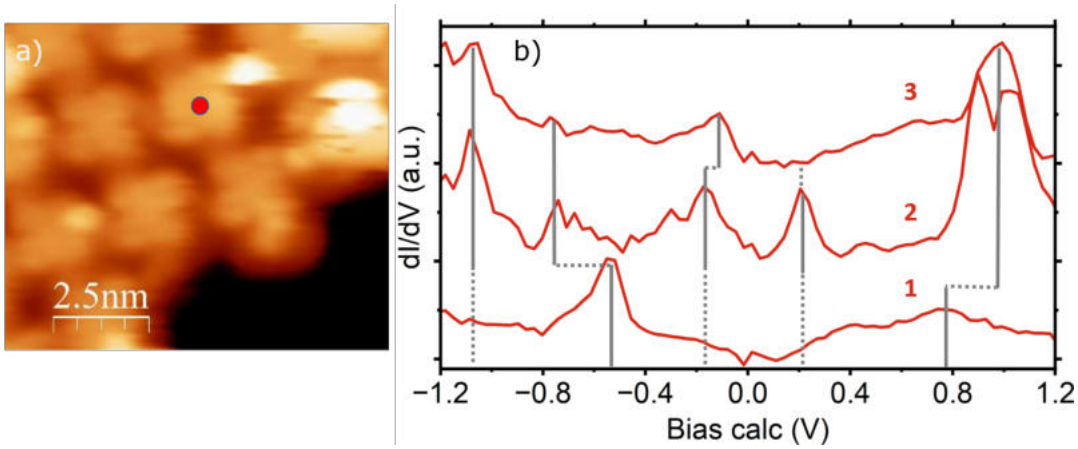

FIGURE 6.23: Spectroscopy on a [Tb(Hex-Pc)$_2$]^0 organised layer a) STM image of [Tb(Hex-Pc)$_2$]^0 layer, with a red dot to indicate the spectroscopy location. U_B=-2 V I_t=7.3 pA. b) dI/dV spectra taken at the position in a). The spectra are taken at the same position. All spectra have been scaled and separated vertically for clarity. Grey lines are drawn to highlight peaks where dotted lines show discontinuities. Spectra were taken using a lock-in amplifier with a modulation voltage of 25 mV

Despite not showing reproducible spectra, there appear to be some recognisable features for spectra performed on large islands that correlate to what has already been recorded for [TbPc$_2$]^0 molecules. For further confirmation, reproducible spectra of multiple islands with a better defined tip position during spectroscopy should be performed.

No Kondo feature measurements were attempted on these islands, due to measuring zero bias anomalies at all times that did not appear to be due to molecules on the tip.

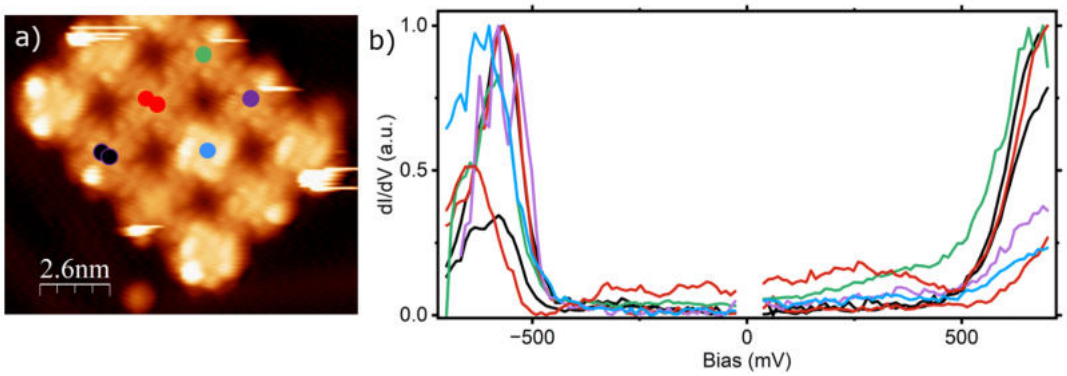

FIGURE 6.24: Spectroscopy on a small island of [Tb(Hex-Pc)$_2$]^0, a) STM image of a small [Tb(Hex-Pc)$_2$]^0 island, with coloured dots to indicate spectroscopy locations. U_B=-0.5 V I_t=9.4 pA. b) dI/dV spectra taken over the positions indicated in a) All spectra have been scaled for clarity. Spectra taken using a lock-in amplifier with a modulation voltage of 25 mV. Points between ±16 mV are removed due to zero bias anomalies, not visible in mathematically derived dI/dV

In Figure 6.24 a), spectra were observed similar to spectra taken on the tetramer of the [Tb(Et-Pc)$_2$]^0. A nearly symmetrical structure around the Fermi level was measured. There is again some variation in the HOMO position shifting from -650

mV to -600 mV. Multiple points of the same colour show where a spectrum was repeated with a different tip state. This is not a high level of reproducibility, but more than spectra performed on larger islands of $[Tb(Hex\text{-}Pc)_2]^0$. Despite the difficulty in analysing data of limited quality, one consistent observation between measurements on the $[Tb(Et\text{-}Pc)_2]^0$ and $[Tb(Hex\text{-}Pc)_2]^0$ systems was the general shape of spectra taken on small islands, although this may be only due to some interaction with the alkyl chains. The bandgap therefore, is measured as ∼1.3 V, the increased length of alkyl chain has decreased the band gap.

Interestingly, the blue spectrum from Figure 6.24 is taken on the permanently chiral molecule discussed in depicted in Figure 6.21. The spectrum on this molecule appears identical to spectra of other molecules in the assembly, indicating that the difference between normal molecules and the permanently chiral molecule is minimal. Given that the spectroscopic features are highly dependent on the orientation of the upper Pc with respect to the lower [12], this result of identical spectra implies that the upper Pc may not be rotated, and this apparent rotation is caused only by hexyl chains.

In summary, some limited conclusions can be drawn from the spectroscopy. For large layers, there appears to be some correlation to the expected structure, further confirming that the molecules observed are the expected intact $[Tb(Hex\text{-}Pc)_2]^0$ molecules. There appears to be some correlation between smaller sized islands and clusters, showing distinct but reproducible spectra for both the $[Tb(Et\text{-}Pc)_2]^0$ and $[Tb(Hex\text{-}Pc)_2]^0$. This is speculative but is the most reproducible observation from the spectroscopy data presented here. The spectroscopy data is not of high quality and needs improvement to further these conclusions, which are highly speculative given the limited data.

6.7 Deposition tests of other alkylated $[TbPc_2]^0$ molecules

Some other species of similar alkyl chain molecules were synthesised for testing but were not studied by STM, only tested in the ESI-CIBD system.

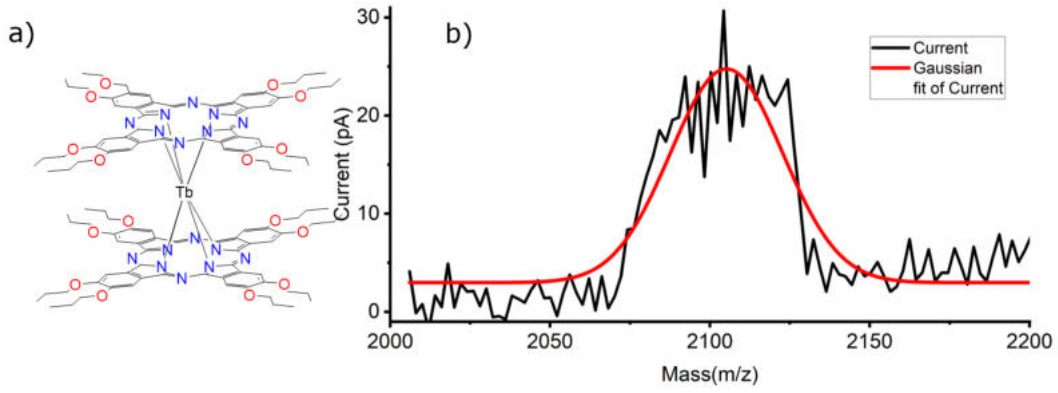

FIGURE 6.25: Overview of Oxy-propyl $[TbPc_2]^0$ molecule a) Molecular model of Oxy-propyl $[TbPc_2]^0$. b) ESI-CIBD mass spectrum of Oxy-propyl $[TbPc_2]^-$

The first molecule shown here, is the Oxy-Propyl $[TbPc_2]^0$ ($[Tb(OPrPc)_2]^0$), which from Figure 6.25 a) has two additional oxygen atoms attached to each benzene ring, and a three carbon propyl chain attached to each oxygen atom. The propyl chain was expected to steer the lattice spacing, similarly to other alkyl chain molecules

studied here. The oxygen may give the alkyl chain greater flexibility and ability to orient, thus creating differing and more interesting conformations. From Figure 6.25 b), a peak of 2105 m/z with a width of 41 m/z was found, which correlates well with the expected 2113 m/z expected. This molecule was not tested in STM as the additional modifications would likely overcomplicate the results on the surface. It could be tested in future experiments and may provide interesting details about how molecules can be designed to have particular desired properties on surfaces.

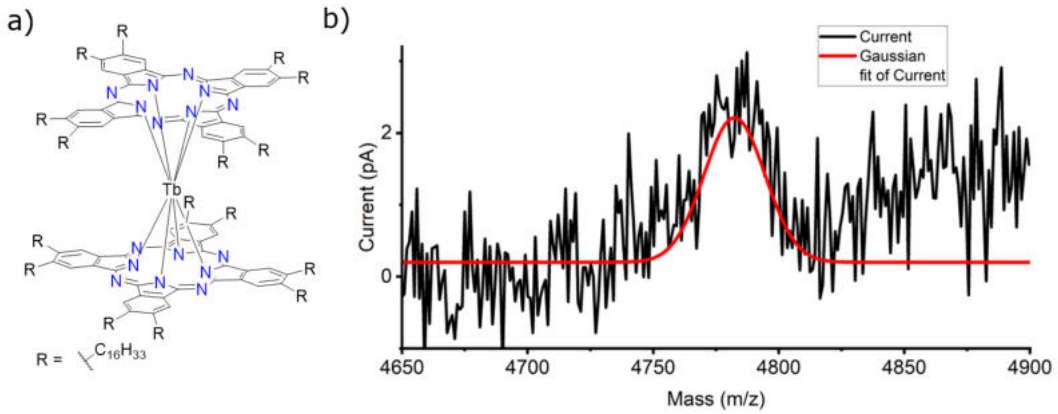

FIGURE 6.26: Overview of 16 carbon chain $[TbPc_2]^0$ molecule a) Molecular model of 16 carbon chain $[TbPc_2]^0$. Kinked lines intersecting alkyl chains display a discontinuity to avoid depicting the long alkyl chains. b)ESI-CIBD mass spectrum of 16 carbon chain $[TbPc_2]^-$

The highest mass molecule sprayed was a 16-carbon alkyl chain $[TbPc_2]^0$. Figure 6.26 a) shows the molecular model. Two 16-carbon chains are attached to each benzene ring. Once again, this molecule was ionised in solution using hydrazine, resulting in a singly charged ion. The mass of the molecule is 4773 Da, resulting in a mass-per-charge ratio of 4773 m/z. In Figure 6.26 b), a small peak is observed at 4782 m/z with a width of 29 m/z. This peak is highly accurate but is very close to the noise level. The signal of 2 pA corresponds to a deposition time of over 100 hours and was not considered viable. If this could be deposited in a reasonable time frame, it would be very interesting to study on surfaces as one would expect longer chain lengths to increase lattice spacing more linearly and thus in a more tunable manner.

6.8 Conclusion and outlook

Based the most straightforward interpretations of the project aims, a tunable lattice system of thermolabile molecules deposited by ESI-CIBD was created on-surface.

The $[Tb(Et\text{-}Pc)_2]^0$ molecule and $[Tb(Hex\text{-}Pc)_2]^0$ were both successfully deposited onto an Au(111) surface. In both cases, semi-regular islands of intact molecules were observed, where the lattice parameters of each islands were perpendicular. The lattice parameters of these islands increased with increasing alkyl chain length, as summarised in the following table.

Molecule	Lattice spacing (nm)	Error (nm)
$[TbPc_2]^0$ (compact)	1.43	0.06
$[TbPc_2]^0$ (regular)	1.5	0.06
$[Tb(Et\text{-}Pc)_2]^0$	1.76	0.1
$[Tb(Hex\text{-}Pc)_2]^0$	2.52	0.05

Due to the thermolabile nature of these molecules, the successful deposition of these molecules intact onto metal surfaces is a novel result. In literature, molecules of this type with large alkyl chains are limited to the solid-liquid interface due to their unsublimability. Alternative methods such as drop casting or matrix-assisted depositions [200–202] are interesting, but the ESI-CIBD technique allows for greater control of the ample parameter space involved in the depositions, and this in principle, can lead to more reproducible depositions once the parameter space is adequately understood and controlled.

Indications for specific conformations of these molecules on surfaces were found. However, this did not provide a complete understanding, and thus, calculations and further experiments are required. Some additional interesting observations were made on these structures, particularly relating to the rotation of the upper Pc relative to the lower Pc.

Some studies were performed to observe the effect of the altered lattice on the electronic structure, but partially due to an incomplete understanding of the conformation of the molecules, no definitive results were successfully drawn from the data. Further experiments with the ESI-CIBD system would provide an understanding of the molecular dissociation on surface impact. Additionally, they may allow one to avoid this dissociation and create larger and more regular islands on the surface, further supported by better defined annealing. This, in turn, may improve the reproducibility of spectroscopy.

In future experiments various longer length alkyl chain molecules could be studied. As discussed, the deposition of the 16 carbon chain $[TbPc_2]^0$ was challenging. Likely, many carbon chain lengths between sixteen and six carbons would be depositable onto surfaces but would allow for a wider range of molecular spacings, and thus a greater control of the magnetic exchange interactions between molecules, but further other distance dependent interactions, where larger distances must be altered to see an effect, such as the RKKY interaction.

The unknown positioning of the unconfined chains in the upper Pc layer made imaging and interpreting images challenging. Possibly by constructing heteroleptic molecules, where the chains are only attached to one of the two Pc rings, as has been previously reported [31, 232], one may achieve better control of the desired tunable lattice spacing, but remove the additional confusion and obscuring of the structure of the upper layer due to the alkyl chains attached to the upper Pc.

Many interesting results have been taken, and the general concepts of creating tunable lattices on surfaces have been developed. Specifically, using the ESI-CIBD system to deposit specially designed thermolabile molecules onto metal surfaces has great potential for future experimentation outside of the scope of this project.

Chapter 7

Thermolabile Di-radical Molecules on the Surface

7.1 Introduction

Following from the successful deposition of an intact radical, the project was continued to investigate a ligand functionalised diradical molecule derived from the previously studied $[TbPc_2]^0$ molecule. This highly reactive diradical would likely begin to react at a temperature far below the sublimation temperature of the molecule and no longer maintain its diradical property, thus necessitating the use of ESD. Furthermore, the use of the mass spectrum of the ESI-CIBD system allows one to verify the charge state of the molecule, giving information about the electronic structure before reaching the surface. Depositing reactive radicals on surfaces is interesting for its applications to the $[TbPc_2]^0$ project but also for further work outside of the scope of this project.

7.2 Electrospraying [NO-Pc(TbPc)]^0 for study on metal surfaces

In this case, the molecule of interest deposited for study was the $[TbPc_2]^0$ with an additional NO group ([NO-Pc(TbPc)]^0) as depicted in 4.7 a). This molecule contains not only the unpaired electron delocalised over the Pc ring, as in the case of the $[TbPc_2]^0$ molecule, but additionally a delocalised electron in the nitroxyl group, which is attached to one of the benzene rings. Therefore. this is a stable di-radical molecule, enabling novel studies into a class of compounds that are generally difficult to investigate in a stable state.

The current most promising application of the $[TbPc_2]^0$ molecule towards quantum computing is to use the nuclear spin as a highly coherent quantum state. Recall that $[TbPc_2]^0$ has a single unpaired electron delocalised on the ligand sytem, however with the addition of a second unpaired electron on the ligand system, the scope of applications towards QIP is further widened. A similar molecule was synthesised and measured by Komeda et al., an [NO-Pc(YPc)]^0 and measured an asymmetric g-factor[250] of the two unpaired spins. These are the same two spins as on the [NO-Pc(TbPc)]^0. The assymetric g-factor improves the ability for individual addressability. Furthermore, having two accessible and measurable unpaired electrons on a single molecule could be used in parallel to implement different operations towards the goal of quantum information processing. The ability to perform processes is dependent on the intramolecular interactions, in particular, how the spins couple. In the case of a strong intramolecular interaction, the additional coupled states could be used as a readily accessible triplet state, being usable as a so-called 'qutrit'. In the

case of a weak intramolecular interaction, the two individual states could be used to construct a Controlled NOT gate (CNOT) [250]. A CNOT gate is an operation that one may perform using two qubits where the state of one qubit is flipped depending on if the other is in a particular state[251, 252]. For example if the control qubit has a state $|0\rangle$ then the CNOT gate does nothing, but if the control qubit has a state of $|1\rangle$ then the CNOT gate will flip the secondary qubit. The CNOT gate is often listed as one of the fudamental 2-qubit gates for implementing a universal set of quantum gates [253]. As stipulated by Divincenzo [72], the ability to implement a universal gate set, and therefore approximate any arbitrary unitary operator by a finite sequence of basis operations, is an important milestone, for universal, fault-tolerant, QIP. The CNOT gate is the most widely utilised 2-qubit gate since: (i) it is the entangling gate that together with the single-qubit Hadamard (H), phase (S) and phase shift gate (T, also known as /8 or S), produce a universal gate set, and (ii) it is readily implemented by well-known and controllable physical interactions in many quantum computing platforms [251, 254]. In our molecular systems, the intramoelcular interactions that may allow a CNOT gate to be implemented may be altered by the surface interaction, so it would need further characterisation on the surface in order to be comprehensively understood.

In literature it has been demonstrated that STM can be used to implement a CNOT gate on the surface [91]. These experiments are based on simpler structures, using only iron and titanium atoms for the measured states. By creating more complex surface structures, a more effective and precisely tuned system could be constructed, where these [NO-Pc(TbPc)]^0 molecules are a possible candidate.

Furthermore, there are some developments in using ESR-STM (Electron spin resonance-STM) or similar techniques [122, 245, 255], possibly allowing for a more sophisticated study of these systems on surfaces. However, this would again encounter the same challenge of more complex spin systems being hard to bring to the surface. Using the ESI-CIBD system allows for a potential future study of more complex spin systems using ESR-STM technology. For the long term future of quantum information processing, molecular qubits studied on surfaces are not currently the most viable method for quantum information processing. However, they may be used not only for further research into the capabilities of these systems but also more viable for specific applications due to their strengths in other areas, such as exceptionally long coherence times.

Aside from the potential applications of these molecules towards quantum information processing, it is also interesting to study these molecules purely as radical molecules on surfaces [256–260]. Furthermore, as highly reactive molecules, they may extend the range of applications that were hitherto impossible due to the difficulty in bringing these molecules to the surface. On surface synthesis remains a popular method for creating more complex architectures on surfaces, but the reactivity of the precursor molecules may prohibit the scope of these studies. Via the use of the ESI-CIBD system, reactions involving more reactive precursor molecules may allow for the construction of more complex structures on surfaces. Nevertheless, the specifics of the diverse applications of studying highly reactive radical molecules on surfaces are outside of the scope of this project.

7.2.1 Depositing [NO-Pc(TbPc)]^0

Figure 7.1 a) depicts the diradical molecule, where two unpaired electrons are depicted, one delocalised over the two Pc rings and one on the nitroxide group. From the TOF ESI-MS in 7.1 b), the molecule mass is measured as 1295.2 m/z.

For electrospraying the $[NO\text{-}Pc(TbPc)]^0$ molecule, the solvent combination used was as follows:

2.5 mM Hydrazine and 100 µM $[NO\text{-}Pc(TbPc)]^0$ solved in 200 µl of tetrahydrofuran, acetonitrile, and trichloromethane in a ratio of 4:2:1 with 0.5 µl of water. Water was used to handle the Hydrazine.

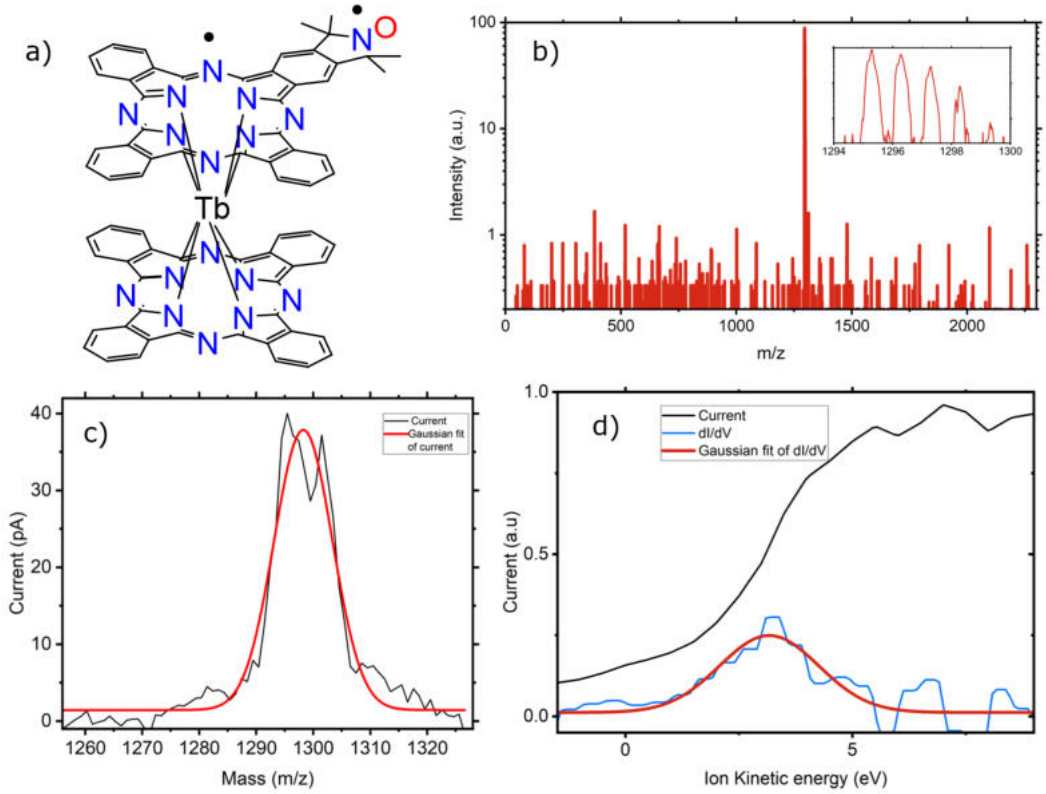

FIGURE 7.1: Overview of $[NO\text{-}Pc(TbPc)]^0$ system a) Structure of $[NO\text{-}Pc(TbPc)]^0$ with black dots to indicate unpaired electrons b) ESI-TOF MS of $[NO\text{-}Pc(TbPc)]^-$, with inset to show peaks corresponding to $[NO\text{-}Pc(TbPc)]^-$ c)ESI-CIBD MS of $[NO\text{-}Pc(TbPc)]^-$, with a fitted Gaussian peak in red. d) Kinetic energy scan of $[NO\text{-}Pc(TbPc)]^-$, with Gaussian fit of dI/dV in red.

The correct mass was found in the ESI-CIBD system, depicted in Figure 7.1 c), with a peak centred at 1298.2±0.2 m/z and a peak width of 12.0 m/z. As discussed in chapter 5, the charge state of the Pc of the molecule is indicated by the colour of the solution. As the molecule is blue in solution once charged, one can be certain that an electron is paired with the unpaired electron delocalised over the Pc. From the peak in Figure 7.1 c), the molecule is singly charged. It is unlikely that the localisation of the added charge has moved from the Pc to the NO group, therefore, it is assumed that the Pc is still charged and that there is still an unpaired electron on the NO group during spraying.

Notably, the molecule returns to its green form rapidly over time. This loss of charge occurred over the course of ∼two hours, which can be longer than the time required for one deposition, depending on ion current and target coverage.

This rapid de-charging was only observed for the $[NO\text{-}Pc(TbPc)]^-$, where other $[TbPc_2]^-$ based molecules studied in this thesis would return to green form over the course of a few days, or even weeks, when using the same concentration of Hydrazine. In order to maintain a high ion current and increase the coverage to a

reasonable level, Hydrazine was added whenever necessary. After reduction with additional Hydrazine, the molecular sample returned to its negatively charged state (blue form), and a peak at the correct m/z position was again recorded. It is assumed that this re-charging does not alter the molecule, with the NO group unpaired electron still present.

It is clear from literature that electron withdrawing groups such as the NO moiety would affect the redox property of a molecule [261]. There may be some additional contribution conformational or structural change due to the addition of a group, making the molecule asymmetric, and thus subtly affecting the redox proprieties [262]. From Komeda et al. [250] cyclic voltammetry, showed that the redox properties of the [NO-Pc(YPc)]^0 is a sum of the redox properties of the [YPc_2]^0 and the NO moiety, and thus would likely be similar for the [NO-Pc(TbPc)]^0. A deeper study to confirm this origin of the more rapid oxidation of the [NO-Pc(TbPc)]$^-$ was not performed.

From Figure 7.1 d), the average molecular kinetic energy was measured as 3.2±0.1 eV with a distribution of 2.6±0.2 eV.

Multiple depositions were performed with varied hydrazine concentration, coverage and landing energy, but the only clear correlations drawn were from varying coverage. These other parameters did not appear to have a significant effect, but would require more controlled experiments to verify definitively.

7.2.2 Overview of observed species

The first deposition discussed is a low coverage sample. The intention was to measure isolated molecules of intact [NO-Pc(TbPc)]^0, in order to measure unreacted groups, as the expectation is that these molecules would interact very readily, and possibly the diradical property would be quenched. Once again, some dissociation of the molecules into single isolated Pcs was observed, as discussed in 5.5. As depicted in Figure 7.2, the heights of the [$TbPc_2$]^0 measured in the previous section are compared to the [NO-Pc(TbPc)]^0 and single Pc. The single Pc is once again less than half the height of the intact [$TbPc_2$]^0, allowing clear identification of its origin, although the presence of Terbium in the centre is not clear. No obvious protrusion is seen on the single Pc which can be attributed to the NO group. As the molecules are heteroleptic, one would assume that 50% of the observed Pcs would contain the NO group. Therefore, the molecule in c) is likely a Pc without the group. This will be addressed in greater detail in a later section.

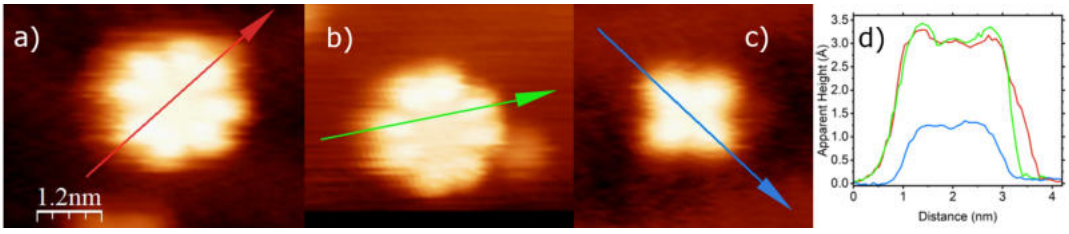

FIGURE 7.2: Comparison of profiles of various [$TbPc_2$]^0 derivatives observed on Au (111), a) Image of an [$TbPc_2$]^0 copied from Figure 5.4, with an indicated line profile, U_B=-0.5 V I_t=19.9 pA b) Presumed intact [NO-Pc(TbPc)]^0 molecule with line profile, U_B=-0.5 V I_t=23.5 pA. c) Single Pc dissociated from [NO-Pc(TbPc)]^0, with line profile, U_B=-0.6 V I_t=22.6 pA d) apparent height profiles corresponding to a-c)

By comparing the profiles taken of the $[TbPc_2]^0$ and the $[NO\text{-}Pc(TbPc)]^0$ from Figures 7.2 a) and b) respectively, the heights are almost identical. Given that the NO group is only attached to one of the benzene rings of one of the phthalocyanines, barring electronic effects, it is expected that the heights would be similar. From this image alone, it is not clear where the NO group is. Adjacent to the molecule in Figure 7.2 b), some contamination is seen in the bottom right.

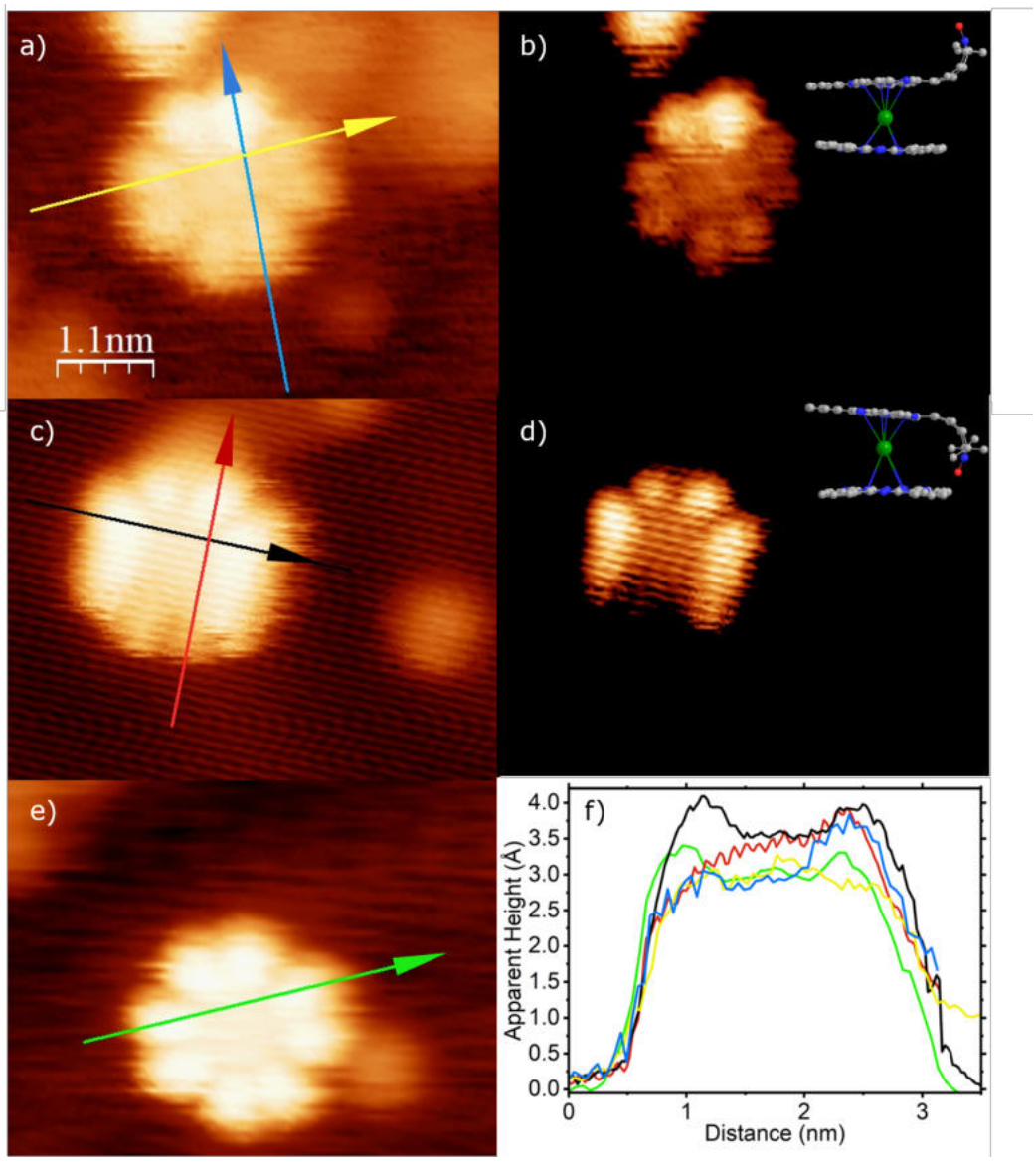

FIGURE 7.3: Comparison of observed intact $[NO\text{-}Pc(TbPc)]^0$ molecules deposited onto Au(111). a) 'upwards protrusion' $[NO\text{-}Pc(TbPc)]^0$ with line profiles highlighted, U_B=-0.5 V I_t=11.6 pA, the scale applies to all images, b) the same image as in a), with contrast adjusted to highlight the height difference, and a simple molecule schematic in top right of image. In model, green represents Terbium, grey carbon, blue nitrogen, red oxygen and hydrogens are not shown. c) 'downwards protrusion' $[NO\text{-}Pc(TbPc)]^0$ with line profiles highlighted, U_B=-0.5 V I_t=11.6 pA, d) the same image as in c), with contrast adjusted to highlight the height difference,and a simple molecule schematic in top right of image. e) $[NO\text{-}Pc(TbPc)]^0$ without protrusion, with line profiles highlighted and a simple molecule schematic in bottom right of image, U_B=-0.5 V I_t=23.5 pA, f) Profiles form a), c) and e) in corresponding colours.

Some examples of molecules with a clear distinction from the $[TbPc_2]^0$ were observed and are depicted in Figure 7.3. It is proposed that this appearance is due to the NO group on the top Pc bending away from the plane of the phthalocyanine backbone. Figure 7.3 a) shows an eight-lobed structure similar to that of the $[TbPc_2]^0$ but with a higher protrusion on two of the lobes. This protrusion is attributed to the electronic repulsion of the NO group. This may be coulombic repulsion between the Nitrogen on the NO groups and the Nitrogens in the Pc ring. In b) the contrast has been adjusted to highlight that this large protrusion is only present on one of the lobes. From f), the profile taken on the molecule in b) shows that the protrusion is 0.5 Å in apparent height. By measuring multiple protrusions, an average protrusion height for protrusions bending upwards was 0.63±0.17 Å. The average height of the planar section (not the protrusion) of the $[TbPc_2]^0$ was measured as 3.28 ±0.2Å, which is lower than that of the $[TbPc_2]^0$. Two averages of greater accuracy are defined by ascribing two species, one with a lower plane, and the other with a higher plane. The lower plane molecules had a height of 3.00 ±0.05 Å, and the higher plane molecules had a height of 3.5±0.1 Å There was no distinction in protrusion heights between the 'lower plane' and 'higher plane' molecules. Given that these molecules have a complex electronic structure due to their diradical nature, this apparent height change is likely not a difference in real height. The clear protrusion on one lobe allows one to define a 'lobe height'.

In Figure 7.3 c), the inverse of a) is observed, where two of the eight lobes appear to bend downwards towards the surface. Rather than for the single protrusion, the lobe appears to bend downwards gradually, as seen from the adjusted contrast image in d). Given that there appears to be spatial overlap between the NO group and the benzene ring, it may be the case that the larger benzene ring will cause a slope when it is displaced downwards, but the smaller NO group causes a sharper protrusion when bending upwards. This sharp protrusion contrasted with gradual bending can be seen by comparing the schematics in each of figure b) and d).This supports that the NO group is causing this protrusion, as when it is pointing upwards, it is observed directly by the tip, but when pointing downwards, the protrusion is not as sharp. From the profile in c) shown in f), the height of the cyclic backbone is measured as 4 Å, which is higher than has been measured for other $[TbPc_2]^0$ molecules. Few molecules were imaged with the lobe pointing down, but nevertheless, they could be separated into two categories, one with a higher plane and the other with a lower plane, as described before. These were measured as 4 ±0.1 Å, and 3.12 ±0.02 Å respectively.

One may expect the NO-group to interact more heavily with the substrate,as has been observed in literature [263]. Aside from expecting one orientation, it is surprising that no molecule was found where the NO-group is clearly in the lower layer. One clear counter-argument to this model, is that the observed contrasts are not due to a changing position of the NO group, but in fact an alteration to the electronic structure, causing a change in contrasts, due to the nature of STM imaging being a convolution of topography and electronic structure. This model will be discussed in a further section and is only a tentative. These are only simple schematics so are not intended to show a real scale.

The majority of isolated molecules were measured at -0.5V and 15-25pA, so these height differences are assumed not to be voltage or current dependent. By measuring the height of the lobe dipping towards the surface relative to the height of the other lobes, the height difference caused by the protrusion is measured as 0.59±0.22 Å. By comparing to the measurement of the upwards protruding molecule, these protrusions appear to be the same size, supporting the claim that they have the same

origin.

Many molecules with no obvious protrusion were measured, such as in e). The average height of these molecules was 3.27 ±0.14 Å. This is both lower and more variable than expected for the $[TbPc_2]^0$. It may be the case that the NO group is still intact but is attached to the lower Pc and thus is not observed directly by STM, although it is unlikely that there is no observed structural difference from an NO-group in the lower layer. Alternatively one could consider that the NO-group has broken off but given the strength of the bonding, this breaking does not seem possible. The apparently varying height, may be a signature that the NO-group is in fact in the lower layer, causing the electronic structure to vary and thus a differing apparent height is measured. It must be noted that the change between differing height molecules is a small difference and it cannot be discounted that this is due to some simpler factor, such as different adsorption sites.

The most common type were those with the protrusion pointing upwards, which had three times the occurrence of the other two species, which had equal occurrence. Furthermore, the lower height molecules were the most common. This does not account for the many molecules that were too heavily agglomerated to comment on their nature.

Some characterisation of molecules was performed, particularly with regards to their dimensions. A molecule with the well understood 8-lobe structure was imaged, as well as some protrusion attributed to the NO-group. The specific conformation of these molecules is not clear and requires further experimentation. A possible conformation was suggested but will be supported with further evidence.

7.2.3 Switching of observed contrasts

In order to better understand the conformation of these molecules, one may use the tip to interact with them. This may reveal some details about their three dimensional conformation and some information regarding intramolecular interactions. Due to the unstable nature of the diradical, it was found that the tip would interact very heavily with the molecule. This interaction sometimes caused the molecules to change between certain previously observed contrasts.

Figure 7.4 depicts one molecule that was imaged multiple times and was altered between images. Clearly, its apparent height is altered but maintains a similar structure. The 8-lobe structure with two lobes pointing downwards is observed. The orientation of the top Pc appears identical to prior to switching, but it is unclear if the rotation of the lower Pc has changed, although this is not likely. From the profiles in c), in the initial image the higher lobes (red profile) were 4 Å, and in the latter image the higher lobes (yellow profile) were 3.4 Å. The downward protrusion was 0.25 Å lower in the latter case. As discussed in the prior section, there was some variation in height measured for these molecules despite having a similar appearance otherwise. These findings imply that these changes are likely only changes in apparent height, given that the physical structure of the molecule appears identical. Given that these molecules were synthesised with two unpaired electrons, this may change during measurements, and thus, the electronic structure of the molecule may have been altered. As STM is a convolution of topography and electronic structure, this may explain the variety of heights measured for similar appearing molecules, if the electronic structure varies due to the variable status of the electrons on the molecules. One would expect a discreet change in the heights based on whether the

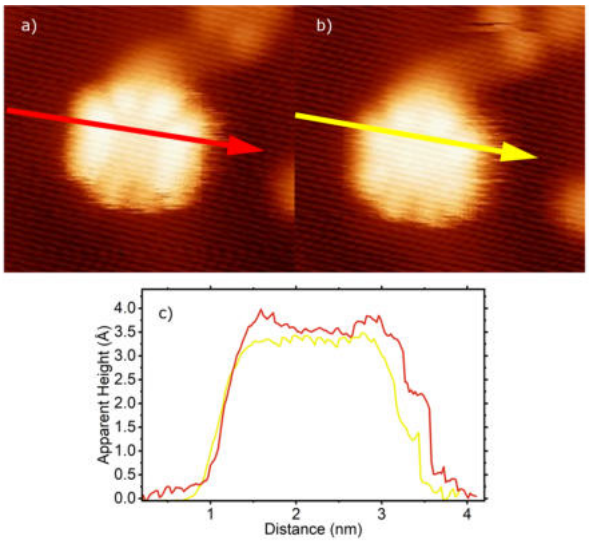

FIGURE 7.4: Observed apparent height change of an [NO-Pc(TbPc)]^0 molecule deposited onto Au(111) a) Image of an [NO-Pc(TbPc)]^0 U_B=-0.5 V I_t=11.6 pA, b) Subsequent image of the same [NO-Pc(TbPc)]^0 molecule imaged sequentially, U_B=-0.5 V I_t=20.0 pA, c) apparent height profiles of line profiles taken in a) and b).

molecule is still a diradical or not, particularly given that only two discreet heights were measured.

The centre of the molecule does not change its apparent height. Given that this centre is due to the Terbium, this further supports that the observed change is due to changes in the ligand.

Another molecule was observed that appears to switch NO group orientation between measurements. The images depicted in Figures 7.3 a), b), and c) were taken sequentially. From a comparison of Figures 7.5 a) b) and c), it appears that the molecule has switched from a state of the protrusion pointing upwards to the protrusion pointing downwards, and finally back to the initial configuration. Additionally, there is a rotation of the upper Pc of the molecule, which is likely a rotation of the entire molecule.

From the profiles depicted in d), The height of the aromatic backbone of the molecule in a) is measured as 4 Å, and the downward protrusion is measured as 3.5 Å. For the molecule in b), the aromatic backbone is measured as 3.4 Å, and the upwards protrusion is measured at a height of 4.3 Å. In the profile taken from c), the height of the aromatic backbone was measured as 4.3 Å, and the downward protrusion was measured as 3.6 Å. The 'aromatic backbone' heights quoted here are measured by averaging over the three lobes on each molecule that are not forming the 'protrusion'. From these measurements, it is clear that the orientation switches between the protrusion pointing upwards and protrusion pointing downwards.

Additionally, the blue and purple profiles are the same shape as the black and yellow profiles but are 0.4 Å higher. Seemingly having switched between the two heights previously defined.

If the assumption of the protrusion being due to the NO group is correct, then the position of the NO group has rotated by 160° (200°) counterclockwise (clockwise) between a) and b) and then 70° (290°) clockwise (counterclockwise).

Despite some uncertainty, this molecule appears to be capable of switching between NO-group orientations reversibly due to scanning, even with mild scanning

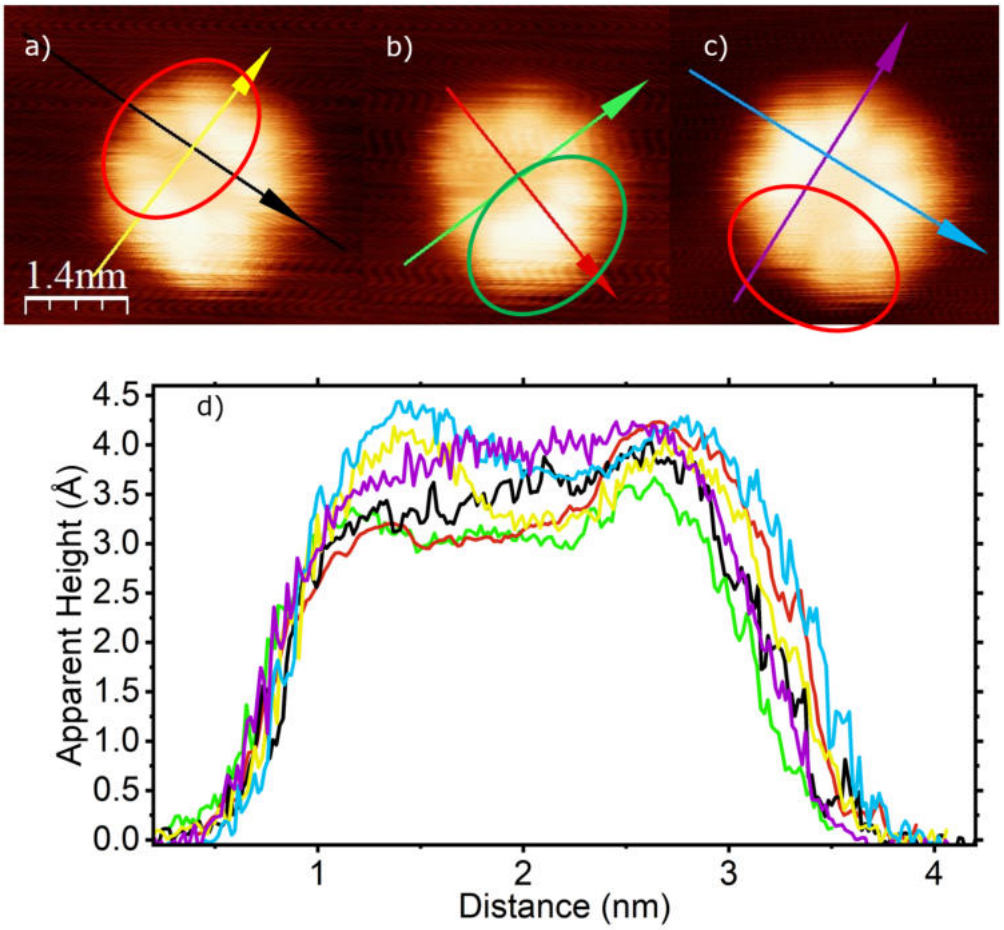

FIGURE 7.5: An [NO-Pc(TbPc)]^0 molecule on Au(111) switching between NO group orientations a) An image of an [NO-Pc(TbPc)]^0 molecule in the protrusion down orientation, with drawn line profiles, red oblong depicts location of downward pointing protrusion, U_B=-0.25 V I_t=25.6 pA, b) An image of the same [NO-Pc(TbPc)]^0 molecule in the protrusion up orientation, with drawn line profiles, green oblong depicts location of upward pointing protrusion U_B=-0.1 V I_t=20.8 pA, c) An image of the same [NO-Pc(TbPc)]^0 molecule in the protrusion down orientation, with drawn line profiles, red oblong depicts location of downward pointing protrusion, U_B=-0.25 V I_t=16.9 pA, d) Apparent height profiles from lines drawn in a)-c).

parameters. Given that the unsubstituted molecule does not show this level of variability and switching, it is assumed that the diradical nature of the molecule causes this. As the NO group is so reactive, it is not surprising that this system may have multiple physical forms, potentially depending on whether the molecule is a diradical or not.

Given that the position of the NO-group appears to change, one would assume it is in the upper layer, and unconfined by the surface, thus having the freedom to switch. As discussed prior, this is surprising when comparing to literature, [263] where one expects the radical group to interact heavily with the Au(111) and thus for the NO group to be attached to the surface.

One alternative explanation is that the molecule has performed a full rotation (salto) and landed upside down via manipulation, and then after further manipulation, returned to its initial position. This is highly unlikely, and one would expect

that the Pc with the NO group always stays in the same relative position.

A more likely alternative explanation is that the NO group is always in contact with the surface, and the adjusted contrasts observed here are due to changes in the electronic structure, possibly depending on the status of the radical.Given how interactive the radical would be expected to be, this seems likely. This would further support that the radical is not quenched for some of the species on the surface.

Whilst the specifics of how the molecule switches has not been shown through data, it is clear that the many different contrasts imaged are simply multiple conformations of the same molecule, and that the molecules can readily switch between these contrasts. Furthermore some limited evidence has been provided supporting the model depicted in figure 7.3.

7.2.4 Overview of a higher coverage sample

A series of samples with different coverages were prepared in order to understand how these molecules interact with each other. As has been previously described, there was significant dissociation of the molecules into single Pcs. It was found that there was a strong interaction between the intact molecules and the dissociated single Pcs, this is expected, given that 50% of Pcs have an intact reactive NO group with an unpaired electron.

Figure 7.6 shows an overview of the species observed for one of these higher coverage depositions. As before, a high level of dissociation occurred. By analysing the different ways the single Pcs interact with each other, one may understand more deeply the way the NO groups interact on the surface. Specific examples of some specific formations of Pcs are highlighted in Figures 7.6 b)-e), but many other examples are seen over the image, as well as examples of other more random formations. These examples will be discussed in greater detail in later sections.

Given that from the prior experiment on unsubstituted Pcs, the isolated Pcs do not self assemble as strongly, nor form clusters, the strong tendency of the Pcs here to form clusters with each other must be due to the NO group. Additionally, there is significant clusterisation of single Pcs around intact double decker molecules. Presumably, the isolated single Pcs that do not form clusters do not contain an NO group. Single intact double decker molecules were less common than clusters. However, this is equally observed for the $[TbPc_2]^0$, where the molecule strongly organises into islands. The trimer of double decker molecules is the most common configuration. There are few clusters of more than three intact molecules, and by comparing to the strong tendency of the unsubstituted molecule to form islands, this lower order clusterisation must be partially driven by the NO group.

Clusters of molecules are observed pinned to the herringbone elbows. This is well reported in literature. The elbows pin the molecules, creating nucleation sites for these interacting clusters. Interestingly, the herringbone elbows pointing to the right, so called pinched elbows, predominantly contain clusters of intact $[NO\text{-}Pc(TbPc)]^0$. In contrast, the left pointing, so called bulged herringbone elbows contain predominantly single Pc clusters. The difference between elbow directions showing different organisations is reported in literature [264–270]. Whilst clusters of single Pcs are more strongly pinned to the bulged elbows, many Pc clusters are observed on the bridge sites of the herringbone. Likely the double deckers become strongly pinned to the pinched elbows and create nucleation sites. The single Pcs with NO groups maintain some mobility on the herringbones, and once the pinched elbows become filled, they can only become pinned to the bulged elbows. The intact NO double

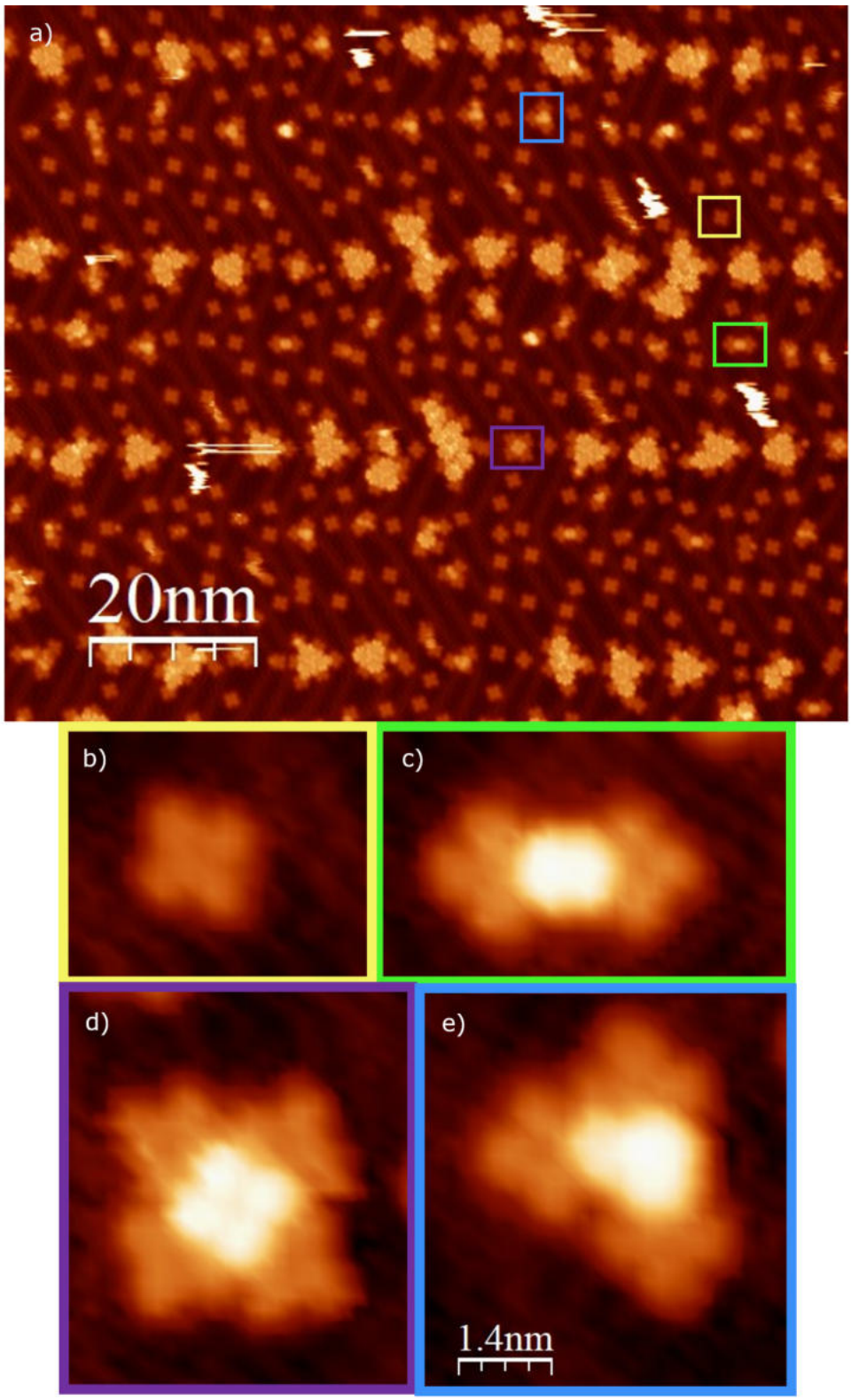

FIGURE 7.6: Overview of a deposition of [NO-Pc(TbPc)]$^-$ onto Au(111), with a focus on dissociated Pcs a) STM image of a large Au(111) terrace with multiple species highlighted, U_B=-0.7 V I_t=11.6 pA b-e) Zoomed images of each highlighted box, taken directly from a) all zoomed images scaled to the same size, with scale depicted in e)

deckers do not have such a strong affinity to the bridge sites, only to the pinched elbows.

Given that the [NO-Pc(TbPc)]^0 is heteroleptic, when it dissociates into two phthalocyanines, one would expect an equal ratio of Pcs with and without an NO group. By comparing Pcs in clusters and isolated Pcs, the ratio is ∼2:1 respectively. Presumably 50% of Pcs have an NO group, therefore by the simplest analysis, this would imply that 25% of the Pcs in clusters do not contain NO groups. 25% is not an immediately explainable number. Given that the specifics of the dissociation mechanism are unknown, it is not possible to assume that Pcs with an NO group and without are in an equal ratio.

7.2.5 Analysis of NO-Pc clusters

By analysing the structure of the clusters of single Pcs observed in Figure 7.6, one may learn more about the nature of the intermolecular interactions and, in particular, how the NO groups drive this organisation.

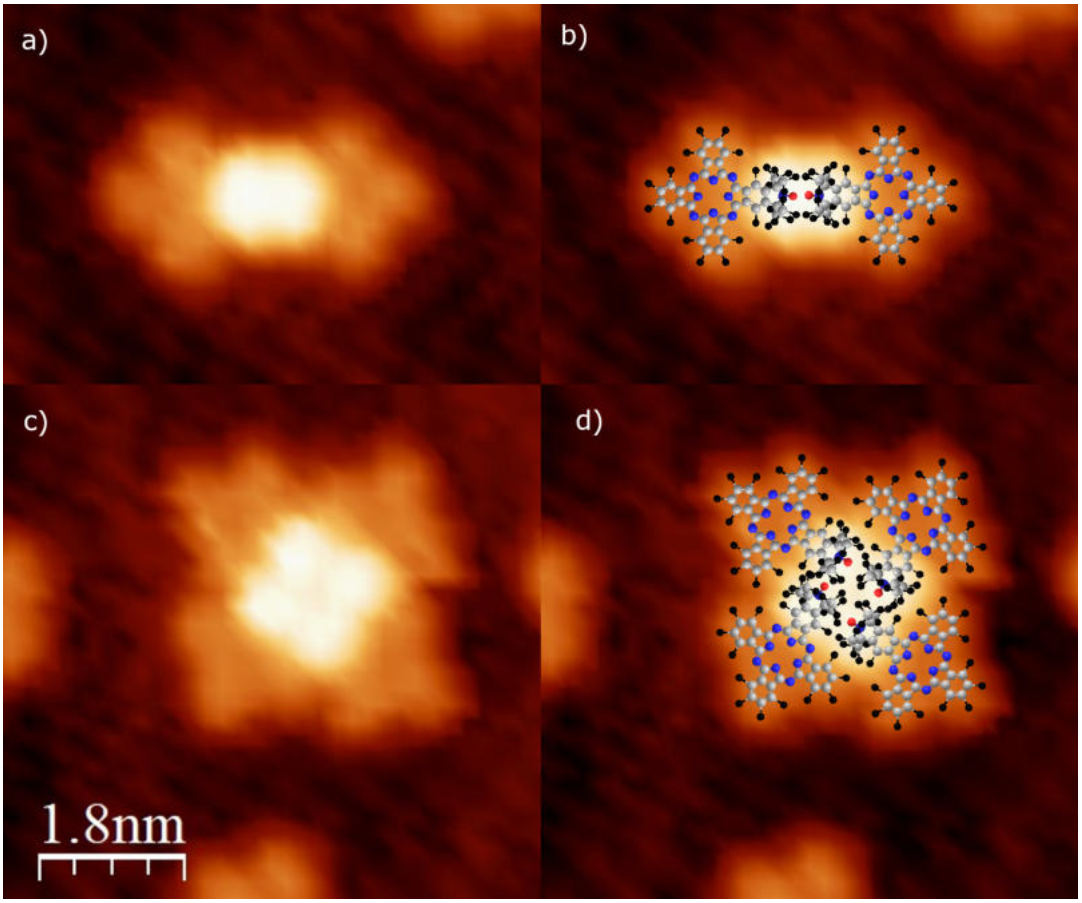

FIGURE 7.7: Modelling of phthalocyanines dissociated from [NO-Pc(TbPc)]^0 molecules deposited onto Au(111). a) Copy of image from Figure 7.6 c). b) image in a) with overlaid model. c) Copy of image from Figure 7.6 d). d) image in c) with overlaid model.

In Figure 7.7, a) a dimer of Pcs is observed, with a large protrusion connecting the two Pcs. The 'connection point' protrudes from the benzene ring, parallel to the arms of the cross structure. It is unclear if this dimerisation is due to one single NO

group or an interaction between two separate NO groups. However, the symmetrical appearance of the dimer through the cross structure implies that there are two NO groups involved. Figure 7.7 b) depicts a model overlaid onto the image in a), where the model is made assuming a Pc size of 1.73 nm using the Van der Waals radii of the H atoms, as discussed in Moeller et al. [271]. By analysing this model, it can be seen that in the two dimensional surface projection, the highly electronegative oxygens appear to overlap as well as the hydrogens. This is not likely since they are assumed to repel each other. If one of the oxygens pushes upwards and the other pushes downwards, the nitrogens and oxygen may interact alternately, creating a strong exchange interaction, likely driving the dimerisation observed on the surface.

From Figure 7.7 c), a tetramer of Pcs is observed, where again, a protrusion linking the Pcs is seen. This is likely to be four NO groups interacting, due to the linking points all protruding directly from the benzene ring where the NO group is located. Each NO group and cross structure is not lying directly opposite the opposing molecule, such as in a) and not perpendicular to adjacent molecules, creating a chiral windmill like structure. This is more clearly seen in the model in d). This rotation away from the perpendicular axes may be due to dipolar interactions between adjacent molecules rather than opposing molecules. The trimer observed in 7.6 e) also shows an irregular interaction by observation of the trimer structure. This variability in NO group coupled structures further proves that is likely a dipolar interaction, and is not chemical in nature. No comment can be made about any spin interaction due to any potential unpaired electrons, due to the limits of the data presented here.

7.2.6 Analysis of [NO-Pc(TbPc)]^0 clusters

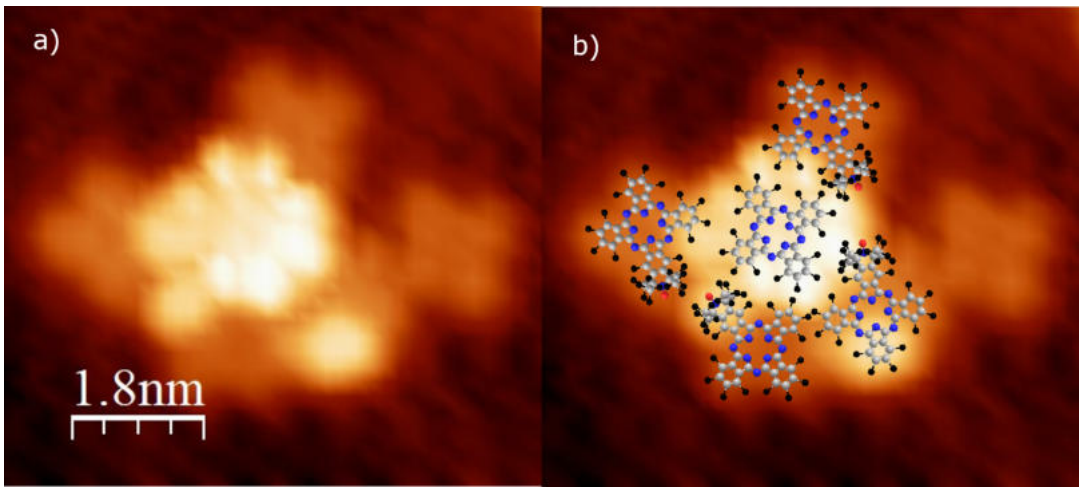

FIGURE 7.8: Modelling of a cluster from deposition of [NO-Pc(TbPc)]$^-$ onto Au(111) a) Zoom of the image taken from Figure 7.6 a). b) Copy of a) with model overlaid

Figure 7.8 a) shows a cluster of Pcs surrounding an intact [NO-Pc(TbPc)]^0. Given that no such structures are observed for the [TbPc$_2$]^0, these cluster formations are clearly stabilised by interactions between the NO groups. The NO must have some interaction with non-NO groups, for example hydrogens on the [NO-Pc(TbPc)]^0 molecule. From this image and various others, there does appear to be some protrusion on certain lobes of the [NO-Pc(TbPc)]^0. However, given that there is significant

overlap with single Pcs, one cannot interpret the same protrusions as for the isolated molecules from imaging alone.

Similar clusters were observed across the surface surrounded by randomly attached Pcs and additional contaminants. The Pc at the bottom of the image appears very close to colliding with the double decker. Observing the model in b), there is no overlap.

Figure 7.9 a) shows an example of a trimer of intact $[NO\text{-}Pc(TbPc)]^0$ surrounded by single Pcs. This is one example, but as seen in Figure 7.6 a), many similar clusters were found on the surface.

The Pcs clustering around the trimer appear to heavily overlap with the Pcs of the double decker. From an initial observation, it appears that the Pcs would not all fit into the bottom layer. In particular, the Pc at the bottom left of the image heavily intersects with the trimer structure. This apparent overlap is more severe than what was observed for the monocluster observed in Figure 7.8. Even considering the fact that this structure is three dimensional, the geometry is still highly confined. One may argue that this is not possible due to overlapping atoms, and that the brighter layer is not an intact double decker, but instead some alternate structure. One may offer an alternative structure that does not have such a confined geometry. For example, given that there is so much dissociation of double deckers into Pcs, it may be the case that these structures are re-formed from dissociated molecules in a new configuration, where the lower layer of Pcs is not aligned with the top layer, allowing for the multiple Pcs at the edge to fit geometrically. In order to understand the larger structures that will be observed later, one must confirm that these are in fact intact molecules, and not some complex re-arrangement of dissociated molecules.

Figure 7.9 b) is adapted from Amokrane et al. [14] with permission from the author. An image taken by Amokrane et al. of an island of $[TbPc_2]^0$ with the model presented in this thesis overlaid on top, where the same scaling of 1.73 nm for the width of the Pc is used to scale the model. From the model, there is evidently some overlap of hydrogens. It does appear that the structure does not fit, likely due to the difficulty in understanding a three dimensional structure projected onto a two dimensional image. Additionally, the free rotation of each molecule with respect to the adjacent molecule does allow the footprint of the structure to be optimised. Given that the islands of the $[TbPc_2]^0$ were measured as 1.43 nm in the compact phase, there must be some overlap of the 1.73 nm wide phthalocyanines.

From Figure 7.9 c), it seems that NO groups on the double decker could not fit into the lower layer, so are thus assumed to be in the second layer. Some protrusions may be seen, but again, it is not possible to define protrusions in these clusters, as any additional groups in the lower layer may not be visible in STM. Clearly the upper layer of Pcs fits well and there is no concern that this proposed structure is incorrect.

From Figure 7.9 d), the proposed positions of Pcs in the lower layer are depicted. The positioning was chosen based on the cross structure of the dissociated Pcs, but otherwise it was only modelled in such a way that overlap between molecules was reduced. Whilst many of the hydrogens are close to colliding, there is no direct overlap. Given that from b) some overlap in the projected model appears possible, this model or similar is likely. This structure is most likely a trimer of intact $[NO\text{-}Pc(TbPc)]^0$ molecules, surrounded by dissociated Pcs, and not some more complex structure made up of layers of recombined dissociated Pcs. Furthermore, the 8-lobe structure observed is very distinctive, no other molecular re-organisation would give such a specific structure, without alignment between the two layers of Pcs as seen for the intact molecule.

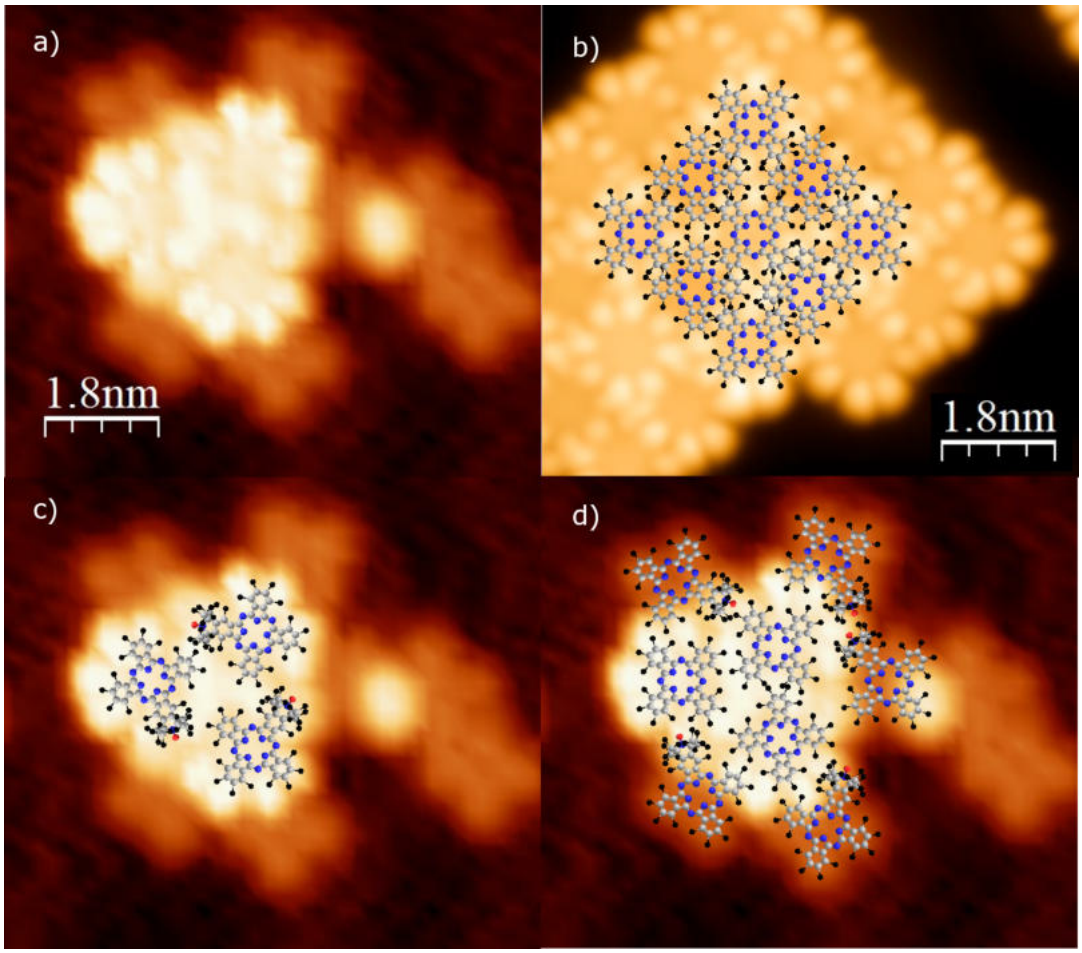

FIGURE 7.9: Modelling of a tricluster from a deposition of $[NO\text{-}Pc(TbPc)]^-$ onto Au(111) a) Zoom of image taken from Figure 7.6 a). b) Figure adapted from Amokrane et al. [14] with a model overlaid using the same calibration as other models in this chapter. c) Image in a) with an overlaid model of the upper layer of Pcs. d) Image in a) with an overlaid model of the lower layer of Pcs.

7.2.7 Analysis of islands of $[NO\text{-}Pc(TbPc)]^0$ molecules

Figure 7.10 a) shows an island of $[NO\text{-}Pc(TbPc)]^0$ on Au(111). The expected 8-lobe structure is observed but is especially pronounced at the edges of the layer. There is also some ring like structure observed at the confluence of four molecules. This island is distinct from the structure of the $[TbPc_2]^0$ and is likely an island of fully intact $[NO\text{-}Pc(TbPc)]^0$. Some smaller molecules are also observed at the edges of the layer and also seen in other images of layers. From the images of clusters of $[NO\text{-}Pc(TbPc)]^0$, they are assigned as dissociated single Pcs. The profile taken in Figure 7.10 c) shows the height of the $[NO\text{-}Pc(TbPc)]^0$ layer. From literature[188, 191, 194], and Figure 5.4, the expected height of an $[TbPc_2]^0$ layer is 3.5 Å. By taking an average of all imaged $[NO\text{-}Pc(TbPc)]^0$ layers, an average of 3.04±0.09 Å is measured, where the error is the standard deviation. The height of these islands correlates quite well to the smaller isolated molecules with the protrusions pointing upwards, as observed in Figure 7.3 a). There does not appear to be a mixture of species organising into islands, where 2 different height species were observed for isolated molecules. The ring like protrusions were also measured and found to have a height of 0.61±0.06 Å.

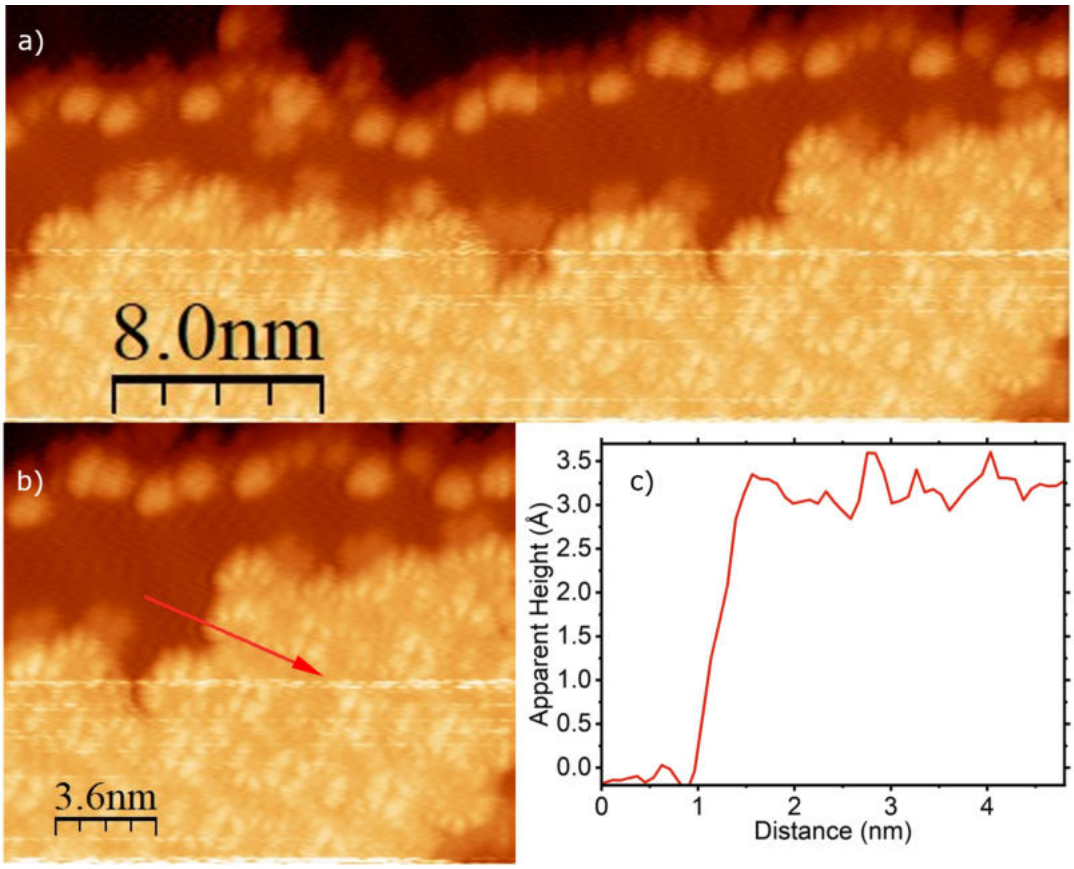

FIGURE 7.10: Line profile of an [NO-Pc(TbPc)]^0 island on Au(111). a) STM image of an [NO-Pc(TbPc)]^0 island surrounded by single Pcs, imaging parameters U_B=-1.8 mV I_t=19.9 pA. b) zoom of a) with line profile position in red. Profile taken from left to right. c) Apparent height profile of line in b).

This appears very similar to the upwards pointing protrusion.

The orientation of the heteroleptic [NO-Pc(TbPc)]^0 is not clear, i.e. it is uncertain if the Pc containing the NO group is only on the upper layer which is not in contact with the surface, or if the layer is some mixture of the two orientations. Assuming that the protrusions discussed in prior sections are due to the NO group pointing upwards, one may assume that all molecules are oriented so that the NO containing Pc is pointing upwards. Further supporting this, the height of the molecules in the island is uniform, and the height correlates well to this species. Given that these molecules can change between NO group orientations, intermolecular interactions in this island may force a specific orientation. However, for the lower coverage sample, the molecules with the protrusion pointing upwards and a lower apparent height were the dominant species. It may be that the larger islands are composed of this species and that this is the most common NO group orientation by a wide margin. This is surprising, as due to the higher interactivity of the NO-group, one would expect it to interact more heavily with the surface, as reported by [263]. This may imply that there is some oversight in the conclusions drawn here. One alternative explanation is that the molecules organised into islands are oriented with the NO-group in contact with the surface, and as such are the dominant species. Other surfaces with higher reactivity, such as copper, would allow a study of how these molecules interact with the surface.

These conclusions would need some further experimentation to be fully verified, but it is an interesting result that the NO group appears to force the orientation of the molecule. Potentially, this will allow one to control the orientation of double decker molecules in future studies.

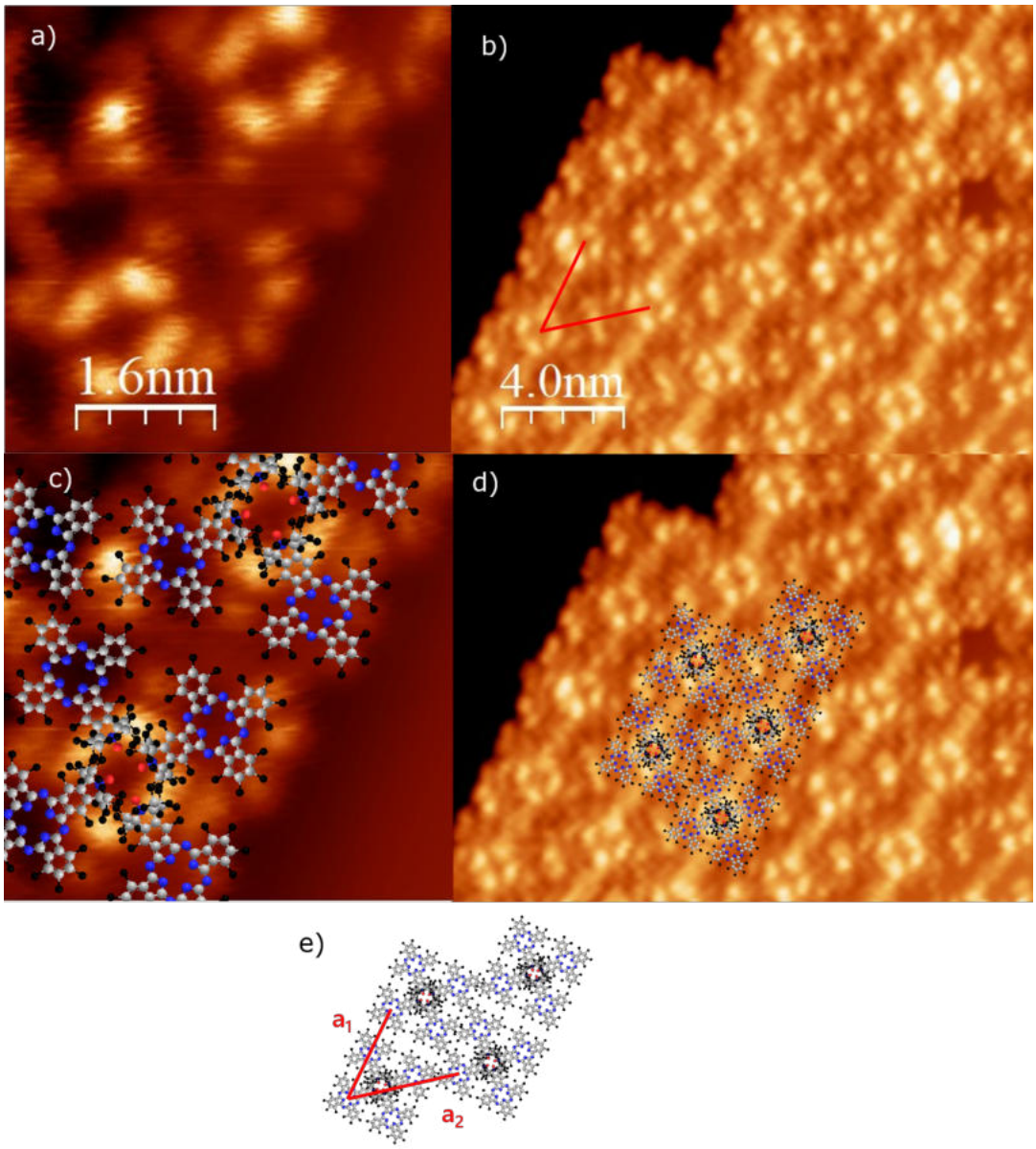

FIGURE 7.11: Higher resolution images of an [NO-Pc(TbPc)]^0 island on Au(111) with overlaid models. a) Constant height STM image of an [NO-Pc(TbPc)]^0 island. Imaged at U_B=-1 V b) Constant current image of an [NO-Pc(TbPc)]^0 island imaged in a), imaging parameters U_B=-770 mV I_t=24.6 pA c) Copy of image in a) with overlaid model of the second layer. d) Copy of the image in b) with overlaid model of the second layer. e) Model of the two dimensional crystal structure, with lattice vectors shown

Figure 7.11 depicts a higher resolution image of an island. To prevent interaction of the tip with the molecules, images of these islands were only taken in constant height mode, such as in Figure 7.11 a), or at higher tip speed, as in Figure 7.11 b). In these images, the ring structure appears clearer, allowing a discussion of its likely origin.

Figures 7.11 c) and d) depict models overlaid onto these higher resolution images. The model implies there is interaction between sets of four molecules. There does appear to be some overlap of hydrogens, but this is limited and is less significant than the overlap observed in Figure 7.9 b) from literature, showing that the model presented here is reasonable. In this model, it is assumed that all four upper layer molecules contain an NO group.

Figure 7.11 e) shows the crystal structure of this island, where the lattice parameters are a_1=3.15 nm and a_2=3.5 nm with an angle of 52° between the vectors. In this case, the basis is not a single molecule, but a tetramer of $[NO\text{-}Pc(TbPc)]^0$. This basis is most clear in c)

The parameters of the tetramer were a square lattice of 1.57±0.04 nm. By observing the periodicity of the ring structure in Figure 7.10 a), it has the same structure as the island displayed in Figure 7.11 e). The image in Figure 7.10 a) does appear to be regular.

From the model in 7.11 e), there is some chirality in the tetramer, similar to the Pc tetramer seen in Figure 7.7 c). The spacing of the Pc tetramer in 7.7 c) was 1.65 nm. As these values are so similar, it is likely that this interaction is of the same origin, which also implies that the interaction driving this island formation is due to the interaction of four NO groups.

From these molecular islands, there is a clear interaction between NO groups, as seen by the repeating 4x4 arrangement. It is not clear if these groups have reacted on the surface, quenching the radical property. If there is a reaction between radicals on the surface, one could suppress this interaction and reaction by performing colder depositions.

By studying various coverages of molecules, larger organisation of both intact $[NO\text{-}Pc(TbPc)]^0$ and single NO-Pcs were observed. From these varying organisations, it was found that the molecules heavily interact with each other via the NO groups. This supports strongly that the NO group is still interactive once reaching the surface.

Investigations of varying molecular coverages revealed extended assemblies of both intact $[NO\text{-}Pc(TbPc)]^0$ and isolated NO-Pc fragments. The observed densely packed clusters at higher coverages, highlight significant intermolecular interactions mediated by the NO groups. This pronounced tendency for NO-driven self-assembly provides compelling evidence that the NO ligands retain their chemical reactivity and electronic functionality post-deposition. Such interactions highlight the robustness of the NO groups' activity on the surface, however this needs further experimentation to draw certain conclusions.

7.2.8 Scanning tunnelling spectroscopy of $[NO\text{-}Pc(TbPc)]^0$

Due to the various physical forms of molecules on the surface, it was not possible to take reproducible spectra. Furthermore, as was discussed in Figures 7.5 and 7.4, the molecules can switch between measurements, which made acquisition of reproducible spectra challenging, given that there were so many possible conformations. As a result, no relevant conclusions can be made from the few spectra taken with some level of reproducibility. The only conclusion that can be drawn is that the spectra taken on $[NO\text{-}Pc(TbPc)]^0$ differ from that of the $[TbPc_2]^0$.

Measurements on the island of $[NO\text{-}Pc(TbPc)]^0$ were not attempted due to an issue where the precise location of spectroscopy was not possible to define.

In order to confirm the presence of the unpaired electron on the NO group, one method would be to measure a Kondo peak not attributed to the Pc. If one could

measure a Kondo peak with a differing Kondo temperature to that of the Pc, this may indicate an unpaired spin. An experimental issue made reproducible spectroscopy close to Fermi level impossible, therefore this remains an open question.

7.3 Conclusion

A deeper understanding of the use of the ESI-CIBD system for depositing stable intact radicals onto surfaces was achieved. Furthermore, a di-radical $[TbPc_2]^0$ molecule was studied on an Au(111) surface. From analysis of the mass to charge ratio of the $[NO\text{-}Pc(TbPc)]^0$ molecule measured with the ESI-CIBD system, it is clear that the molecule is singly charged, and it is highly likely that the unpaired electron is present on the NO group.

From some isolated molecules, protrusions most likely due to the NO groups were observed. These were uncommon and only observed when depositions of very low coverage were performed. These intact molecules were capable of switching between a number of NO group orientations, thus giving some supporting evidence that the molecule is still a diradical on the surface, due to a remaining unpaired electron on the NO group.

At higher coverages, the molecules interact strongly and form clusters. This strong interaction was assumed to be due to the NO groups, supporting that the molecule may be a diradical upon contact with the surface. Large islands of intact $[NO\text{-}Pc(TbPc)]^0$ where the NO groups clearly interact were found.

The molecules were found to switch between NO group orientations, implying that these ligands are still highly interactive. They were found to change in height, and the assigned NO group was found to switch between pointing upwards and pointing downwards.

Spectroscopic studies attempted to understand the electronic structure of these molecules but were inconsistent.

Some interesting progress towards depositing intact radicals on the surface has been achieved. The molecules certainly arrive to the surface as a radical, but it cannot be excluded that they are suppressed once they begin to interact on the surface.

For its potential application towards quantum information processing, the study of these molecules on the surface still needs significant further experimentation and development. The presence of the diradical has neither been proved nor disproved; therefore, it remains a possibility. From a more general perspective, the principle of depositing highly unstable molecules onto the surface was successful. The ESI is promising as a method to deposit highly reactive groups without quenching the radical property, opening many new possibilities for experiments outside the scope of the study discussed here.

Chapter 8

Conclusion

This thesis is concerned with the stable deposition of thermolabile molecules in UHV onto metals via the technique of electrospray deposition for study with STM. The molecules were charged in solution prior to electrospray. Mass spectra were taken of these molecules to verify their charge state and ensure that the intact molecule was carried into the gas phase in a UHV environment. These ions were subsequently deposited onto surfaces and imaged via STM. By imaging and manipulation of molecular structures using the STM tip, the molecular structures, conformations, and organisations were probed, analysed, and measured. Scanning tunneling spectroscopy was measured on some molecular structures, both as a method of characterisation and to study the Kondo effect.

The molecules of interest were derivatives of the $[TbPc_2]^0$ SMM base. Where the functionalisation of the molecule reduces the stability of the molecule relative to its evaporation temperature, thus making it thermolabile.

If one were to attempt deposition by sublimation, one would expect decomposition of the molecule. For the $[Tb(Et\text{-}Pc)_2]^0$ and $[Tb(Hex\text{-}Pc)_2]^0$, decomposition from sublimation was measured. This decomposition would lead to disorder upon the surface and possibly contamination of the chamber. Electrospray deposition circumvents these issues, allowing intact transfer of molecules traditionally deemed 'non-depositable' due to their thermal instability. This capability unlocks the study of surface architectures previously inaccessible via conventional methods.

The study of surface structures composed of thermolabile molecules was split into three distinct projects.

In the fifth chapter, the unsubstituted $[TbPc_2]^0$ was deposited using the ESI-CIBD system. Necessarily, the charge state of the molecule is altered during the spraying process. The viability of the ESI-CIBD system was confirmed by a comparative study of $[TbPc_2]^0$ deposition on the Au(111) surface for both ESD and sublimation based deposition. Despite radical quenching during charging for electrospray, the Kondo effect—arising from the unpaired electron delocalised over the Pc ligand was observed post-deposition via STS. This confirmed the restoration of the radical state on the surface, with electronic properties identical to sublimated samples. While fragmentation into Pc components occurred, it mirrored sublimation results, confirming ESI-CIBD's capability to deposit intact molecules. This method circumvents decomposition risks inherent to sublimation, enabling studies of thermolabile derivatives previously restricted to solid-liquid interfaces.

The sixth chapter discusses the deposition of functionalised $[TbPc_2]^0$ with ethyl ($[Tb(Et\text{-}Pc)_2]^0$) and hexyl ($[Tb(Hex\text{-}Pc)_2]^0$) substituents attached. This created tunable surface lattices, with lattice spacings increasing from 1.43 nm (compact $[TbPc_2]^0$)

to 1.76 nm ($[Tb(Et\text{-}Pc)_2]^0$) to 2.52 nm ($[Tb(Hex\text{-}Pc)_2]^0$). These semi-regular assemblies demonstrated the potential to modulate intermolecular distances for controlling magnetic interactions (e.g., exchange, RKKY). Challenges in imaging unconfined alkyl chains highlighted the need for heteroleptic designs. This advances the study of thermolabile systems in UHV environments.

Finally the 7th chapter discusses the deposition of diradical $[NO\text{-}Pc(TbPc)]^0$ revealed conformational switching of NO groups suggesting a radical property. High-coverage clusters exhibited strong intermolecular interactions, likely mediated by unpaired electrons, though spectroscopic confirmation was not successful. While the diradical's on-surface stability requires further validation, ESI-CIBD proved effective in delivering reactive species without quenching their electronic properties.

By combining electrospray deposition with STM/STS, this work bridges the gap between organic chemistry and surface science, enabling the study of fragile, functionalized molecules in well-defined environments. The findings highlight the potential of electrospray for depositing complex molecular systems and pave the way for exploring emergent quantum phenomena in surface-supported architectures.

Bibliography

[1] Thirunavukkarasu Thangavel et al. “Cooperative Spin-Crossover in a Neutral Dinuclear Complex Based on a Functionalized Triazole Ligand”. In: *Crystal Growth & Design* 25.8 (Apr. 2025). Publisher: American Chemical Society, pp. 2674–2682. ISSN: 1528-7483. DOI: 10.1021/acs.cgd.5c00158. URL: https://doi.org/10.1021/acs.cgd.5c00158.

[2] Víctor García-López et al. “Heteroleptic Iron(II) Spin-Crossover Complexes Based on a 2,6-Bis(pyrazol-1-yl)pyridine-type Ligand Functionalized with a Carboxylic Acid”. In: *Inorganic Chemistry* 58.18 (Sept. 2019). Publisher: American Chemical Society, pp. 12199–12208. ISSN: 0020-1669. DOI: 10.1021/acs.inorgchem.9b01526. URL: https://doi.org/10.1021/acs.inorgchem.9b01526.

[3] Daniel Vidal, Jordi Cirera, and Jordi Ribas-Arino. “Fine-tuning of the spin-crossover properties of Fe(III) complexes via ligand design”. en. In: *Physical Chemistry Chemical Physics* 25.17 (May 2023). Publisher: The Royal Society of Chemistry, pp. 12490–12499. ISSN: 1463-9084. DOI: 10.1039/D3CP00250K. URL: https://pubs.rsc.org/en/content/articlelanding/2023/cp/d3cp00250k.

[4] Laia Navarro, Fileto Rodriguez, and Jordi Cirera. “Controlling the spin-crossover behavior of the [Cr(indenyl)2] family via ligand functionalization”. en. In: *Dalton Transactions* 50.25 (June 2021). Publisher: The Royal Society of Chemistry, pp. 8704–8710. ISSN: 1477-9234. DOI: 10.1039/D1DT00481F. URL: https://pubs.rsc.org/en/content/articlelanding/2021/dt/d1dt00481f.

[5] Naoki Ogiwara et al. “Ligand-Functionalization-Controlled Activity of Metal–Organic Framework-Encapsulated Pt Nanocatalyst toward Activation of Water”. In: *Nano Letters* 20.1 (Jan. 2020). Publisher: American Chemical Society, pp. 426–432. ISSN: 1530-6984. DOI: 10.1021/acs.nanolett.9b04124. URL: https://doi.org/10.1021/acs.nanolett.9b04124.

[6] Swetlana Schauermann et al. “Ligand-functionalized surfaces for chemoselective heterogeneous catalysis”. In: *Surface Science* 748 (Oct. 2024), p. 122539. ISSN: 0039-6028. DOI: 10.1016/j.susc.2024.122539. URL: https://www.sciencedirect.com/science/article/pii/S0039602824000906.

[7] Macarena G. Alférez et al. “Ligand Postsynthetic Functionalization with Fluorinated Boranes and Implications in Hydrogenation Catalysis”. In: *ACS Catalysis* 13.24 (Dec. 2023). Publisher: American Chemical Society, pp. 16055–16066. DOI: 10.1021/acscatal.3c02764. URL: https://doi.org/10.1021/acscatal.3c02764.

[8] Wenlei Zhang et al. "Exploring the Fundamental Roles of Functionalized Ligands in Platinum@Metal–Organic Framework Catalysts". In: *ACS Applied Materials & Interfaces* 12.47 (Nov. 2020). Publisher: American Chemical Society, pp. 52660–52667. ISSN: 1944-8244. DOI: 10.1021/acsami.0c15340. URL: https://doi.org/10.1021/acsami.0c15340.

[9] Alexander C. Fischer et al. "A Blessing and a Curse: Remote Ligand Functionalization Modulates 3MLCT Relaxation in Group 6 Tricarbonyl Complexes". In: *Inorganic Chemistry* 64.12 (Mar. 2025). Publisher: American Chemical Society, pp. 6100–6114. ISSN: 0020-1669. DOI: 10.1021/acs.inorgchem.4c05383. URL: https://doi.org/10.1021/acs.inorgchem.4c05383.

[10] Andrea Caneschi et al. "Alternating current susceptibility, high field magnetization, and millimeter band EPR evidence for a ground S = 10 state in [Mn12O12(Ch3COO)16(H2O)4].2CH3COOH.4H2O". In: *Journal of the American Chemical Society* 113.15 (July 1991). Publisher: American Chemical Society, pp. 5873–5874. ISSN: 0002-7863. DOI: 10.1021/ja00015a057. URL: https://doi.org/10.1021/ja00015a057.

[11] Matteo Mannini et al. "Magnetic behaviour of TbPc2 single-molecule magnets chemically grafted on silicon surface". en. In: *Nature Communications* 5.1 (Aug. 2014). Publisher: Nature Publishing Group, p. 4582. ISSN: 2041-1723. DOI: 10.1038/ncomms5582. URL: https://www.nature.com/articles/ncomms5582.

[12] Tadahiro Komeda et al. "Observation and electric current control of a local spin in a single-molecule magnet". en. In: *Nature Communications* 2.1 (Mar. 2011). Publisher: Nature Publishing Group, p. 217. ISSN: 2041-1723. DOI: 10.1038/ncomms1210. URL: https://www.nature.com/articles/ncomms1210.

[13] Tadahiro Komeda et al. "Variation of Kondo Temperature Induced by Molecule–Substrate Decoupling in Film Formation of Bis(phthalocyaninato)terbium(III) Molecules on Au(111)". In: *ACS Nano* 8.5 (May 2014). Publisher: American Chemical Society, pp. 4866–4875. ISSN: 1936-0851. DOI: 10.1021/nn500809v. URL: https://doi.org/10.1021/nn500809v.

[14] Anis Amokrane et al. "Role of -Radicals in the Spin Connectivity of Clusters and Networks of Tb Double-Decker Single Molecule Magnets". In: *ACS Nano* 11.11 (Oct. 2017). MAG ID: 2762999442 S2ID: 7cb727801849dffe5af4b18481220469195a72f2, pp. 10750–10760. DOI: 10.1021/acsnano.7b05804.

[15] Rabei Barhoumi et al. "Screening the 4f-electron spin of TbPc2 single-molecule magnets on metal substrates by ligand channeling". en. In: *Nanoscale* 11.44 (Nov. 2019). Publisher: The Royal Society of Chemistry, pp. 21167–21179. ISSN: 2040-3372. DOI: 10.1039/C9NR05873G. URL: https://pubs.rsc.org/en/content/articlelanding/2019/nr/c9nr05873g.

[16] Paniz Rahmani et al. "One-Step Ligand-Exchange Method to Produce Quantum Dot–DNA Conjugates for DNA-Directed Self-Assembly". In: *ACS Applied Materials & Interfaces* 14.42 (Oct. 2022). Publisher: American Chemical Society, pp. 47359–47368. ISSN: 1944-8244. DOI: 10.1021/acsami.2c10580. URL: https://doi.org/10.1021/acsami.2c10580.

[17] Ritesh Haldar et al. "Oxidative polymerization of terthiophene and a substituted thiophene monomer in metal-organic framework thin films". In: *European Polymer Journal* 109 (Dec. 2018), pp. 162–168. ISSN: 0014-3057. DOI: 10.1016/j.eurpolymj.2018.09.040. URL: https://www.sciencedirect.com/science/article/pii/S0014305718314113.

[18] Weijin Li et al. "Advanced Bifunctional Oxygen Reduction and Evolution Electrocatalyst Derived from Surface-Mounted Metal–Organic Frameworks". en. In: *Angewandte Chemie International Edition* 59.14 (2020). _eprint: https://onlinelibrary.wiley.com/doi/pdf/10.1002/anie.201916507, pp. 5837–5843. ISSN: 1521-3773. DOI: 10.1002/anie.201916507. URL: https://onlinelibrary.wiley.com/doi/abs/10.1002/anie.201916507.

[19] Weijin Li et al. "Unprecedented High Oxygen Evolution Activity of Electrocatalysts Derived from Surface-Mounted Metal–Organic Frameworks". In: *Journal of the American Chemical Society* 141.14 (Apr. 2019). Publisher: American Chemical Society, pp. 5926–5933. ISSN: 0002-7863. DOI: 10.1021/jacs.9b00549. URL: https://doi.org/10.1021/jacs.9b00549.

[20] Shargeel Ahmad et al. "MetalOrganic Framework Thin Film-Based Dye Sensitized Solar Cells with Enhanced Photocurrent". eng. In: *Materials (Basel, Switzerland)* 11.10 (Oct. 2018), p. 1868. ISSN: 1996-1944. DOI: 10.3390/ma11101868.

[21] Ming-Shui Yao et al. "Layer-by-Layer Assembled Conductive Metal–Organic Framework Nanofilms for Room-Temperature Chemiresistive Sensing". en. In: *Angewandte Chemie International Edition* 56.52 (2017). _eprint: https://onlinelibrary.wiley.com/doi/pdf/10.1002/anie.201709558, pp. 16510–16514. ISSN: 1521-3773. DOI: 10.1002/anie.201709558. URL: https://onlinelibrary.wiley.com/doi/abs/10.1002/anie.201709558.

[22] Yuan Lin et al. "Layer-by-Layer Growth of Preferred-Oriented MOF Thin Film on Nanowire Array for High-Performance Chemiresistive Sensing". en. In: *Angewandte Chemie International Edition* 60.49 (2021). _eprint: https://onlinelibrary.wiley.com/doi/pdf/10.1002/anie.202111519, pp. 25758–25761. ISSN: 1521-3773. DOI: 10.1002/anie.202111519. URL: https://onlinelibrary.wiley.com/doi/abs/10.1002/anie.202111519.

[23] Xin Chen et al. "Charge. transport, conductivity and Seebeck coefficient in pristine and TCNQ loaded preferentially grown metal-organic framework films". eng. In: *Journal of Physics. Condensed Matter: An Institute of Physics Journal* 34.40 (Aug. 2022). ISSN: 1361-648X. DOI: 10.1088/1361-648X/abe72f.

[24] J. Christopher Love et al. "Self-assembled monolayers of thiolates on metals as a form of nanotechnology". eng. In: *Chemical Reviews* 105.4 (Apr. 2005), pp. 1103–1169. ISSN: 0009-2665. DOI: 10.1021/cr0300789.

[25] Makoto Fujita. "Metal-directed self-assembly of two- and three-dimensional synthetic receptors". en. In: *Chemical Society Reviews* 27.6 (Jan. 1998). Publisher: The Royal Society of Chemistry, pp. 417–425. ISSN: 1460-4744. DOI: 10.1039/A827417Z. URL: https://pubs.rsc.org/en/content/articlelanding/1998/cs/a827417z.

[26] Koji Miyake et al. "Alkyl chain length dependence of the self-organized structure of alkyl-substituted phthalocyanines." In: *Langmuir* 24.9 (Apr. 2008). MAG ID: 1992411916 S2ID: e7acc889dcca32d003fbb7360f3a137e7bfe5dd1, pp. 4708–4714. DOI: 10.1021/la702564m.

[27] J. A. Sánchez-García et al. "Tuning the surface morphology in self-organized ion beam nanopatterning of Si(001) via metal incorporation: from holes to dots". eng. In: *Nanotechnology* 19.35 (Sept. 2008), p. 355306. ISSN: 0957-4484. DOI: 10.1088/0957-4484/19/35/355306.

[28] B. Cirera et al. "Preservation of electronic properties of double-decker complexes on metallic supports". en. In: *Physical Chemistry Chemical Physics* 19.12 (2017). Publisher: Royal Society of Chemistry, pp. 8282–8287. DOI: 10.1039/C6CP08239D. URL: https://pubs.rsc.org/en/content/articlelanding/2017/cp/c6cp08239d.

[29] Borja Cirera et al. "Thermal selectivity of intermolecular versus intramolecular reactions on surfaces". en. In: *Nature Communications* 7.1 (Mar. 2016). Publisher: Nature Publishing Group, p. 11002. ISSN: 2041-1723. DOI: 10.1038/ncomms11002. URL: https://www.nature.com/articles/ncomms11002.

[30] D. X. Shi et al. "Role of Lateral Alkyl Chains in Modulation of Molecular Structures on Metal Surfaces". In: *Physical Review Letters* 96.22 (June 2006). Publisher: American Physical Society, p. 226101. DOI: 10.1103/PhysRevLett.96.226101. URL: https://link.aps.org/doi/10.1103/PhysRevLett.96.226101.

[31] Tadahiro Komeda et al. "Variation of Kondo Peak Observed in the Assembly of Heteroleptic 2,3-Naphthalocyaninato Phthalocyaninato Tb(III) Double-Decker Complex on Au(111)". In: *ACS Nano* 7.2 (Feb. 2013). Publisher: American Chemical Society, pp. 1092–1099. ISSN: 1936-0851. DOI: 10.1021/nn304035h. URL: https://doi.org/10.1021/nn304035h.

[32] Andreas Walz. "Compact and versatile electrospray - controlled ion beam deposition with adjustable frequency RF ion guides and extended mass range". en. In: (2020).

[33] Andreas Walz et al. "Navigate Flying Molecular Elephants Safely to the Ground: Mass-Selective Soft Landing up to the Mega-Dalton Range by Electrospray Controlled Ion-Beam Deposition". In: *Analytical Chemistry* 94.22 (June 2022). Publisher: American Chemical Society, pp. 7767–7778. ISSN: 0003-2700. DOI: 10.1021/acs.analchem.1c04495. URL: https://doi.org/10.1021/acs.analchem.1c04495.

[34] Stephan Rauschenbach et al. "Electrospray Ion Beam Deposition: Soft-Landing and Fragmentation of Functional Molecules at Solid Surfaces". In: *ACS Nano* 3.10 (Oct. 2009). Publisher: American Chemical Society, pp. 2901–2910. ISSN: 1936-0851. DOI: 10.1021/nn900022p. URL: https://doi.org/10.1021/nn900022p.

[35] Kelvin Anggara et al. "Landing Proteins on Graphene Trampoline Preserves Their Gas-Phase Folding on the Surface". In: *ACS Central Science* 9.2 (Feb. 2023). Publisher: American Chemical Society, pp. 151–158. ISSN: 2374-7943. DOI: 10.1021/acscentsci.2c00815. URL: https://doi.org/10.1021/acscentsci.2c00815.

[36] X. Wu et al. "Imaging single glycans". en. In: *Nature* 582.7812 (June 2020). Publisher: Nature Publishing Group, pp. 375–378. ISSN: 1476-4687. DOI: 10.1038/s41586-020-2362-1. URL: https://www.nature.com/articles/s41586-020-2362-1.

[37] Kelvin Anggara et al. "Direct observation of glycans bonded to proteins and lipids at the single-molecule level". In: *Science* 382.6667 (Oct. 2023). Publisher: American Association for the Advancement of Science, pp. 219–223. DOI: 10.1126/science.adh3856. URL: https://www.science.org/doi/10.1126/science.adh3856.

[38] Wei Ran et al. "Depositing Molecular Graphene Nanoribbons on Ag(111) by Electrospray Controlled Ion Beam Deposition: Self-Assembly and On-Surface Transformations". en. In: *Angewandte Chemie International Edition* 61.14 (2022). _eprint: https://onlinelibrary.wiley.com/doi/pdf/10.1002/anie.202111816, e202111816. ISSN: 1521-3773. DOI: 10.1002/anie.202111816. URL: https://onlinelibrary.wiley.com/doi/abs/10.1002/anie.202111816.

[39] Xuejiao Zhang et al. "Controlled Formation of Nanoribbons and Their Heterostructures via Assembly of Mass-Selected Inorganic Ions". en. In: *Advanced Materials* 36.23 (2024). _eprint: https://onlinelibrary.wiley.com/doi/pdf/10.1002/adma.202310817, p. 2310817. ISSN: 1521-4095. DOI: 10.1002/adma.202310817. URL: https://onlinelibrary.wiley.com/doi/abs/10.1002/adma.202310817.

[40] Dennis Schäfter et al. "Molecular One- and Two-Qubit Systems with Very Long Coherence Times". en. In: *Advanced Materials* 35.38 (2023). _eprint: https://onlinelibrary.wiley.com/doi/pdf/10.1002/adma.202302114, p. 2302114. ISSN: 1521-4095. DOI: 10.1002/adma.202302114. URL: https://onlinelibrary.wiley.com/doi/abs/10.1002/adma.202302114.

[41] S. L. Bayliss et al. "Optically addressable molecular spins for quantum information processing". In: *Science* 370.6522 (Dec. 2020). Publisher: American Association for the Advancement of Science, pp. 1309–1312. DOI: 10.1126/science.abb9352. URL: https://www.science.org/doi/10.1126/science.abb9352.

[42] Nathanael P. Kazmierczak, Ruben Mirzoyan, and Ryan G. Hadt. "The Impact of Ligand Field Symmetry on Molecular Qubit Coherence". In: *Journal of the American Chemical Society* 143.42 (Oct. 2021). Publisher: American Chemical Society, pp. 17305–17315. ISSN: 0002-7863. DOI: 10.1021/jacs.1c04605. URL: https://doi.org/10.1021/jacs.1c04605.

[43] Aimei Zhou, Zhecheng Sun, and Lei Sun. "Stable organic radical qubits and their applications in quantum information science". In: *The Innovation* 5.5 (Sept. 2024), p. 100662. ISSN: 2666-6758. DOI: 10.1016/j.xinn.2024.100662. URL: https://www.sciencedirect.com/science/article/pii/S2666675824001000.

[44] Akio Yamauchi et al. "Modulation of triplet quantum coherence by guest-induced structural changes in a flexible metal-organic framework". en. In: *Nature Communications* 15.1 (Sept. 2024). Publisher: Nature Publishing Group, p. 7622. ISSN: 2041-1723. DOI: 10.1038/s41467-024-51715-w. URL: https://www.nature.com/articles/s41467-024-51715-w.

[45] Akio Yamauchi et al. “Room-temperature quantum coherence of entangled multiexcitons in a metal-organic framework”. In: *Science Advances* 10.1 (Jan. 2024). Publisher: American Association for the Advancement of Science, eadi3147. DOI: 10.1126/sciadv.adi3147. URL: https://www.science.org/doi/10.1126/sciadv.adi3147.

[46] Richard P. Feynman. “Quantum mechanical computers”. en. In: *Foundations of Physics* 16.6 (June 1986), pp. 507–531. ISSN: 1572-9516. DOI: 10.1007/BF01886518. URL: https://doi.org/10.1007/BF01886518.

[47] Richard P. Feynman. “Simulating physics with computers”. en. In: *International Journal of Theoretical Physics* 21.6 (June 1982), pp. 467–488. ISSN: 1572-9575. DOI: 10.1007/BF02650179. URL: https://doi.org/10.1007/BF02650179.

[48] Rebecca Schwerdt. *Sender-binding Encryption : Towards Finding the Weakest Encryption Security to Realise Secure Communication*. de. 2025. DOI: 10.5445/IR/1000181209. URL: https://publikationen.bibliothek.kit.edu/1000181209.

[49] Robin M. Berger et al. “Composable Long-Term Security with Rewinding”. de. In: *Theory of Cryptography. 21th International Conference, TCC 2023. Proceedings, Part 1. Ed.: G. Rothblum*. ISSN: 0302-9743. 2023. ISBN: 978-3-031-48614-2. URL: https://publikationen.bibliothek.kit.edu/1000163188.

[50] Anthony Paul. “The Impact of Quantum Computing on Cryptographic Systems”. In: (May 2024).

[51] Anton Robert et al. “Resource-efficient quantum algorithm for protein folding”. en. In: *npj Quantum Information* 7.1 (Feb. 2021). Publisher: Nature Publishing Group, pp. 1–5. ISSN: 2056-6387. DOI: 10.1038/s41534-021-00368-4. URL: https://www.nature.com/articles/s41534-021-00368-4.

[52] Hakan Doga et al. “A Perspective on Protein Structure Prediction Using Quantum Computers”. In: *Journal of Chemical Theory and Computation* 20.9 (May 2024). Publisher: American Chemical Society, pp. 3359–3378. ISSN: 1549-9618. DOI: 10.1021/acs.jctc.4c00067. URL: https://doi.org/10.1021/acs.jctc.4c00067.

[53] Hsin-Yuan Huang et al. “Quantum advantage in learning from experiments”. en. In: *Science* 376.6598 (June 2022). arXiv:2112.00778 [quant-ph], pp. 1182–1186. ISSN: 0036-8075, 1095-9203. DOI: 10.1126/science.abn7293. URL: http://arxiv.org/abs/2112.00778.

[54] Kazuyuki Ishii. “Functional singlet oxygen generators based on phthalocyanines”. In: *Coordination Chemistry Reviews*. 19th International Symposium on the Photophysics and Photochemistry of Coordination Compounds 256.15 (Aug. 2012), pp. 1556–1568. ISSN: 0010-8545. DOI: 10.1016/j.ccr.2012.03.022. URL: https://www.sciencedirect.com/science/article/pii/S0010854512000628.

[55] Xian-Fu Zhang et al. “Synthesis, fluorescence, excited triplet state properties and singlet oxygen generation of *para*-(*tert*-butylphenoxy) substituted phthalocyanines containing group IV A central elements”. In: *Dyes and Pigments* 99.2 (Nov. 2013), pp. 480–488. ISSN: 0143-7208. DOI:

10.1016/j.dyepig.2013.06.010. URL: https://www.sciencedirect.com/science/article/pii/S0143720813002246.

[56] Xingshu Li et al. "New application of phthalocyanine molecules: from photodynamic therapy to photothermal therapy by means of structural regulation rather than formation of aggregates". en. In: *Chemical Science* 9.8 (Feb. 2018). Publisher: The Royal Society of Chemistry, pp. 2098–2104. ISSN: 2041-6539. DOI: 10.1039/C7SC05115H. URL: https://pubs.rsc.org/en/content/articlelanding/2018/sc/c7sc05115h.

[57] George W. Gokel and Len Barbour. *Comprehensive Supramolecular Chemistry II*. en. Google-Books-ID: BOlGDgAAQBAJ. Elsevier, June 2017. ISBN: 978-0-12-803199-5.

[58] M. F. Craciun et al. "Electronic Transport through Electron-Doped Metal Phthalocyanine Materials". In: *Advanced Materials* 18.3 (2006). _eprint: https://onlinelibrary.wiley.com/doi/pdf/10.1002/adma.200501268, pp. 320–324. ISSN: 1521-4095. DOI: 10.1002/adma.200501268. URL: https://onlinelibrary.wiley.com/doi/abs/10.1002/adma.200501268.

[59] "Volumes in This Set". In: *The Porphyrin Handbook*. Ed. by Karl M. Kadish, Kevin M. Smith, and Roger Guilard. Amsterdam: Academic Press, Jan. 2003, p. ii. ISBN: 978-0-08-092391-8. DOI: 10.1016/B978-0-08-092391-8.50001-7. URL: https://www.sciencedirect.com/science/article/pii/B9780080923918500017.

[60] Avery P. Yuen et al. "Photovoltaic properties of M-phthalocyanine/fullerene organic solar cells". In: *Solar Energy* 86 (June 2012). ADS Bibcode: 2012SoEn...86.1683Y, pp. 1683–1688. ISSN: 0038-092X. DOI: 10.1016/j.solener.2012.03.019. URL: https://ui.adsabs.harvard.edu/abs/2012SoEn...86.1683Y.

[61] Dieter Wöhrle and Dieter Meissner. "Organic Solar Cells". In: *Advanced Materials* 3.3 (1991). _eprint: https://onlinelibrary.wiley.com/doi/pdf/10.1002/adma.19910030303, pp. 129–138. ISSN: 1521-4095. DOI: 10.1002/adma.19910030303. URL: https://onlinelibrary.wiley.com/doi/abs/10.1002/adma.19910030303.

[62] D. Schlettwein et al. "Light-induced dioxygen reduction at thin film electrodes of various porphyrins". In: *The Journal of Physical Chemistry* 95.4 (Feb. 1991). Publisher: American Chemical Society, pp. 1748–1755. ISSN: 0022-3654. DOI: 10.1021/j100157a049. URL: https://doi.org/10.1021/j100157a049.

[63] Nawal Sekkat et al. "Like a Bolt from the Blue: Phthalocyanines in Biomedical Optics". en. In: *Molecules* 17.1 (Jan. 2012). Number: 1 Publisher: Molecular Diversity Preservation International, pp. 98–144. ISSN: 1420-3049. DOI: 10.3390/molecules17010098. URL: https://www.mdpi.com/1420-3049/17/1/98.

[64] Zhou Jiang et al. "Pharmaceutical development, composition and quantitative analysis of phthalocyanine as the photosensitizer for cancer photodynamic therapy". In: *Journal of Pharmaceutical and Biomedical Analysis*. Review Papers on Pharmaceutical and Biomedical Analysis 2013 87 (Jan. 2014), pp. 98–104. ISSN: 0731-7085. DOI: 10.1016/j.jpba.2013.05.014. URL: https://www.sciencedirect.com/science/article/pii/S073170851300215X.

[65] Gheorghe Taran et al. “Thermalization of Nuclear Spins in Lanthanide Molecular Magnets”. In: *Inorganic Chemistry* 62.22 (June 2023). Publisher: American Chemical Society, pp. 8598–8604. ISSN: 0020-1669. DOI: 10.1021/acs.inorgchem.3c00530. URL: https://doi.org/10.1021/acs.inorgchem.3c00530.

[66] International Union of Pure and Applied Chemistry (IUPAC). *radical (free radical)*. DOI: 10.1351/goldbook.R05066. URL: https://doi.org/10.1351/goldbook.R05066.

[67] Cristiano Benelli and Dante Gatteschi. *Introduction to Molecular Magnetism: From Transition Metals to Lanthanides*. Journal Abbreviation: Introduction to Molecular Magnetism: From Transition Metals to Lanthanides Pages: 450 Publication Title: Introduction to Molecular Magnetism: From Transition Metals to Lanthanides. Apr. 2015. ISBN: 978-3-527-33540-4. DOI: 10.1002/9783527690541.

[68] Naoto Ishikawa et al. “Lanthanide Double-Decker Complexes Functioning as Magnets at the Single-Molecular Level”. In: *Journal of the American Chemical Society* 125.29 (July 2003). Publisher: American Chemical Society, pp. 8694–8695. ISSN: 0002-7863. DOI: 10.1021/ja029629n. URL: https://doi.org/10.1021/ja029629n.

[69] Naoto Ishikawa et al. “Upward temperature shift of the intrinsic phase lag of the magnetization of Bis(phthalocyaninato)terbium by ligand oxidation creating an S = 1/2 spin”. eng. In: *Inorganic Chemistry* 43.18 (Sept. 2004), pp. 5498–5500. ISSN: 0020-1669. DOI: 10.1021/ic049348b.

[70] Romain Vincent et al. “Electronic read-out of a single nuclear spin using a molecular spin transistor”. en. In: *Nature* 488.7411 (Aug. 2012). Publisher: Nature Publishing Group, pp. 357–360. ISSN: 1476-4687. DOI: 10.1038/nature11341. URL: https://www.nature.com/articles/nature11341.

[71] Stefan Thiele et al. “Electrically driven nuclear spin resonance in single-molecule magnets”. In: *Science* 344.6188 (June 2014). Publisher: American Association for the Advancement of Science, pp. 1135–1138. DOI: 10.1126/science.1249802. URL: https://www.science.org/doi/10.1126/science.1249802.

[72] David P. DiVincenzo. *Topics in Quantum Computers*. en. arXiv:cond-mat/9612126. Dec. 1996. DOI: 10.48550/arXiv.cond-mat/9612126. URL: http://arxiv.org/abs/cond-mat/9612126.

[73] T. D. Ladd et al. “Quantum computers”. en. In: *Nature* 464.7285 (Mar. 2010). Publisher: Nature Publishing Group, pp. 45–53. ISSN: 1476-4687. DOI: 10.1038/nature08812. URL: https://www.nature.com/articles/nature08812.

[74] F. Dolde et al. “Electric-field sensing using single diamond spins”. en. In: *Nature Physics* 7.6 (June 2011). Publisher: Nature Publishing Group, pp. 459–463. ISSN: 1745-2481. DOI: 10.1038/nphys1969. URL: https://www.nature.com/articles/nphys1969.

[75] R. Hanson, O. Gywat, and D. D. Awschalom. "Room-temperature manipulation and decoherence of a single spin in diamond". In: *Physical Review B* 74.16 (Oct. 2006). Publisher: American Physical Society, p. 161203. DOI: 10.1103/PhysRevB.74.161203. URL: https://link.aps.org/doi/10.1103/PhysRevB.74.161203.

[76] Michal Gulka et al. "Room-temperature control and electrical readout of individual nitrogen-vacancy nuclear spins". en. In: *Nature Communications* 12.1 (July 2021). Publisher: Nature Publishing Group, p. 4421. ISSN: 2041-1723. DOI: 10.1038/s41467-021-24494-x. URL: https://www.nature.com/articles/s41467-021-24494-x.

[77] Floor van Riggelen-Doelman et al. "Coherent spin qubit shuttling through germanium quantum dots". en. In: *Nature Communications* 15.1 (July 2024). Publisher: Nature Publishing Group, p. 5716. ISSN: 2041-1723. DOI: 10.1038/s41467-024-49358-y. URL: https://www.nature.com/articles/s41467-024-49358-y.

[78] A. M. J. Zwerver et al. "Qubits made by advanced semiconductor manufacturing". en. In: *Nature Electronics* 5.3 (Mar. 2022). Publisher: Nature Publishing Group, pp. 184–190. ISSN: 2520-1131. DOI: 10.1038/s41928-022-00727-9. URL: https://www.nature.com/articles/s41928-022-00727-9.

[79] Davide Castelvecchi. "Welcome anyons! Physicists find best evidence yet for long-sought 2D structures". en. In: *Nature* 583.7815 (July 2020). Bandiera_abtest: a Cg_type: News Publisher: Nature Publishing Group Subject_term: Condensed-matter physics, Quantum physics, Quantum information, pp. 176–177. DOI: 10.1038/d41586-020-01988-0. URL: https://www.nature.com/articles/d41586-020-01988-0.

[80] A. Yu. Kitaev. "Fault-tolerant quantum computation by anyons". In: *Annals of Physics* 303.1 (Jan. 2003), pp. 2–30. ISSN: 0003-4916. DOI: 10.1016/S0003-4916(02)00018-0. URL: https://www.sciencedirect.com/science/article/pii/S0003491602000180.

[81] Frank Arute et al. "Quantum supremacy using a programmable superconducting processor". en. In: *Nature* 574.7779 (Oct. 2019). Publisher: Nature Publishing Group, pp. 505–510. ISSN: 1476-4687. DOI: 10.1038/s41586-019-1666-5. URL: https://www.nature.com/articles/s41586-019-1666-5.

[82] Dongxin Gao et al. "Establishing a New Benchmark in Quantum Computational Advantage with 105-qubit Zuchongzhi 3.0 Processor". In: *Physical Review Letters* 134.9 (Mar. 2025). Publisher: American Physical Society, p. 090601. DOI: 10.1103/PhysRevLett.134.090601. URL: https://link.aps.org/doi/10.1103/PhysRevLett.134.090601.

[83] Sirui Cao et al. "Generation of genuine entanglement up to 51 superconducting qubits". en. In: *Nature* 619.7971 (July 2023). Publisher: Nature Publishing Group, pp. 738–742. ISSN: 1476-4687. DOI: 10.1038/s41586-023-06195-1. URL: https://www.nature.com/articles/s41586-023-06195-1.

[84] J. A. Schreier et al. “Suppressing charge noise decoherence in superconducting charge qubits”. In: *Physical Review B* 77 (May 2008). Publisher: APS ADS Bibcode: 2008PhRvB..77r0502S, p. 180502. ISSN: 0163-18291098-0121. DOI: 10.1103/PhysRevB.77.180502. URL: https://ui.adsabs.harvard.edu/abs/2008PhRvB..77r0502S.

[85] Nicolas Maring et al. “A versatile single-photon-based quantum computing platform”. en. In: *Nature Photonics* 18.6 (June 2024). Publisher: Nature Publishing Group, pp. 603–609. ISSN: 1749-4893. DOI: 10.1038/s41566-024-01403-4. URL: https://www.nature.com/articles/s41566-024-01403-4.

[86] Alberto Politi, Jonathan C. F. Matthews, and Jeremy L. O’Brien. “Shor’s Quantum Factoring Algorithm on a Photonic Chip”. In: *Science* 325 (Sept. 2009). ADS Bibcode: 2009Sci...325.1221P, p. 1221. ISSN: 0036-8075. DOI: 10.1126/science.1173731. URL: https://ui.adsabs.harvard.edu/abs/2009Sci...325.1221P.

[87] Minzhao Liu et al. “Certified randomness using a trapped-ion quantum processor”. en. In: *Nature* 640.8058 (Apr. 2025). Publisher: Nature Publishing Group, pp. 343–348. ISSN: 1476-4687. DOI: 10.1038/s41586-025-08737-1. URL: https://www.nature.com/articles/s41586-025-08737-1.

[88] D.J. Wineland et al. “Experimental issues in coherent quantum-state manipulation of trapped atomic ions”. In: *Journal of Research of the National Institute of Standards and Technology* 103.3 (May 1998), p. 259. ISSN: 1044677X. DOI: 10.6028/jres.103.019. URL: https://nvlpubs.nist.gov/nistpubs/jres/103/3/j33win.pdf.

[89] Rainer Blatt and David Wineland. “Entangled states of trapped atomic ions”. In: *Nature* 453 (June 2008). ADS Bibcode: 2008Natur.453.1008B, pp. 1008–1015. ISSN: 0028-0836. DOI: 10.1038/nature07125. URL: https://ui.adsabs.harvard.edu/abs/2008Natur.453.1008B.

[90] Matias Urdampilleta et al. “Magnetic Interaction Between a Radical Spin and a Single-Molecule Magnet in a Molecular Spin-Valve”. In: *ACS Nano* 9.4 (Apr. 2015). Publisher: American Chemical Society, pp. 4458–4464. ISSN: 1936-0851. DOI: 10.1021/acsnano.5b01056. URL: https://doi.org/10.1021/acsnano.5b01056.

[91] Yu Wang et al. “An atomic-scale multi-qubit platform”. In: *Science* 382.6666 (Oct. 2023). Publisher: American Association for the Advancement of Science, pp. 87–92. DOI: 10.1126/science.ade5050. URL: https://www.science.org/doi/10.1126/science.ade5050.

[92] Denis Janković et al. “Noisy qudit vs multiple qubits: conditions on gate efficiency for enhancing fidelity”. en. In: *npj Quantum Information* 10.1 (June 2024). Publisher: Nature Publishing Group, pp. 1–10. ISSN: 2056-6387. DOI: 10.1038/s41534-024-00829-6. URL: https://www.nature.com/articles/s41534-024-00829-6.

[93] Jean-Gabriel Hartmann et al. “Nonlinearity of the Fidelity in Open Qudit Systems: Gate and Noise Dependence in High-dimensional Quantum Computing”. en-GB. In: *Quantum* 9 (Apr. 2025). Publisher: Verein zur Förderung des Open Access Publizierens in den Quantenwissenschaften, p. 1690. DOI: 10.22331/q-2025-04-07-1690. URL: https://quantum-journal.org/papers/q-2025-04-07-1690/.

[94] Andrea Morello. "Quantum search on a single-atom qudit". en. In: *Nature Nanotechnology* 13.1 (Jan. 2018). Publisher: Nature Publishing Group, pp. 9–10. ISSN: 1748-3395. DOI: 10.1038/s41565-017-0049-z. URL: https://www.nature.com/articles/s41565-017-0049-z.

[95] C. Godfrin et al. "Operating Quantum States in Single Magnetic Molecules: Implementation of Grover's Quantum Algorithm". In: *Physical Review Letters* 119.18 (Nov. 2017). Publisher: American Physical Society, p. 187702. DOI: 10.1103/PhysRevLett.119.187702. URL: https://link.aps.org/doi/10.1103/PhysRevLett.119.187702.

[96] Gary Siuzdak et al. "Mass spectrometry and viral analysis". In: *Chemistry & Biology* 3.1 (Jan. 1996), pp. 45–48. ISSN: 1074-5521. DOI: 10.1016/S1074-5521(96)90083-6. URL: https://www.sciencedirect.com/science/article/pii/S1074552196900836.

[97] J. B. Fenn et al. "Electrospray ionization for mass spectrometry of large biomolecules". eng. In: *Science (New York, N.Y.)* 246.4926 (Oct. 1989), pp. 64–71. ISSN: 0036-8075. DOI: 10.1126/science.2675315.

[98] Matthias Wilm. "Principles of electrospray ionization". eng. In: *Molecular & cellular proteomics: MCP* 10.7 (July 2011), p. M111.009407. ISSN: 1535-9484. DOI: 10.1074/mcp.M111.009407.

[99] Hugo Y. Samayoa-Oviedo et al. "Design and Performance of a Soft-Landing Instrument for Fragment Ion Deposition". eng. In: *Analytical Chemistry* 93.43 (Nov. 2021), pp. 14489–14496. ISSN: 1520-6882. DOI: 10.1021/acs.analchem.1c03009.

[100] Hugo Y. Samayoa-Oviedo et al. "Spontaneous ligand loss by soft landed [Ni(bpy) 3] 2+ ions on perfluorinated self-assembled monolayer surfaces". en. In: *Chemical Science* 15.28 (2024). Publisher: Royal Society of Chemistry, pp. 10770–10783. DOI: 10.1039/D4SC02527J. URL: https://pubs.rsc.org/en/content/articlelanding/2024/sc/d4sc02527j.

[101] Paul Fremdling et al. "A Preparative Mass Spectrometer to Deposit Intact Large Native Protein Complexes". In: *ACS Nano* 16.9 (Sept. 2022). Publisher: American Chemical Society, pp. 14443–14455. ISSN: 1936-0851. DOI: 10.1021/acsnano.2c04831. URL: https://doi.org/10.1021/acsnano.2c04831.

[102] Julio J. Conde, Paloma Ferreira-Aparicio, and Antonio M. Chaparro. "Electrospray Deposition: A Breakthrough Technique for Proton Exchange Membrane Fuel Cell Catalyst Layer Fabrication". In: *ACS Applied Energy Materials* 4.8 (Aug. 2021). Publisher: American Chemical Society, pp. 7394–7404. DOI: 10.1021/acsaem.1c01445. URL: https://doi.org/10.1021/acsaem.1c01445.

[103] Sarah H. Park et al. "Efficient electrospray deposition of surfaces smaller than the spray plume". en. In: *Nature Communications* 14.1 (Aug. 2023). Publisher: Nature Publishing Group, p. 4896. ISSN: 2041-1723. DOI: 10.1038/s41467-023-40638-7. URL: https://www.nature.com/articles/s41467-023-40638-7.

[104] Kelvin Anggara et al. “Exploring the Molecular Conformation Space by Soft Molecule–Surface Collision”. In: *Journal of the American Chemical Society* 142.51 (Dec. 2020). Publisher: American Chemical Society, pp. 21420–21427. ISSN: 0002-7863. DOI: 10.1021/jacs.0c09933. URL: https://doi.org/10.1021/jacs.0c09933.

[105] Jonas Warneke. “Gas-phase ion chemistry of [B12X12]2 (X = F, Cl, Br, I, CN). A brief review of twelve years of researching twelvevertexed dianions and their fragments”. In: *International Journal of Mass Spectrometry* 496 (Feb. 2024), p. 117169. ISSN: 1387-3806. DOI: 10.1016/j.ijms.2023.117169. URL: https://www.sciencedirect.com/science/article/pii/S1387380623001604.

[106] Gargi S. Jagdale et al. “Electrospray deposition for single nanoparticle studies”. en. In: *Analytical Methods* 13.36 (Sept. 2021). Publisher: The Royal Society of Chemistry, pp. 4105–4113. ISSN: 1759-9679. DOI: 10.1039/D1AY01295A. URL: https://pubs.rsc.org/en/content/articlelanding/2021/ay/d1ay01295a.

[107] Dennis Meier et al. “Structural adaptations of electrosprayed aromatic oligoamide foldamers on Ag(111)”. en. In: *Chemical Communications* 58.64 (Aug. 2022). Publisher: The Royal Society of Chemistry, pp. 8938–8941. ISSN: 1364-548X. DOI: 10.1039/D2CC03286D. URL: https://pubs.rsc.org/en/content/articlelanding/2022/cc/d2cc03286d.

[108] A. Jaworek and A. T. Sobczyk. “Electrospraying route to nanotechnology: An overview”. In: *Journal of Electrostatics* 66.3 (Mar. 2008), pp. 197–219. ISSN: 0304-3886. DOI: 10.1016/j.elstat.2007.10.001. URL: https://www.sciencedirect.com/science/article/pii/S0304388608000028.

[109] Fangshun Yang et al. “Control of Intermediates and Products by Combining Droplet Reactions and Ion Soft-Landing”. en. In: *Angewandte Chemie International Edition* 63.4 (2024). _eprint: https://onlinelibrary.wiley.com/doi/pdf/10.1002/anie.202314784, e202314784. ISSN: 1521-3773. DOI: 10.1002/anie.202314784. URL: https://onlinelibrary.wiley.com/doi/abs/10.1002/anie.202314784 (visited on 08/19/2025).

[110] Matthew Edmondson et al. “On-Surface Synthesis of Ni-Porphyrin-Doped Graphene Nanoribbons”. In: *ACS Nano* 18.49 (Dec. 2024). Publisher: American Chemical Society, pp. 33390–33397. ISSN: 1936-0851. DOI: 10.1021/acsnano.4c09188. URL: https://doi.org/10.1021/acsnano.4c09188.

[111] Henrik Gotfredsen et al. “Bending a photonic wire into a ring”. en. In: *Nature Chemistry* 14.12 (Dec. 2022). Publisher: Nature Publishing Group, pp. 1436–1442. ISSN: 1755-4349. DOI: 10.1038/s41557-022-01032-w. URL: https://www.nature.com/articles/s41557-022-01032-w.

[112] Lukas Krumbein et al. “Fast Molecular Compression by a Hyperthermal Collision Gives Bond-Selective Mechanochemistry”. In: *Physical Review Letters* 126.5 (Feb. 2021). Publisher: American Physical Society, p. 056001. DOI: 10.1103/PhysRevLett.126.056001. URL: https://link.aps.org/doi/10.1103/PhysRevLett.126.056001.

[113] G. Binnig et al. “Tunneling through a controllable vacuum gap”. In: *Applied Physics Letters* 40.2 (Jan. 1982), pp. 178–180. ISSN: 0003-6951. DOI: 10.1063/1.92999. URL: https://doi.org/10.1063/1.92999.

[114] G. Binnig et al. “Surface Studies by Scanning Tunneling Microscopy”. In: *Physical Review Letters* 49.1 (July 1982). Publisher: American Physical Society, pp. 57–61. DOI: 10.1103/PhysRevLett.49.57. URL: https://link.aps.org/doi/10.1103/PhysRevLett.49.57.

[115] G. Binnig et al. “7 \ifmmode\times\else\texttimes\fi{} 7 Reconstruction on Si(111) Resolved in Real Space”. In: *Physical Review Letters* 50.2 (Jan. 1983). Publisher: American Physical Society, pp. 120–123. DOI: 10.1103/PhysRevLett.50.120. URL: https://link.aps.org/doi/10.1103/PhysRevLett.50.120.

[116] Gerd Binnig and Heinrich Rohrer. “Scanning tunneling microscopy—from birth to adolescence”. en. In: *Reviews of Modern Physics* 59.3 (July 1987), pp. 615–625. ISSN: 0034-6861. DOI: 10.1103/RevModPhys.59.615. URL: https://link.aps.org/doi/10.1103/RevModPhys.59.615.

[117] G. Binnig, C. F. Quate, and Ch. Gerber. “Atomic Force Microscope”. In: *Physical Review Letters* 56.9 (Mar. 1986). Publisher: American Physical Society, pp. 930–933. DOI: 10.1103/PhysRevLett.56.930. URL: https://link.aps.org/doi/10.1103/PhysRevLett.56.930.

[118] R. Wiesendanger et al. “Observation of vacuum tunneling of spin-polarized electrons with the scanning tunneling microscope”. In: *Physical Review Letters* 65.2 (July 1990). Publisher: American Physical Society, pp. 247–250. DOI: 10.1103/PhysRevLett.65.247. URL: https://link.aps.org/doi/10.1103/PhysRevLett.65.247.

[119] A. J. Heinrich et al. “Single-atom spin-flip spectroscopy”. eng. In: *Science (New York, N.Y.)* 306.5695 (Oct. 2004), pp. 466–469. ISSN: 1095-9203. DOI: 10.1126/science.1101077.

[120] Dimas G. de Oteyza et al. “Direct imaging of covalent bond structure in single-molecule chemical reactions”. eng. In: *Science (New York, N.Y.)* 340.6139 (June 2013), pp. 1434–1437. ISSN: 1095-9203. DOI: 10.1126/science.1238187.

[121] R. M. Overney et al. “Friction measurements on phase-separated thin films with a modified atomic force microscope”. en. In: *Nature* 359.6391 (Sept. 1992). Publisher: Nature Publishing Group, pp. 133–135. ISSN: 1476-4687. DOI: 10.1038/359133a0. URL: https://www.nature.com/articles/359133a0.

[122] Taner Esat et al. “A quantum sensor for atomic-scale electric and magnetic fields”. en. In: *Nature Nanotechnology* 19.10 (Oct. 2024). Publisher: Nature Publishing Group, pp. 1466–1471. ISSN: 1748-3395. DOI: 10.1038/s41565-024-01724-z. URL: https://www.nature.com/articles/s41565-024-01724-z.

[123] Sebastian Loth et al. “Bistability in atomic-scale antiferromagnets”. eng. In: *Science (New York, N.Y.)* 335.6065 (Jan. 2012), pp. 196–199. ISSN: 1095-9203. DOI: 10.1126/science.1214131.

[124] D. M. Eigler and E. K. Schweizer. “Positioning single atoms with a scanning tunnelling microscope”. en. In: *Nature* 344.6266 (Apr. 1990). Publisher: Nature Publishing Group, pp. 524–526. ISSN: 1476-4687. DOI: 10.1038/344524a0. URL: https://www.nature.com/articles/344524a0.

[125] M. F. Crommie, C. P. Lutz, and D. M. Eigler. "Confinement of Electrons to Quantum Corrals on a Metal Surface". In: *Science* 262.5131 (Oct. 1993). Publisher: American Association for the Advancement of Science, pp. 218–220. DOI: 10.1126/science.262.5131.218. URL: https://www.science.org/doi/10.1126/science.262.5131.218.

[126] Niklas Romming et al. "Writing and Deleting Single Magnetic Skyrmions". In: *Science* 341.6146 (Aug. 2013). Publisher: American Association for the Advancement of Science, pp. 636–639. DOI: 10.1126/science.1240573. URL: https://www.science.org/doi/10.1126/science.1240573.

[127] Saw-Wai Hla et al. "Inducing All Steps of a Chemical Reaction with the Scanning Tunneling Microscope Tip: Towards Single Molecule Engineering". In: *Physical Review Letters* 85.13 (Sept. 2000). Publisher: American Physical Society, pp. 2777–2780. DOI: 10.1103/PhysRevLett.85.2777. URL: https://link.aps.org/doi/10.1103/PhysRevLett.85.2777.

[128] Bogdana Borca et al. "Electric-Field-Driven Direct Desulfurization". In: *ACS Nano* 11.5 (May 2017). Publisher: American Chemical Society, pp. 4703–4709. ISSN: 1936-0851. DOI: 10.1021/acsnano.7b00612. URL: https://doi.org/10.1021/acsnano.7b00612.

[129] G. A Somorjai. "The surface science of heterogeneous catalysis". In: *Surface Science* 299-300 (Jan. 1994), pp. 849–866. ISSN: 0039-6028. DOI: 10.1016/0039-6028(94)90702-1. URL: https://www.sciencedirect.com/science/article/pii/0039602894907021.

[130] Michael Bowker. "Catalysis resolved using scanning tunnelling microscopy". en. In: *Chemical Society Reviews* 36.10 (Aug. 2007). Publisher: The Royal Society of Chemistry, pp. 1656–1673. ISSN: 1460-4744. DOI: 10.1039/B412139M. URL: https://pubs.rsc.org/en/content/articlelanding/2007/cs/b412139m.

[131] Anisoara Socoliuc et al. "Atomic-scale control of friction by actuation of nanometer-sized contacts". eng. In: *Science (New York, N.Y.)* 313.5784 (July 2006), pp. 207–210. ISSN: 1095-9203. DOI: 10.1126/science.1125874.

[132] J. Bardeen. "Tunnelling from a Many-Particle Point of View". In: *Physical Review Letters* 6.2 (Jan. 1961). Publisher: American Physical Society, pp. 57–59. DOI: 10.1103/PhysRevLett.6.57. URL: https://link.aps.org/doi/10.1103/PhysRevLett.6.57.

[133] J. Tersoff and D. R. Hamann. "Theory of the scanning tunneling microscope". In: *Physical Review B* 31.2 (Jan. 1985). Publisher: American Physical Society, pp. 805–813. DOI: 10.1103/PhysRevB.31.805. URL: https://link.aps.org/doi/10.1103/PhysRevB.31.805.

[134] Bert Voigtländer. *Scanning Probe Microscopy: Atomic Force Microscopy and Scanning Tunneling Microscopy*. en. NanoScience and Technology. Berlin, Heidelberg: Springer, 2015. ISBN: 978-3-662-45239-4 978-3-662-45240-0. DOI: 10.1007/978-3-662-45240-0. URL: https://link.springer.com/10.1007/978-3-662-45240-0.

[135] W. Shockley. "On the surface states associated with a periodic potential". In: *Physical Review* 56.4 (1939), pp. 317–323. DOI: 10.1103/PhysRev.56.317.

[136] L. C. Davis et al. “Theory of the local density of surface states on a metal: Comparison with scanning tunneling spectroscopy of a Au(111) surface”. en. In: *Physical Review B* 43.5 (Feb. 1991), pp. 3821–3830. ISSN: 0163-1829, 1095-3795. DOI: 10.1103/PhysRevB.43.3821. URL: https://link.aps.org/doi/10.1103/PhysRevB.43.3821.

[137] Ph. Avouris, I. -W. Lyo, and P. Molinàs-Mata. “STM studies of the interaction of surface state electrons on metals with steps and adsorbates”. In: *Chemical Physics Letters* 240.5 (July 1995), pp. 423–428. ISSN: 0009-2614. DOI: 10.1016/0009-2614(95)00577-Q. URL: https://www.sciencedirect.com/science/article/pii/000926149500577Q.

[138] Joseph Anthony Stroscio and William J. Kaiser. *Scanning tunneling microscopy*. eng. Methods of experimental physics. Boston: Academic Press, 1993. ISBN: 978-0-12-475972-5.

[139] R. Juraschek and F. W. Röllgen. “Pulsation phenomena during electrospray ionization”. In: *International Journal of Mass Spectrometry* 177.1 (Aug. 1998), pp. 1–15. ISSN: 1387-3806. DOI: 10.1016/S1387-3806(98)14025-3. URL: https://www.sciencedirect.com/science/article/pii/S1387380698140253.

[140] S. Verdoold et al. “A generic electrospray classification”. In: *Journal of Aerosol Science* 67 (Jan. 2014), pp. 87–103. ISSN: 0021-8502. DOI: 10.1016/j.jaerosci.2013.09.008. URL: https://www.sciencedirect.com/science/article/pii/S0021850213002012.

[141] Michel Cloupeau and Bernard Prunet-Foch. “Electrohydrodynamic spraying functioning modes: a critical review”. In: *Journal of Aerosol Science* 25.6 (Sept. 1994), pp. 1021–1036. ISSN: 0021-8502. DOI: 10.1016/0021-8502(94)90199-6. URL: https://www.sciencedirect.com/science/article/pii/0021850294901996.

[142] Geoffrey Taylor. “Disintegration of Water Drops in an Electric Field”. In: *Proceedings of the Royal Society of London Series A* 280 (July 1964). ADS Bibcode: 1964RSPSA.280..383T, pp. 383–397. ISSN: 0080-46301364-5021. DOI: 10.1098/rspa.1964.0151. URL: https://ui.adsabs.harvard.edu/abs/1964RSPSA.280..383T.

[143] Lord Rayleigh. “XX. On the equilibrium of liquid conducting masses charged with electricity”. In: *The London, Edinburgh, and Dublin Philosophical Magazine and Journal of Science* 14.87 (Sept. 1882). Publisher: Taylor & Francis _eprint: https://doi.org/10.1080/14786448208628425, pp. 184–186. ISSN: 1941-5982. DOI: 10.1080/14786448208628425. URL: https://doi.org/10.1080/14786448208628425.

[144] Denis Duft et al. “Rayleigh jets from levitated microdroplets”. en. In: *Nature* 421.6919 (Jan. 2003). Publisher: Nature Publishing Group, pp. 128–128. ISSN: 1476-4687. DOI: 10.1038/421128a. URL: https://www.nature.com/articles/421128a.

[145] Wolfgang Paul and Helmut Steinwedel. “Notizen: Ein neues Massenspektrometer ohne Magnetfeld”. en. In: *Zeitschrift für Naturforschung A* 8.7 (July 1953). Publisher: De Gruyter Section: Zeitschrift für Naturforschung A, pp. 448–450. ISSN: 1865-7109. DOI: 10.1515/zna-1953-0710. URL: https:

//www.degruyterbrill.com/document/doi/10.1515/zna-1953-0710/html?srsltid=AfmBOoq0yk1BPidrTbTCo0rgxdvViJKP8n3aO7jcHVov2IuR6QbeMKdD.

[146] W. Paul and M. Raether. "Das elektrische Massenfilter". de. In: *Zeitschrift für Physik* 140.3 (May 1955), pp. 262–273. ISSN: 0044-3328. DOI: 10.1007/BF01328923. URL: https://doi.org/10.1007/BF01328923.

[147] Wolfgang Paul. "Electromagnetic traps for charged and neutral particles". In: *Reviews of Modern Physics* 62.3 (July 1990). Publisher: American Physical Society, pp. 531–540. DOI: 10.1103/RevModPhys.62.531. URL: https://link.aps.org/doi/10.1103/RevModPhys.62.531.

[148] Zhaohui Du. "A new tandem quadrupole mass analyzer". English. PhD thesis. Ottawa: National Library of Canada = Bibliothèque nationale du Canada, 2001.

[149] Peter Dawson. *Quadrupole Mass Spectrometry and Its Applications*. en-US. Jan. 1976. ISBN: 978-0-444-41345-1. URL: https://shop.elsevier.com/books/quadrupole-mass-spectrometry-and-its-applications/dawson/978-0-444-41345-1.

[150] Dieter Gerlich. "Inhomogeneous RF Fields: A Versatile Tool for the Study of Processes with Slow Ions". en. In: *Advances in Chemical Physics*. _eprint: https://onlinelibrary.wiley.com/doi/pdf/10.1002/9780470141397.ch1. John Wiley & Sons, Ltd, 1992, pp. 1–176. ISBN: 978-0-470-14139-7. DOI: 10.1002/9780470141397.ch1. URL: https://onlinelibrary.wiley.com/doi/abs/10.1002/9780470141397.ch1.

[151] Manuel Vogel. "Handbook of Charged Particle Optics, 2nd edition, edited by J. Orloff". In: *Contemporary Physics - CONTEMP PHYS* 51 (July 2010), pp. 367–367. DOI: 10.1080/00107510903220705.

[152] Konenkov Nikolai and V. Kratenko. "Characteristics of a quadrupole mass filter in the separation mode of a few stability regions". In: *International Journal of Mass Spectrometry and Ion Processes* 108 (Oct. 1991), pp. 115–136. DOI: 10.1016/0168-1176(91)85029-L.

[153] P.H. Dawson and Yu Bingqi. "The second stability region of the quadrupole mass filter. I. Ion optical properties". en. In: *International Journal of Mass Spectrometry and Ion Processes* 56.1 (Feb. 1984), pp. 25–39. ISSN: 01681176. DOI: 10.1016/0168-1176(84)85076-4. URL: https://linkinghub.elsevier.com/retrieve/pii/0168117684850764.

[154] M. H. Friedman, A. L. Yergey, and J. E. Campana. "Fundamentals of ion motion in electric radio-frequency multipole fields". en. In: *Journal of Physics E: Scientific Instruments* 15.1 (Jan. 1982), p. 53. ISSN: 0022-3735. DOI: 10.1088/0022-3735/15/1/010. URL: https://dx.doi.org/10.1088/0022-3735/15/1/010.

[155] Conny Hägg and Imre Szabo. "New ion-optical devices utilizing oscillatory electric fields. II. Stability of ion motion in a two-dimensional hexapole field". In: *International Journal of Mass Spectrometry and Ion Processes* 73.3 (Nov. 1986), pp. 237–275. ISSN: 0168-1176. DOI: 10.1016/0168-1176(86)80002-7. URL: https://www.sciencedirect.com/science/article/pii/0168117686800027.

[156] Raphael Hellwig. *Alkyne-Based Nanostructures on Silver Substrates*. Springer Theses. Cham: Springer International Publishing, 2018. ISBN: 978-3-030-00996-0 978-3-030-00997-7. DOI: 10.1007/978-3-030-00997-7. URL: http://link.springer.com/10.1007/978-3-030-00997-7.

[157] Voltastrasse 5 SPECS GmbH 13355 Berlin (DE). *JT-STM Brochure*. URL: http://www.specs.de/cms/upload/PDFs/%20SPECS__pekte/2010_2_JT-STM_brochure_final_web.pdf.

[158] Tobias Kaposi. "A Compact and Versatile Electrospray Ion Beam Deposition Setup: Advanced Sample Preparation for Experiments in Surface Science". PhD thesis. Technische Universität München, 2016. URL: https://mediatum.ub.tum.de/1292664.

[159] W. J. De Haas and J. De Boer. "The electrical resistance of platinum at low temperatures". In: *Physica* 1.7 (May 1934), pp. 609–616. ISSN: 0031-8914. DOI: 10.1016/S0031-8914(34)80247-9. URL: https://www.sciencedirect.com/science/article/pii/S0031891434802479.

[160] W. Meissner and B. Voigt. "Messungen mit Hilfe von flüssigem Helium XI Widerstand der reinen Metalle in tiefen Temperaturen". In: *Annalen der Physik* 399 (Jan. 1930). ADS Bibcode: 1930AnP...399..892M, pp. 892–936. ISSN: 0003-3804. DOI: 10.1002/andp.19303990803. URL: https://ui.adsabs.harvard.edu/abs/1930AnP...399..892M.

[161] J. Kondo. "Resistance Minimum in Dilute Magnetic Alloys". In: *Progress of Theoretical Physics* 32 (July 1964). ADS Bibcode: 1964PThPh..32...37K, pp. 37–49. ISSN: 0033-06840033-068X. DOI: 10.1143/PTP.32.37. URL: https://ui.adsabs.harvard.edu/abs/1964PThPh..32...37K.

[162] H. Suhl. "Dispersion Theory of the Kondo Effect". In: *Physical Review* 138.2A (Apr. 1965). Publisher: American Physical Society, A515–A523. DOI: 10.1103/PhysRev.138.A515. URL: https://link.aps.org/doi/10.1103/PhysRev.138.A515.

[163] J. Friedel. "On some electrical and magnetic properties of metallic solid solutions". In: *Canadian Journal of Physics* 34.12A (Dec. 1956). Publisher: NRC Research Press, pp. 1190–1211. ISSN: 0008-4204. DOI: 10.1139/p56-134. URL: https://cdnsciencepub.com/doi/10.1139/p56-134.

[164] B. Coqblin. "Kondo Effect (Theory)". In: *Encyclopedia of Condensed Matter Physics*. Ed. by Franco Bassani, Gerald L. Liedl, and Peter Wyder. Oxford: Elsevier, Jan. 2005, pp. 61–65. ISBN: 978-0-12-369401-0. DOI: 10.1016/B0-12-369401-9/01156-6. URL: https://www.sciencedirect.com/science/article/pii/B0123694019011566.

[165] Alexander Cyril Hewson. *The Kondo Problem to Heavy Fermions*. Cambridge Studies in Magnetism. Cambridge: Cambridge University Press, 1993. ISBN: 978-0-521-59947-4. DOI: 10.1017/CBO9780511470752. URL: https://www.cambridge.org/core/books/kondo-problem-to-heavy-fermions/EDBEDC3F4492DD3EE27E02259935705A.

[166] Johann Kroha. *Interplay of Kondo Effect and RKKY Interaction*. en. arXiv:1710.00192 [cond-mat]. Sept. 2017. DOI: 10.48550/arXiv.1710.00192. URL: http://arxiv.org/abs/1710.00192.

[167] P. Nozières. "A "fermi-liquid" description of the Kondo problem at low temperatures". en. In: *Journal of Low Temperature Physics* 17.1 (Oct. 1974), pp. 31–42. ISSN: 1573-7357. DOI: 10.1007/BF00654541. URL: https://doi.org/10.1007/BF00654541.

[168] Kenneth G. Wilson. "The renormalization group: Critical phenomena and the Kondo problem". In: *Reviews of Modern Physics* 47.4 (Oct. 1975). Publisher: American Physical Society, pp. 773–840. DOI: 10.1103/RevModPhys.47.773. URL: https://link.aps.org/doi/10.1103/RevModPhys.47.773.

[169] Kenneth G. Wilson. "The renormalization group and critical phenomena". In: *Reviews of Modern Physics* 55.3 (July 1983). Publisher: American Physical Society, pp. 583–600. DOI: 10.1103/RevModPhys.55.583. URL: https://link.aps.org/doi/10.1103/RevModPhys.55.583.

[170] N. Andrei. "Diagonalization of the Kondo Hamiltonian". In: *Physical Review Letters* 45.5 (Aug. 1980). Publisher: American Physical Society, pp. 379–382. DOI: 10.1103/PhysRevLett.45.379. URL: https://link.aps.org/doi/10.1103/PhysRevLett.45.379.

[171] P. B. Wiegmann. "Exact solution of the s-d exchange model (Kondo problem)". en. In: *Journal of Physics C: Solid State Physics* 14.10 (Apr. 1981), p. 1463. ISSN: 0022-3719. DOI: 10.1088/0022-3719/14/10/014. URL: https://dx.doi.org/10.1088/0022-3719/14/10/014.

[172] P. W. Anderson. "Localized Magnetic States in Metals". In: *Physical Review* 124.1 (Oct. 1961). Publisher: American Physical Society, pp. 41–53. DOI: 10.1103/PhysRev.124.41. URL: https://link.aps.org/doi/10.1103/PhysRev.124.41.

[173] Markus Ternes, Andreas J Heinrich, and Wolf-Dieter Schneider. "Spectroscopic manifestations of the Kondo effect on single adatoms". en. In: *Journal of Physics: Condensed Matter* 21.5 (Dec. 2008), p. 053001. ISSN: 0953-8984. DOI: 10.1088/0953-8984/21/5/053001. URL: https://dx.doi.org/10.1088/0953-8984/21/5/053001.

[174] V. Madhavan et al. "Tunneling into a single magnetic atom: spectroscopic evidence of the kondo resonance". eng. In: *Science (New York, N.Y.)* 280.5363 (Apr. 1998), pp. 567–569. ISSN: 1095-9203. DOI: 10.1126/science.280.5363.567.

[175] U. Fano. "Effects of Configuration Interaction on Intensities and Phase Shifts". In: *Physical Review* 124.6 (Dec. 1961). Publisher: American Physical Society, pp. 1866–1878. DOI: 10.1103/PhysRev.124.1866. URL: https://link.aps.org/doi/10.1103/PhysRev.124.1866.

[176] Werner A Hofer, Gilberto Teobaldi, and Nicolas Lorente. "Creating pseudo-Kondo resonances by field-induced diffusion of atomic hydrogen". en. In: *Nanotechnology* 19.30 (June 2008), p. 305701. ISSN: 0957-4484. DOI: 10.1088/0957-4484/19/30/305701. URL: https://dx.doi.org/10.1088/0957-4484/19/30/305701.

[177] L. Y. L. Shen and J. M. Rowell. "Zero-Bias Tunneling Anomalies—Temperature, Voltage, and Magnetic Field Dependence". In: *Physical Review* 165.2 (Jan. 1968). Publisher: American Physical Society, pp. 566–577. DOI: 10.1103/PhysRev.165.566. URL: https://link.aps.org/doi/10.1103/PhysRev.165.566.

[178] D. Goldhaber-Gordon et al. "Kondo effect in a single-electron transistor". en. In: *Nature* 391.6663 (Jan. 1998). Publisher: Nature Publishing Group, pp. 156–159. ISSN: 1476-4687. DOI: 10.1038/34373. URL: https://www.nature.com/articles/34373.

[179] Sara M. Cronenwett, Tjerk H. Oosterkamp, and Leo P. Kouwenhoven. "A Tunable Kondo Effect in Quantum Dots". In: *Science* 281.5376 (July 1998). Publisher: American Association for the Advancement of Science, pp. 540–544. DOI: 10.1126/science.281.5376.540. URL: https://www.science.org/doi/10.1126/science.281.5376.540.

[180] A. Kogan et al. "Measurements of Kondo and Spin Splitting in Single-Electron Transistors". In: *Physical Review Letters* 93.16 (Oct. 2004). Publisher: American Physical Society, p. 166602. DOI: 10.1103/PhysRevLett.93.166602. URL: https://link.aps.org/doi/10.1103/PhysRevLett.93.166602.

[181] T. A. Costi. "Magnetic field dependence of the thermopower of Kondo-correlated quantum dots: Comparison with experiment". In: *Physical Review B* 100.15 (Oct. 2019). Publisher: American Physical Society, p. 155126. DOI: 10.1103/PhysRevB.100.155126. URL: https://link.aps.org/doi/10.1103/PhysRevB.100.155126.

[182] Chunwei Hsu et al. "Magnetic-Field Universality of the Kondo Effect Revealed by Thermocurrent Spectroscopy". In: *Physical Review Letters* 128.14 (Apr. 2022). Publisher: American Physical Society, p. 147701. DOI: 10.1103/PhysRevLett.128.147701. URL: https://link.aps.org/doi/10.1103/PhysRevLett.128.147701.

[183] Alexander F. Otte et al. "The role of magnetic anisotropy in the Kondo effect". en. In: *Nature Physics* 4.11 (Nov. 2008). Publisher: Nature Publishing Group, pp. 847–850. ISSN: 1745-2481. DOI: 10.1038/nphys1072. URL: https://www.nature.com/articles/nphys1072.

[184] Wenjie Liang et al. "Kondo resonance in a single-molecule transistor". en. In: *Nature* 417.6890 (June 2002). Publisher: Nature Publishing Group, pp. 725–729. ISSN: 1476-4687. DOI: 10.1038/nature00790. URL: https://www.nature.com/articles/nature00790.

[185] Jiwoong Park et al. "Coulomb blockade and the Kondo effect in single-atom transistors". en. In: *Nature* 417.6890 (June 2002). Publisher: Nature Publishing Group, pp. 722–725. ISSN: 1476-4687. DOI: 10.1038/nature00791. URL: https://www.nature.com/articles/nature00791.

[186] K. Nagaoka et al. "Temperature Dependence of a Single Kondo Impurity". In: *Physical Review Letters* 88.7 (Feb. 2002). Publisher: American Physical Society, p. 077205. DOI: 10.1103/PhysRevLett.88.077205. URL: https://link.aps.org/doi/10.1103/PhysRevLett.88.077205.

[187] Patrick Lawes et al. "Hierarchical Self-Assembly and Conformation of Tb Double-Decker Molecular Magnets: Experiment and Molecular Dynamics". en. In: *Nanomaterials* 13.15 (Aug. 2023), p. 2232. ISSN: 2079-4991. DOI: 10.3390/nano13152232. URL: https://www.mdpi.com/2079-4991/13/15/2232.

[188] Eufemio Moreno Pineda et al. "Surface confinement of TbPc $_2$ -SMMs: structural, electronic and magnetic properties". en. In: *Dalton Transactions* 45.46 (2016), pp. 18417–18433. ISSN: 1477-9226, 1477-9234. DOI: 10.1039/C6DT03298B. URL: https://xlink.rsc.org/?DOI=C6DT03298B.

[189] Ying-Shuang Fu et al. "Reversible Chiral Switching of Bis(phthalocyaninato) Terbium(III) on a Metal Surface". In: *Nano Letters* 12.8 (Aug. 2012). Publisher: American Chemical Society, pp. 3931–3935. ISSN: 1530-6984. DOI: 10.1021/nl302166z. URL: https://doi.org/10.1021/nl302166z.

[190] Jörg Schwöbel et al. "Real-space observation of spin-split molecular orbitals of adsorbed single-molecule magnets". en. In: *Nature Communications* 3.1 (July 2012). Publisher: Nature Publishing Group, p. 953. ISSN: 2041-1723. DOI: 10.1038/ncomms1953. URL: https://www.nature.com/articles/ncomms1953.

[191] Keiichi Katoh, Tadahiro Komeda, and Masahiro Yamashita. "Surface morphologies, electronic structures, and Kondo effect of lanthanide(III)-phthalocyanine molecules on Au(111) by using STM, STS and FET properties for next generation devices". en. In: *Dalton Transactions* 39.20 (May 2010). Publisher: The Royal Society of Chemistry, pp. 4708–4723. ISSN: 1477-9234. DOI: 10.1039/B926121D. URL: https://pubs.rsc.org/en/content/articlelanding/2010/dt/b926121d.

[192] Syed Mohammad Fakruddin Shahed et al. "Observation of Yu–Shiba–Rusinov States and Inelastic Tunneling Spectroscopy for Intramolecule Magnetic Exchange Interaction Energy of Terbium Phthalocyanine (TbPc) Species Adsorbed on Superconductor NbSe2". In: *ACS Nano* 16.5 (May 2022). Publisher: American Chemical Society, pp. 7651–7661. ISSN: 1936-0851. DOI: 10.1021/acsnano.1c11221. URL: https://doi.org/10.1021/acsnano.1c11221.

[193] Anis Amokrane. "Tunneling spectroscopy of mono- and di-nuclear organometallic molecules on surfaces". fr. In: (Feb. 2016).

[194] Rabei Barhoumi. "Positioning and addressing single molecule magnets with an STM tip". en. PhD thesis. Université de Strasbourg ; Karlsruher Institut für Technologie, Sept. 2019. URL: https://theses.hal.science/tel-03360706.

[195] Ben Warner et al. "Sub-molecular modulation of a 4f driven Kondo resonance by surface-induced asymmetry". eng. In: *Nature Communications* 7 (Sept. 2016), p. 12785. ISSN: 2041-1723. DOI: 10.1038/ncomms12785.

[196] Hai Cao et al. "Hierarchical self-assembly of enantiopure and racemic helicenes at the liquid/solid interface: from 2D to 3D". en. In: *Nanoscale* 9.45 (Nov. 2017). Publisher: The Royal Society of Chemistry, pp. 18075–18080. ISSN: 2040-3372. DOI: 10.1039/C7NR06700C. URL: https://pubs.rsc.org/en/content/articlelanding/2017/nr/c7nr06700c.

[197] Himani Malik et al. "Solvent- and Temperature-Dependent Assembly in Monolayer Films of a Ferrocene-Naphthyridine Hybrid on HOPG". eng. In: *Chemistry, an Asian Journal* 16.11 (June 2021), pp. 1430–1437. ISSN: 1861-471X. DOI: 10.1002/asia.202100187.

[198] G. Bussetti et al. "Controlling drop-casting deposition of 2D Pt-octaethyl porphyrin layers on graphite". In: *Synthetic Metals* 195 (Sept. 2014), pp. 201–207. ISSN: 0379-6779. DOI: 10.1016/j.synthmet.2014.06.011. URL: https://www.sciencedirect.com/science/article/pii/S0379677914002161.

[199] Abigail Bellamy-Carter et al. "Self-assembly of a strapped linear porphyrin oligomer on HOPG". en. In: *Scientific Reports* 11.1 (Oct. 2021). Publisher: Nature Publishing Group, p. 20388. ISSN: 2045-2322. DOI: 10.1038/s41598-021-99881-x. URL: https://www.nature.com/articles/s41598-021-99881-x.

[200] Toyo Kazu Yamada et al. "Energy gap opening by crossing drop cast single-layer graphene nanoribbons". eng. In: *Nanotechnology* 29.31 (Aug. 2018), p. 315705. ISSN: 1361-6528. DOI: 10.1088/1361-6528/aac36b.

[201] Nico Balzer et al. "Synthesis and Surface Behaviour of NDI Chromophores Mounted on a Tripodal Scaffold: Towards Self-Decoupled Chromophores for Single-Molecule Electroluminescence". en. In: *Chemistry – A European Journal* 27.47 (2021). _eprint: https://onlinelibrary.wiley.com/doi/pdf/10.1002/chem.202101264, pp. 12144–12155. ISSN: 1521-3765. DOI: 10.1002/chem.202101264. URL: https://onlinelibrary.wiley.com/doi/abs/10.1002/chem.202101264.

[202] Ryan D. McCurdy et al. "Synergetic Bottom-Up Synthesis of Graphene Nanoribbons by Matrix-Assisted Direct Transfer". In: *Journal of the American Chemical Society* 143.11 (Mar. 2021). Publisher: American Chemical Society, pp. 4174–4178. ISSN: 0002-7863. DOI: 10.1021/jacs.1c01355. URL: https://doi.org/10.1021/jacs.1c01355.

[203] Jiangliang Yin et al. "Backbone Engineering of Monodisperse Conjugated Polymers via Integrated Iterative Binomial Synthesis". In: *Journal of the American Chemical Society* 145.34 (Aug. 2023). Publisher: American Chemical Society, pp. 19120–19128. ISSN: 0002-7863. DOI: 10.1021/jacs.3c08143. URL: https://doi.org/10.1021/jacs.3c08143.

[204] Dmitry A. Erzunov et al. "Synthesis, Spectroscopic Properties and Redox Behavior Kinetics of Rare-Earth Bistetrakis-4-[3-(3,4-dicyanophenoxy)phenoxy]phthalocyaninato Metal Complexes with Er, Lu and Yb". en. In: *Molecules* 26.8 (Jan. 2021). Number: 8 Publisher: Multidisciplinary Digital Publishing Institute, p. 2181. ISSN: 1420-3049. DOI: 10.3390/molecules26082181. URL: https://www.mdpi.com/1420-3049/26/8/2181.

[205] Michael Sekita et al. "Tuning the Electron Acceptor in Phthalocyanine-Based Electron Donor–Acceptor Conjugates". en. In: *Chemistry – A European Journal* 21.52 (2015). _eprint: https://onlinelibrary.wiley.com/doi/pdf/10.1002/chem.201503237, pp. 19028–19040. ISSN: 1521-3765. DOI: 10.1002/chem.201503237. URL: https://onlinelibrary.wiley.com/doi/abs/10.1002/chem.201503237.

[206] Luiza M. F. Dantas et al. "Electrocatalytic oxidation of hydrazine in alkaline media promoted by iron tetrapyridinoporphyrazine adsorbed on graphite surface". en. In: *Journal of the Brazilian Chemical Society* 19 (2008). Publisher: Sociedade Brasileira de Química, pp. 720–726. ISSN: 0103-5053, 1678-4790. DOI: 10.1590/S0103-50532008000400016. URL: https://www.scielo.br/j/jbchs/a/JmYG8PgCqNQ5rCrnHMxrVCm/?lang=en.

[207] Karl M. Kadish et al. “Electrochemistry of a Double-Decker Lutetium(III) Phthalocyanine in Aqueous Media. The First Evidence for Five Reductions”. In: *The Journal of Physical Chemistry B* 105.40 (Oct. 2001). Publisher: American Chemical Society, pp. 9817–9821. ISSN: 1520-6106. DOI: 10.1021/jp012636y. URL: https://doi.org/10.1021/jp012636y.

[208] Peihua Zhu et al. “Comparative Electrochemical Study of Unsubstituted and Substituted Bis(phthalocyaninato) Rare Earth(III) Complexes”. en. In: *European Journal of Inorganic Chemistry* 2004.3 (2004). _eprint: https://onlinelibrary.wiley.com/doi/pdf/10.1002/ejic.200300509, pp. 510–517. ISSN: 1099-0682. DOI: 10.1002/ejic.200300509. URL: https://onlinelibrary.wiley.com/doi/abs/10.1002/ejic.200300509.

[209] Jose H. Zagal, Sergio Lira, and Soledad Ureta-Zañartu. “A mechanistic study of the electro-oxidation of hydrazine on phthalocyanines of VO, Cr, Mn, Ni, Cu and Zn attached to graphite electrodes”. In: *Journal of Electroanalytical Chemistry and Interfacial Electrochemistry* 210.1 (Oct. 1986), pp. 95–110. ISSN: 0022-0728. DOI: 10.1016/0022-0728(86)90316-5. URL: https://www.sciencedirect.com/science/article/pii/0022072886903165.

[210] K. Kizaki et al. “Coupling between the photo-excited cyclic system and the 4f electronic system in a lanthanide single molecule magnet”. en. In: *Chemical Communications* 53.45 (June 2017). Publisher: The Royal Society of Chemistry, pp. 6168–6171. ISSN: 1364-548X. DOI: 10.1039/C7CC02960H. URL: https://pubs.rsc.org/en/content/articlelanding/2017/cc/c7cc02960h.

[211] J. Kroger et al. “Self-organization of cobalt-phthalocyanine on a vicinal gold surface revealed by scanning tunnelling microscopy”. In: *Surface Science*. ECOSS-24 601.18 (Sept. 2007), pp. 4180–4184. ISSN: 0039-6028. DOI: 10.1016/j.susc.2007.04.091. URL: https://www.sciencedirect.com/science/article/pii/S0039602807003937 (visited on 05/28/2025).

[212] Lars Smykalla et al. “Self-Metalation of Phthalocyanine Molecules with Silver Surface Atoms by Adsorption on Ag(110)”. In: *The Journal of Physical Chemistry C* 119.30 (July 2015). Publisher: American Chemical Society, pp. 17228–17234. ISSN: 1932-7447. DOI: 10.1021/acs.jpcc.5b04977. URL: https://doi.org/10.1021/acs.jpcc.5b04977.

[213] Tadahiro Komeda, Hironari Isshiki, and Jie Liu. “Metal-free Phthalocyanine (H2Pc) Molecule Adsorbed on the Au (111) Surface: Formation of a Wide Domain Along a Single Lattice Direction”. In: *Science and Technology of Advanced Materials* 11 (Jan. 2011), p. 054602. DOI: 10.1088/1468-6996/11/5/054602.

[214] Wojciech Kamiński, Grażyna Antczak, and Karina Morgenstern. “Bistable H2Pc Molecular Conductance Switch on Ag(100)”. In: *The Journal of Physical Chemistry C* 126.39 (Oct. 2022). Publisher: American Chemical Society, pp. 16767–16776. ISSN: 1932-7447. DOI: 10.1021/acs.jpcc.2c03485. URL: https://doi.org/10.1021/acs.jpcc.2c03485.

[215] Islam Saiful et al. “Ligand Rotation Induced Oxidation State Change and Spin Appearance of the Bis(phthalocyaninato)cerium (CePc2) Molecule on the Au(111) Surface”. In: *The Journal of Physical Chemistry C* 126.40 (Oct. 2022). Publisher: American Chemical Society, pp. 17152–17163. ISSN:

1932-7447. DOI: 10.1021/acs.jpcc.2c04234. URL: https://doi.org/10.1021/acs.jpcc.2c04234.

[216] Rouzhaji Tuerhong et al. "Two-Dimensional Organometallic Kondo Lattice with Long-Range Antiferromagnetic Order". In: *The Journal of Physical Chemistry C* 122.34 (Aug. 2018). Publisher: American Chemical Society, pp. 20046–20054. ISSN: 1932-7447. DOI: 10.1021/acs.jpcc.8b07059. URL: https://doi.org/10.1021/acs.jpcc.8b07059 (visited on 05/26/2025).

[217] Jan Girovsky et al. "Long-range ferrimagnetic order in a two-dimensional supramolecular Kondo lattice". en. In: *Nature Communications* 8.1 (May 2017). Publisher: Nature Publishing Group, p. 15388. ISSN: 2041-1723. DOI: 10.1038/ncomms15388. URL: https://www.nature.com/articles/ncomms15388 (visited on 05/26/2025).

[218] Noriyuki Tsukahara et al. "Evolution of Kondo Resonance from a Single Impurity Molecule to the Two-Dimensional Lattice". In: *Physical Review Letters* 106.18 (May 2011). Publisher: American Physical Society, p. 187201. DOI: 10.1103/PhysRevLett.106.187201. URL: https://link.aps.org/doi/10.1103/PhysRevLett.106.187201 (visited on 05/26/2025).

[219] Piers Coleman. *Heavy Fermions and the Kondo Lattice: a 21st Century Perspective*. en. arXiv:1509.05769 [cond-mat]. Sept. 2015. DOI: 10.48550/arXiv.1509.05769. URL: http://arxiv.org/abs/1509.05769 (visited on 05/26/2025).

[220] Fang Xie et al. *Kondo-lattice phenomenology of twisted bilayer WSe$_2$ from compact molecular orbitals of topological bands*. en. arXiv:2503.21769 [cond-mat]. Mar. 2025. DOI: 10.48550/arXiv.2503.21769. URL: http://arxiv.org/abs/2503.21769 (visited on 05/31/2025).

[221] Stefan Kirchner et al. "Colloquium: Heavy-electron quantum criticality and single-particle spectroscopy". In: *Reviews of Modern Physics* 92.1 (Mar. 2020). Publisher: American Physical Society, p. 011002. DOI: 10.1103/RevModPhys.92.011002. URL: https://link.aps.org/doi/10.1103/RevModPhys.92.011002 (visited on 05/31/2025).

[222] Pramod Kumar, Guangze Chen, and J. L. Lado. "Kondo lattice mediated interactions in flat-band systems". In: *Physical Review Research* 3.4 (Nov. 2021). Publisher: American Physical Society, p. 043113. DOI: 10.1103/PhysRevResearch.3.043113. URL: https://link.aps.org/doi/10.1103/PhysRevResearch.3.043113 (visited on 05/31/2025).

[223] Philipp Gegenwart, Qimiao Si, and Frank Steglich. "Quantum criticality in heavy-fermion metals". en. In: *Nature Physics* 4.3 (Mar. 2008). Publisher: Nature Publishing Group, pp. 186–197. ISSN: 1745-2481. DOI: 10.1038/nphys892. URL: https://www.nature.com/articles/nphys892 (visited on 05/30/2025).

[224] Subir Sachdev and Bernhard Keimer. "Quantum criticality". In: *Physics Today* 64.2 (Feb. 2011), pp. 29–35. ISSN: 0031-9228. DOI: 10.1063/1.3554314. URL: https://doi.org/10.1063/1.3554314 (visited on 05/30/2025).

[225] Hengcan Zhao et al. "Quantum-critical phase from frustrated magnetism in a strongly correlated metal". en. In: *Nature Physics* 15.12 (Dec. 2019). Publisher: Nature Publishing Group, pp. 1261–1266. ISSN: 1745-2481. DOI: 10.1038/s41567-019-0666-6. URL: https://www.nature.com/articles/s41567-019-0666-6 (visited on 05/31/2025).

[226] Wenjin Zhao et al. "Gate-tunable heavy fermions in a moiré Kondo lattice". en. In: *Nature* 616.7955 (Apr. 2023). Publisher: Nature Publishing Group, pp. 61–65. ISSN: 1476-4687. DOI: 10.1038/s41586-023-05800-7. URL: https://www.nature.com/articles/s41586-023-05800-7 (visited on 05/31/2025).

[227] Mireille Lavagna and Catherine Pepin. *The Kondo Lattice Model*. arXiv:cond-mat/9903093. Mar. 1999. DOI: 10.48550/arXiv.cond-mat/9903093. URL: http://arxiv.org/abs/cond-mat/9903093 (visited on 05/31/2025).

[228] Sudip Chakravarty, Bertrand I. Halperin, and David R. Nelson. "Two-dimensional quantum Heisenberg antiferromagnet at low temperatures". In: *Physical Review B* 39.4 (Feb. 1989). Publisher: American Physical Society, pp. 2344–2371. DOI: 10.1103/PhysRevB.39.2344. URL: https://link.aps.org/doi/10.1103/PhysRevB.39.2344 (visited on 05/31/2025).

[229] Haoyu Hu, Lei Chen, and Qimiao Si. "Quantum critical metals and loss of quasiparticles". en. In: *Nature Physics* 20.12 (Dec. 2024). Publisher: Nature Publishing Group, pp. 1863–1873. ISSN: 1745-2481. DOI: 10.1038/s41567-024-02679-7. URL: https://www.nature.com/articles/s41567-024-02679-7 (visited on 05/31/2025).

[230] John A. Hertz. "Quantum critical phenomena *". In: *Basic Notions Of Condensed Matter Physics*. Num Pages: 20. CRC Press, 1994. ISBN: 978-0-429-49411-6.

[231] Chung-Jui Yu et al. "Spin and Phonon Design in Modular Arrays of Molecular Qubits". In: *Chemistry of Materials* 32.23 (Dec. 2020). Publisher: American Chemical Society, pp. 10200–10206. ISSN: 0897-4756. DOI: 10.1021/acs.chemmater.0c03718. URL: https://doi.org/10.1021/acs.chemmater.0c03718 (visited on 05/28/2025).

[232] Koji Miyake et al. "Molecular Motion of Surface-Immobilized Double-Decker Phthalocyanine Complexes". In: *Journal of the American Chemical Society* 131.49 (Dec. 2009). Publisher: American Chemical Society, pp. 17808–17813. ISSN: 0002-7863. DOI: 10.1021/ja904629d. URL: https://doi.org/10.1021/ja904629d.

[233] Tao Ye et al. "Tuning Interactions between Ligands in Self-Assembled Double-Decker Phthalocyanine Arrays". In: *Journal of the American Chemical Society* 128.34 (Aug. 2006). Publisher: American Chemical Society, pp. 10984–10985. ISSN: 0002-7863. DOI: 10.1021/ja060029o. URL: https://doi.org/10.1021/ja060029o.

[234] David Bléger et al. "An optimized alkyl chain-based binding motif for 2D self-assembly : a comprehensive crystallographic approach". en. In: *Nanoscale* 5.4 (2013). Publisher: Royal Society of Chemistry, pp. 1452–1455. DOI: 10.1039/C2NR33509C. URL: https://pubs.rsc.org/en/content/articlelanding/2013/nr/c2nr33509c.

[235] Jaegeun Noh and Masahiko Hara. "Molecular-scale growth processes of alkanethiol self-assembled monolayers on Au(111)". In: *Riken Rev.* 38 (Jan. 2001).

[236] Christopher G. Williams et al. "Dehydrocyclization of peripheral alkyl groups in porphyrins at Cu(100) and Ag(111) surfaces". In: *Surface Science* 653 (Nov. 2016), pp. 130–137. ISSN: 0039-6028. DOI: 10.1016/j.susc.2016.06.013. URL: https://www.sciencedirect.com/science/article/pii/S0039602816301649.

[237] Vicki H. Wysocki et al. "Surface-Induced Dissociation of Small Molecules, Peptides, and Non-covalent Protein Complexes". In: *Journal of the American Society for Mass Spectrometry* 19.2 (Feb. 2008), pp. 190–208. ISSN: 1044-0305. DOI: 10.1016/j.jasms.2007.11.005. URL: https://www.ncbi.nlm.nih.gov/pmc/articles/PMC2709493/.

[238] Alyssa Q. Stiving et al. "Surface-Induced Dissociation: An Effective Method for Characterization of Protein Quaternary Structure". In: *Analytical Chemistry* 91.1 (Jan. 2019). Publisher: American Chemical Society, pp. 190–209. ISSN: 0003-2700. DOI: 10.1021/acs.analchem.8b05071. URL: https://doi.org/10.1021/acs.analchem.8b05071.

[239] Henrik Grönbeck and Hannu Häkkinen. "Polymerization at the AlkylthiolateAu(111) Interface". In: *The Journal of Physical Chemistry B* 111.13 (Apr. 2007). Publisher: American Chemical Society, pp. 3325–3327. ISSN: 1520-6106. DOI: 10.1021/jp0700128. URL: https://doi.org/10.1021/jp0700128.

[240] Jaegeun Noh and Masahiko Hara. "Final Phase of Alkanethiol Self-Assembled Monolayers on Au(111)". In: *Langmuir* 18.6 (Mar. 2002). Publisher: American Chemical Society, pp. 1953–1956. ISSN: 0743-7463. DOI: 10.1021/la010803f. URL: https://doi.org/10.1021/la010803f.

[241] Jaegeun Noh. "Surface Potential Change Depending on Molecular Orientation of Hexadecanethiol Self-Assembled Monolayers on Au(111)". In: *Bulletin of the Korean Chemical Society* 30.6 (June 2009), pp. 1309–1312. DOI: 10.5012/BKCS.2009.30.6.1309. URL: https://doi.org/10.5012/BKCS.2009.30.6.1309.

[242] G. E. Poirier and E. D. Pylant. "The Self-Assembly Mechanism of Alkanethiols on Au(111)". In: *Science* 272.5265 (1996). Publisher: American Association for the Advancement of Science, pp. 1145–1148. ISSN: 0036-8075. URL: https://www.jstor.org/stable/2889938.

[243] Elie Geagea et al. "Activation, Transportation, and Reaction of Alkyl Radicals on a Si(111)-B Surface by a Scanning Tunneling Microscope Tip". In: *The Journal of Physical Chemistry C* 127.12 (Mar. 2023). Publisher: American Chemical Society, pp. 6002–6009. ISSN: 1932-7447. DOI: 10.1021/acs.jpcc.2c08799. URL: https://doi.org/10.1021/acs.jpcc.2c08799.

[244] Chris J. Baddeley and Neville V. Richardson. "Chirality at Metal Surfaces". en. In: *Scanning Tunneling Microscopy in Surface Science*. Ed. by Michael Bowker and Philip R. Davies. 1st ed. Wiley, Dec. 2009, pp. 1–27. ISBN: 978-3-527-31982-4 978-3-527-62882-7. DOI: 10.1002/9783527628827.ch1. URL: https://onlinelibrary.wiley.com/doi/10.1002/9783527628827.ch1.

[245] Ryo Kawaguchi et al. "Spatially Resolving Electron Spin Resonance of -Radical in Single-molecule Magnet". In: *Nano Letters* 23.1 (Jan. 2023). Publisher: American Chemical Society, pp. 213–219. ISSN: 1530-6984. DOI: 10.1021/acs.nanolett.2c04049. URL: https://doi.org/10.1021/acs.nanolett.2c04049.

[246] Xin Liao et al. "Altering Spin Distribution of Tb2Pc3 via Molecular Chirality Manipulation". In: *Journal of the American Chemical Society* 146.9 (Mar. 2024). Publisher: American Chemical Society, pp. 5901–5907. ISSN: 0002-7863. DOI: 10.1021/jacs.3c11882. URL: https://doi.org/10.1021/jacs.3c11882.

[247] Masahiro Taniguchi et al. "STM observation of molecular chirality and alignment on solid surface". In: *Journal of Molecular Catalysis A: Chemical*. Special Issue dedicated to Professor Juro Horiuti in commemoration of his centennial birthday and his contribution to science. 199.1 (May 2003), pp. 65–71. ISSN: 1381-1169. DOI: 10.1016/S1381-1169(03)00019-0. URL: https://www.sciencedirect.com/science/article/pii/S1381116903000190.

[248] Ting Chen et al. "Linear dislocation tunes chirality: STM study of chiral transition and amplification in a molecular assembly on an HOPG surface". en. In: *Chemical Communications* 19 (May 2009). Publisher: The Royal Society of Chemistry, pp. 2649–2651. ISSN: 1364-548X. DOI: 10.1039/B817525J. URL: https://pubs.rsc.org/en/content/articlelanding/2009/cc/b817525j.

[249] A. Mugarza et al. "Orbital Specific Chirality and Homochiral Self-Assembly of Achiral Molecules Induced by Charge Transfer and Spontaneous Symmetry Breaking". In: *Physical Review Letters* 105.11 (Sept. 2010). Publisher: American Physical Society, p. 115702. DOI: 10.1103/PhysRevLett.105.115702. URL: https://link.aps.org/doi/10.1103/PhysRevLett.105.115702.

[250] Joe Komeda et al. "Selective Transition Enhancement in a g-Engineered Diradical". en. In: *Chemistry – A European Journal* 30.42 (2024). _eprint: https://onlinelibrary.wiley.com/doi/pdf/10.1002/chem.202400420, e202400420. ISSN: 1521-3765. DOI: 10.1002/chem.202400420. URL: https://onlinelibrary.wiley.com/doi/abs/10.1002/chem.202400420.

[251] Michael A. Nielsen and Isaac L. Chuang. *Quantum computation and quantum information*. eng. 10th anniversary edition. OCLC: 43641333. Cambridge: Cambridge University Press, 2000. ISBN: 978-0-521-63235-5. URL: http://catdir.loc.gov/catdir/samples/cam031/00028911.html.

[252] Adriano Barenco et al. "Elementary gates for quantum computation". In: *Physical Review A* 52.5 (Nov. 1995). Publisher: American Physical Society, pp. 3457–3467. DOI: 10.1103/PhysRevA.52.3457. URL: https://link.aps.org/doi/10.1103/PhysRevA.52.3457.

[253] Colin P. Williams. "Quantum Gates". en. In: *Explorations in Quantum Computing*. Ed. by Colin P. Williams. London: Springer, 2011, pp. 51–122. ISBN: 978-1-84628-887-6. DOI: 10.1007/978-1-84628-887-6_2. URL: https://doi.org/10.1007/978-1-84628-887-6_2.

[254] Marc Bataille. "Quantum circuits of $$\texttt {CNOT}$$gates: optimization and entanglement". en. In: *Quantum Information Processing* 21.7 (July 2022), p. 269. ISSN: 1573-1332. DOI: 10.1007/s11128-022-03577-8. URL: https://doi.org/10.1007/s11128-022-03577-8 (visited on 06/02/2025).

[255] Veronica Mugnaini et al. "Towards the detection of single polychlorotriphenylmethyl radical derivatives by means of Electron Spin Noise STM". In: *Solid State Sciences*. E-MRS symposium N and R 11.5 (May 2009), pp. 956–960. ISSN: 1293-2558. DOI: 10.1016/j.solidstatesciences.2007.09.021. URL: https://www.sciencedirect.com/science/article/pii/S1293255807002713.

[256] Elisabeth M. Fatila et al. "High-Spin Ribbons and Antiferromagnetic Ordering of a MnII-Biradical-MnII Complex". In: *Journal of the American Chemical Society* 135.36 (Sept. 2013). Publisher: American Chemical Society, pp. 13298–13301. ISSN: 0002-7863. DOI: 10.1021/ja4067783. URL: https://doi.org/10.1021/ja4067783.

[257] Ryan Requist et al. "Kondo conductance across the smallest spin 1/2 radical molecule". In: *Proceedings of the National Academy of Sciences* 111.1 (Jan. 2014). Publisher: Proceedings of the National Academy of Sciences, pp. 69–74. DOI: 10.1073/pnas.1322239111. URL: https://www.pnas.org/doi/10.1073/pnas.1322239111.

[258] Junbo Wang et al. "Universal inter-molecular radical transfer reactions on metal surfaces". en. In: *Nature Communications* 15.1 (Apr. 2024). Publisher: Nature Publishing Group, p. 3030. ISSN: 2041-1723. DOI: 10.1038/s41467-024-47252-1. URL: https://www.nature.com/articles/s41467-024-47252-1.

[259] Akio Yoshimori. "Does a localized spin of adsorbed NO survive on Cu(111)?" In: *Surface Science* 342.1 (Nov. 1995), pp. L1101–L1103. ISSN: 0039-6028. DOI: 10.1016/0039-6028(95)00820-9. URL: https://www.sciencedirect.com/science/article/pii/0039602895008209.

[260] Ryuto Yasui, Daiki Shimizu, and Kenji Matsuda. "Large Enhancement of the Single-Molecular Conductance of a Molecular Wire through a Radical Substituent". en. In: *Chemistry – A European Journal* 28.27 (2022). _eprint: https://onlinelibrary.wiley.com/doi/pdf/10.1002/chem.202104242, e202104242. ISSN: 1521-3765. DOI: 10.1002/chem.202104242. URL: https://onlinelibrary.wiley.com/doi/abs/10.1002/chem.202104242.

[261] A. Giraudeau, H. J. Callot, and M. Gross. "Effects of electron-withdrawing substituents on the electrochemical oxidation of porphyrins". In: *Inorganic Chemistry* 18.1 (Jan. 1979). Publisher: American Chemical Society, pp. 201–206. ISSN: 0020-1669. DOI: 10.1021/ic50191a042. URL: https://doi.org/10.1021/ic50191a042 (visited on 05/28/2025).

[262] Alexander G. Martynov et al. "Redox-Triggered Switching of Conformational State in Triple-Decker Lanthanide Phthalocyaninates". eng. In: *Molecules (Basel, Switzerland)* 27.19 (Oct. 2022), p. 6498. ISSN: 1420-3049. DOI: 10.3390/molecules27196498.

[263] Haitao Zhang and Carmen Herrmann. "Interaction between TEMPO Radicals and Gold Surfaces". In: *The Journal of Physical Chemistry C* 127.38 (Sept. 2023). Publisher: American Chemical Society, pp. 19202–19212. ISSN: 1932-7447. DOI: 10.1021/acs.jpcc.3c04401. URL: https://doi.org/10.1021/acs.jpcc.3c04401.

[264] Konstantin M. Schüttler et al. "Low-temperature nucleation and growth of Zn on Au(111) and thermal stability toward (surface) alloy formation". In: *The Journal of Chemical Physics* 155.12 (Sept. 2021), p. 124704. ISSN: 0021-9606. DOI: 10.1063/5.0054980. URL: https://doi.org/10.1063/5.0054980.

[265] W. G. Cullen and P. N. First. "Island shapes and intermixing for submonolayer nickel on Au(111)". In: *Surface Science* 420.1 (Jan. 1999), pp. 53–64. ISSN: 0039-6028. DOI: 10.1016/S0039-6028(98)00817-6. URL: https://www.sciencedirect.com/science/article/pii/S0039602898008176.

[266] P. Ohresser et al. "Magnetism of small Fe clusters on Au(111) studied by x-ray magnetic circular dichroism". In: *Physical Review B* 64.10 (Aug. 2001). Publisher: American Physical Society, p. 104429. DOI: 10.1103/PhysRevB.64.104429. URL: https://link.aps.org/doi/10.1103/PhysRevB.64.104429.

[267] Karina Morgenstern et al. "Cobalt growth on two related close-packed noble metal surfaces". In: *Surface Science* 601.9 (May 2007), pp. 1967–1972. ISSN: 0039-6028. DOI: 10.1016/j.susc.2007.02.018. URL: https://www.sciencedirect.com/science/article/pii/S0039602807001446.

[268] C. S. Casari et al. "Direct observation of the basic mechanisms of Pd island nucleation on Au(111)". In: *Physical Review B* 79.19 (May 2009). Publisher: American Physical Society, p. 195402. DOI: 10.1103/PhysRevB.79.195402. URL: https://link.aps.org/doi/10.1103/PhysRevB.79.195402.

[269] F. Donati et al. "Nucleation and growth mechanisms of Fe on Au(111) in the sub-monolayer regime". In: *Surface Science* 606.7 (Apr. 2012), pp. 702–710. ISSN: 0039-6028. DOI: 10.1016/j.susc.2011.12.008. URL: https://www.sciencedirect.com/science/article/pii/S0039602811004778.

[270] Andrew W. Stephenson et al. "Nucleation and growth of catalytically active Pd islands on Au(111)-22 × studied by scanning tunnelling microscopy". In: *Surface Science* 398.1 (Feb. 1998), pp. 172–183. ISSN: 0039-6028. DOI: 10.1016/S0039-6028(98)80021-6. URL: https://www.sciencedirect.com/science/article/pii/S0039602898800216.

[271] M. Fendrich et al. "Hindered rotation of a copper phthalocyanine molecule on C60: Experiments and molecular mechanics calculations". In: *Physical Review B* 73 (Mar. 2006). DOI: 10.1103/PhysRevB.73.115433.

Part III

Appendix

Publications

Published

Lawes P, Boero M, Barhoumi R, Klyatskaya S, Ruben M, Bucher JP. "Hierarchical Self-Assembly and Conformation of Tb Double-Decker Molecular Magnets: Experiment and Molecular Dynamics". en. In: *Nanomaterials* 13.15 (Aug. 2023)

Patrick LAWES

Molécules thermolabiles déposées par électrospray et sondées par STM

Résumé

L'auto-organisation des centres de spin d'atomes magnétiques habillés par des ligands, appelés « Single Molecule Magnets » (SMM) a fait l'objet de nombreuses études à ce jour. Dans cette thèse, nous nous limiterons aux modifications apportées aux complexes Bis(phthalocyaninato) de terbium (TbPc2). Afin d'étudier cette classe de molécules plus en détail, nous les fonctionnalisons avec des ligands permettant un ajustement de leurs propriétés en vue de leurs applications dans les technologies quantiques telles que le traitement quantique de l'information. Or, l'étude de molécules exotiques sur des surface par microscopie à effet tunnel (STM) dans un environnement d'ultravide (UHV) est souvent limitée par leur thermolabilité. Les molécules complexes étant plus grosses sont généralement thermolabiles et ne peuvent donc pas être déposées par la méthode standard de dépôt par sublimation sous UHV. C'est pourquoi nous utilisons ici la technologie émergente du dépôt par électrospray, plus précisément : Electrospray Ionisation-Controlled Ion Beam Deposition (ESI-CIBD).

Mot clés : Aimant monomoléculaire, Microscope d'effet tunnel, Electrospray ionisation

Résumé en anglais

The self-organization of spin centres of magnetic atoms dressed by ligands, so called single molecule magnets (SMMs), is widely studied and reported. In this thesis, the study is confined to modifications on the bis(phthalocyaninato) terbium complexes (TbPc2). In order to study these molecules in greater detail, more exotic ligands can be functionalised to the molecule in order to tune surface properties, allowing for wider development of expanding quantum technologies, such as quantum information processing. The study of newer more exotic molecules on surface in ultra high vacuum (UHV) by scanning tunnel microscopy (STM) are often limited by their thermolability. Molecules of greater volume and thus greater complexity are generally highly thermolabile and thus not depositable by the standard UHV deposition method of sublimation. As such the emerging technology of electrospray deposition has been used, specifically the so named Electrospray Ionisation-Controlled Ion Beam Deposition (ESI-CIBD) system.

Key words: Single molecule magnets, Scanning tunneling microscope, electrospray ionisation